ADVANCED CHARACTERIZATION OF BATTERY CELL DYNAMICS

ADVANCED CHARACTERIZATION OF BATTERY CELL DYNAMICS

By MARVIN MESSING, M.A.Sc, B.Eng.

A Thesis Submitted to the School of Graduate Studies in Partial Fulfilment of the Requirements for the Degree of Doctor of Philosophy

McMaster University

DOCTOR OF PHILOSOPHY (2021), McMaster University, Hamilton, Ontario

(Mechanical Engineering)

TITLE:	Advanced Characterization of Battery Cell Dynamics
AUTHOR:	Marvin Messing, M.A.Sc, B.Eng.
SUPERVISOR:	Professor Saeid R. Habibi
NUMBER OF PAGES:	xx, 223

Lay Abstract

Replacing conventional gasoline/diesel powered cars with battery powered vehicles is part of a solution to the climate crisis. However, the initial costs paired with range anxiety stops many from switching to electric cars. Both cost and range are related to the battery pack. To achieve the best possible range for the lowest possible cost, battery packs must be carefully controlled by sophisticated algorithms. Unfortunately, battery range or health cannot be measured directly, but must be inferred through measurable indicators. This thesis explores battery behavior under different operating conditions and develops improved methods which can be used to determine battery health and/or range. A powerful method usually used only in laboratory settings is studied and improved to make it more suitable for implementation in electric cars. In this work it is used for accurate battery health determination. Furthermore, a strategy for improving battery range determination at low temperatures is also proposed.

Abstract

Battery Electric Vehicles (BEV) are gaining market share but still must overcome several engineering challenges related to the lithium-ion battery packs powering them. The batteries must be carefully managed to optimize safety and performance. The estimation of battery states, which cannot be measured directly, is an important part of battery management and remains an active area of research since small gains in estimation accuracy can help reduce cost and increase BEV range.

This thesis presents several improvements to battery state estimation using different methods. Electrochemical Impedance Spectroscopy (EIS) is receiving increased attention from researchers as a method for state estimation and diagnostics for real-time applications. Due to battery relaxation behaviour, long rest times are commonly used before performing the EIS measurement. In this work, methods were developed to significantly shorten the required rest times, and a State of Health (SoH) estimation strategy was proposed by taking advantage of the relaxation effect as measured by EIS. This method was demonstrated to have an estimation error of below 1%.

At low temperatures, the accuracy of the battery model becomes poor due to the non-linear battery response to current. By using an adaptive filter called the Interacting Multiple Model (IMM) filter, the next part of this work showed how to significantly improve low temperature State of Charge (SoC) estimation. Further reduction in estimation errors was achieved by pairing the IMM with the Smooth Variable Structure Filter (SVSF), for SoC estimation errors below 2%.

The work presented in this thesis also includes the application of Deep Neural Networks (DNN) for SoC estimation from EIS data. Finally, an extensive aging study was conducted and an

accelerated protocol was compared to a realistic drive cycle based protocol using EIS as a characterization tool.

Keywords:

Batteries, State Estimation, Electrochemical Impedance Spectroscopy, Adaptive Filtering, Battery Aging, Deep Neural Networks

Acknowledgement

First, I would like to thank my supervisor at McMaster, Dr. Saeid Habibi as well as my supervisor at Cadex, Dr. Tina Shoa who worked together to provide this opportunity for me and supported me throughout. I would also like to thank my supervisory committee members Dr. Gillian Goward and Dr. Ryan Ahmed for their feedback.

My thanks also to the Natural Sciences and Engineering Research Council of Canada (NSERC), Ontario Graduate Scholarship (OGS) program, Queen Elizabeth II Graduate Scholarship in Science and Technology awards program, and Cadex Electronics for financial support.

Special thanks also to our industry partner Cadex Electronics for allowing me the use of lab space and equipment as well as support my projects with technical guidance.

At the Center for Mechatronics and Hybrid Technologies (CMHT) I would like to thank Cam Fisher, Jessica Petrunti, Zeina Tawakol and my fellow grad students with special thanks to Sara Rahimifard for her friendship and support, and Ben Miethig for welcoming me with open arms on my first day and his continued friendship. I would also like to thank Dr. Phil Kollmeyer for sharing his battery testing knowledge.

I am forever grateful for the support and encouragement from my family and friends, with special thanks to my partner Erin for her love and support, and for enduring my absence for many months while I was splitting my time between Vancouver and Hamilton.

Co-Authorship

This thesis has been prepared in accordance with the regulations for a sandwich thesis format or as a compilation of research papers stipulated by the faculty of graduate studies at McMaster University. This thesis consists of the following papers:

Paper I

M. Messing, T. Shoa and S. Habibi, ***"Lithium-Ion Battery Relaxation Effects,"*** *Published in 2019 IEEE Transportation Electrification Conference and Expo (ITEC)*, 2019, pp. 1-6, doi: 10.1109/ITEC.2019.8790449[1].

Marvin Messing conducted the literature review, designed experiments, designed and built test equipment, conducted experiments, analyzed results, and wrote paper I.

Dr. Shoa and Dr. Habibi provided research guidance and edited the paper.

Paper II

M. Messing, T. Shoa and S. Habibi, ***"Electrochemical Impedance Spectroscopy With Practical Rest-Times for Battery Management Applications,"*** *Published in IEEE Access*, vol. 9, pp. 66989-66998, 2021, doi: 10.1109/ACCESS.2021.3077211.

Marvin Messing conducted the literature review, designed experiments, designed and built test equipment, conducted experiments, analyzed results, and wrote paper II.

Dr. Shoa and Dr. Habibi provided research guidance and edited the paper.

Paper III

M. Messing, T. Shoa and S. Habibi, ***"Estimating Battery State of Health using Electrochemical Impedance Spectroscopy and the Relaxation Effect,"*** *Published in Journal of Energy Storage*, vol. 43, Article 103210, 2021, doi: 10.1016/j.est.2021.103210.

Marvin Messing conducted the literature review, designed experiments, designed and built test equipment, conducted experiments, analyzed results, and wrote paper III.

Dr. Shoa and Dr. Habibi provided research guidance and edited the paper.

Paper IV

M. Messing, T. Shoa, R. Ahmed and S. Habibi, ***"Battery SoC Estimation from EIS using Neural Nets,"*** *Published in 2020 IEEE Transportation Electrification Conference & Expo (ITEC)*, 2020, pp. 588-593, doi: 10.1109/ITEC48692.2020.9161523[1].

Marvin Messing conducted the literature review, designed experiments, designed and built test equipment, conducted experiments, analyzed results, and wrote paper IV.

Dr. Shoa, Dr. Ahmed and Dr. Habibi provided research guidance and edited the paper.

Paper V

M. Messing, S. Rahimifard, T. Shoa, and S. Habibi, ***"Low Temperature, Current Dependent Battery State Estimation using Interacting Multiple Model Strategy,"*** *Published in IEEE Access*, 2021, doi: 10.1109/ACCESS.2021.3095938.

Marvin Messing conducted the literature review, designed experiments, designed and built test equipment, conducted experiments, analyzed results, and wrote the majority of paper V.

Sara Rahimifard provided SVSF-VBL Matlab modules, drafted the background theory sections on SVSF, and provided paper edits.

Dr. Shoa and Dr. Habibi provided research guidance and edited the paper.

Paper VI

M. Messing, T. Shoa and S. Habibi, ***"EIS from Accelerated and Realistic Battery Aging,"*** *Published in 2021 IEEE Transportation Electrification Conference & Expo (ITEC)*, 2021, pp. 720-725, doi: 10.1109/ITEC51675.2021.9490091[1]

Marvin Messing conducted the literature review, designed experiments, designed and built test equipment, conducted experiments, analyzed results, and wrote paper VI.

Dr. Shoa, Dr. Ahmed and Dr. Habibi provided research guidance and edited the paper.

[1] In reference to IEEE copyrighted material which is used with permission in this thesis, the IEEE does not endorse any of McMaster's products or services. Internal or personal use of this material is permitted. If interested in reprinting/republishing IEEE copyrighted material for advertising or promotional purposes or for creating new collective works for resale or redistribution, please go to http://www.ieee.org/publications_standards/publications/rights/rights_link.html to learn how to obtain a License from RightsLink.

Permission to Use

In presenting this thesis in partial fulfillment of the requirements for a Postgraduate degree from McMaster University, I agree that the Libraries of this University may make it freely available for inspection. I further agree that the permission for copying this thesis in any manner, in whole or in part for scholarly purposes, may be granted by the professors who supervised my thesis work or, in their absence, by the Head of the Department or the Faculty Dean in which my thesis work was conducted. It is understood that any copying or publication or use of this thesis or parts thereof for financial gain shall not be allowed without my written permission. It is also understood that due recognition shall be given to me and McMaster University in any scholarly use which may be made of any material in my thesis. Requests for permission to copy or to make other use of material in this thesis, in whole or part, should be addressed to:

Head of the Department of Mechanical Engineering
McMaster University
Faculty of Engineering
1280 Main Street West
Hamilton, Ontario L8S 4L6
Canada

Table of Contents

Table of Figures

List of Tables

Chapter 1: Introduction

To have one or several vehicles standing at the ready at any time to quickly get people to near locations within tens or even hundreds of kilometers is one of the great luxuries enjoyed by many since the late 20th century. Although public transportation is well developed in many countries, there is nothing quite like the feeling of freedom that comes with owning a vehicle. However, the majority of vehicles still emit exhaust gases which contribute to two major issues: 1) air pollution and 2) the climate crisis. The findings of a recent study on global air pollution highlight again the need to remove sources of pollution from densely populated areas [1], where people and vehicles are found in large concentrations. For example, the study found that over one million people die each year due to air pollution in China alone. In addition, it found that air pollution is causing a reduction of almost two years in the global average life expectancy. The sources and impact of the climate crisis are detailed in a United Nations (UN) report, which predicts further increases in flooding, droughts and hurricanes around the world, if Greenhouse Gas (GHG) emissions are not reduced drastically [2]. Global transportation comprises around 15% of all GHG emissions [3]. In the United States, this percentage is almost double (29%) and almost 60% of that is due to light duty vehicles [4]. Therefore, the automotive industry is heavily investing in Electric Vehicles (EV) as part of the solution to the global air pollution problem and climate crisis.

Battery packs in EVs are overdesigned to carry more capacity than they use. This is done to ensure that the battery operating range stays within safe charge and discharge limits [5],

[6]. However, accurately determining those limits over a wide range of operating conditions and variations in battery designs is a significant challenge [7]. EV battery packs are continuously monitored by Battery Management Systems (BMS) which contain advanced algorithms to achieve optimal and safe operation. Extensive research is currently carried out find new ways to maximize the useable battery capacity. One of the most challenging aspects of battery management is the estimation of hidden battery states. This thesis explores state estimation for lithium-ion batteries and EV applications. The findings of this thesis contribute to the improvement of battery state estimation through in-depth research into impedance spectroscopy, adaptive filters, and machine learning methods. In this Chapter, background material is reviewed in Sections 1.1 to 1.8 including introductions to Lithium-Ion batteries, impedance spectroscopy, state estimation, neural networks and battery testing. In Section 1.9 the research hypotheses and contributions are described. Section 1.10 provides an outline of the thesis.

1.1 LITHIUM-ION BATTERIES

Lithium-ion chemistries dominate the market for secondary batteries, especially, for all-electric vehicles [8]. A lithium-ion battery consists of an anode (negative electrode), electrolyte, a separator, and a positive electrode (cathode), as shown in Figure 1-1. During the charge process, electrons flow into the anode and combine with lithium-ions to intercalate lithium into the electrode. During discharge, electrons flow out of the anode and into the cathode to intercalate there [9]. The porous separator ensures that electrons cannot pass from anode to cathode without an external circuit. There is a tendency for electrolyte

reduction at the negative electrode (Anode) due to its low potential. This causes the electrolyte to react with the electrode and leads to the formation of the Solid Electrolyte Interphase (SEI) layer. After the SEI layer has formed, it protects the electrode from further undesirable reactions with the electrolyte. On the positive electrode a similar layer is called the Cathode Electrolyte Interphase (CEI) [10]. The CEI is thinner since there is only a small, or no driving potential on the cathode.

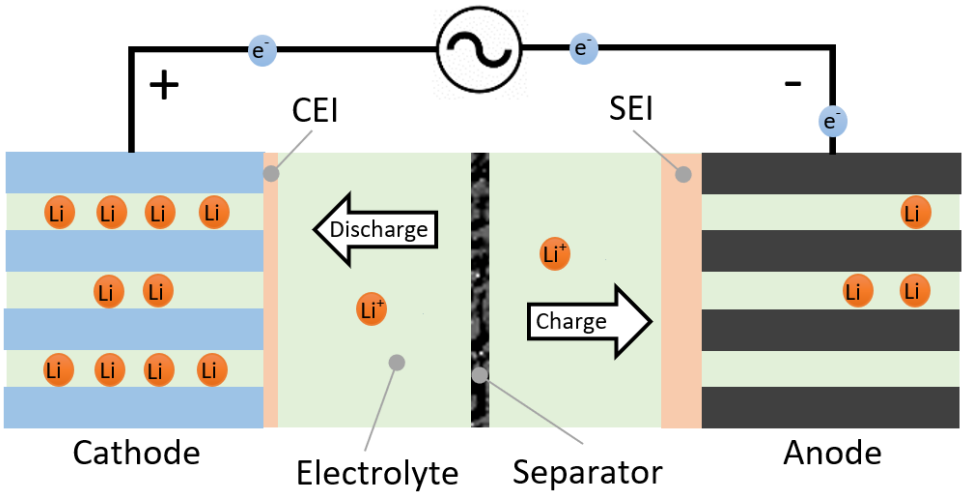

Figure 1-1: Lithium-ion battery components and operation

There are several variants of lithium-ion chemistries with a broad range of properties. Lithium cobalt oxide (LCO) batteries are the most common type in many applications. However, the high cost, poor durability and low availability of cobalt makes LCO an unfavourable choice for large battery packs [11,12]. Instead, nickel cobalt aluminum oxide (NCA) cells can eliminate some of the drawbacks of LCO, but safety concerns remain. Specifically, the risk of thermal runaway is high in NCA batteries which has lead to several EV fires [12]. Nickel manganese cobalt oxide (NMC) lithium-ion cells have high energy

density [12] and are, therefore, chosen by some car manufactures for EV battery packs. However, the thermal runaway risk is still present, although only at higher temperatures compare to NCA. Examples of catastrophic battery failure also exist for NMC battery packs [12]. Lithium-ion phosphate (LFP) and LCO with spinal lithium titanium oxides (LTO) anodes deliver the best results in terms of safety, but energy density is reduced [8]. Thus, the selection of presently commercialized lithium-ion batteries is a trade-off between energy density (which translates to EV range) and safety.

There is growing concern that conventional lithium-ion batteries (LIB) cannot meet the increasing energy storage demands for mobile applications. Therefore, improvements to lithium-based and alternative chemistries are constantly explored. One promising improvement to lithium-ion chemistries is the use of Solid-State Electrolyte (SSE) instead of organic solvents. The use of SSE allows for increased energy density, increased battery safety as well as reduced volume due to bi-polar cell stacking [13], [14]. However, challenges concerning the transport properties of SSEs as well as the scalability of manufacturing processes must be addressed before SSEs become a viable solution. Nonetheless, Solid State Batteries (SSB) are presently regarded as the next leap forward in battery technology.

Some advances have been made in the development of sodium-ion batteries (NIB). In [15] the progress and challenges are discussed. NIBs show promising performance; however, more studies are required to form a complete picture of the properties of NIBs with regards to lifetime, safety, and cost.

1.1.1 Aging Mechanisms & Stressors

The useful lifetime of a lithium-ion battery is a function of its operating conditions. To achieve maximum lifetime, the battery should be kept at room temperature and charged or discharged at low current, strictly between optimal voltage limits. However, for automotive applications, for example, the operating temperatures can range from -30°C to +52°C [16], charge rate is high, to reduce charging time, and discharge profiles depend on the driving habits of the operator. The impact of deviating from optimal operating conditions and the resulting battery degradation, are studied extensively in literature, for a range of automotive battery types. Gao et al. studied voltage limits as well as charge rates of an 18650 LCO battery and found a drastic increase in degradation rates, for voltages above 4.2 V and charge rates above 1C [17]. Su et al. applied different stressors and found that charge current, charge voltage, temperature, charge current, and discharge current contribute heavily to battery degradation of an 18650 NCA battery [18]. They separate degradation due to temperature into low-temperature (below 25°C) degradation and high-temperature (above 25°C) degradation. This difference in temperature degradation mechanisms was also found by Waldmann et al., for an 18650 NMC battery [19]. A prismatic NMC cell was studied by Waag et al. to show the change in battery impedance (see Section 1.1.2) with temperature, SoC, and aging; however, the aging procedure is not specified [20]. Leng et al. used a prismatic LCO battery to study the effect of temperature on the parameters of a combined electrochemical-electric model [21]. They found the parameters changed significantly with increased operating temperature between 25°C and 55°C and related each

parameter to the degradation of components inside the battery. In addition, they showed the degradation of the electrodes to be the main contributor to aging.

Another form of battery aging is calendar aging which refers to degradation that occurs while the battery is at rest over long periods of time. Calendar aging was investigated by [22–25], but no clear consensus exists. This may be due to a combination of different behaviours between chemistries as shown by [25], who showed different aging behaviors with temperature for LMO, NMC, LFP, and NCA. The lack of consensus may also be due to additional degradation introduced by testing procedures as mentioned by [22] who argue that some types of characterization tests introduce additional aging. Since calendar aging happens slowly over a long period of time, it is often difficult to distinguish it from degradation caused by diagnostic testing.

Finally, some studies show that vibration also causes battery degradation [26,27]. However, a recent study by Hooper et al. [28] shows only a small, yet statistically significant, increase in ohmic resistance after an equivalent vibration profile of 10 years of EV driving, for 18650 NCA cells. This study included control samples to differentiate degradation related to vibration from calendar aging.

A detailed review of lithium-ion battery aging mechanisms is given by [11]. The main mechanisms are the growth of SEI, the buildup of other surface films on the electrodes, and the break-down of electrode material. The initial formation of the SEI is important for the operation of the battery as it electrically separates the electrolyte from the electrode. However, over time it grows by consuming lithium-ions which causes capacity fade.

1.1.2 IMPEDANCE

The components of the battery as well as the electrochemical reactions taking place during battery operation cause several overpotentials (or losses). Figure 1-2 shows a typical voltage drop which occurs when current is drawn from the battery. The voltage profile shows three drop regions which represent different overpotentials. These overpotentials can be grouped as follows:

1. Overpotential η_O manifests as the immediate voltage drop observed within a few milliseconds after current is applied. It is caused by the ohmic resistances of the cell which include current collectors, the solid parts of the electrodes, electrolyte resistance, and interface resistances between current collectors and electrodes.

2. Overpotential η_C causes a further voltage drop within a few seconds and is a combination of charge transfer losses η_{CT}, SEI losses η_{SEI} and contact resistance losses η_{CC}.

$$\eta_C = \eta_{CT} + \eta_{SEI} + \eta_{CC} \quad (1\text{-}1)$$

3. Overpotential η_D is a result of diffusion losses from lithium inside the electrodes (solid state) as well as from lithium ions in the electrolyte (liquid state) and occurs during sustained current draw.

Each of the overpotentials occur because of some form of opposition to current flow through the battery. This current flow opposition is measured by impedance, a combination of resistance and reactance (capacitive and inductive) effects. The impedance of a battery changes depending on the battery chemistry and materials used, the excitation signal, the SoC, the SoH and the battery temperature. In Section 1.2 a method is introduced that can

identify the impedance of the different battery components in a non-destructive, in-vivo way. Studying battery impedance under different operating conditions can provide insight into battery dynamics and battery states. In Section 1.3 battery models are described which imitate the impedance behavior of batteries. Accurate battery models are a crucial part of battery state estimation. In the next section the battery relaxation effect is discussed which is closely related to the impedance characteristics of a battery.

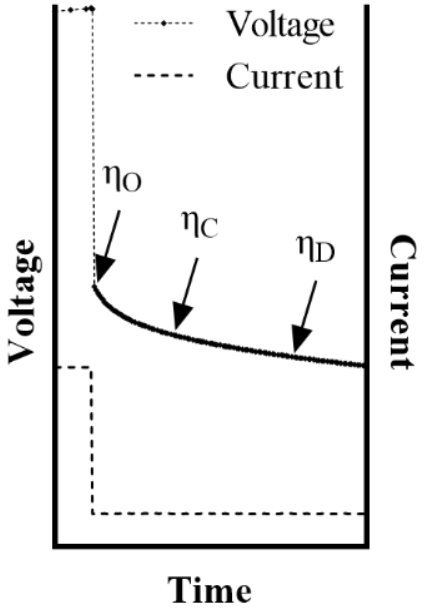

Figure 1-2: Overpotentials Caused by Impedances

1.1.3 RELAXATION EFFECT

When a load is applied to a battery its voltage drops due to overpotentials which occur because of impedances as described in the previous section. If the load is removed the battery voltage does not instantly rise back to a constant Open Circuit Voltage (OCV) but instead recovers slowly, stabilizing over time. This is known as the battery relaxation effect. Figure 1-3 shows battery voltage behaviour during a discharge pulse followed by a rest

period at OCV. At the start of the rest period, the voltage rises immediately to recover the ohmic losses. During the first few minutes of the rest period, the voltage continues to rise as lithium ions diffuse back into the electrodes as shown in Figure 1-4b. The relaxation effect continues for hours after that with the voltage increasing slowly over time while lithium is diffusing inside the electrodes to equalize micro potentials as shown in Figure 1-4a [29], [30]. The relaxation effect has several implications for battery characterization and management:

- Battery models must reflect relaxation behaviour. The accuracy of battery models is crucial to the performance of state estimation algorithms, so they must capture both load conditions and rest conditions accurately. Additional battery model terms may be necessary to capture the time constants associated with the long-term effects.
- The OCV of a battery is a useful quantity for SoC estimation. However, true OCV only occurs when the relaxation effect has slowed sufficiently. This means long rest times are required before accurate OCV can be measured.
- Rest times must be included for most test procedures to ensure consistent response of the battery. A relaxed battery will respond differently to loads than a battery which was recently excited. Therefore, rest times of 1 to 4 hours are usually observed in between excitation tests.

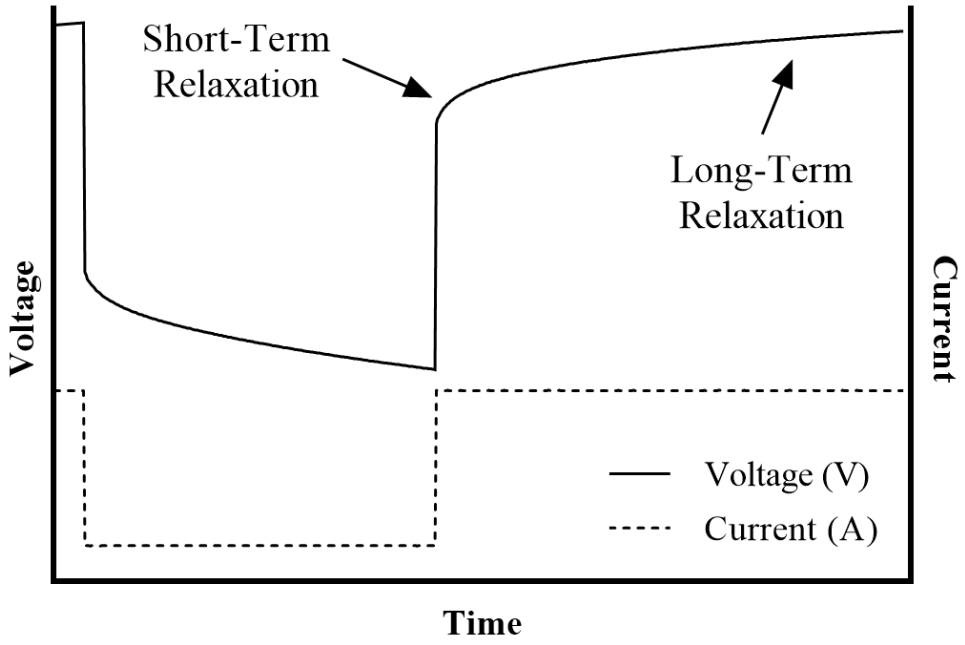

Figure 1-3: Battery Voltage Relaxation.

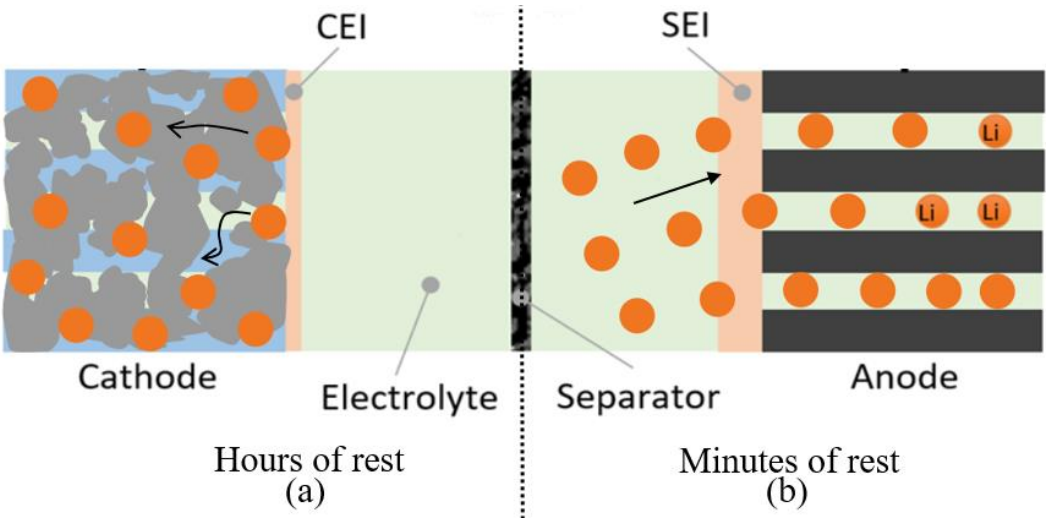

Figure 1-4: Battery Relaxation Effect Process Long Term (a), Short Term (b).

In the next section, an impedance measurement technique is described for which the impact of the relaxation effect on measurement results must be considered.

1.2 ELECTROCHEMICAL IMPEDANCE SPECTROSCOPY

One of the major areas of research presented in this thesis concerns the results obtained using Electrochemical Impedance Spectroscopy (EIS). EIS can reveal a detailed snapshot of the impedance of the internal components of batteries, which can be interpreted to indicate the health of various components, the battery state, temperature, and fault conditions. EIS is based on small signal excitation at different frequencies. For example, in Galvanostatic EIS (GEIS) a sinusoidal current signal is applied to the battery at different frequencies and the corresponding voltage response is measured. The current signal must be sufficiently low for the battery to remain in its linear response region, but high enough to maintain adequate signal to noise ratio. The current value which satisfies these requirements depends on the battery type and size as well as hardware characteristics of the measurement equipment. A linear response of the battery is usually ensured if the battery voltage stays within +/- 10 mV throughout the EIS test. A voltage-controlled version of EIS, called Potentiostatic EIS (PEIS), can guarantee this voltage range by applying voltage and measuring the current. PEIS is primarily used in the work described in this thesis. The measured EIS data can be converted to frequency domain using the Discrete Fourier Transform (DFT) [31] to produce a characteristic plot called the Nyquist plot as shown in Figure 1-5.

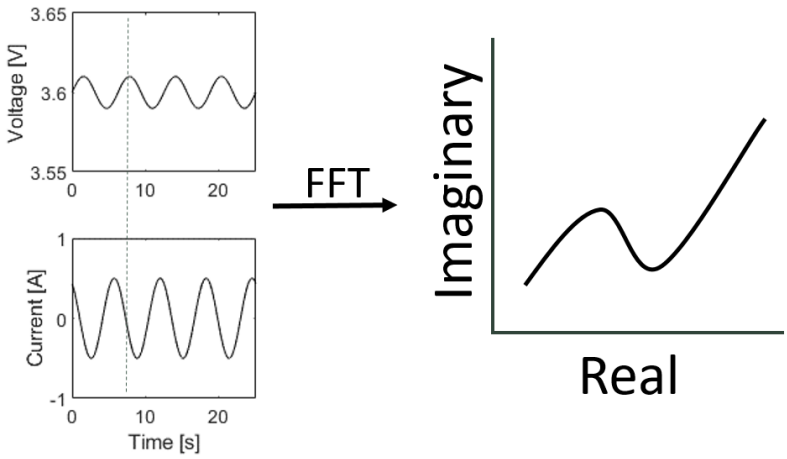

Figure 1-5: EIS Signal and Analysis

Given a sine wave signal $f(i)$ in time domain with discrete points i from 0 to $N-1$, the DFT $F(n)$ at point n in the frequency domain can be calculated for each n from 0 to $N-1$ using Equation 1-3.

$$F(n) = \frac{1}{N}\sum_{i=0}^{N-1} f(i) \exp\left(-j\frac{2\pi n i}{N}\right) \quad (1\text{-}2)$$

The DFT $F(n)$ produces complex numbers (real and imaginary pairs) for each n which correspond to frequencies from 0 to the sampling frequency f_s. The exact frequency f_n for each n is calculated using Equation 1-3.

$$f_n = \frac{n}{N} f_s \quad (1\text{-}3)$$

However, the highest frequency f_{max} which can be observed is half of the sampling frequency according to the Nyquist theorem as shown in Equation 1-4.

$$f_{max} = \frac{1}{2} f_s \quad (1\text{-}4)$$

Therefore, only the first half of the DFT results from $n = 0$ to $n = \frac{N-1}{2}$ produce meaningful results, beyond that the results repeat. The following is an example of the DFT calculation:

Assuming $f(i) = \sin\left(\frac{2\pi f_1 i}{f_s}\right)$ with $f_1 = 10Hz$ and $f_s = 0.5kHz$, $N = \frac{f_s}{f_1} = 50$ points are obtained for one sine wave period as shown in Figure 1-6a. The Matlab implementation of the Fast Fourier Transform (FFT), a more computationally efficient version of the DFT, can be used to obtain the transformed sine wave data. Figure 1-6b shows the magnitude of the FFT output for frequencies from 0 to f_s. The first peak corresponds to the frequency of the time domain sine wave signal with the frequency domain index $n = 1$, which can be found using Equation 1-3. The complex valued FFT result at $n = 1$ is $F(1) = 1.55 - j25.18$ with an absolute value of $|F| = 25.23$.

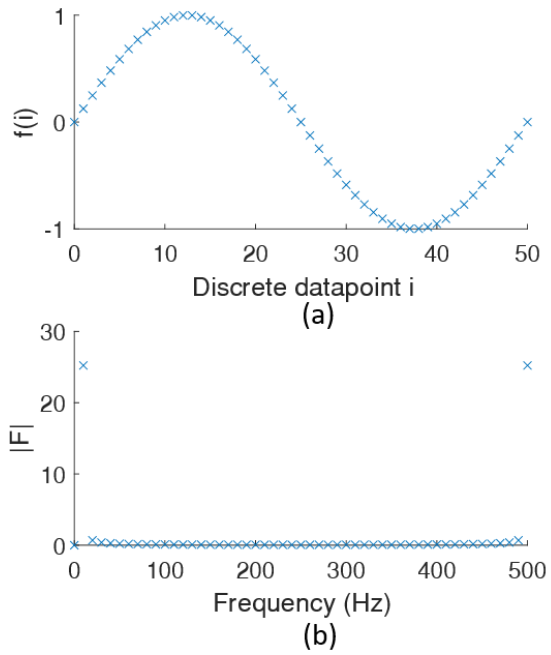

Figure 1-6: A discrete time domain sine wave (a) transformed in to the frequency domain using the Fourier Transform (b).

The signal in the example above could be one frequency of the EIS signal applied to a battery, a sine wave with 1 Ampere amplitude for example. The impedance can then be

calculated using Equation 1-5. Here, $F_{in}(n)$ is the FFT (or DFT) of the input signal and $F_{out}(n)$ the FFT of the output signal, the voltage response of the battery in the case of this example. The frequency domain index corresponding to the signal frequency f_n is $n = 1$. Finally, the impedance Z is obtained using Ohm's law $R = \frac{V}{I}$, or in this case, the FFT of the voltage signal at index n divided by the FFT of the current signal at index n is equal to the impedance as shown in Equation 1-5.

$$Z = F_{out}(1)/F_{in}(1) \tag{1-5}$$

The above method assumes a signal which is low in noise and has an integer valued number of periods per sine wave frequency. The former depends on the quality of the instrumentation and the latter on the signal generation. If the signals are noisy, the measurements can be averaged over several sinewave periods to produce improved results. If the signal contains incomplete sine wave periods, windowing can be applied to the FFT to remove the incomplete signal parts. In laboratory settings, potentiostats are frequently used to perform EIS tests. These devices contain precision circuitry to generate clean sine waves and accurately measure the response of electrochemical devices such as batteries. Most modern portentiostats also include on-board signal post-processing features.

The impedance Z for frequency f_n represents a point on the Nyquist plot, where the real part of Z is plotted against the imaginary part. By convention, the imaginary part is multiplied by -1. Figure 1-7 shows an example of a Nyquist plot with real and imaginary pairs plotted for EIS excitation signals between 700 Hz and 0.4 Hz [32]. EIS, Nyquist plots

and how the data can be used for battery modeling are discussed more in Chapters 2, 3 and 5.

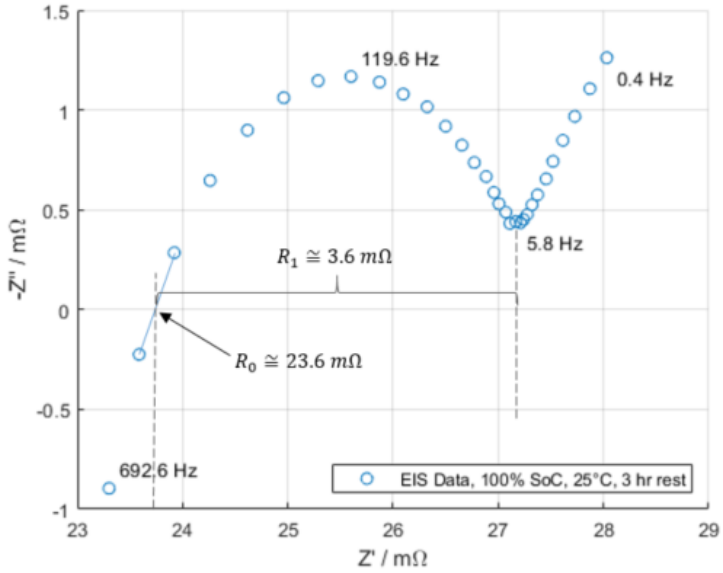

Figure 1-7: Nyquist plot showing EIS results in frequency domain [32].

EIS is used heavily in laboratory settings for battery characterization. However, studies have indicated some success in implementing feasible setups to perform EIS on-board a vehicle for real-time diagnostics. Abedi et al. [33] reviewed state-of-the art methods for implementing online EIS and found that efforts are centered on utilizing parts of existing balancing circuitry to generate the EIS signal. Further real-time EIS solutions are discussed in Chapters 3 and 6.

1.3 BATTERY MODELING

Battery models fall into three categories: Electrochemical Models (EM) (based on fundamental equations), empirical white box models, and empirical black box models. Black box models are usually used to model not just the measurable behaviour of a battery,

but also the hidden states. Battery states and black box models are discussed in sections 1.4 and 1.7. EMs have the potential to be highly accurate since they can closely reflect the real behaviour of batteries. However, to increase accuracy, more complex processes must be modeled, increasing the overall complexity of the model. In particular, differential equations are frequently used for EMs, requiring significant computational resources. In addition, constants associated with the physical processes must be parameterized by performing extensive laboratory experiments [34]. Therefore, EMs are impractical for real time applications, such as battery management systems in electric vehicles (EV) [35]. In contrast, empirical models can be simple and still provide high accuracy, but only for a limited range of conditions. Furthermore, accuracy is often hard to interpret since it depends on the quality of the underlying data and experiments [36]. Still, empirical models can provide a suitable trade-off between accuracy and complexity.

The most popular white-box models are equivalent circuit models (ECM). ECMs model batteries as circuits of ideal electrical components (resistors, capacitors) to approximate processes inside the battery. For example, the overpotentials described in Section 1.1.2 could be modeled using the circuit shown in Figure 1-8a [37]. In this circuit, series resistances are used to represent the ohmic resistances at the anode and cathode, and resistor-capacitor (RC) pairs model impedances of the interface layers (SEI and CEI), electrode/electrolyte charge transfer, and electrode diffusion. However, the values for each capacitance and resistance must be determined experimentally, and simple, non-destructive battery tests cannot distinguish between anode and cathode overpotentials. In addition, the SEI impedance is much more dominant than the CEI impedance, so CEI is often omitted.

Instead, the anode and cathode circuit elements are combined into a series resistance followed by RC pairs as shown in Figure 1-8b. Depending on the application, additional RC-elements can be added to capture battery behaviour more closely. For example, dynamic load profiles of EV applications may require additional RC element with small time constants. Stationary battery applications, where load profiles are constant for longer periods of time, may required larger time constants.

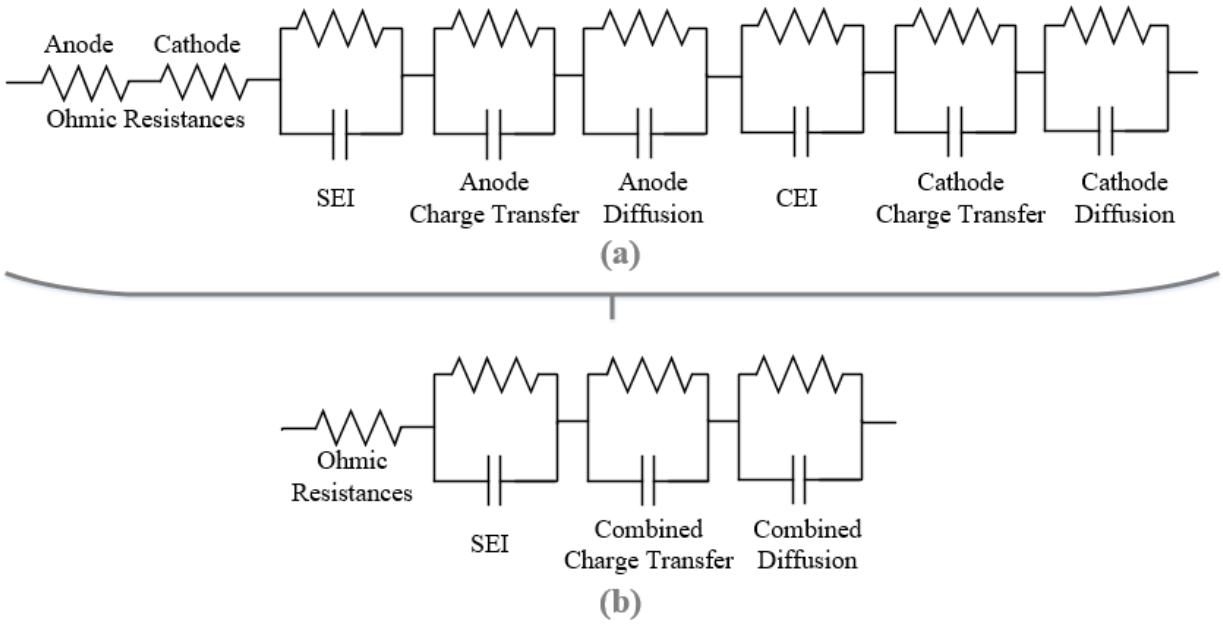

Figure 1-8: ECM to model battery internal processes separated for anode and cathode (a) and combined (b).

Figure 1-9 shows the fundamental ECM which consists of RC parallel pairs repeated n times in series. Since RC pairs only loosely represent the physical processes, n can be increased to model experimental data more closely. Many different circuits have been proposed to increase accuracy with fewer circuit elements, each with their own advantages and drawbacks [38]. However, there are an infinite number of circuit configurations

possible for any experimental result, which questions the relevance of fitted parameters. Each circuit element must be carefully related to physical phenomena inside the battery to give ECM models more relevance.

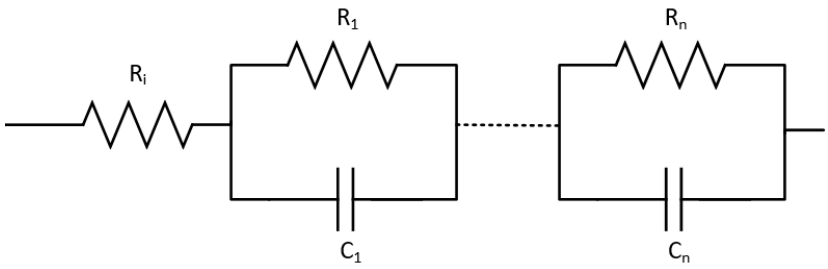

Figure 1-9: RC battery model of order n

Nonetheless, ECMs are used in EVs for battery state estimation due to their simplicity. First and second order RC circuits were compared by [39], showing a reduction in SoC estimation error for the higher order models. In [40], a third order RC circuit was used, showing further reduction in estimation error. ECM parameters are usually obtained using a discharge pulse method, where the characteristics of the voltage response can be related to resistance and capacitance values. A common protocol is the hybrid pulse power characterization (HPPC) pulse [41] which is used by the US Department of Energy (DoE).

ECM parameters can also be obtained by fitting the circuit to the characteristic frequency response of a battery using EIS (Section 1.2). EIS gives a much more detailed picture of the battery response and shows the limitations of RC based circuits as shown by Farmann et al. [7]. They showed how RC-based circuits can only roughly approximate the shape of the battery impedance response. In the next section, impedance models are introduced, an improved version of ECMs which can model EIS data more closely.

1.3.1 IMPEDANCE MODELS

The impedance profile of a battery holds useful information about its internal condition. Impedance is the combination of reactance and resistance and comes from the interaction between different materials inside a battery, the material characteristics, and from chemical reactions [42] as was introduced in Section 1.1.2. A detailed picture of the battery impedance can be obtained using EIS as described in Section 1.2. A Nyquist plot obtained from EIS data of a fresh lithium-ion cell is shown in Figure 1-10a. The ECM shown in the previous section (Figure 1-9) with $n = 2$ can be used to fit to the Nyquist plot. For this data, with $n = 2$ (i.e. two RC-elements) the charge transfer process and the diffusion process are captured. The SEI impedance is negligible here, due to the high SoH and specific properties of the cell used. The ECM fit is shown in Figure 1-10b. As is apparent in the figure, the ECM fit does not follow the data very closely. This is because processes like charge transfer in a battery are non-ideal and, therefore, exhibit a distribution of time constants, rather than a single time constant modeled by one RC-branch. Increasing n can capture more time constants and improve the fit, however, the model complexity grows and the meaning of model parameters is obscured.

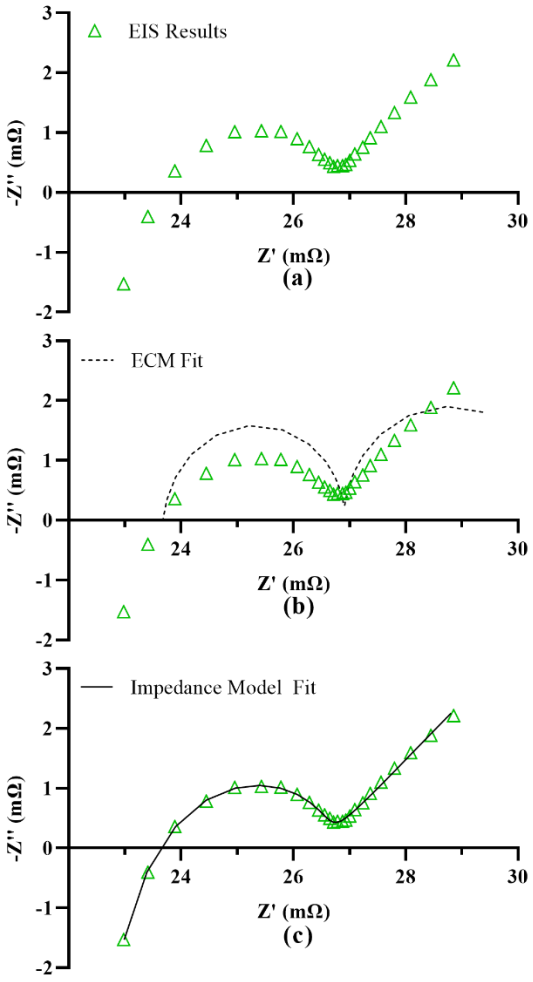

Figure 1-10: EIS Nyquist plot (a), with RC model fit (b), with fractional fit (c).

Alternatively, the ECM can be refined by introducing a non-ideal circuit component: The Constant Phase Element (CPE) [31]. The CPE can model the capacitive behaviour of non-ideal processes with only a single additional model parameter α, the constant phase exponent. The CPE impedance is slightly modified from the ideal capacitor impedance ($Z_C = \frac{1}{i\omega C}$) as shown in Equation 1-6.

$$Z_{CPE} = \frac{1}{Q(i\omega)^{\alpha}} \tag{1-6}$$

Here, Q is related to the capacity in units of ($F\ s^{\alpha-1}\ cm^{-1}$). The exponent α has a range of $0 \leq \alpha \leq 1$, and for $\alpha = 1$, $Z_{CPE} = Z_C$ (with $Q = C$), and the CPE becomes an ideal capacitor. The CPE models a non-ideal capacitor which has an imaginary component as well as a real component. Physically this means the capacitor is "leaking", i.e. experiencing a current drain. The CPE can also be used in parallel with a resistor and the combined circuit is called a Zarc element. Figure 1-11 shows a circuit which uses a Zarc element to model the charge transfer processes (anode and cathode combined) and a CPE to model diffusion processes (also anode and cathode combined). In addition, an inductor is added to model the inductive effects resulting from cell connections and measurement cables at high frequencies. Such models are often referred to as impedance models to distinguish them from RC circuits [43]. The fit of this model to the EIS data is shown in Figure 1-10c. This model can accurately reflect the impedance behaviour of the battery. The Zarc element ($Q_1, \alpha_1||R_1$) results in a depressed semi-circle due to the use of the CPE. This better reflects the multiple time constants associated with the charge transfer processes, which is non-ideal due to surface roughness and porous electrodes. The CPE in series creates an angled line, where the angle is defined by the exponent α. If $\alpha = 1$, the angle is 90° resulting in a vertical line representing an ideal capacitor. This series CPE (Q_2, α_2) models the non-ideal diffusion processes inside the battery electrodes.

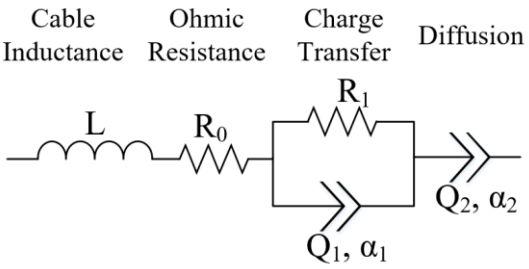

Figure 1-11: Impedance model used to model EIS response

The complex impedance Z, of the impedance model in Figure 1-11 changes with frequency ω according to Equation 1-7, where the time constant $\tau = \left(R_p Q_p\right)^{1/\alpha}$.

$$Z(\omega) = i\omega L + R_s + \frac{R_p}{1+R_p Q_p (i\omega\tau)^{\alpha}} + \frac{1}{Q_d (i\omega)^{\beta}} \tag{1-7}$$

A special case of the CPE is the Warburg element given by Equation 1-8. This equation is of a similar form as the impedance for a CPE, but with $a = 0.5$, resulting in a line at a 45° angle on the Nyquist plot.

$$Z_{wb} = \frac{1}{W(i\omega)^{0.5}} \tag{1-8}$$

As batteries age, the SEI layer increases and starts to contribute significantly to the battery impedance at frequencies around 0.5kHz to 0.1kHz. To model the SEI layer impedance, a second ZARC element can be used or a traditional RC element.

Impedance models are frequently used throughout this thesis to model EIS data. In particular, impedance models proved to be suitable to capture battery relaxation effects, as shown in Chapters 2, 3, and 4. Chapter 3 employs a useful property of RC models to validate EIS data. This is discussed in the next section.

1.3.2 KRAMERS-KRONIG TRANSFORM AND THE VOIGT-CIRCUIT

As was stated in the previous section, an n^{th} order ECM such as shown in Figure 1-9 (also known as a Voigt-Circuit) can still fit to EIS results with low error if n is increased sufficiently. A near perfect fit can be obtained with $n = 20$ or higher, but the model becomes impractical and meaningless. However, the Voigt-Circuit model can still be used as part of a validation procedure for EIS results called the Kramers-Kronig (KK) transform. The KK transform makes use of the fact that the real components Z' of the EIS results can be obtained from only the imaginary components Z'' (and vise versa) using Equation 1-9 to calculate Z'' and Equation 1-10 to calculate Z' at signal frequency ω.

$$Z''(\omega) = -\left(\frac{2\omega}{\pi}\right)\int_0^\infty \frac{Z'(x)-Z'(\omega)}{x^2-\omega^2}dx \quad (1\text{-}9)$$

$$Z'(\omega) = Z'(\infty) + \frac{2}{\pi}\int_0^\infty \frac{xZ''(x)-\omega Z''(\omega)}{x^2-\omega^2}dx \quad (1\text{-}10)$$

The KK transform itself is difficult or impossible to implement for real datasets due to the infinite limits of the integrals. However, any linear circuit is KK-transformable, which means that if a dataset can be approximated using a linear circuit, such as the Voigt circuit, the dataset is also KK-transformable [31]. This means that if a good fit to the Voigt-Circuit can be obtained, EIS data can be shown to be KK-transformable, and, therefore, valid. This method is used in Chapter 3 to ensure the validity of EIS results. Furthermore, the method is extended such that it can be used to filter out noise from the EIS data.

1.3.3 OPTIMIZATION FOR PARAMETERIZATION

Impedance models are parameterized by optimizing an objective function such as the mean square error (MSE) shown in Equation 1-11:

$$MSE = \frac{\sum_{i=1}^{n}(y_i - \hat{y}_i)^2}{n} \quad (1\text{-}11)$$

where y_i is a measurement data point, $\hat{y}_i$ is the model prediction, and n is the number of data points. For impedance models with equations in frequency domain, the most common optimization method used to minimize the MSE is the Levenberg-Marquardt (damped least-squares) algorithm [22,44,45]. The genetic algorithm (GA) is frequently used for time domain optimization [46–48]. The particle swarm optimization (PSO) algorithm is used by some for time domain battery model parameterization [7,40]. The PSO algorithm is also used for EIS model fitting in the work presented in this thesis. Chapter 4 includes a set of upper and lower parameter bounds suitable to fit EIS data obtained from Samsung INR2170-50E cylindrical battery cells using the PSO algorithm.

1.4 Battery State Estimation

The State of Charge (SoC) and State of Health (SoH) of a battery are fundamental quantities which must be estimated for safe and efficient battery operation. Other states, such as State of Power (SoP), which indicates how much power can safely be drawn from a battery, are derived from these states. SoP is usually calculated by taking into account the predicted battery voltage after applying current over a small time-delta of 1 to 20 seconds [7]. Farmann et al. [49] reviewed SoP methods and grouped them into two categories: characteristic maps (CM) and equivalent circuit models (ECM). CMs are maps which store the power value that can be drawn from a battery under different SoCs, temperatures and currents. ECM based methods are used in the same way for SoC estimation which is discussed in the next section.

1.4.1 State of Charge

The most important information a battery user requires is how much longer the battery can be used until it must be recharged. This depends on the application specific battery usage and on the amount of charge remaining inside the battery. State of charge is a quantity to indicate the remaining charge of a battery, defined as the percentage of charge available with respect to the maximum available charge. SoC is also used to keep the battery within a safe operating range during operation. Unfortunately, SoC cannot be measured directly, but must instead be estimated from measurable quantities such as voltage, current, and temperature. SoC estimation can be grouped into three categories: direct methods, model-based methods, and data-driven methods.

Battery current (I) can be used directly to calculate SoC from the charge added to, or removed from the battery. The known initial charge (C_i) is required as a starting point from which the accumulated charge over time is integrated. The result is divided by the maximum available capacity (C_n) as shown in Equation 1-12 [38]. This method is frequently referred to as coulomb or amp-hour counting.

$$SoC = 1 - \frac{\int Idt + C_i}{C_n} \tag{1-12}$$

The accuracy of the coulomb counting method depends on the accuracy of the current and time measurements since measurement errors are amplified during the integration. In addition, the required starting reference charge (C_i) will drift over time [50] because of the measurement errors.

OCV can be used to estimated SoC by using a battery characteristic OCV-SoC relationships which must be determined offline beforehand. Since true OCV rarely occurs during normal battery operation, battery models are used to estimate OCV under a given load. The accuracy of the OCV-SoC method depends on the accuracy of the OCV-SoC data, the accuracy of the battery model, as well as voltage and current measurement accuracies [51]. Kalman filters (KF) are used to achieve optimal SoC estimation in the presence of modelling, measurement, and process noise [52]. Usually, battery model equations are non-linear, but can be linearized and used in the Extended Kalman Filter (EKF). The EKF is described in detail in Chapter 6.2.2. Sepasi et al. [53] use the EKF with a 2nd-order RC model to estimate SoC for new and aged batteries, by updating the model parameters online. The linearization in the EKF can reduce the accuracy of the estimator, especially if the modelling and measurement equations are highly non-linear. Therefore, improvements were made to the EKF to retain estimator accuracy with non-linear equations. Pan et al. [54] used a 1^{st}-oder RC model with an EKF and a grey model to avoid linearization. A fractional order model was used with an unscented Kalman filter (UKF) by Mu et al. [46] to find more accurate estimates using the unscented transform. The accuracy of the EKF or UKF is highly dependant on the accuracy of the system model. Since it is often hard to find accurate models for real applications, efforts have been made to improve estimation robustness for inaccurate models. The Smooth Variable Structure Filter (SVSF) is a robust filtering method, described in detail in Chapter 6.2.3. The SVSF was used by Afshari et al. [40] and Ahmed et al. [47] with a 3^{rd}-order RC model and electrochemical model, respectively. With the SVSF, a boundary can be defined for uncertainties and noise levels

of the system which ensures convergence of the estimate to a value within the boundary. In Chapter 6, the EKF and the SVSF are used together with the Interacting Multiple Model (IMM) filter for low temperature SoC estimation. The IMM is used in cases where several models are possible, but the correct one is unknown (see Chapter 6.2.4). The IMM uses the likelihood of each model to compute a blended state estimate. EKF, SVSF, and IMM are also discussed in detail in Chapter 6.

Data driven methods use advanced machine learning techniques to predict SoC from a given usage profile. The accuracy of such models depends on the amount, diversity, and quality of the data used to train the model. Tong et al. [55] used three neural networks to predict SoC for idle, charge, and discharge conditions. The networks were trained with drive cycles and validated with discharge pulses. Chemali et al. [56] used deep neural networks to estimate SoC at different temperatures. Neural networks are introduced in detail in Section 1.6 and applied to SoC estimation from EIS data in Chapter 5.

1.4.2 State of Health

As discussed in the previous section, SoC is an important quantity which must be estimated. However, as the battery ages, SoC estimation algorithms must adapt to account for changes in the battery behaviour. This can be accomplished if the state of health is known. As was the case with the SoC, SoH is a hidden quantity which cannot be measured directly. Similar to SoC estimation, SoH estimation can be grouped into categories: direct measurement methods, indirect analysis methods, adaptive filtering methods, data driven methods, and physical modelling methods. Most of these are reviewed by Xiong et al. [57]. Li et al. [58]

developed a single particle electrochemical model which can predict SEI growth and crack propagation at different operating temperatures and track SoH this way. Pastor-Fernandez et al. [59] compared results from EIS and IC-DV (incremental capacity and differential voltage) data to identify degradation mechanisms. To overcome barriers of using EIS in real time applications, Mingant et al. [60] proposed a quasi-electrochemical impedance spectrum which requires less precise equipment. Tian et al. [61] used a fractional order impedance model in combination with incremental capacity analysis to account for SoH. The SVSF used by Afshari et al. [40] for SoC estimation can estimate SoH from a chattering parameter of the filter. Li et al. [62] applied a Gaussian filter to incremental capacity analysis to identify features of interest for SoH estimation. Yang et al. [63] identified time constants during the constant voltage (CV) charge region and related them to the SoH of the battery. Eddahech et al. [64] also investigated the CV region during charge, but related it to degradation mechanisms during calendar aging. Hu et al. [65] used HPPC tests, sparse Bayesian predictive modelling, and the concept of statistical sample entropy to model the change in the pulse response with SoH. Further SoH estimation techniques are reviewed in Chapter 4, where the battery relaxation effect (Section 1.1.3) is combined with EIS (Section 1.2) to estimate SoH.

1.5 Fractional Order Calculus

The impedance models introduced in Section 1.3.1 can often achieve higher voltage modeling accuracy. However, to use the impedance model for state estimation in a similar way as ECMs (for example, with Kalman filters), the model equation must be in time

domain. Translating a complex impedance equation such as (1-7) into time domain is a non-trivial task. One approach is to simply approximate non-ideal elements such as the CPE using a string of RC-pairs as shown in Figure 1-12. However, this adds a lot of additional model parameters which is undesirable. A relatively new approach uses fractional order calculus (FOC) [44,46,61,66–68] instead to convert fractional order impedance elements into time domain, also shown in Figure 1-12.

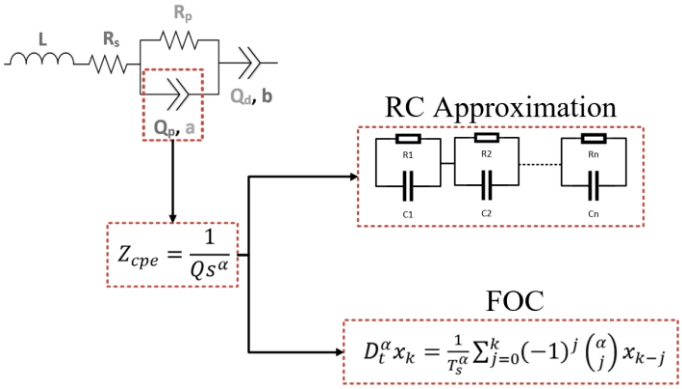

Figure 1-12: Representation of CPE element with RC approximation or FOC.

FOC involves the use of the fractional order operator D_t^{α} which is defined by Equation 1-13, for a time domain measurement x_k at discrete timestep k with sample rate T_s. Here, α is the fractional order exponent from the CPE impedance, and $\binom{\alpha}{j}$ is the binomial coefficient calculated using Equation 1-14 by making use of the Gamma function Γ.

$$D_t^{\alpha} x_k = \frac{1}{T_s^{\alpha}} \sum_{j=0}^{k} (-1)^j \binom{\alpha}{j} x_{k-j} \tag{1-13}$$

$$\binom{\alpha}{j} = \begin{cases} \frac{\alpha!}{j!(\alpha-j)!} = \frac{\Gamma(\alpha+1)}{\Gamma(j+1)\Gamma(\alpha-j+1)} \\ 1 \end{cases} \tag{1-14}$$

Figure 1-13 shows impedance models which have been converted for time domain use. Mauracher et al. [69] transformed the Warburg impedance in the model shown in Figure

1-13c into time domain by first approximating the element as a string of RC pairs and assuming each RC pair to have equal values. Wang et al. [70] as well as De Sutter et al. [42] used FOC to convert the impedance of a CPE to time domain and parameterized the model shown in Figure 1-13a using time domain discharge pulses. Eddine et al. [67] translated the Warburg impedance into time domain using FOC for the model shown in Figure 1-13b, parameterized the model using time domain discharge pulses and validated the results using EIS data. Ideally, EIS should also be used to parameterize impedance models as it provides the most complete impedance profile. To obtain the model parameters for all discharge currents, EIS can be collected under a DC bias current which is possible only for lower currents. At higher currents, the battery would discharge significantly over the duration of the EIS measurement, changing the result, or fully discharging the battery. Xu et al. [43] parameterized a Warburg element with EIS data in frequency domain and used FOC to convert the impedance to time domain. This was possible because the portion of the Nyquist plot modelled by the Warburg element does not change significantly with discharge current. Kollmeyer et al. [71] used time domain pulses to obtain ohmic resistance values under different discharge currents and used the results to scale EIS data. They then used the scaled EIS and the RC pair conversion method to parameterize the model shown Figure 1-13c.

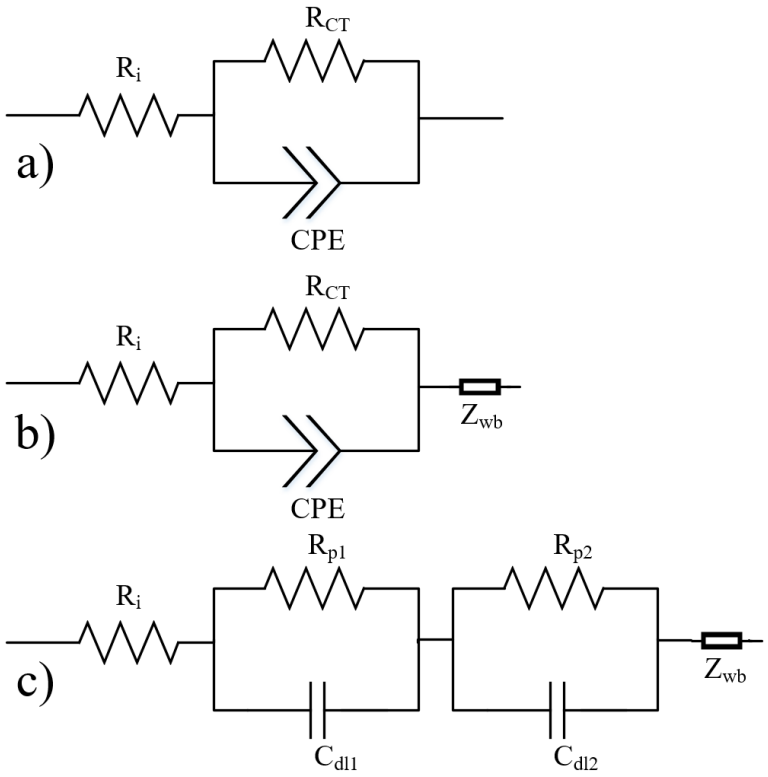

Figure 1-13: Common impedance models

1.6 DEEP NEURAL NETWORKS

Machine learning techniques are used in a large variety of applications and battery state estimation is one of them. In Chapter 5 deep neural networks are used for estimation of SoC from EIS data and from battery models parameterized with EIS data. This section serves as a general introduction to neural networks and deep neural networks.

The concept of Artificial Neural Networks (ANN) is based on early models of human brain function. A basic ANN consists of three layers, an input layer a hidden layer and an output layer. The number of elements of the input layer and output layer depend on the application and available data. For example, in the case of binary classification from a set of n measurements, the input layer would have n elements, one for each measurement, and the

output layer would have two elements, one for each class. The hidden layer consists of one or more neurons, the basic building block of ANNs shown in Figure 1-14. A neuron j of hidden layer L takes in inputs α_0^{L-1} from the previous layer (for example the input layer) to compute an output, or activation, α_j^L via an **activation function** $\sigma(z^L)$ from the weighted input z^L. The weighted input z^L is computed from weights w_i and biases b_i using Equation 1-15.

$$z^L = \sum_{i=0}^{n} w_i a_i^{L-1} + b_i \tag{1-15}$$

A step function could be used for the activation function σ to achieve threshold-like behaviour of the neuron. However, the fact that the step function is discontinuous presents a challenge for training procedures introduced later in this section. Instead, the **Sigmoid** function is used, a smooth, differentiable version of the step function shown in Equation 1-16.

$$\sigma(z^L) = \frac{1}{1+e^{-z^L}} \tag{1-16}$$

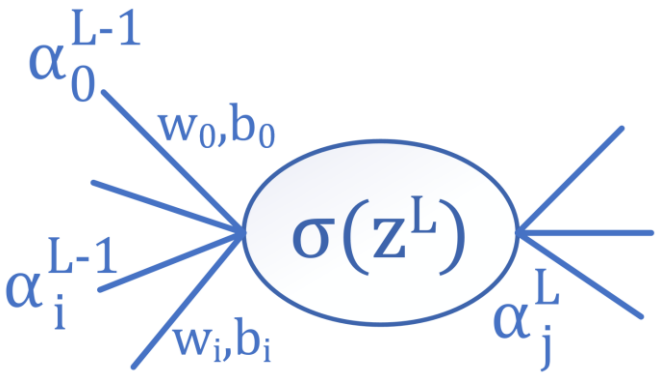

Figure 1-14: Neuron

Several neurons can be combined to form a network structure as shown in Figure 1-15. Neural networks with large number of layers and neurons have proven to be capable of

solving complex problems and referred to as a Deep Neural Networks (DNN). By tuning the weights and biases, the network can be used to, for example, perform classification. A given set of inputs will propagate through the network and produce a probability of the inputs belonging to a certain class, based on the activation of the different neurons and the interaction between them [72].

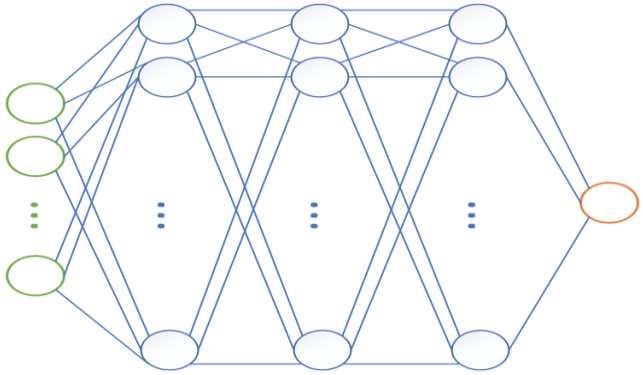

Figure 1-15: Simple Neural Network

Tuning of the weights and biases requires an optimization algorithm. For optimization problems in general, an algorithm should modify the tuning parameters and then evaluate the performance of the system to be optimized by minimizing a const function C. In the case of multi-layer neural networks, a complication arises from the fact that the tuning parameters of the hidden layers are not directly connected to the output, which means the desired output values of the hidden layers are unknown. However, the cost evaluated at the output layer can be backpropagated through the hidden layers. Therefore, neural networks are optimized, or trained, using the backpropagation algorithm with the gradient descent optimization method. The method works as follows [73]. In general, the error δ^L at the output of layer L can be calculated using Equation 1-17, where $\nabla_a C$ is the gradient of the

cost function, $\odot$ denotes the Hadamard product (element wise vector product), σ' the derivative of the activation function and z^L the weighted input at layer L (Equation 1-17).

$$\delta^L = \nabla_a C \odot \sigma'(z^L) \tag{1-17}$$

The error δ^L can then be related to the error of the previous layer δ^{L-1} using Equation 1-18, where $(w^L)^T$ is the transpose of the weights of layer L.

$$\delta^{L-1} = ((w^L)^T \delta^L) \odot \sigma'(z^{L-1}) \tag{1-18}$$

Finally, the gradient at each layer can be calculated using Equation 1-19, where w is the weight of a neuron with error δ_{out} and a_{in} the activation of the previous neuron. b is the bias of the perceptron, and δ is the error evaluated at the same neuron as the bias.

$$\frac{\partial C}{\partial w} = a_{in}\delta_{out}, \ \frac{\partial C}{\partial b} = \delta \tag{1-19}$$

With the equations introduced above, the gradient between any two nodes connected between adjacent layers can be calculated and used in the gradient descent algorithm to find the direction of possible minima of the cost function C.The gradient descent method itself includes a tuning parameter η called the learning rate, which is related to the step size the algorithm takes in its search of solutions. Parameters other than the weights and biases of the network are referred to as hyper parameters and must be carefully chosen. In the case of the learning rate, η must be selected to be large enough such that the gradient descent algorithm learns fast enough, but not too high for the algorithm to overshoot solutions.

The data used to train the DNN should be split into training data and validation data as a basic way to protect against overfitting. During training, the inputs of the whole training set are fed to the network and the cost function is used to compare the network output against a ground truth. This repeated until a set number of cycles, or **Epochs**, are completed.

The number of epochs can potentially be large, especially if the network starts with poor initialization of parameters. Several methods exist to improve the performance of DNN training. The selection of the cost function plays an important role in the speed with which the training converges to a minimum. The quadratic cost function shown in Equation 1-20 for example may be a desired choice, where n is the number of training samples, x is the training sample, $y(x)$ is the ground truth evaluation given x and $\alpha^L(x)$ is the DNN output given x.

$$C = \frac{1}{2n}\sum_x \|y(x) - \alpha^L(x)\|^2 \tag{1-20}$$

However, the partial derivates of the quadratic cost function are proportional to the derivate of the activation function σ', which becomes small far away from the threshold. As a result, learning is slow for values far from the solution. The speed of learning can be improved by using the cross-entropy cost function shown in Equation 1-21 instead.

$$C = -\frac{1}{n}\sum_x \left[y(x)\ln\big(\alpha(x)\big) + (1-y)\ln\big(1-\alpha(x)\big)\right] \tag{1-21}$$

The partial derivates of the cross-entropy function turn out to be proportional to the activation function σ, instead of its derivative. This means that a badly initialized DNN can still produce large enough gradients to learn faster.

Several other modifications and hyper parameters exist and those relevant to the results shown in Chapter 5 are introduced next:

Stochastic Gradient Descent: The speed of the gradient descent algorithm can be improved by randomly sampling the dataset into small batches and using the batches for training instead of the entire dataset. The gradients computed from the batches serve as

close approximations of the gradients of the whole dataset but take less time to compute. This method is called Stochastic Gradient Descent (SGD). In addition to the learning rate, SGD requires the size of the batches as another hyper parameter.

L2 Regularization: Increasing the number of neurons and layers can improve the performance of the DNN. However, if training sets are limited in size, the DNN is likely to overfit to the training data as the number of parameters grow. To protect against overfitting, L2 regularization can be used. This method adds a weighting factor to the cost function as shown in Equation 1-22. Here, the first half of the equation is the regular quadratic cost function, and the second term is the L2 regularization factor. This factor is the sum of squares of the weights of the network scaled by $\frac{\lambda}{2n}$ where n is the size of the training set and λ is a new hyper parameter.

$$C = \frac{1}{2n}\sum_x \|y(x) - \alpha^L(x)\|^2 + \frac{\lambda}{2n}\sum_w w^2 \quad (1\text{-}22)$$

Using L2 regularization forces the learned weights to be small, only allowing bigger weights if significant C reduction is achieved. Avoiding large differences between weights promotes generalization of the network.

Pruning: The large number of model parameters required to run a completed DNN can be impractical of constrained embedded applications. However, not all model parameters are equally important. In fact, a large number of neurons can be removed without significantly reducing the network performance. Pruning works by choosing a threshold and removing all neurons with weights below this threshold. This process can be repeated until the highest network performance with the desired number of parameters is achieved.

1.7 BATTERY TESTING & AGING

In this section, some of the battery testing methods used throughout this thesis are introduced. The following tests were used:

1) Break-in Procedure

The first time a battery cell is tested, it needs to undergo a break-in procedure consisting of several charge and discharge cycles to stabilize the batteries' response. All batteries used in the experimental parts of this thesis were first cycled 10 times for this reason.

2) Capacity Test

The capacity test determines the SoH of the battery by coulomb counting during discharge. For this test, the battery is first fully charged according to manufacturer specifications, followed by a rest, followed by a complete discharge during which the coulomb counting is performed. The total coulombs counted during the discharge step (assuming an initial charge of zero) are the measured capacity of the cell.

3) OCV-SoC Test

The OCV-SoC test provides the data used for the OCV-SoC lookup tables for state estimation algorithms. For this test, the battery is first fully charged according to manufacturer specifications. After a rest period, the battery is discharged at very low current until the lower cut-off voltage is reached. Following another rest, the battery is charged at the same low current until the upper voltage cut-off is reached. Since low current is used for this test, the voltage measured during discharge and charge is close to OCV. Lower current will result in more accurate OCV measurements, but the test duration will

increase. Figure 1-16 shows example OCV-SoC datasets for a new (100% SoH) and an aged (80% SoH) Samsung INR2170-50E cylindrical battery cell. The shape of the OCV-SoC curve depends on the type of battery used. The cylindrical NMC batteries used in this study show a relatively steep OCV-SoC curve slope. Other chemistries can exhibit OCV-SoC curves with a nearly horizontal section between 80% and 20% SoC. Obtaining a distinct SoC value from OCV becomes less accurate for near horizontal parts of the OCV-SoC curve. The steeper slopes shown in Figure 1-16, on the other hand, allow for more accurate readings since the points on the curve are more clearly separated. As the battery ages, the OCV-SoC behavior changes slightly, mostly at high SoC (>80%) and at low SoC (<20%). In the middle region the results are similar for fresh and aged cells. Also shown in Figure 1-16 are polynomial fits for both curves. Polynomial orders of 10th or higher are typically needed to fit OCV-SoC curves. The OCV-SoC test procedure is described in more detail in Chapter 6, where it is used as part of SoC estimation algorithms.

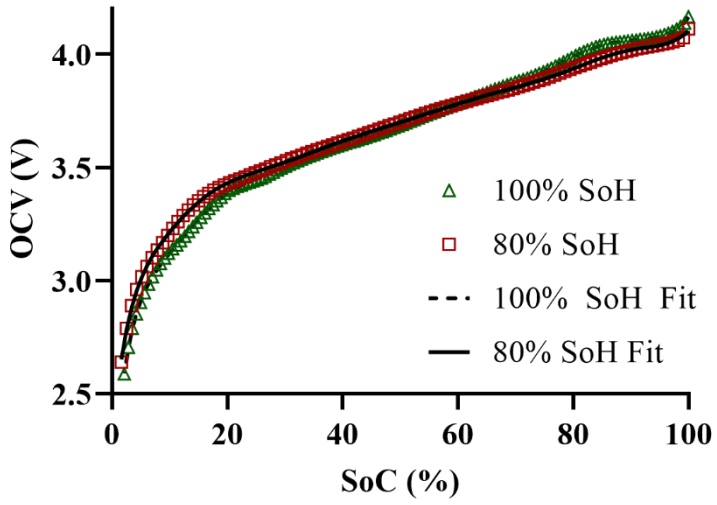

Figure 1-16: Experimental OCV-SoC curve results for new and aged batteries.

4) EIS Test

EIS provides information about the battery impedance behaviour and can be used to parameterize impedance models. The EIS test is performed using a potentiostat. Since this is one of the most used tests in this study, the test details are described repeatably in method sections of Chapters 2, 3, 4, and 7.

5) Charge Discharge aging

The most common form of aging is cycle aging where batteries are continuously charged and discharged to full charge and full discharge depth. While this method can be relatively fast, the way the battery ages is different from realistic conditions in EV applications. As a result, battery behaviour after cycle aging may be different from its behaviour after field operation, particularly when considering impedance profiles. The cycle aging procedure is described in detail in Chapter 7 where it is compared to realistic drive cycle aging.

6) Drive cycle aging

Realistic battery aging is a time and resource intensive process by which battery cells are artificially aged in controlled laboratory settings. Instead of full charge and discharge cycles, standardized drive cycles are used to age batteries. These drive cycles are provided for example by the US Environmental Protection Agency (EPA) and consist of speed vs. time data for different driving scenarios. To be able to use EPA drive cycles in battery aging, the speed vs. time data must be converted to battery load demand. This can be achieved using a simple vehicle model as shown in Figure 1-17.

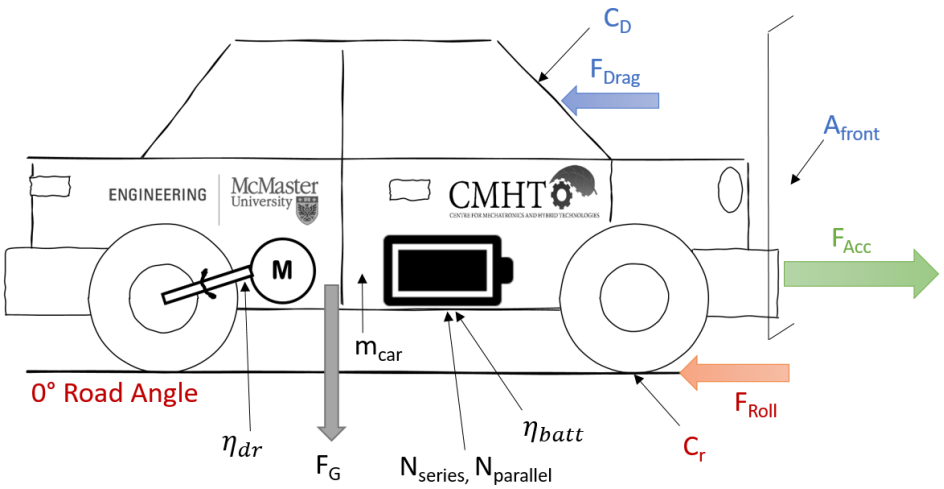

Figure 1-17: Simple Vehicle Model

This model considers forces acting on a vehicle such as drag due to air (F_{Drag}) and rolling resistance (F_{roll}) from the tires on the road (assuming flat roads, zero road angle). These forces must be overcome to achieve the speeds demanded by the EPA drive cycle, using the power provided by the battery. The battery losses are approximated with a constant efficiency number (η_{batt}). Further losses due to drivetrain (transmission and motor) inefficiencies are approximated by η_{dr}. While not suitable for exact range simulations, the simple model can provide representative load profiles to use for battery aging. The details of this model including model parameters and equations are provided in Chapter 7. Chapter 7 also describes an aging study which compares charge/discharge cycle aging with realistic drive cycle aging.

1.8 Custom Battery Cell Tester

The research reported in several parts of this thesis required experimental data from lithium-ion batteries under various operating conditions. A custom battery test system was designed to perform different types of battery experiments. The design of the test system

was subject to the following three key requirements: 1) the voltage and current sensing must be accurate enough to achieve an amp-hour counting accuracy of less then 0.5 %, 2) all experiments shall run autonomously while ensuring battery operation stays within safe limits, and 3) the system shall be open to extension of functionality. Figure 1-18 shows an overview of the components and connections of the test system and Table 1-1 lists each of the devices used.

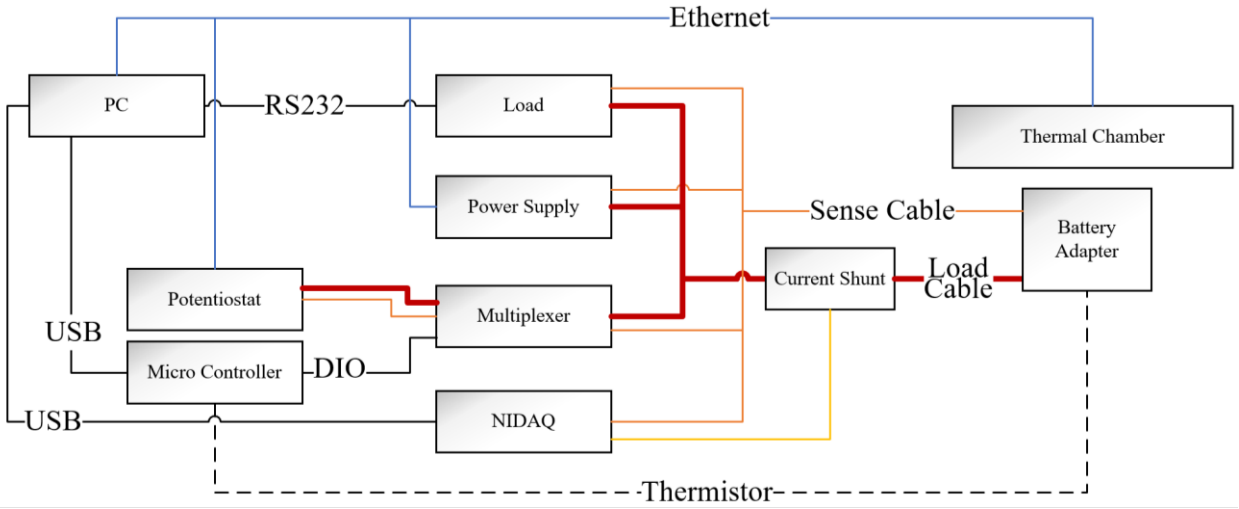

Figure 1-18: Custom battery test system diagram (only one channel shown)

Any Windows 7 (or higher) PC can be used to run the system, so no PC is specified. The PC hosts custom software to control the devices used to perform various battery tests. To charge and discharge batteries a power supply and a load were used, respectively. Both power supply and load support 4 individual channels, allowing the system to test four individual cells simultaneously. The load is controlled via RS232 serial communication, and the power supply via Ethernet. The battery voltage is measured using the NI9239, 4 channel analog input module which is housed in the National Instruments Data Acquisition

(NIDAQ) chassis. Battery current is measured via the voltage drop across a shunt resistor. This voltage drop is measured by the NI9219, 4 channel analog input model, which is also housed in the NIDAQ chassis, and controlled via the Universal Serial Bus (USB) connection. The Ethernet controlled potentiostat used in this work has only a single channel, however, a custom designed multiplexer allows for automated switching of the potentiostat between each of the four channels. Four mechanical relays are used to switch each of the two load lines (positive and negative) as well as each of the two sense lines from the potentiostat to a battery adapter.

Table 1-1: Custom battery test system parts list

Name	Manufacturer	Model	Description
Potentiostat	BioLogic	SP150	1 channel
Load	Agilent	N3306A	4 channels, 20V/15A/300W
Power Supply	Agilent	N6773A	4 channels, 60V/60A/300W
NIDAQ	National Instruments	cDAQ-9178	8 slot chassis
Analog Input	National Instruments	NI9239	4 channel NIDAQ module to sense battery voltage
Analog Input	National Instruments	NI9219	4 channel NIDAQ module to sense shunt voltage
Thermal Chamber	Thermotron	T8200	-10°C to +40°C
Micro Controller	Arduino	Uno	Multiplexer control and thermistor sensing
Current Shunt	Riedon	RSN-100-100B	$1m\Omega$ resistance for current measurement
Thermistor	Semitec	103AT-11	One thermistor per battery
Multiplexer	Cadex Electronics	Custom	Multiplexes the potentiostat to 4 channels
Battery Adapter	Cadex Electronics	Custom	With Kelvin connection (Section 1.8.1)

Figure 1-19 shows a diagram of the multiplexer illustrating one active channel and one disconnected channel (grey connections). Each set of four relays is controlled by an

Arduino microcontroller, through its Digital Inputs/Outputs (DIO). The same microcontroller also measures the battery temperature via thermistors. The microcontroller is attached to the PC via USB. A thermal chamber houses each of the four battery adapters and is able to maintain a stable environment. The thermal chamber is controlled via Ethernet. The battery adapters are discussed in detail in Section 1.8.1.

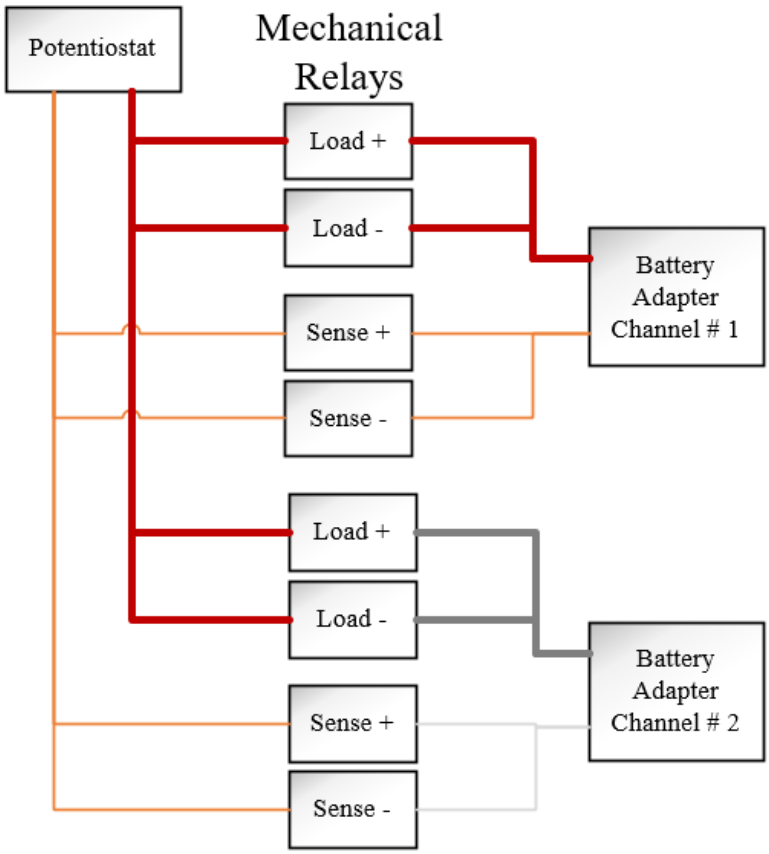

Figure 1-19: Multiplexer diagram for 2 channels

The different parts of the system are orchestrated by custom software running on a host PC. The software was developed in Python 3.7 with an architecture as shown in Figure 1-20.

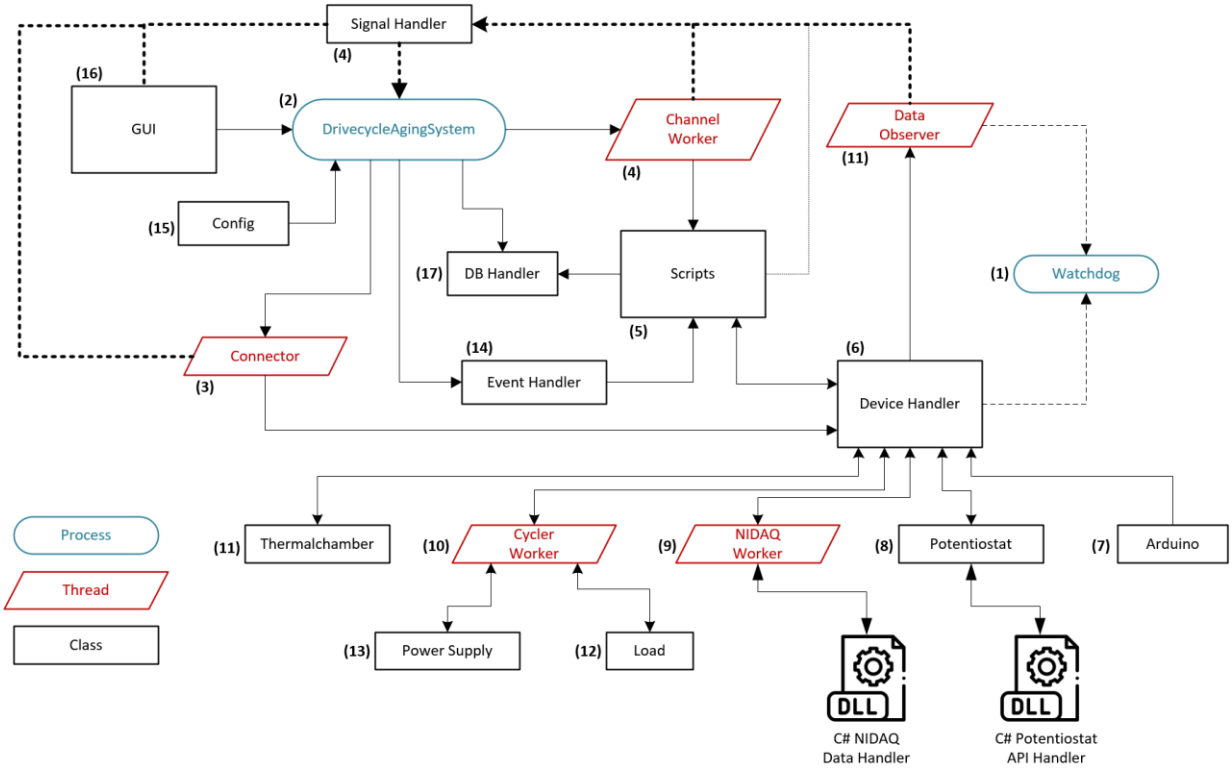

Figure 1-20: Custom battery test system software architecture

The software consists of two separate processes, several threads, and many classes. Processes are isolated from each other since each uses its own Python interpreter instance. Threads run code in parallel within the same processes. Classes contain groups of methods to perform the different functions of the system.

A watchdog program, Figure 1-20 block (1) runs independently of the main program as a separate Python process such that the watchdog can shut-down and re-start the test system in case of malfunction, or if safety parameters are exceeded. The watchdog starts the Drivecycle aging system process (2), which opens up the Graphical User Interface (GUI) (16) shown in Figure 1-21. Pressing the “Connect” button starts a thread to establish communication with the different hardware devices (3). Next, the channel worker (4) is

stated which contains four threads, one for each channel. The scripts class (5) contains functions which represent different experiments which can be performed using this system. Pressing a "Start" button next to a channel row on the GUI (Figure 1-21) will prompt the user to select from a list of experiments as well as select a battery ID.

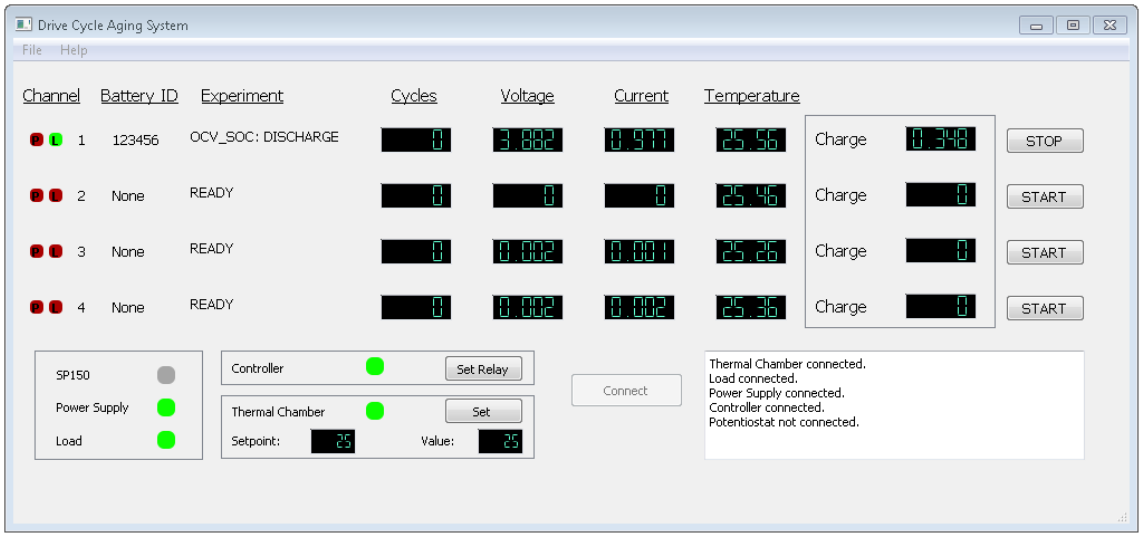

Figure 1-21: Graphical user interface for custom battery test system

Battery IDs must first be registered in the underlying Microsoft SQL Server relational Database (DB), which is controlled by the DB handler (17). After entering the required information, the experiment is started via the event handler (14). The event handler will also stop the experiment if a stop button is pressed. While an experiment is running, different devices will be used by the scripts class (5) via the device handler class (6). The simplest devices to control are the thermal chamber (simple read/set of temperature) and the Arduino microcontroller (set multiplexer channel/read thermistor temperature). To be able to run custom current profiles such as drivecycles, the load (12) and power supply (13) must be controlled via its own thread, the cycler worker (10). Cycler refers to the

combination of load and power supply. The Potentiostat is not directly controlled by Python code, instead a C# API library is used. This is because well designed C# example code was already available from the manufacturer of the potentiostat. Fortunately, C# code exported as a Dynamically Linked Library (DLL) file can be integrated into Python via the Pythonnet library. A similar approach was used for the NIDAQ, where the direct control of the NIDAQ is also performed in C#. This was done due to the high sampling rates required by the NIDAQ modules, which are too fast for Python to handle. Via the C# layer, measurements can be buffered and down sampled to be made available to Python at a much slower rate. The data is sampled periodically, requiring another thread, the NIDAQ worker (9). The data is also independently monitored by the data observer (11).

During the execution of experiments, the GUI displays select measurements, such as voltage, current, temperature, charge (in Ampere-hours), and aging cycles (if applicable, depending on selected test). The active test step is also displayed along with the battery ID for each channel. Data and events are communicated to and from the GUI to the rest of the system via a publisher/subscriber signal architecture, facilitated by the signal handler class (4). A subscriber (for example a part of the GUI) can be attached to a publisher (for example the data observer) without the need for the two parts to be aware of each other. The publisher does not know which are all the subscribers, it simply sends out its message. This is illustrated in Figure 1-20 via the dotted lines creating weak connections between the GUI and the rest of the system. This publisher/subscriber architecture is a common Object-Oriented (OO) design pattern. Another OO design patter which was used is the Model-View-Controller (MVC) pattern. The MVC pattern further simplifies the decoupling of

GUI (front-end) and “system” (back-end) by sharing a single “data model” object between front-end and back-end. The data model is the data carrier where experiment data, shared settings, as well as the back-end status is stored. The publisher signals are then used to notify different parts of the system of relevant changes to the data model.

Finally, the data collected from the experiments is fed into the DB, again via the DB handler (17). The DB architecture is shown in Figure 1-22. Batteries are stored in the “Batteries” table, each with a reference (foreign key) to a battery model from the “BatteryModels” table which in turn references a manufacturer from the “Manufacturers” table. When a new experiment is started, a new entry into the “MasterExperiments” table is created using the battery ID provided by the user via the GUI. Each experiment can contain one or more steps, which are recorded separately in the “Experiments” table. The data obtained from the experiments comes in two forms, time domain data (voltage, current, temperature, etc) and EIS results (real, imaginary, frequency). The “ExperimentLogs” table contains the time domain data and the “EISDatas” table the EIS data. Since many different drive cycles are frequently used in this work, they are also stored in this DB in the “DriveCycles” and “DriveCycleDatas” tables. Specific drive cycles can also be linked to specific experiments via the “ExperimentDriveCycleLinks” table. The data stored in this DB can be accessed directly from MATLAB, where scripts can be written to automate data retrieval. The system described in this section enabled accurate, repeatable, time efficient and reliable battery experiments, and was instrumental in obtaining the various results presented in this thesis.

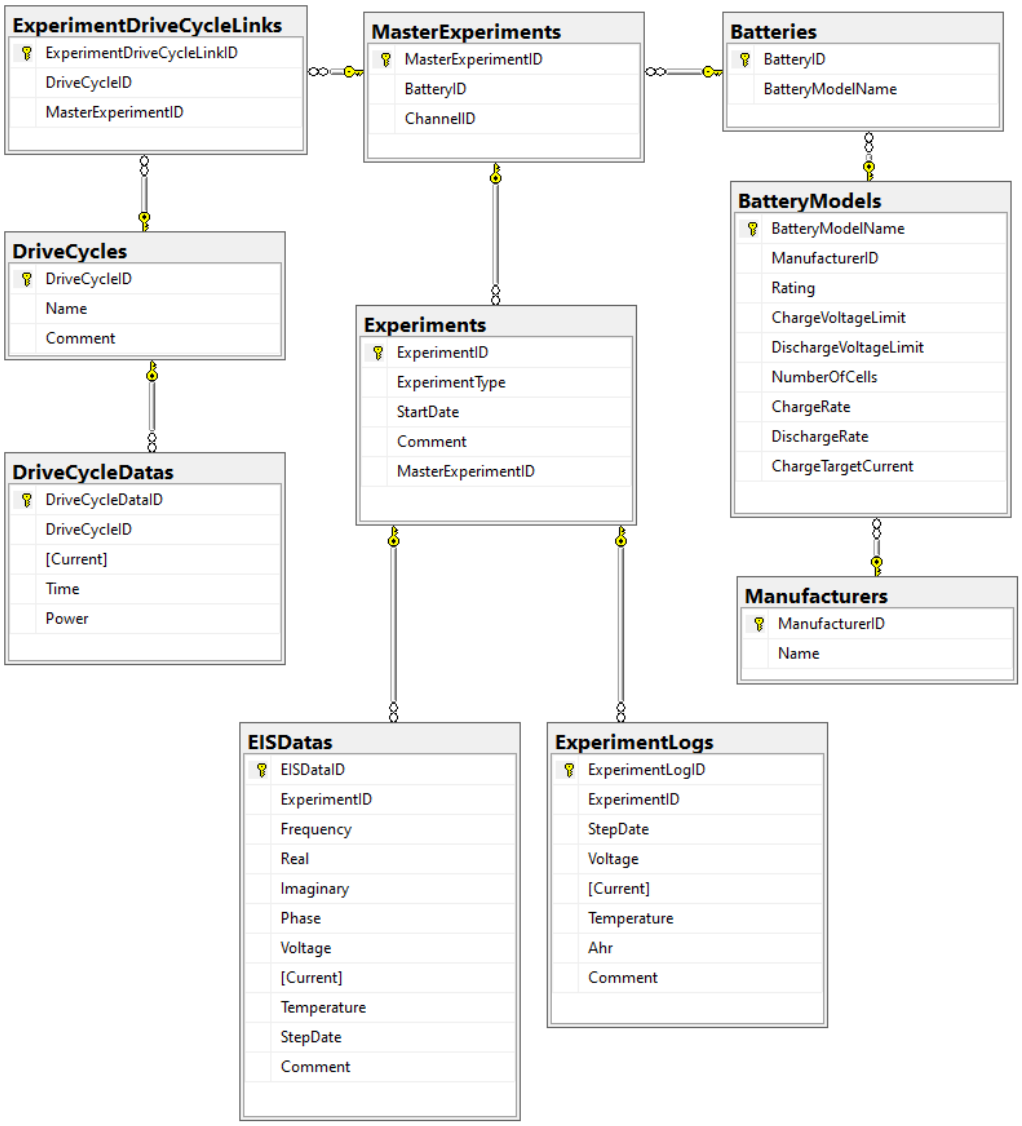

Figure 1-22: Database architecture for custom battery test system

1.8.1 BATTERY ADAPTER

The test system includes a custom adapter to attach batteries to the devices using four-point measurement (Kelvin connection). A Kelvin connection separates current carrying (load) wires from sense wires. If a sense wire shares the same conductor as a load wire, the measured voltage includes the battery voltage as well as an additional voltage drop across

the shared conductor. This additional voltage drop also varies with current, which makes it difficult to predict for calibration. The adapter shown in Figure 1-23 implements a Kelvin connection for a cylindrical battery cell to avoid any additional voltage drop. Nickel tabs welded to the positive and negative terminals of the battery extend outwards to allow connections on both ends. The adapter also includes screw terminal blocks to connect larger load cables from the load and power supply. The side with the terminal blocks is the load carrying side, and the opposite side is for sense lines. The adapter base was machined from a block of ABS plastic.

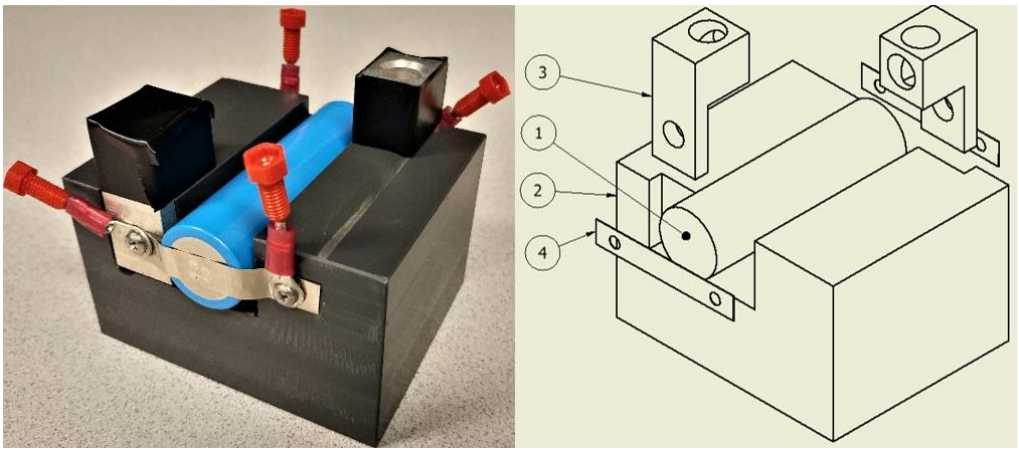

Figure 1-23: Custom battery adapter for custom battery test system. 1 – battery, 2 – adapter base, 3 – screw terminal connector, 4 – nickel tab.

Figure 1-24 shows a 3D printed welding fixture which was used to align the tabs on both sides of the battery during the welding processes. The figure shows the fixture with the top of a battery visible in the center, and a nickel tab placed in a slot on top. Once both tabs are welded on the top and bottom of the battery, the tabs can be gently folded up and the battery can be extracted using the clearance slot. Without this fixture, alignment cannot be

guaranteed. If the welded tabs are not parallel to each other, the battery cannot be properly attached to the adapter.

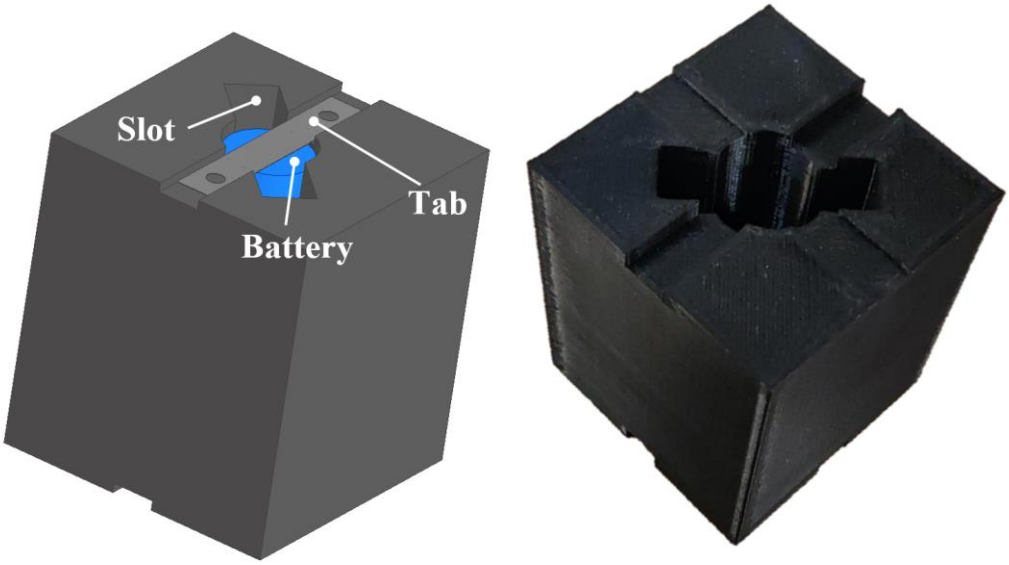

Figure 1-24: Battery welding fixture

1.9 RESEARCH CONTRIBUTIONS

In this section, the hypotheses which formed the basis for this thesis are stated, an overview of the project contributions is provided, and primary and secondary contributions are presented.

1.9.1 HYPOTHESES

The following hypotheses formed the basis for the results shown in this thesis:

1) *Hypothesis 1: EIS Measurement duration can be shortened by reducing the rest time requirement through understanding the battery relaxation effect.*

EIS is a powerful technique with a lot of potential to significantly improve diagnostics in BMSs. However, the long rest times required to ensure stable conditions create a barrier to

the successful implementation of EIS for real time, EV applications. Rest times are usually required to avoid measurement drift and other instabilities. Some methods exist which can compensate for measurement drift, however, the impact of shorter rest times on EIS measurements under different battery operating conditions is not well understood.

2) *Hypothesis 2: The battery relaxation effect contains information about the battery SoH which can be extracted using EIS.*

The battery relaxation effect is known to correlate well with SoH. However, proposed SoH estimation methods based on the relaxation effect require fully charged or fully discharged batteries or other conditions difficult to achieve in real time applications. EIS can be used to rapidly characterize the relaxation effect and estimate the SoH in the process.

3) *Hypothesis 3: The IMM can be used to improve SoC estimation at low temperatures by considering C-rate specific models.*

The IMM is a useful filter to blend several independent system models into a unified state estimate. At room temperature or above, a single ECM can accurately model the response of a battery independent of current. However, at low temperatures, the battery response changes as current increases, reducing the accuracy of the ECM. In the context of state estimation, the updating of model parameters in real time is only possible for slow changing conditions such as temperature, SoH and SoC. Current in EV applications can change significantly within seconds, making state estimation un-observable. Instead, multiple battery models each dedicated to specific regions of current magnitudes can be used and unified with the IMM.

1.9.2 CONTRIBUTIONS

Figure 1-25 provides a graphical overview of the different parts of the thesis project. The major parts of this project, which are published as journal papers, are highlighted with red. Conference papers are marked with black. Finally, non-published contributions in the area of battery testing are also included. Next, the primary and secondary contributions are listed.

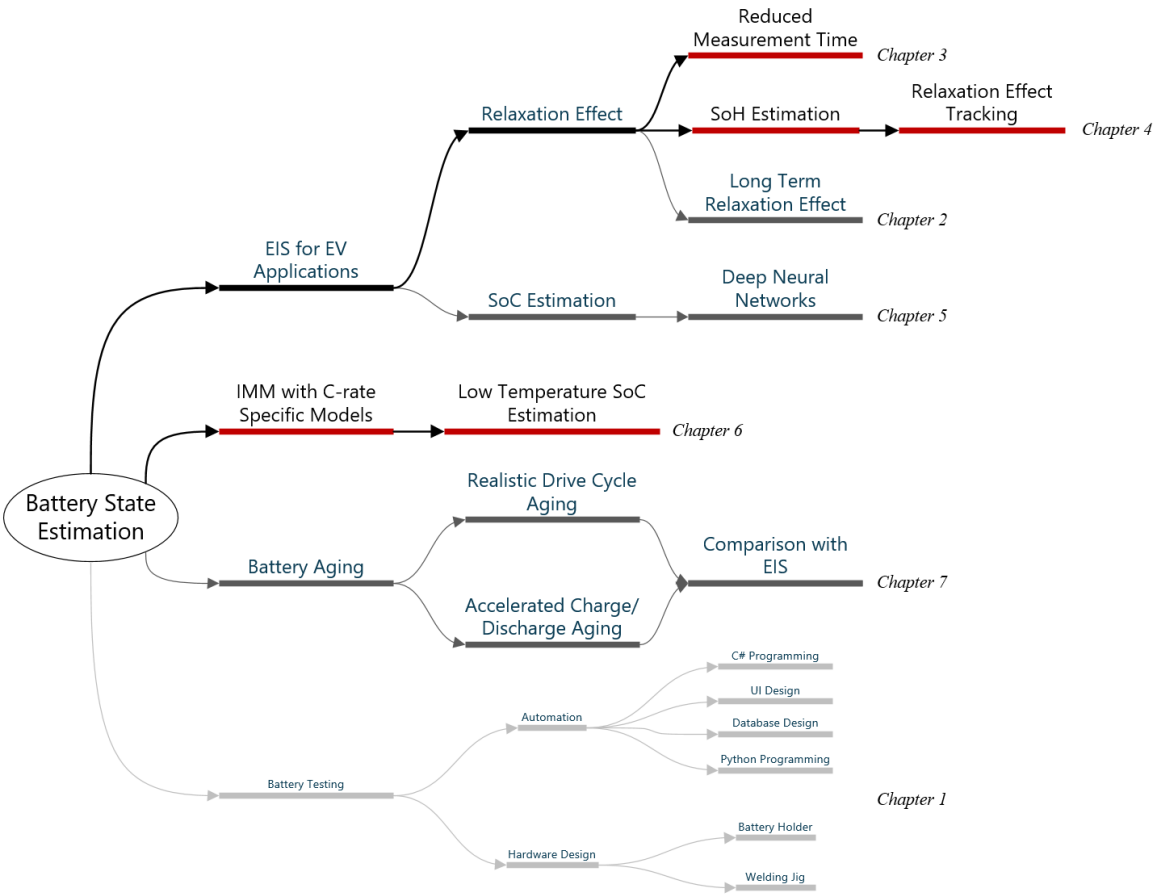

Figure 1-25: Contributions Overview

1.9.2.1 PRIMARY CONTRIBUTIONS

The primary contributions of this work are itemized and briefly described in this section.

1. Characterized the short-term battery relaxation effect to reduce EIS rest time requirements and shorten testing times (Chapter 3).

This first contribution is further to Hypothesis 1 and based on in-depth research into the battery relaxation effect and its impact on EIS measurements. Several hours of rest are usually required before EIS can be measured to simply avoid the rest-time effect. In Chapter 3 methods and results are presented to help understand the relaxation effect and to significantly reduce the rest time requirement to 5 minutes under controlled conditions.

2. Used the battery relaxation effect together with EIS to develop a new method for SoH determination (Chapter 4).

The battery relaxation effect changes as the battery ages. However, as shown in literature, this property of the relaxation effect is difficult to capture with time-domain methods. In Chapter 4 a method is proposed to use impedance modelling and EIS to capture the battery SoH information contained within the relaxation effect. Further to Hypothesis 2, this method can determine SoH within an error of 2%.

3. Developed an improved low temperature SoC estimation strategy using the IMM with SVSF and C-rate specific battery models (Chapter 6).

Battery SoC estimation shows increased errors at low operating temperatures, due to the increased non-linear response of the battery with current (or C-rate). In Chapter 6, a method is proposed to blend three battery models, each specialized for a different C-rate range, into a single SoC estimate. This is achieved through the used of the IMM-SVSF filter, which is shown to have an SoC estimation error below 2%. This is in response to Hypothesis 3.

4. Characterized the long-term battery relaxation effect with EIS and showed its impact on impedance model parameters (Chapter 2).

As part of the general research into the battery relaxation effect, the long-term relaxation effect was characterized with EIS. In Chapter 2, the EIS results were modeled with an impedance model to show how model parameters change with relaxation as well as SoC and temperature.

5. Demonstrated SoC estimation with deep neural networks from frequency domain EIS data as well as impedance model parameters (Chapter 5).

The large EIS dataset obtained as part of the research into the relaxation effect proved to be complex due to its many dimensions (rest time, SoC, temperature). DNNs lend themselves well to such complex data and were used in Chapter 5 to estimate SoC from EIS data.

6. Conducted an aging study to compare accelerated aging to realistic drive cycle aging using EIS to show differences in impedance characteristics at different SoH (Chapter 7).

The impedance characteristics of aged batteries are dependent on how they are aged. To understand the impact of different aging pathways, an extensive aging study was conducted. In Chapter 7 the results of this study, comparing charge/discharge aging to drive cycle aging, are presented. The impedance characterization throughout the aging tests give insight into the impact of each aging method.

1.9.2.2 SECONDARY CONTRIBUTIONS

A number of additional contributions are listed and briefly explained in this section.

1. Developed Voigt-circuit based filtering method to improve EIS data analysis (Chapter 3).

Reduced rest times prior to EIS measurement can introduce drift and noise into the EIS data due to the battery relaxation effect. To smooth out EIS results, a Voigt-circuit was used as a filter. The use of this filter allowed for consistent comparison of EIS measurements as well as tracking of the relaxation effect. The filter is described in Chapter 3.

2. Compared the performance of the SVSF and EKF as part of the IMM filter for battery SoC estimation applications (Chapter 6).

In Chapter 6 the IMM-EKF was shown to significantly improve SoC estimation at low temperature. In addition, the IMM-SVSF was shown to be able to further reduce the SoC estimation error due to its adaptive properties and robust estimation.

3. Developed simple EV model to convert speed vs. time driving schedules to drive cycle current profiles (Chapter 7).

An EV model based on Tesla Model 3 was developed using basic vehicle dynamics and constant powertrain efficiencies. The model is described in detail in Chapter 7 and used for realistic battery aging.

4. Published case study on impedance model fitting from EIS data.

Methods for impedance model fitting to EIS measurements are not widely accessible. Fundamentals and equations can be found in literature, but few tutorials and examples exist. As part of this research project, a case study was made available online demonstrating impedance model fitting with real EIS results using MATLAB as a framework. The case study can be found online [32].

5. Designed and implemented a multi-channel battery test system (Chapter 1).

To perform accurate battery characterization as well as realistic drive cycle aging tests, a custom battery test system was designed. This test system is capable of performing fully automated tests on four cells at the same time. The detailed implementation of the test system is described in Section 1.8.

1.10 THESIS OUTLINE

Chapter 2 provides a literature review on the long-term battery relaxation effect with focus on the impact of the relaxation effect on battery modeling. Results are presented showing how model parameters change during the relaxation effect for batteries at different SoCs and temperatures.

Chapter 3 provides a literature review on characterization of the battery relaxation effect with EIS. In addition, the technical challenges regarding EIS measurement and the relaxation effect are discussed. A filtering strategy is proposed to obtain consistent EIS measurements during the short-term relaxation effect. Finally, results are presented to show how different conditions impact the relaxation effect and EIS measurement with short rest times.

Chapter 4 provides a literature review on the use of the relaxation effect as well as the use of EIS for SoH estimation. In this chapter a new method for SoH estimation is proposed combining the relaxation effect and EIS measurements.

Chapter 5 provides a literature review on SoC estimation techniques with special focus on machine learning methods. Furthermore, the chapter presents SoC estimation results for a deep neural network trained on EIS data.

Chapter 6 provides a literature review on low temperature SoC estimation techniques and presents the technical challenges related to current dependant battery models for SoC estimation. The IMM-SVSF low temperature SoC estimation strategy is presented in this chapter.

Chapter 7 presents and discusses results of the accelerated and realistic aging studies. The vehicle model equations are also introduced in this chapter.

Chapter 8 provides the conclusions and discusses future work.

Chapter 2: Lithium-Ion Battery Relaxation Effects

Marvin Messing[1,2], Tina Shoa[2], Saeid Habibi[1]

[1]Department of Mechanical Engineering, McMaster University, Hamilton, ON, Canada,

[2]Cadex Electronics, Richmond, BC, Canada

This paper is published in 2019 IEEE Transportation Electrification Conference and Expo (ITEC), 2019, pp. 1-6, doi: 10.1109/ITEC.2019.8790449. This paper is republished here with permission[2].

ABSTRACT

The accurate estimation of the state-of-charge (SoC) of lithium-ion batteries is crucial for safely operating electric vehicles. One way to obtain information about SoC is to utilize battery impedance profiles. Effects of temperature, SoC, and state-of-health (SoH) on impedance have been studied using Electrochemical impedance spectroscopy (EIS) but the effect of relaxation period following a charge or discharge cycle requires more attention. In this study EIS results are obtained with respect to relaxation period at different SoCs and temperatures. An impedance model is fit to the data and the change of model parameters with relaxation is analyzed. The results show that the behaviour of the model parameters is in good agreement with electrochemical theory. Furthermore, it is found that changes in some model parameters are significant when compared to changes in SoC. This highlights the need to account for the relaxation effect when measuring battery impedance.

[2] In reference to IEEE copyrighted material which is used with permission in this thesis, the IEEE does not endorse any of McMaster's products or services. Internal or personal use of this material is permitted. If interested in reprinting/republishing IEEE copyrighted material for advertising or promotional purposes or for creating new collective works for resale or redistribution, please go to http://www.ieee.org/publications_standards/publications/rights/rights_link.html to learn how to obtain a License from RightsLink.

2.1 INTRODUCTION

Lithium-ion batteries (LiB) are the current choice for many applications due to their energy density, and long life-span [1]. However, charge and discharge rates, voltage levels, and temperature have to be carefully managed to ensure the safe operation of LiBs [2]. The quality of battery management depends on the accuracy of the estimation of battery states such as state of charge (SoC), and state of health (SoH). These states have to be estimated since they cannot be measured. Instead, battery voltage, current, and temperature are measured, and used in estimation strategies [3]. The most important estimate is the SoC which indicates how much energy is left in the battery. The SoC changes non-linearly as the battery is discharged and depends on the discharge profile. All charge is depleted once the lower voltage limit – which is determined by the manufacturer – is reached. One factor determining the accuracy of SoC estimation is the SoH of the battery. The SoH affects the maximum capacity that the battery can supply at any point in its life, relative to the initial rated capacity. The SoH changes due to aging mechanisms inside the battery [4], which depend on the operating conditions during the lifetime of the battery. Therefore, SoC must be estimated using measurable signals such as voltage, current, and temperature, but also by factoring in how the behaviour of the battery changes as a function of SoH.

The management of LiBs is particularly important for battery packs in electric vehicles (EV). A wide variety of parameter estimation techniques are available for EV applications, collectively covering most operating conditions and individually showing reasonable tracking accuracy [5].

However, the challenge remains to find a more accurate, reliable, universal, and feasible estimation strategy.

Battery states are also related to battery impedance. Battery impedance holds useful information about the internal condition of the battery. Impedance is the combination of reactance and resistance. In batteries, impedance comes from the interaction between different materials, the material characteristics themselves, and chemical reactions [6]. Impedance can be modeled using fundamental electrical circuit components such as resistors and capacitors. However, imperfect circuit elements must be used to increase the modeling accuracy. Models containing such imperfect elements are referred to in this work as impedance models, to distinguish them from ideal equivalent circuit models (ECM).

Electrochemical impedance spectroscopy (EIS) is a method frequently used to characterize the impedance of batteries. In this method, the battery response to a small, sinusoidal signal at multiple frequencies is measured. Using the Fourier transform the time domain response can be converted to frequency domain. From the frequency domain data, a characteristic Nyquist plot can be constructed and used to gain insight into the state of the battery, including its internal resistances, capacities and time constants. To accomplish this, the impedance response of a battery is fit to ECMs or impedance models to mimic electrical systems that result in a similar shape of the Nyquist plot, in response to EIS. Any elements used in ECMs or impedance models must relate to internal characteristics of the battery to be meaningful [7]. Hardware to implement EIS is not usually found on-board battery management systems (BMS) in EVs because of the added cost and complexity of the

electronics [8]. However, some recent studies have shown EIS implementations utilizing existing electronics [9], [10]. If hardware barriers can be overcome, EIS could provide valuable measurements that can be used in SoC estimation algorithms. Another concern with EIS is that measurements are dependent on a variety of factors such as SoC, SoH, temperature, and time of measurement with respect to other battery excitation (charge/discharge) – known as relaxation. Therefore, the relationships between these variables and the shape of the Nyquist plot must be studied and understood. Many have studied the impact of SoC, SoH, and temperature [11]–[14], however, few have shown the impact of relaxation. In [15], discharge pulses were used to measure the change in lithium-ion battery impedance with relaxation. They found that many ECM parameters change with relaxation for different SoCs and discharge currents. In [16] the change in OCV with relaxation time was analyzed. Here, time constants of ECM parameters were related to SoH. Relaxation was investigated by [17]–[19]. The relaxation effect was acknowledged by [15] as part of an impedance characterization study and changes in the Nyquist plot were shown to 40 hours. They concluded that impedance changes due to relaxation are small compared to impedance changes due to temperature and SoC but significant enough to require the relaxation effect to be accounted for when comparing impedance results. In [18] the Nyquist plots were shown to stabilize after relaxation of 4 hours under constant SoC and temperature. In [19] relaxation effects were shown to still be visible after 10 hours, and a range of SoCs and temperatures were tested. Both [18] and [19] tested different lithium ion chemistries and battery formats, and developed models to explain the cause of relaxation.

The proposed study aims to provide insight into the variation of EIS in relation to relaxation effects for a range of battery conditions for a state of the art commercial, cylindrical cell. In addition, the impact of relaxation on the parameters of an impedance model is analyzed.

2.2 EXPERIMENTAL

A custom battery test bench was designed to perform unattended relaxation experiments by integrating a BioLogic SP150 potentiostat with Agilent loads and power supplies (N3306A, N6773A respectively) and a Testequity 1007C thermal chamber. In this study a new Samsung INR21700-48G, 4.8 Ah, cylindrical lithium ion battery was used. The cell was conditioned by 10 full charge discharge cycles. The cell was charged as specified by the manufacture's datasheet starting with a constant current (CC) phase at 0.3C 4.2V followed by a constant voltage (CV) phase to 0.02C cut-off current. Full discharge was done at 0.2C to 2.5 V in CC mode, and SoC targets between 100% and 30% were obtained at 0.2C as well using ampere-hour counting. EIS data was collected between frequencies of 30 mHz to 30 kHz with a voltage amplitude of 5 mV, 6 points per decade and 5 sine wave periods per frequency. EIS data was measured immediately after reaching the target SoC (via discharge only), and re-measured at 30, 60, 180, 300, and 420 minutes. The relaxation test was performed at 25 °C and 40 °C cell surface temperature.

2.3 RESULTS AND DISCUSSION

The EIS response of a battery was measured as described in the previous section to capture the relaxation effect. The relaxation test was repeated three times to ensure the repeatability

of the impedance data. It was found that relaxation effects could be distinguished from repeatability errors. The average standard deviation of the impedance was found to be 4.6e-05 mΩ. Figure 2-1: Nyquist plots for 100%, 70% and 30% SoC at 25°C and 40°C. shows Nyquist plots for impedance data at 24 °C and 40 °C and how the impedance changes from 100 % to 70 % to 30 % SoC. In the following subsections the impedance data is fit to a model and the change of model parameters with respect to the relaxation effect is analyzed.

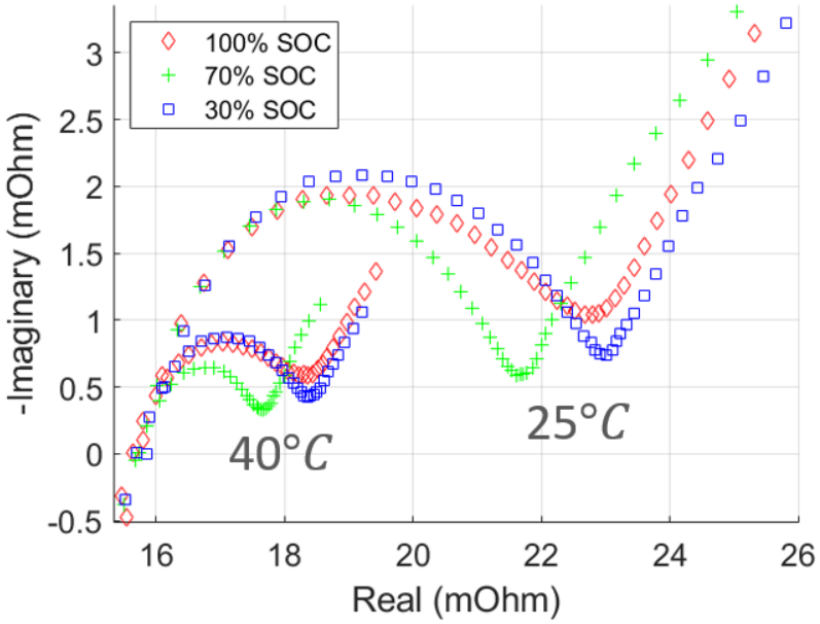

Figure 2-1: Nyquist plots for 100%, 70% and 30% SoC at 25°C and 40°C.

2.3.1 Impedance Model

Figure 2-2a shows an ECM adopted from [22] and used in this work. The complex impedance Z of this ECM changes with frequency ω according to (2-1), where the time constant $\tau = \left(R_p Q_p\right)^{1/\alpha}$.

$$Z(\omega) = i\omega L + Rs + Rp/(1 + RpQp(i\omega\tau)\alpha) + 1/Qp(i\omega)\beta \qquad (2\text{-}1)$$

Here, i is the applied current magnitude, L is the inductance due to cables used for measurment, and R_s is the ohmic resistance of the battery. R_p and Q_p, α define the polarization resistance and a constant phase element (CPE) for capacitive effects from the electric double layer. Together they form a ZArc element. Finally, Q_d, β defines another CPE to capture the solid-state diffusion process. The impedance model can fit the EIS data well as shown in Figure 2-2b for impedance data after discharge to 90% SoC with no rest and 7 hours of rest. The impedance model parameters were optimized using a combination of non-linear least squares and particle swarm optimization algorithms.

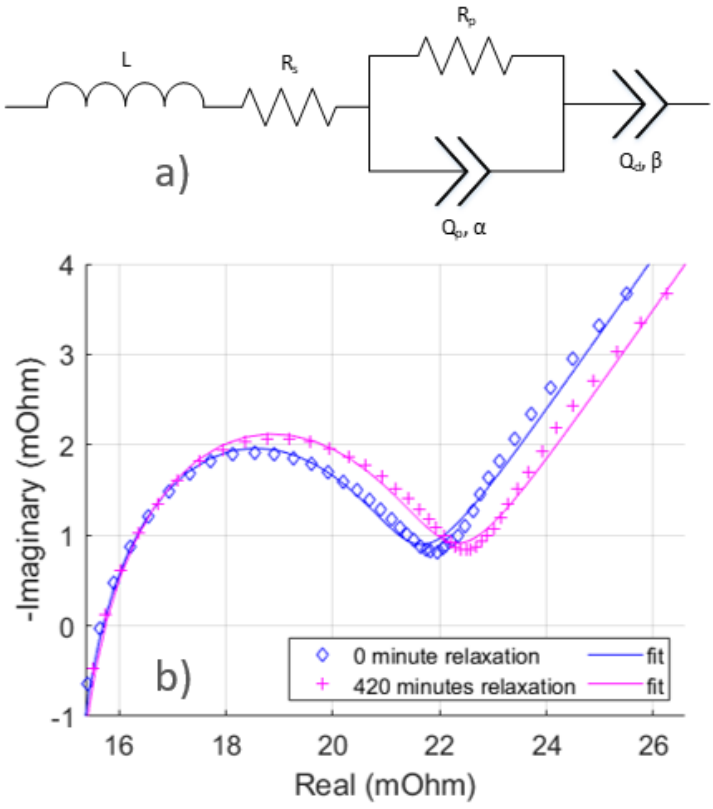

Figure 2-2: Impedance model used to model relaxation effect a), and model fit to relaxation data at 25°C and 90% SoC b).

However, neither algorithm was able to produce fits with consistent fitting error. Figure 2-3 shows how the fitting error changes for different SoCs and relaxation times. The model fit has greater error at zero rest and stabilizes to a constant value for data at 60 minutes and after. This fitting error must be considered when analyzing the relaxation results.

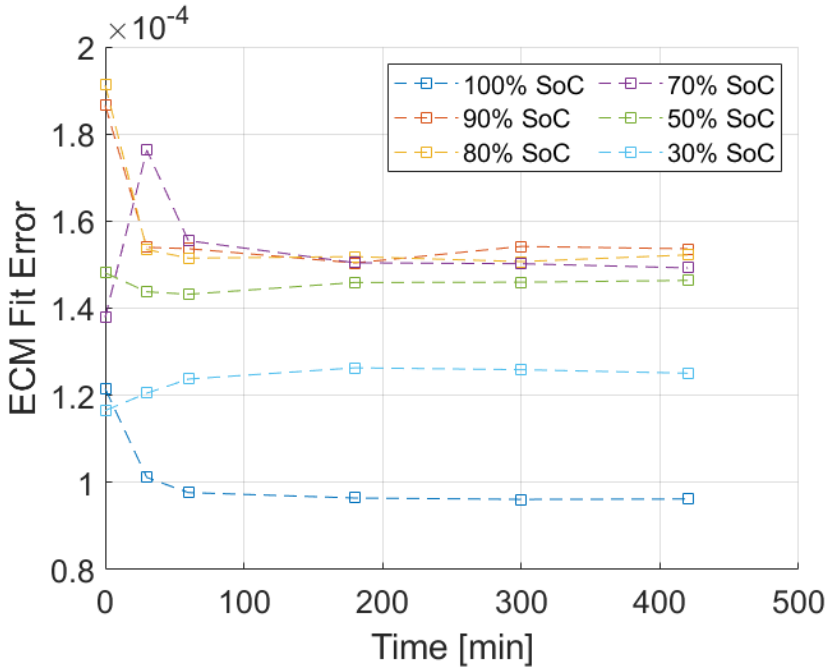

Figure 2-3: Impedance model fitting error with different SoCs over different rest times.

Figure 2-4 shows how the fit evolves with relaxation time at 25 °C and 40 °C. The change of the Nyquist plot between 5 and 7 hours is small but still present and is smaller at higher temperature when compared to the lower temperature. It can be observed that after 5 hours the change in battery impedance has slowed significantly. However, it is unclear when exactly it has slowed significantly enough such that any further impedance changes are negligible. Changes in impedance may be deemed negligible if the change has minimal impact on the fitting of an impedance model. This is because ultimately the impedance

model may be used to further analyze the battery behaviour and, therefore, the accuracy and consistency of the model becomes important.

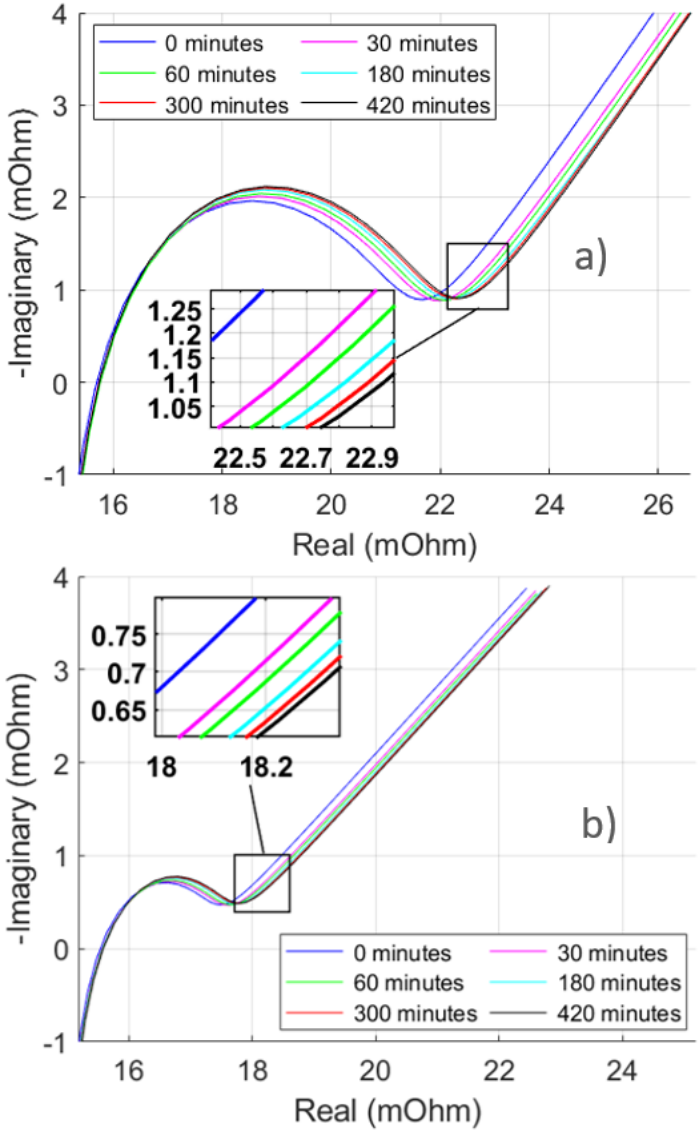

Figure 2-4: Modelled relaxation effect at 90% SoC and 25°C a), and 40°C b).

2.3.2 Relaxation Effect

To understand how the parameters of the model shown in Figure 2-2a change with relaxation time, the percentage change of each parameter P from its value at 7 hours (420

minutes) P_{420} was calculated using (2-2). P_t is the value of a model parameter (one of L, R_s, Q_d, Q_p, R_p, a, or b) at relaxation time *t*. The datasets for each parameter were fit with exponential functions to model the rate of change during relaxation.

$$\Delta_{420} = \frac{Pt - P420}{P420} \quad (2\text{-}2)$$

Figure 2-5 shows Δ_{420} at $25\,°C$ for each model parameter at three SoCs, 100 % a), 90 % b), 70 % c), and 30 % d). The inductance L and the ohmic resistance R_s stabilize within 10 minutes in all cases. The changes of L and R_s before 10 minutes are inconsonant and likely due to the error introduced by the fitting process as discussed in the previous section. At 100% SoC the parameters with the longest relaxation time are Q_p and R_p, i.e. two components of the ZArc element. The depression constant a (or α) for the first semi-circle does not change. The depression constant for the second semi-circle b (or β) shows a smooth decay at a fast rate. The second CPE parameter Qd on the other hand shows noisy data points. This may be explained by little or no lithium diffusion at 100% SoC due to low availability of intercalation sites on the anode. At 90% SoC, where more intercalation sites are available and the relatively high cell potential accelerates diffusion, Qd behaves similar to Rp. At 70 % Qd stabilizes rapidly again which may indicate a point where the cell potential (driving force) and the SoC (available intercalation sites) work together to equalize concentration gradients [21]. This is reflected by the lower initial values of Δ_{420} for Qp and Rp. However, while the difference is lower initially, it takes longer for parameters to stabilize due to many available intercalation cites for the lithium and, therefore, potentially longer travel paths [19].

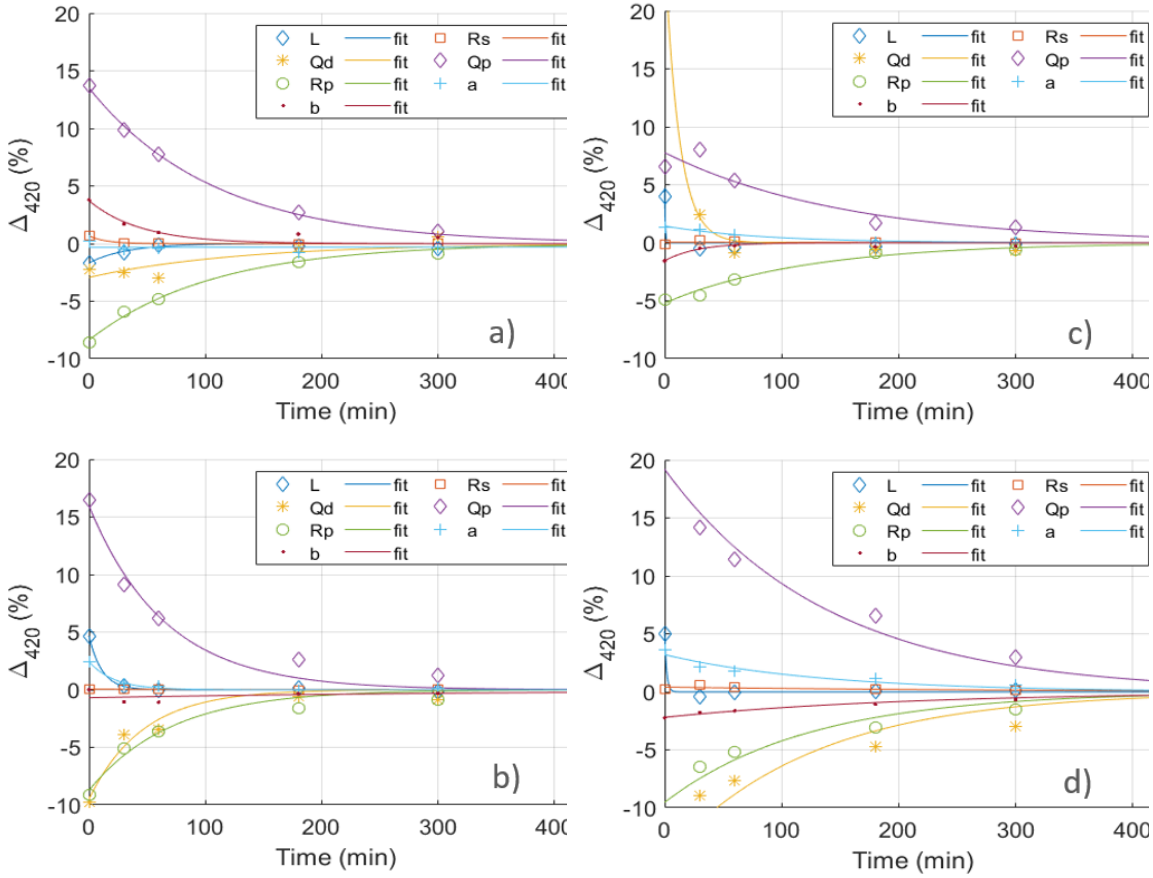

Figure 2-5: Percentage change in impedance model parameters from values at 420 minutes at 25°C for a) 100% SoC, b) 90% SoC, c) 70% SoC and d) 30% SoC.

Finally, at 30 % SoC the cell potential is low, such that Qp, Rp and Qd equalize slowly despite the large number of available interalation cites. In fact, the relaxation is slowest at 30 % for all three parameters. Lithium slowly diffuses into and through the electrode to find intercalation cites during relaxation. At low SoC this process is slow because of the reduced driving potential. The exponential fit to the Qp dataset at 30 % SoC (Figure 2-5d) suggests that at 420 minutes (7 hours) the cell has not yet stabilized.

At 40 °C (Figure 2-6) the model parameters change in a way similar to that at 25 °C. The parameters stabilize faster at higher SoC and slower at lower SoC, with 30 % showing the slowest rate of stabilization. The polarization parameters Qp and Rp stabilize at a slightly slower rate at 40 °C compared with 25 °C. This is unexpected because of higher reaction kinetics at higher temperatures. However, the decrease in rate is small, such that additional data will be needed to understand this trend. In contrast, Qd does stabilize faster in all cases as expected. At 100 % SoC, both diffusion parameters exhibit noisy behaviour again. At 40 °C the exponential fit for Qp and Rp at 70 % SoC (Figure 2-5c) and Qp at 30 % (Figure 2-6d) do not reach steady state, suggesting again that further rest is required.

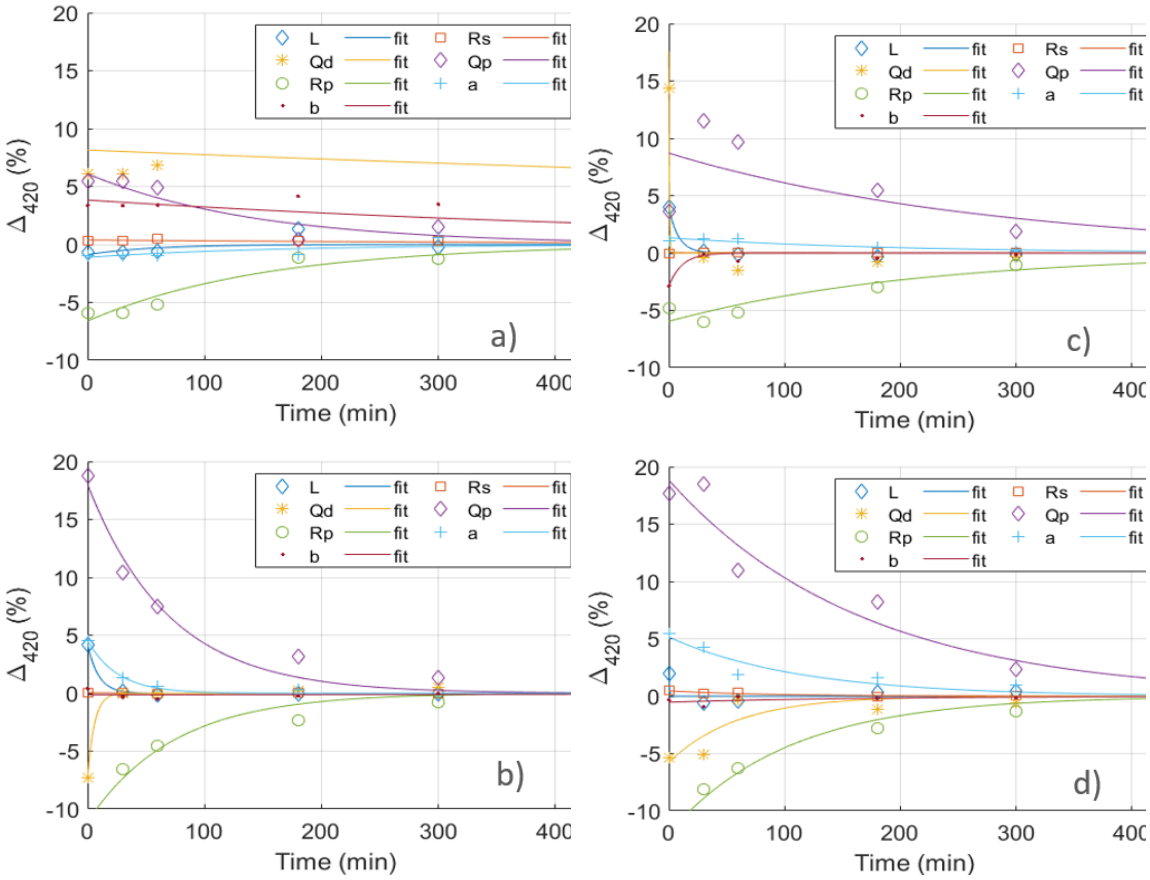

Figure 2-6: Percentage change in impedance model parameters from values at 420 minutes at 40°C for a) 100% SoC, b) 90% SoC, c) 70% SoC and d) 30% SoC.

2.3.3 IMPEDANCE MAPS

Figure 2-7 shows how the dominant model parameters Q_p, R_p, and Q_d change with time and SoC at 25 $°C$. The relaxation effect manifests mostly at the edges of the three-dimensional plots. These plots visualize the difference in magnitudes of the parameter change due to relaxation and due to SoC. At the middle range of SoCs (80 % to 40 %) the parameter changes due to relaxation become insignificant when compared to the parameter changes due to SoC. However, the relaxation effect does cause significant parameter changes at the edges of the SoC range (> 90 % and < 40 %). This is evident in Figure 2-7a and c for Q_p

and R_p at 25 $°C$. At 40 $°C$ the same can be seen in Figure 2-8c for R_p only. The magnitudes of the parameter values also change significantly between 25 $°C$ and 40 $°C$. The diffusion CPE parameter Q_d exhibits a linear trend with SoC from 90 % SoC for both temperatures. This is a useful property of SoC estimation.

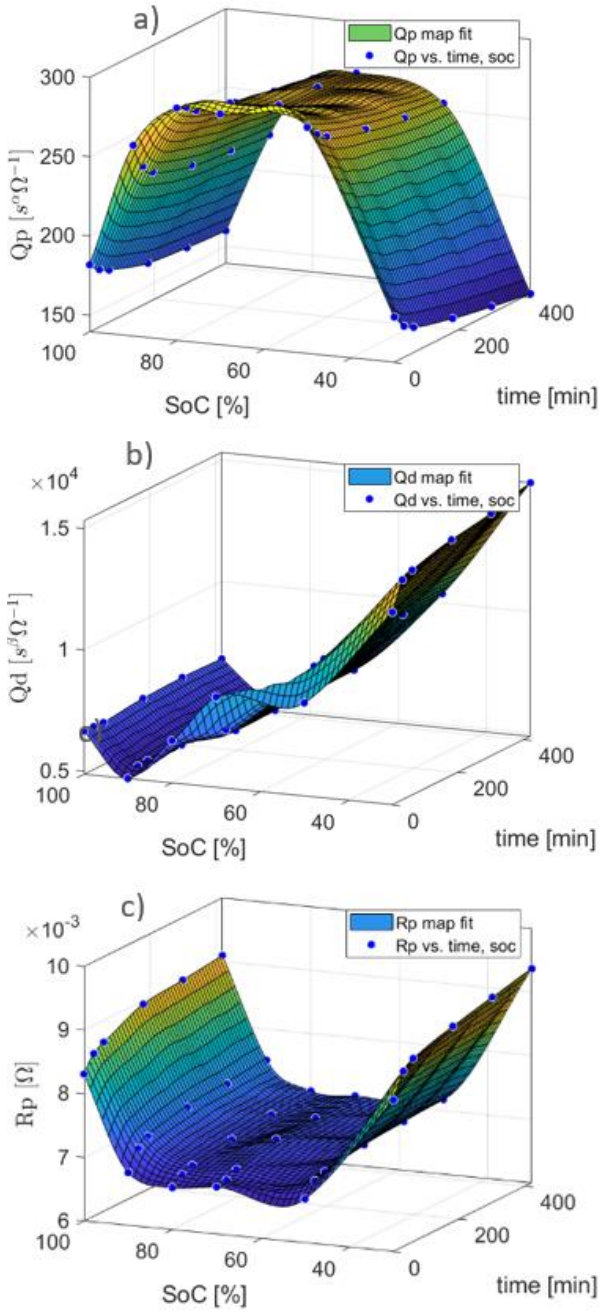

Figure 2-7: Impedance maps showing values for a) Qp, b) Qd and c) Rp for different SoCs and rest times at 25°C.

The need for rest time during experiments can be eliminated with the help of impedance maps shown in Figure 2-7 and Figure 2-8, since measurements at 0 minutes can be

extrapolated to rest time values. This is especially important for real time applications for EIS measurement where rest times are impractical.

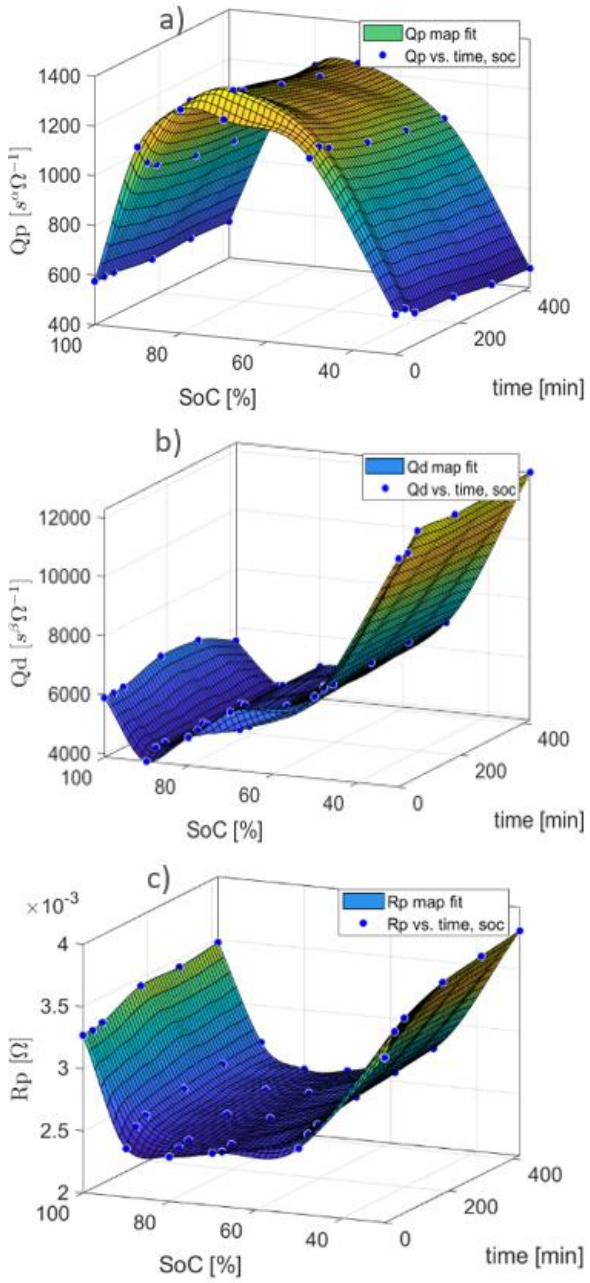

Figure 2-8: Impedance maps showing values for Qp, Rp, and Qd for different SoCs and rest times at 25°C (a-c), and 40°C (d-f).

2.4 CONCLUSION

In the work presented in this paper the relaxation effect of a commercial lithium ion battery was characterized using EIS and impedance modelling. A suitable impedance model was found in literature and used to model the relaxation effect. The change of each model parameter with relaxation time was analyzed and found to be consistent with electrochemical theory. Results at 40 $°C$ indicate a small decrease in relaxation rate which must be investigated further as it is contrary to previous literature findings. Impedance maps show that the changes in model parameters due to relaxation are significant at certain conditions when compared to the changes in parameters due to SoC and temperature. This should be validated by assessing the impact of the change in model parameters due to relaxation on the accuracy of the model. This work highlights again the need for careful consideration of the relaxation effect. The study will be expanded to longer rest times as well as different temperatures, charge/discharge rates, battery types, and impedance model in future work.

REFERENCES

[1] M. A. Hannan, M. S. H. Lipu, A. Hussain, and A. Mohamed, "A review of lithium-ion battery state of charge estimation and management system in electric vehicle applications: Challenges and recommendations," *Renew. Sustain. Energy Rev.*, vol. 78, no. August 2016, pp. 834–854, 2017.

[2] R. Xiong, J. Cao, Q. Yu, H. He, and F. Sun, "Critical Review on the Battery State of Charge Estimation Methods for Electric Vehicles," *IEEE Access*, vol. 6, pp. 1832–1843, 2018.

[3] L. Ungurean, G. Cârstoiu, M. V Micea, and V. Groza, "Battery state of health estimation : a structured review of models , methods and commercial devices," no. July 2016, pp. 151–181, 2017.

[4] M. M. Kabir and D. Demirocak, "Degradation mechanisms in Li-ion batteries: a state-of- the-art review," *Int. J. energy Res.*, vol. 41, no. April 2017, pp. 1963–1986, 2017.

[5] M. U. Cuma and T. Koroglu, "A comprehensive review on estimation strategies used in hybrid and battery electric vehicles," *Renew. Sustain. Energy Rev.*, vol. 42, pp.

517–531, 2015.
[6] M. Schönleber, C. Uhlmann, P. Braun, A. Weber, and E. Ivers-Tiffée, "A Consistent Derivation of the Impedance of a Lithium-Ion Battery Electrode and its Dependency on the State-of-Charge," *Electrochim. Acta*, vol. 243, pp. 250–259, 2017.
[7] R. Cottis and S. Turgoose, *Electrochemical Impedance and Noise*. Houston: NACE International, 1999.
[8] J. Meng *et al.*, "An Overview and Comparison of Online Implementable SOC Estimation Methods for Lithium-Ion Battery," *IEEE Trans. Ind. Appl.*, vol. 54, no. 2, pp. 1583–1591, 2018.
[9] E. Din, C. Schaef, K. Moffat, and J. T. Stauth, "A scalable active battery management system with embedded real-time electrochemical impedance spectroscopy," *IEEE Trans. Power Electron.*, vol. 32, no. 7, pp. 5688–5698, 2017.
[10] X. Wei, X. Wang, and H. Dai, "Practical on-board measurement of lithium ion battery impedance based on distributed voltage and current sampling," *Energies*, vol. 11, no. 1, 2018.
[11] P. Kollmeyer, A. Hackl, and A. Emadi, "Li-ion battery model performance for automotive drive cycles with current pulse and EIS parameterization," *2017 IEEE Transp. Electrif. Conf. Expo, ITEC 2017*, pp. 486–492, 2017.
[12] C. Pastor-Fernández, K. Uddin, G. H. Chouchelamane, W. D. Widanage, and J. Marco, "A Comparison between Electrochemical Impedance Spectroscopy and Incremental Capacity-Differential Voltage as Li-ion Diagnostic Techniques to Identify and Quantify the Effects of Degradation Modes within Battery Management Systems," *J. Power Sources*, vol. 360, pp. 301–318, 2017.
[13] U. Westerhoff, T. Kroker, K. Kurbach, and M. Kurrat, "Electrochemical impedance spectroscopy based estimation of the state of charge of lithium-ion batteries," *J. Energy Storage*, vol. 8, pp. 244–256, 2016.
[14] B. Fridholm, T. Wik, and M. Nilsson, "Robust recursive impedance estimation for automotive lithium-ion batteries," *J. Power Sources*, vol. 304, pp. 33–41, 2016.
[15] H. Wang, M. Tahan, and T. Hu, "Effects of rest time on equivalent circuit model for a li-ion battery," *Proc. Am. Control Conf.*, vol. 2016–July, pp. 3101–3106, 2016.
[16] P. S. Attidekou, C. Wang, M. Armstrong, S. M. Lambert, and P. A. Christensen, "A New Time Constant Approach to Online Capacity Monitoring and Lifetime Prediction of Lithium Ion Batteries for Electric Vehicles (EV)," *J. Electrochem. Soc.*, vol. 164, no. 9, pp. A1792–A1801, 2017.
[17] W. Waag, S. Käbitz, and D. U. Sauer, "Experimental investigation of the lithium-ion battery impedance characteristic at various conditions and aging states and its influence on the application," *Appl. Energy*, vol. 102, pp. 885–897, 2013.
[18] A. Barai, G. Chouchelamane, Y. Guo, A. McGordon, and P. Jennings, "A study on the impact of lithium-ion cell relaxation on electrochemical impedance spectroscopy," *J. Power Sources*, vol. 280, no. Special Issue, pp. 74–80, 2015.
[19] F. M. Kindermann, A. Noel, S. V. Erhard, and A. Jossen, "Long-term equalization effects in Li-ion batteries due to local state of charge inhomogeneities and their impact on impedance measurements," *Electrochim. Acta*, vol. 185, pp. 107–116, 2015.
[20] J. Schmitt, A. Maheshwari, M. Heck, S. Lux, and M. Vetter, "Impedance change and capacity fade of lithium nickel manganese cobalt oxide-based batteries during calendar aging," *J. Power Sources*, vol. 353, pp. 183–194, 2017.
[21] T. R. Jow, S. A. Delp, J. L. Allen, J.-P. Jones, and M. C. Smart, "Factors Limiting Li + Charge Transfer Kinetics in Li-Ion Batteries," *J. Electrochem. Soc.*, vol. 165, no. 2, pp. 361–367, 2018.

Chapter 3: Electrochemical Impedance Spectroscopy with Practical Rest-times for Battery Management Applications

Marvin Messing[1,2], Tina Shoa[2], Saeid Habibi[1]

[1]Department of Mechanical Engineering, McMaster University, Hamilton, ON, Canada,

[2]Cadex Electronics, Richmond, BC, Canada

This paper is published in IEEE Access, vol. 9, pp. 66989-66998, 2021, doi: 10.1109/ACCESS.2021.3077211. This paper is republished here with permission.

ABSTRACT

The State of Charge (SoC), State of Health (SoH), and State of available Power (SoaP) of Lithium-Ion Batteries (LiB) are critical quantities which cannot be measured but must be estimated by Battery Management Systems (BMS) instead. A technique known as Electrochemical Impedance Spectroscopy (EIS) provides a non-destructive way of measuring battery impedance, offering detailed insight into the battery state of operation. Several challenges must be solved in to utilize EIS as part of the BMS, including the defining of operating conditions at which to perform the sensitive EIS measurement. In laboratory conditions, several hours of rest are used to ensure a stable response of the battery, but such rest times are impractical for BMS applications. This paper proposes a methodology combining drift compensation and a Voigt-circuit used as a filter to obtain valid EIS data with short rest times under different operating conditions. Extensive tests were conducted on lithium nickel manganese cobalt (NMC) batteries to evaluate the methodology and show how the different operating conditions impact the rest time required

for valid EIS measurement. The results show that rest times between 5 and 30 minutes can be used to obtain useful EIS data for a wide range of operating conditions.

3.1 INTRODUCTION

In this paper, we address some of the challenges pertaining to Electrochemical Impedance Spectroscopy (EIS) measurements for applications in Battery Management Systems (BMS). Specifically, the impact of the battery relaxation effect on EIS measurements is examined to determine the shortest possible rest required before valid EIS results can be obtained under various operating conditions. Extensive experiments have been conducted on Lithium nickel manganese cobalt (LiNiMnCoO2 or NMC) batteries. This paper proposes a methodology that combines drift compensation and Voigt-circuit based filtering to produce valid EIS results. In addition, different battery relaxation behavior is induced using discharge pulses of different current rates (C-rate) to understand the relationship between battery discharge and relaxation. The discharge pulses are performed at different SoCs and temperatures, and EIS measurements are obtained for each case at different rest times. This section discusses the motivation and technical challenges, summarizes recent relevant literature, presents the main paper contributions, and provides an outline of the rest of the paper.

3.1.1 MOTIVATION AND TECHNICAL CHALLENGES

Battery management systems (BMS) perform multitude of functions that impact the performance and the safe operation of batteries in advanced applications. Lithium-ion batteries (LiB) are currently the preferred choice for energy storage in Electric Vehicles

(EVs) as well as many other applications, primarily due to their high energy density and their relatively long cycle life [1]. The BMS must estimate, in real-time, the battery's State of Charge (SoC), State of available Power (SoaP) and SoH, but this continues to remain a challenge [2], [3]. SoC provides an indication of how much driving range remains before the battery must be charged. However, as the SoC decreases, the battery voltage also drops, which means more current is required at lower SoC to achieve the same power compared to high SoC. SoaP provides a way of predicting the available power output within the voltage and current limits of the cell in the battery pack. SoH determines the total available capacity of a battery and gives insight into the battery behavior as it changes with age. Inaccuracies in SoH estimates lead to further inaccuracies in the SoC and SoaP estimates, and, as a result, battery packs in EVs are over engineered to account for these uncertainties [4]. A variety of methods exist to estimate SoC, SoH, and SoaP for BMS and EV applications including model-based filters and observers [5]–[12] machine learning methods [13], [14] and methods based on direct measurement of charge/discharge behavior of the battery [15] as well as several others [16]. In laboratory settings, advanced instrumentation and exhaustive test methods are used to extract additional information from the battery and infer SoC and SoH. One such method is EIS, which measures the impedance of a battery [17]. In EIS, a sinusoidal voltage or current signal of small amplitude is applied to the battery at different frequencies. Using the Fast Fourier transform (FFT) of these signals, the impedance of the battery is obtained by calculating its amplitude and phase responses for each frequency. The real and imaginary component pairs of the complex impedance can be plotted to provide the Nyquist plot. The battery impedance and its

representation of Nyquist plot changes depending on the state of the battery. In general, the high cost of EIS hardware as well as length of test times make EIS characterization unfeasible for integration into BMS [18], however, efforts are being made to change this by developing more cost-effective ways to generate EIS [19]. The hardware requirements depend on the desired frequency range and the range of the internal resistance of the batteries used. Furthermore, the hardware should be able to maintain a sufficiently high signal to noise ratio, while only exciting the battery within its linear operating range. Using potentiostatic EIS (PEIS) allows for the control of the excitation voltage such that linearity is maintained. However, the lower the battery internal resistance, the higher the output currents that must be measured. To avoid high output currents, galvanostaic EIS (GEIS) can be used, where current is the input signal and voltage is measured. For GEIS the current must be carefully chosen such that the signal to noise ratio of the voltage measurement is sufficiently high, but the linear operating range of the battery is not exceeded and the excitation does not cause the battery to heat up significantly. Din et al. [20] combined active balancing circuitry and a control strategy to produce sinusoidal battery cell excitation. They used a switched inductor ladder configuration which allows dissipation of power from one cell to another, reducing energy loss. Their results show close agreement when compared to lab-grade measurements. Wei et al. [21] proposed a hardware solution for exciting 12 battery cells in series with a single current signal, and measured the voltage response of each cell. They use a DC to AC converter to generate the pack input signal. Lohmann et al. [22] proposed a method for extracting impedance spectra from conventional driving cycle data. In this scenario, the electric motor of the EV generates the signal. However, and

as a result, the frequency range is limited to that of the drive cycles. The studies reviewed above provide possible answers for practical EIS as part of a BMS, however, consideration of relaxation effects and required rest times before measurement are largely omitted. In the next part of this section, studies which discuss relaxation effects are reviewed.

3.1.2 Relaxation Effect and EIS Measurement

EIS varies according to the battery's SoH and SoC amongst other factors. To use EIS in practical applications, the impact of different measurement conditions must be investigated. SoC, SoH, and temperature were investigated in several studies [23]–[27] in laboratory settings for the purpose of battery characterization. In most EIS studies, a rest time period of 1 to 24 hours is used after charge or discharge and before the EIS measurement [28]. This is done to ensure that only the small signal EIS excitation is causing the battery response measured by EIS. During normal discharge, the battery response is highly non-linear, and once the discharge is stopped, the battery voltage rises rapidly (relaxation effect). Over time, the voltage stabilizes, and EIS is usually measured once the relaxation effect has slowed significantly, to avoid contribution of the relaxation effect to the EIS measurement. Kindermann et al. [28] presented a thorough investigation of the long-term relaxation effects under different conditions and for different types of batteries. They showed that battery relaxation still impacts EIS results after 40 hours, and low SoC and low temperature slow the rate of relaxation. Barai et al. [29] also studied the long-term relaxation effect as well as its impact on cell resistance and capacitance, showing that ohmic resistance is independent of relaxation, but capacitance follows a logarithmic trend. Waag

et al. [30] acknowledged the relaxation effect and demonstrated changes in the Nyquist plot after 40 hours. They concluded that the impact of the relaxation effect is small compared to the impact of SoC and temperature, but significant enough to account for it when interpreting EIS results since the relaxation effect can change the EIS measurement by 5 to 10%. The relaxation effect was also investigated without the use of EIS by Wang et al. [31], who used a current pulse followed by different rest times to extract rest time dependent parameters for a second-order equivalent circuit model. They found robust trends for changes in model parameters with rest time, discharge current and SoC. Zinth et. al. [32] investigated changes in graphite anode electrodes using neutron diffraction to track the impact of different discharge rates on the relaxation effect. They showed long lasting effects for low temperatures beyond 11 hours. Deverakonda et al. [27] studied the impact of the relaxation effect on the parameters of the Thevenin equivalent circuit model after different discharge and charge currents for lead acid batteries. In our previous study on relaxation [33], we investigated how fractional order impedance model parameters change with the long-term relaxation effect at different SoCs and temperatures.

The above studies all focus on the behavior and implications of the battery relaxation effect over long periods of time, conclude that the relaxation effect is still present after days of rest, and largely use 1 to 3 hours before performing EIS measurements. However, no solutions exist for obtaining EIS results with short rest times (<1 hour). Short rest times are desirable to reduce measurement times for BMS applications, but validity of EIS measurements must be ensured by filtering out measurement contributions from the relaxation effect. The objective of the present study is to address this gap by investigating

the short-term relaxation effect of different severity induced by discharge pulses for different SoCs, and temperatures to define operating points for EIS measurement with short rest time.

3.1.3 CONTRIBUTIONS

This paper presents the following original contributions and conclusions: (1) A methodology using drift compensation and a Voigt-circuit as a filter to convert short rest-time EIS measurements to valid EIS data is proposed (2) a method comparing EIS measurements obtained during relaxation effects is developed (3) it is shown that EIS measurements with short term relaxation times are valid and useful under specific conditions (4) the effect of discharge pulse depths is only visible up to 30 minutes of rest for high SoC, and temperatures at and above 25°C.

3.1.4 PAPER OUTLINE

The paper is organized as follows. Section 3.2 discusses EIS validity, drift compensation, Kramer-Kronigs relations and then introduces a methodology which combines these methods with a Voigt-circuit used as a filter for obtaining valid EIS results with short rest times. In Section 3.3, the experimental methods used for investigating the relaxation effect are described. Section 3.4 describes a method to simplify analysis of the relaxation effect. Section 3.5 discusses the general variation in behavior of the relaxation effect under different experimental conditions including changes in SoC and temperature, evaluates short rest time EIS validity, and shows how the combination of discharge pules, SoC, and

temperature impacts the relaxation effect and EIS results. Concluding remarks are provided in Section 3.6.

3.2 SHORT TERM EIS MEASUREMENT METHOD

When a discharge pulse is applied to a battery, the rate of the relaxation effect changes depending on the C-rate. Higher C-rates, for example 5C, cause more pronounced and longer relaxation behavior. Figure 3-1 shows Nyquist plots after a 5C discharge pulse at different rest times for three tests (sets 1 to 3) conducted on different days, but with constant operating conditions (90% SoC, 25°C). The results show that the EIS measurements are repeatable enough to clearly distinguish different rest times, suggesting that the relaxation effect yields repeatable results when measured with EIS. This repeatability of the short-term relaxation effect suggests it is worth measuring EIS with short rest times if the effects of relaxation are understood and properly compensated.

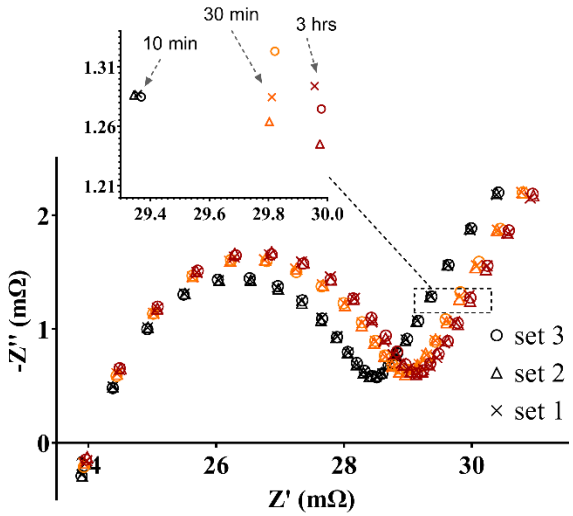

Figure 3-1: Three repeats of EIS measurements (set 1, 2 and 3) for different rest times after a 5C discharge pulse.

An EIS measurement is considered valid if it is applied to a system that satisfies the criteria of linearity, stability and causality [17]. EIS can be applied to non-linear systems such as batteries only if they remain within a piece-wise linear operating region, normally following long rest periods and requiring small amplitudes of input excitations. Collecting an EIS spectrum with short rest times after a high current discharge will cause drift in the measurement as shown in Figure 3-2 for 1 minute of rest after a discharge pulse, thereby violating causality and stability. Nonetheless, EIS can still be used in this case by applying drift compensation and by using the Kramer-Kronigs transformable Voigt circuit as a filter, which are discussed in this section.

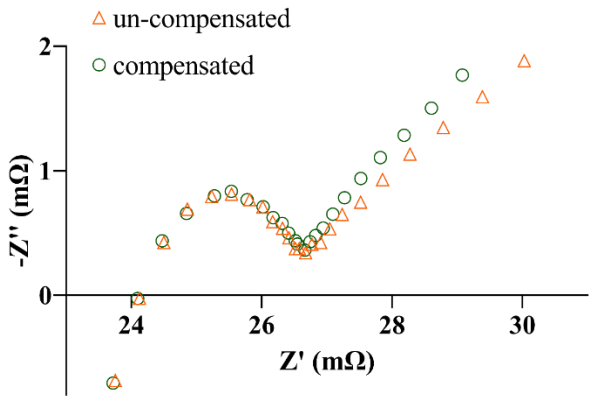

Figure 3-2: Effect of drift compensation with 1-minute rest.

Drift in the EIS measurement can be compensated by following the procedure described by Zahner [74], which is implemented in most modern potentiostats. In this method, multiple periods of the EIS excitation signal are measured at each frequency to determine the non-periodic (under drift), mean DC component. The mean DC component is then subtracted from the signal to obtain a drift-corrected signal. This signal still contains non-periodic components, which are identified and eliminated in the frequency domain after applying

the FFT. The resulting EIS measurement, after drift compensation, is also shown in Figure 3-2.

The Kramer-Kronigs transform calculates the imaginary part (Z'') of the impedance from the real part (3-1) or the real part (Z') from the imaginary part (3-2) given a frequency ω as follows.

$$Z''(\omega) = -\left(\frac{2\omega}{\pi}\right)\int_0^\infty \frac{Z'(x)-Z'(\omega)}{x^2-\omega^2}dx \quad (3\text{-}1)$$

$$Z'(\omega) = Z'(\infty) + \frac{2}{\pi}\int_0^\infty \frac{xZ''(x)-\omega Z''(\omega)}{x^2-\omega^2}dx \quad (3\text{-}2)$$

This transform only applies if the linearity, stability, and causality criteria are satisfied, thus providing a way of validating EIS measurements. However, EIS cannot be measured for frequencies (x) from zero to infinity, making the KK-transform itself impossible to implement. To circumvent this limitation, the EIS spectra were fitted to a Voigt circuit shown in Figure 3-3. A good fit, with random residuals and low mean-square-error (MSE), indicates a valid EIS spectrum, since the Voigt circuit is known to be KK-transformable [17], [35].

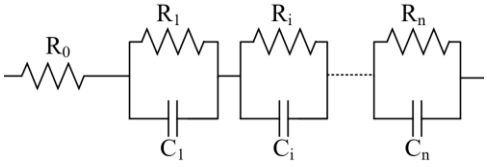

Figure 3-3: Voigt Circuit

Equation 3-3 defines the Voigt circuit, where the impedance $Z = Z' + jZ''$, the sum of real and imaginary parts given a frequency ω_k:

$$Z(\omega_k) = \sum_{i=1}^{n} \frac{R_i}{1+(\omega_k\tau_i)^2} - j\sum_{i=1}^{n} \frac{\omega_k\tau_i R_i}{1+(\omega_k\tau_i)^2} \quad (3\text{-}3)$$

Here, $\tau_i = {}^{1}/_{\omega_i}$ are the time constants and ω_i are the experimental frequencies. Equation 3-3 was extended as shown in (3-4):

$$Z(\omega_k) = j\omega_k L - j\frac{1}{\omega_k C} + R_0 + \sum_{i=1}^{n}\frac{R_i}{1+j\omega_k\tau_i} \quad (3\text{-}4)$$

A capacitor (with capacitance C) and an inductor (with inductance L) were added in series. The resistances R_i are the only unknowns, since the capacitances $C_i = \tau_i/R_i$. The time constants τ_i may be computed for each frequency ω_i, but fewer time constants may be necessary to avoid overfitting. Overfitting can be detected by computing the ratio, μ, of the sum of positive and negative R_i parameters as described by Schonleber et. al [36] and shown in (3-5).

$$\mu = 1 - \frac{\sum_{R_i<0}|R_i|}{\sum_{R_i\geq 0}|R_i|} \quad (3\text{-}5)$$

This ratio μ measures oscillations in the Voigt fit which result from noise or measurement errors. Oscillations in the Voigt fit are only mathematically possible with some of the R_i's (the only unknowns in Voigt fit) are negative. Therefore, μ relates the amount of positive R_i elements to the amount of negative R_i's. If μ has a value of one, the amount of negative R_i's is small and no overfitting occurs.

Figure 3-4a shows an example of EIS data used in this study (5-minute rest after 5C discharge) and the corresponding Voigt circuit fit. The Nyquist plot (Figure 3-4a) as well as the gain and phase plots (Figure 3-4b) show close agreement between the EIS measurements and Voigt fit. To further evaluate the goodness of fit, the residuals (Figure 3-4c) and the MSE (Figure 3-4d) are considered. The residuals appear to resemble white noise, as shown in Figure 3-4c for 5 minutes of rest, suggesting that the Voigt fit is valid

for EIS at short rest times. The MSE stabilizes after 10 minutes indicating that short rest time EIS results are Kramer-Kronigs transformable. The MSE can be used to determine a threshold value below which EIS results are considered valid. This is discussed further in Section 3.5.2 with additional datasets.

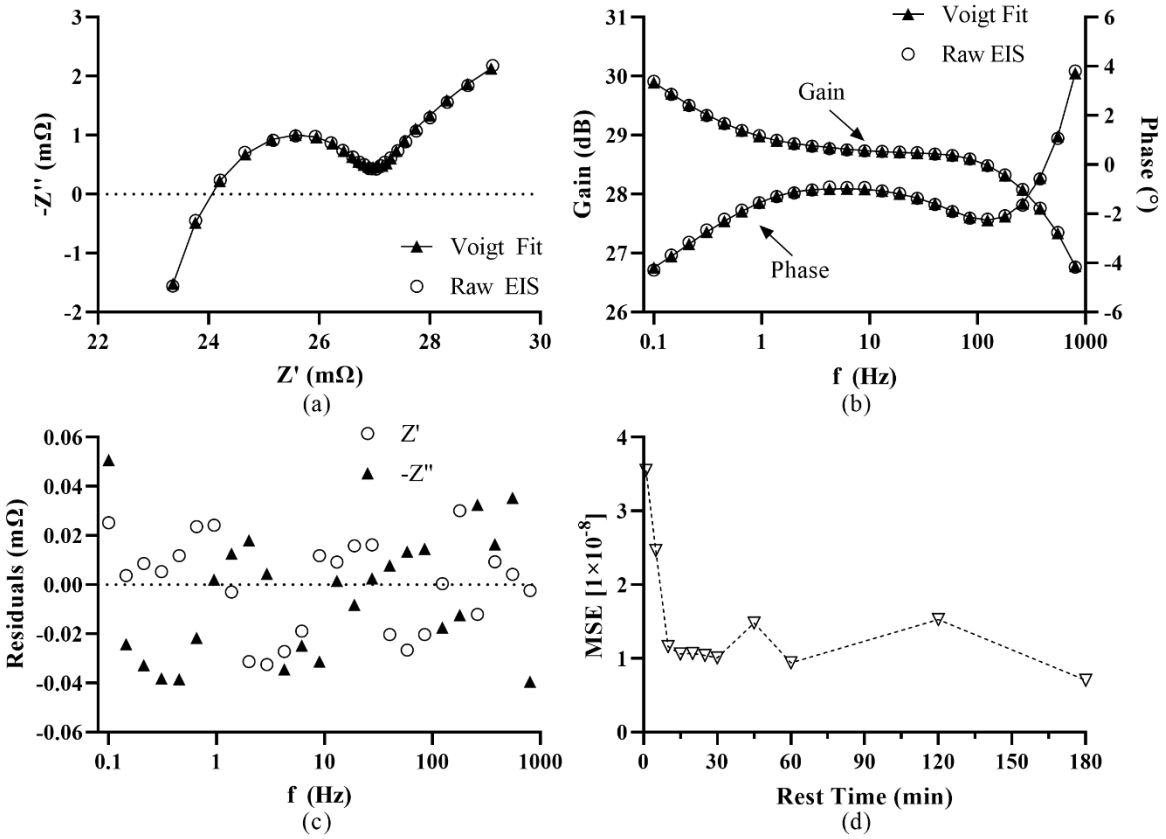

Figure 3-4: Real and imaginary EIS data with Voigt fit at 5-minute rest (a), EIS gain and phase with Voigt fit at 5-minute rest (b), Voigt fit residuals at 5-minute rest (c), Voigt fit MSE for various rest times and datasets (d) all after 5C discharge.

The validated EIS data still includes a small amount of noise. When analyzing a single dataset, this noise is small enough to not be of concern. However, when comparing consecutive EIS measurements, as is done in this study for different rest times, the noise of

different EIS datasets compounds. Figure 3-5 shows the difference of two (raw) EIS gain plots exhibiting compounded noise in the mid frequency range. The Voigt circuit can help to reduce this noise. Instead of using the EIS measurements directly, the output of the Voigt model can be used. To do this, the Voigt-circuit is first fit to the complex impedance (real and imaginary) pairs of the EIS data. Then the measurement frequency of each complex impedance pair is used as an input to the Voigt circuit model, creating a new, modeled set of real and imaginary pairs. The modeled complex impedance pairs are similar to the measured ones, as shown, for example, in Figure 3-5b in the gain plot. However, when considering again the difference of two consecutive datasets, a smoothing effect can be observed. Figure 3-5 also shows the difference of two modeled (filtered) EIS gain plots. The Voigt-model filtered plot is significantly smoother than the raw EIS plot in Figure 3-5. In Section 3.4 a method is introduced that uses the difference between consecutive EIS scans and relies on the smoothing effect of the Voigt filter.

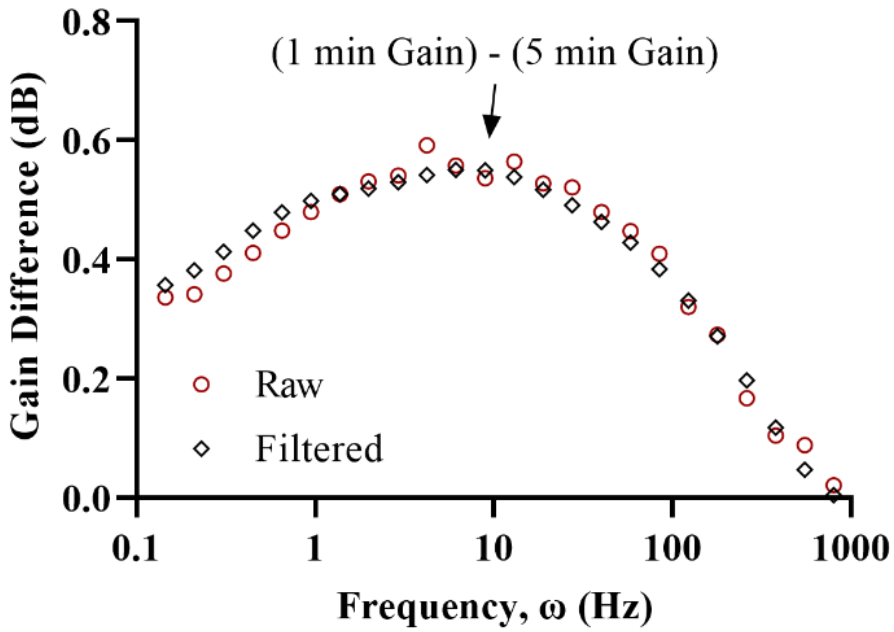

Figure 3-5: Voigt filter smoothing result.

The full procedure combining drift-compensation and Voigt-circuit filtering is shown in Figure 3-6. During the Voigt-circuit fitting procedure, μ, shown in (3-5), is used to prevent overfitting. If the MSE of the Voigt-circuit fit is found to be sufficiently low, the output of the Voigt-circuit fit is used to generate new EIS datapoints at the measurement frequencies. The combination of all steps shown in Figure 3-6 reduces the impact of the relaxation effect on EIS measurements. The residuals and MSE resulting from the Voigt circuit fit are used as criteria to determine if EIS results are valid. In the next section, experiments are described to test this proposed methodology.

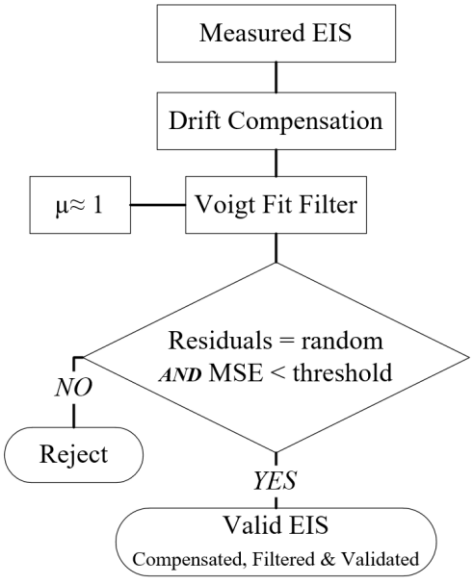

Figure 3-6: Short rest time EIS measurement methodology.

3.3 EIS CHARACTERIZATION AND EXPERIMENTS

This section describes characterization and experiments designed to further investigate the impact of the relaxation effect on EIS and to analyze the usefulness and limitations of using Voigt-circuit filtering together with drift compensation as introduced in the previous section. To induce relaxation behavior of different magnitudes, a protocol was developed consisting of discharge pulses between 1C and 5C with each having a discharge duration of 15s followed by a 3-hour rest. During the rest period, EIS was measured periodically. The protocol is shown in Figure 3-7 and consists of the following steps:

1. The battery is fully charged (CC-CV mode at 0.3C to 4.2V and 0.02C cutoff current).

2. The battery is discharged at 0.2C to a specific SoC target determined by coulomb counting and by subtracting the charge lost during the pulse such that the SoC target will be reached after the discharge pulse;

3. A 5C discharge pulse is applied for 15 seconds;

4. EIS is measured every 5 minutes until 30 minutes past the initial pulse discharge, then after every 15 minutes until 1 hour, and every hour until 3 hours is past;

5. Steps 1 to 4 are repeated for 4C, 3C, 2C, and 1C discharge pulses.

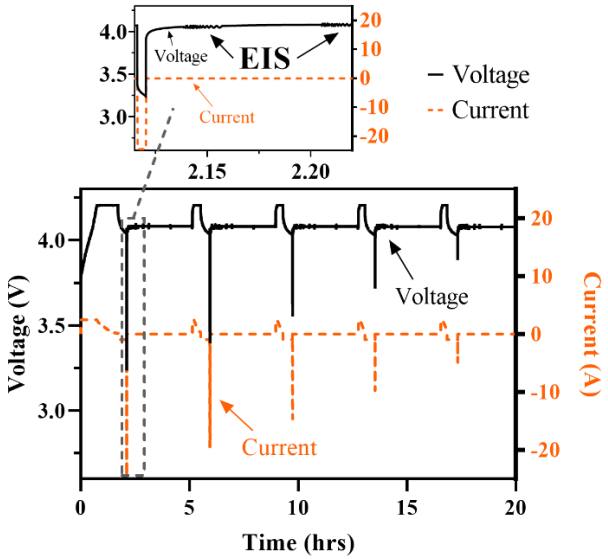

Figure 3-7: Experimental protocol showing where EIS measurements are taken with respect to discharge pulses of different C-rates.

The schematic of the experimental setup that was used for the experiments in this study is shown in Figure 3-8 for one channel. It consisted of the following devices:

- A BioLogic SP150 potentiostat for EIS measurement with a single multiplexed measurement channel.

- Agilent loads and power supplies (N3306A, N6733A respectively) with four channels each to supply and draw current.
- A National Instruments data acquisition (NI-DAQ) module with NI 9219 to measure cell voltage and NI 9201 to measure shunt voltage to obtain the cell current, with four measurement channels per module.
- A Testequity 1007C thermal chamber to control cell temperature.
- Custom software (written in Python) to control and automate testing with all the devices.

The batteries used in this study were fresh Samsung INR21700-50E, 4.9Ah, cylindrical lithium ion cells also shown in Figure 3-8. Prior to any tests, the new battery cells were conditioned with 10 charge/discharge cycles.

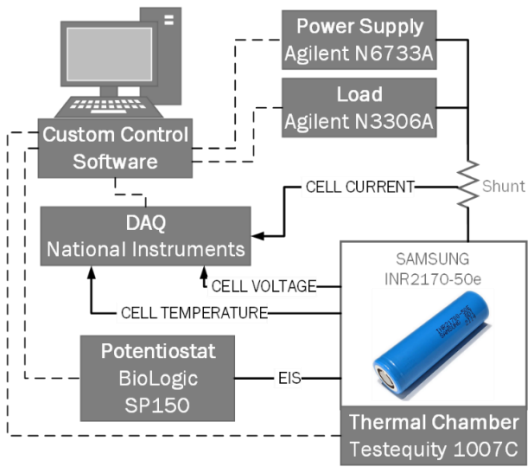

Figure 3-8: Schematic of experimental setup and battery cell.

EIS was performed between 800 Hz and 0.1 Hz, with a voltage amplitude of 10 mV, 6 points per decade, and two sine wave periods per frequency. The drift compensation option

of the potentiostat was applied in all cases to reduce the effect of drift as described in Section 3.2.

3.4 RELAXATION EFFECT ANALYSIS METHOD

Discharge pulses of different C-rates cause different relaxation behavior which causes differences in EIS results. If this difference is large, the C-rate must be considered for the interpretation of the EIS results. Otherwise, the results may be mis-interpreted. Visually evaluating the differences in Nyquist plots is not very useful, so a method is proposed in this section which allows for a quantitative comparison of the impact of different C-rates on EIS results. In this method, the percent difference between the magnitude of the impedance following the lowest (1C) and highest (5C) discharge pulses was calculated for various rest times as shown in (3-6).

$$\Delta Z(\omega) = 100 \times \frac{abs(|Z(\omega)|_{1C} - |Z(\omega)|_{5C})}{|Z(\omega)|_{5C}} \quad (3\text{-}6)$$

Here, $|Z(\omega)|_{1C}$ and $|Z(\omega)|_{5C}$ are the magnitudes of the impedance data for one frequency ω after 1C and 5C discharge pulses, respectively. Figure 3-9 shows $\Delta Z(\omega)$ for different frequencies and rest times. Between 10 and 0.1 Hz, $\Delta Z(\omega)$ shows a flat region for all rest times. To further simplify comparison of the rest time effect across different operating conditions and C-rates, $\Delta Z(5)$ is used as a representative value from this flat region. This value at 5Hz will be referred to as simply ΔZ in the remainder of this paper. As evident in Figure 3-9, ΔZ becomes smaller and smaller as the battery rests. This indicates that the differences in relaxation rates induced by 1C and 5C discharge pulses is only significant

for a short time after which the relaxation rates merge. This is discussed further and for various operating conditions in the next section.

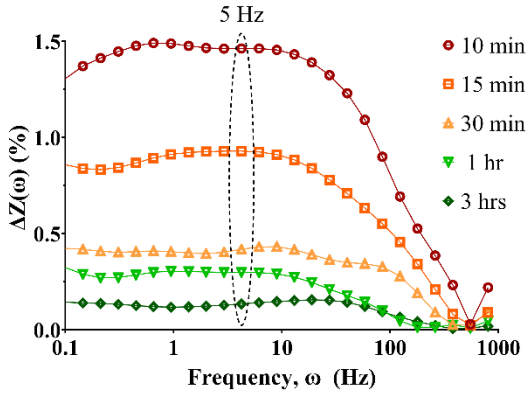

Figure 3-9: ΔZ(ω) for different frequencies and rest times.

3.5 Results & Discussion

In this section the relaxation effect is analyzed using the methods described in the previous sections with EIS data collected under different battery operating conditions. This section is organized as follows: 1. The impact of the discharge pulses at different C-rates on the EIS results is shown under constant operating conditions; 2. The effectiveness of the short-term measurement and filtering methodology is evaluated for different SoCs and temperatures using the MSE of the Voight fit; and 3. The combined impact of SoC, temperature and C-rate of the discharge pulses on the relaxation behavior is presented.

3.5.1 Relaxation Effect and C-Rate

Figure 3-10 shows how Nyquist plots change over time after pulses of different C-rates (between 1C and 5C). The plots for each of the different C-rates are clearly separated after 10 minutes of rest time due to the different relaxation behaviors caused by the various

discharge depths. After 30 minutes of rest, however, all five datasets merge together to become nearly indistinguishable. After 3 hours (180 minutes), the datasets overlap completely, but have shifted further due to the continuing relaxation effect, however, in a manner independent of the foregoing discharge pulse depth. Figure 3-10 also shows that the lower the C-rate, i.e. the lower the initial disturbance, the smaller the difference between the disturbed and the rested EIS results.

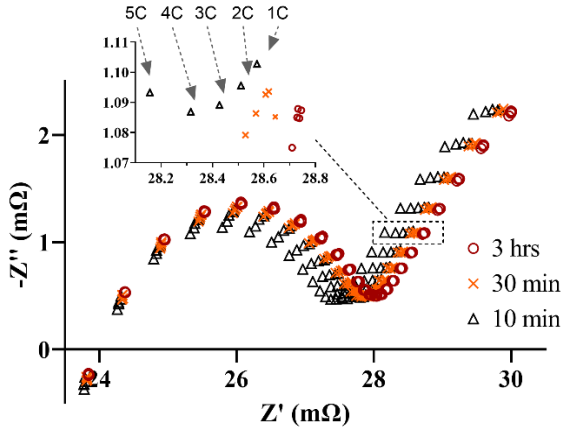

Figure 3-10: Evolution of Nyquist plots measured at different rest times after different C-rates.

As was shown in Figure 3-9 (Section 3.4) for measurements at 90% SoC, and 25°C, $\Delta Z(\omega)$, which evaluates the difference in EIS results after 1C and 5C discharge pulses, is large initially for rest times of 10 minutes and 15 minutes. After 30 minutes of rest time, $\Delta Z(\omega)$ is similar to its values after 3 hours. These results suggest that rest times may be shortened significantly, from the 3 hours conventionally observed to 30 minutes, since the effect of C-rate becomes small. With this rest time of 30 minutes, EIS results can be interpreted without considering (or measuring) the C-rate which induced the relaxation effect. If C-rate is measured it can be used to inform EIS interpretation, or EIS measurements can be

limited to follow low C-rates (1C or less) only. In either case, rest times may be shortened to less than 30 minutes if validity of the EIS measurement can be ensured. This is discussed in the next section.

3.5.2 Relaxation Effect and Voigt-Fit MSE

The previous section showed that the differences in Nyquist plots after 1C and 5C discharge pulses becomes small after 30 minutes of rest. In this section, the MSE of the Voigt-fit (see Section 3.2) is used to further investigate the short-term relaxation effect for different operating conditions. Figure 3-11a shows the Voigt-fit MSE for different rest times and different SoCs all measured at 25 °C. For rest times below 25 minutes, the spread of MSE is relatively large. After 25 minutes, although there are some outliers, the MSE stays within smaller clusters. Figure 3-11b shows the Voigt-fit MSE for different C-rates and different temperatures, all measured at 90% SoC. Here, the clusters are similar to Figure 3-11a, however, the MSE at 10°C is consistently higher and shows a large variance. This suggests that the Voigt-fit is of low quality, and EIS results may not be valid even after 3 hours of rest at low temperature. This is due to low temperatures causing the battery to relax at a much slower rate, which was also shown by Kindermann et al. [28]. The implication for the short-term relaxation affect is that much longer rest times are required to obtain valid EIS results at lower temperatures. For all other conditions observed, the MSE appears to stabilize quickly. To better understand this, the MSEs for the valid conditions were combined and the mean and standard deviation (SD) for each rest time was obtained, as shown in Figure 3-11c. After 1-minute rest, the mean is high, and a large SD can be seen.

Between 5 to 20 minutes of rest, the means are similar and the SD error bars overlap, but the means are much lower than after 1 minute of rest. Finally, between 25 minutes and 3 hours of rest, the means are even lower and in a similar range with overlapping error bars. Therefore, for best results, a 25 min rest should be observed. However, rest times as low as 5 minutes will produce EIS results with only slightly elevated Voigt-fit MSEs, which may still be valid. Rest times of less than 5 minutes will not produce valid EIS results.

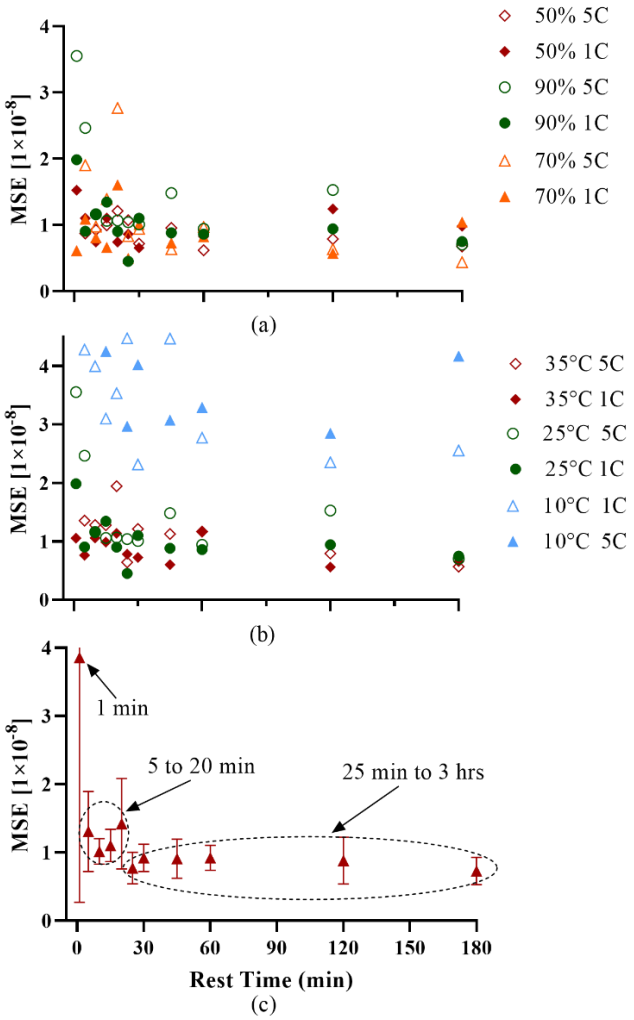

Figure 3-11: Voigt-fit MSE for different C-rates and SoCs (a), MSE for different C-rates and temperatures (b), mean and SD of combined conditions (c).

3.5.3 Relaxation Effect and ΔZ

The previous section showed how the Voigt-fit MSE changes with different SoCs, temperatures and C-rates. To better visualize the effects of different C-rates in combination with SoC and temperature, ΔZ (Section 3.4) is plotted over rest time in Figure 3-12a and Figure 3-12b, respectively, with 90% SoC, 25°C at 30 minutes of rest used as a reference. The Nyquist plots for each condition are also shown for each case. In Figure 3-12a, the impact of rest time and SoC on ΔZ is shown. ΔZ increases as the SoC decreases, which means longer rest times are required for lower SoCs to sufficiently reduce the effect of C-rate on the EIS results. At 70% SoC ΔZ reaches a value below the reference after 60 minutes of rest. At 50% SoC ΔZ is still above the threshold even after 3 hours of rest. This can also be seen in the Nyquist plots from EIS measurements with 30-minute rest times after 1C and 5C discharge as shown in Figure 3-12b. At 90% SoC, the Nyquist plots for the two C-rates overlap, however, at 50% SoC, a significant gap exists between the two plots. This suggests, only high SoCs should be used when measuring EIS with short rest times after large discharge rates precede the measurement.

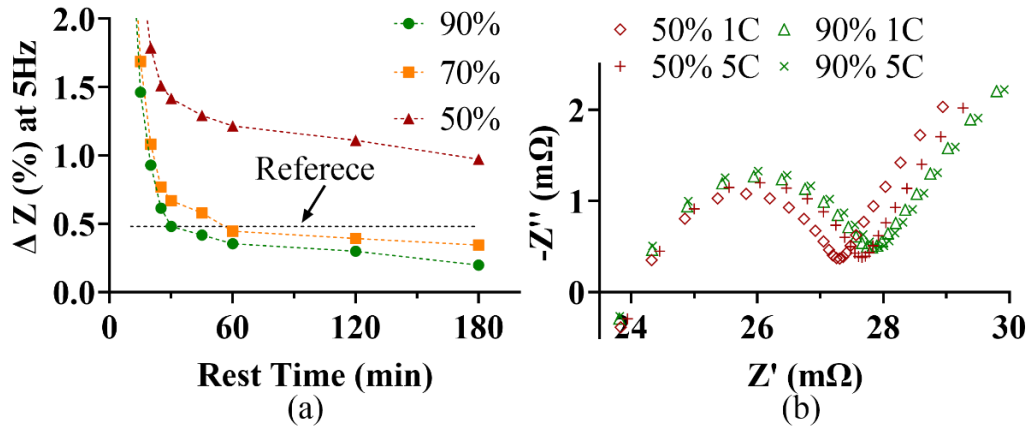

Figure 3-12: ΔZ for 90%, 70% and 50% SoC compared to reference at 25°C and 90% SoC (a). Nyquist plots for 90% and 50% SoC after 30 minutes of rest (b).

Figure 3-13a shows ΔZ for different temperatures. Increasing the temperature from 25°C to 35°C has no significant impact on the relaxation behavior. However, decreasing the temperature to 10°C increases the time it takes to reduce ΔZ, suggesting that, again, lower temperatures are not suitable for EIS measurements with short rest times. At 10°C, ΔZ reaches below the reference after approximately 2.5 hours of rest, however, as was shown in the previous section, EIS results at 10°C may still not be valid even after 3 hours of rest. At higher temperatures, ΔZ starts out much lower than at 25°C at 5 minutes rest and then rapidly decreases to match the values at 25°C for longer rest times. The Nyquist plots corresponding to the different temperatures are shown in Figure 3-13b, showing overlapping plots for higher temperatures, but a small gap for the 10°C case. The results discussed above show that the 30-minutes rest time is sufficient for room temperature and above, as long as the SoC remains high. Lower SoCs and lower temperatures still show a large difference in EIS results even after 3 hours of rest, so care must be taken when

interpreting EIS under such conditions. The findings on rest times for different operating conditions for relaxation induced by a 5C discharge pulse are summarized in Table 3-1.

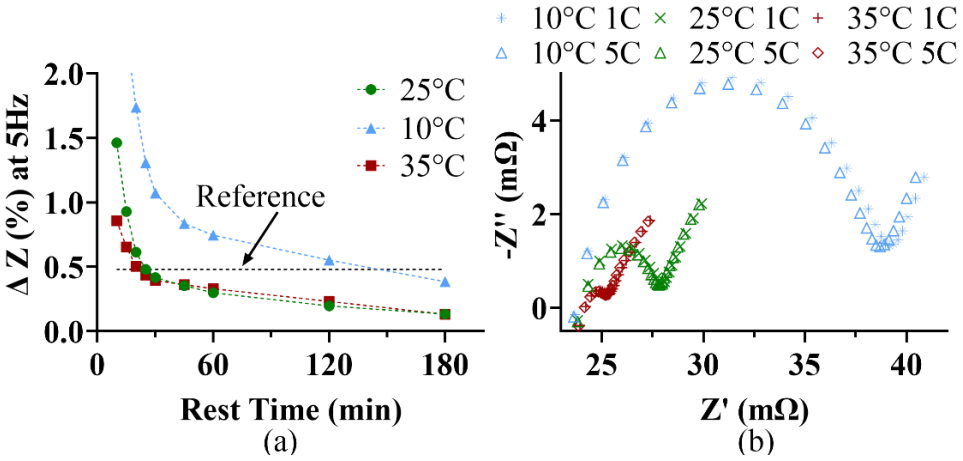

Figure 3-13: ΔZ at 25°C, 35°C and 10°C compared to reference at 25°C and 90% SoC (a). Nyquist plots for the same temperatures (b).

Table 3-1: Summary of Minimum Rest Time for Different Conditions

Temperature ($°C$)	SoC (%)	C-rate	Rest Time (min)
	90	5	30
≥ 25	70	5	60
	50	5	> 180
10	90	5	> 180

The results shown in this study are applicable to batteries with NMC cathodes. The relationship between the relaxation effect and battery chemistry is not well researched in literature. However, the long term (48 hours) relaxation rate of NMC was compared to Lithium Manganese (LiMn) and Lithium-Iron-Phosphate (LFP) chemistries by Kindermann et al. [28] showing that NMC and LiMn relaxation rates are within 2% of each other. This suggests that the NMC results shown in this work may be applicable to other

chemistries as well. LFP showed a faster relaxation rate compared to NMC and LFP which suggests rest times are less important for LFP.

The focus of this paper is on the relaxation effect of single cells; however, similar relaxation behavior can likely be observed for battery modules with cells in parallel, and therefore equal voltages. Several new methods for BMS-compatible EIS allow for cell voltage measurement as described in Section 3.1.1 [20], [21]. Combined with such methods, the findings in this paper are intended to provide BMS engineers with suitable operating points at which to perform the EIS measurements under different conditions. Furthermore, BMS generated EIS may require filtering and validation for which the Voigt filter approach introduced here is suitable.

3.6 CONCLUSION

EIS measurements obtained after C-rate pulses and short rest times must be compensated and filtered due to drift caused by the rapid change of the battery voltage. In this study, EIS was measured for batteries of different SoC and at different temperatures, with short rest times after different discharge pulses by utilizing drift compensation methods and validating EIS results using the Kramer-Kronigs. Furthermore, a method was proposed to use the Voigt-circuit as a filter to further improve EIS measurements at short rest times. It was found that using this method valid EIS results could be obtained for EIS measurements as low as 5 minutes as long as temperatures remain at room temperature or above. Furthermore, it was found that the effect of different C-rate pulses disappears after 30 minutes of rest for batteries at 90% SoC and above 25°C. However, batteries at SoCs below

90% as well as batteries at temperatures of 10°C require longer rest times to eliminate the effect of large C-rates.

ACKNOWLEDGEMENT

We thank Cadex Electronics for their facilities, support and expertise.

REFERENCES

[1] M. A. Hannan, M. S. H. Lipu, A. Hussain, and A. Mohamed, "A review of lithium-ion battery state of charge estimation and management system in electric vehicle applications: Challenges and recommendations," Renewable and Sustainable Energy Reviews, vol. 78. pp. 834–854, 2017.

[2] R. Xiong, J. Cao, Q. Yu, H. He, and F. Sun, "Critical Review on the Battery State of Charge Estimation Methods for Electric Vehicles," IEEE Access, vol. 6, pp. 1832–1843, 2018.

[3] M. U. Cuma and T. Koroglu, "A comprehensive review on estimation strategies used in hybrid and battery electric vehicles," Renew. Sustain. Energy Rev., vol. 42, pp. 517–531, 2015.

[4] L. Ungurean, G. Cârstoiu, M. V Micea, and V. Groza, "Battery state of health estimation : a structured review of models , methods and commercial devices," no. July 2016, pp. 151–181, 2017.

[5] R. Ahmed, M. El Sayed, I. Arasaratnam, J. Tjong, and S. Habibi, "Reduced-Order Electrochemical Model Parameters Identification and State of Charge Estimation for Healthy and Aged Li-Ion Batteries—Part II: Aged Battery Model and State of Charge Estimation," IEEE J. Emerg. Sel. Top. Power Electron., vol. 2, no. 3, pp. 678–690, 2014.

[6] X. Lai et al., "Co-estimation of state of charge and state of power for lithium-ion batteries based on fractional variable-order model," J. Clean. Prod., vol. 255, no. 11, pp. 10319–10329, 2020.

[7] S. Habibi, "The Smooth Variable Structure Structure Filter," Proc. IEEE, vol. 95, no. 5, 2007.

[8] R. Ahmed et al., "Model-Based Parameter Identification of Healthy and Aged Li-ion Batteries for Electric Vehicle Applications," SAE Int. J. Altern. Powertrains, vol. 4, no. 2, pp. 233–247, 2015.

[9] S. A. Gadsden, M. Al-Shabi, and S. R. Habibi, "Estimation Strategies for the Condition Monitoring of a Battery System in a Hybrid Electric Vehicle," ISRN Signal Process., vol. 2011, no. 1, 2011.

[10] S. A. Gadsden, M. Al-Shabi, I. Arasaratnam, and S. R. Habibi, "Combined cubature Kalman and smooth variable structure filtering: A robust nonlinear estimation strategy," Signal Processing, vol. 96, no. PART B, pp. 290–299, 2014.

[11] S. A. Gadsden, S. R. Habibi, and T. Kirubarajan, "A novel interacting multiple model method for nonlinear target tracking," 13th Conf. Inf. Fusion, Fusion 2010, 2010.

[12] S. A. Gadsden, M. El Sayed, and S. R. Habibi, "Derivation of an optimal boundary layer width for the smooth variable structure filter," Proc. Am. Control Conf., pp.

4922–4927, 2011.
[13] M. Ismail, R. Dlyma, A. Elrakaybi, R. Ahmed, and S. Habibi, “Battery state of charge estimation using an Artificial Neural Network,” 2017 IEEE Transp. Electrif. Conf. Expo, ITEC 2017, pp. 342–349, 2017.
[14] C. Vidal, P. Malysz, P. Kollmeyer, and A. Emadi, “Machine Learning Applied to Electrified Vehicle Battery State of Charge and State of Health Estimation: State-of-the-Art,” IEEE Access, vol. 8, pp. 52796–52814, 2020.
[15] Y. Li et al., “A quick on-line state of health estimation method for Li-ion battery with incremental capacity curves processed by Gaussian filter,” J. Power Sources, vol. 373, no. November 2017, pp. 40–53, 2018.
[16] M. Berecibar, I. Gandiaga, I. Villarreal, N. Omar, J. Van Mierlo, and P. Van Den Bossche, “Critical review of state of health estimation methods of Li-ion batteries for real applications,” Renew. Sustain. Energy Rev., vol. 56, pp. 572–587, 2016.
[17] A. Lasia, Electrochemical Impedance Spectroscopy EIS, and Corrosion. New York: Springer, 2014.
[18] J. Meng et al., “An Overview and Comparison of Online Implementable SOC Estimation Methods for Lithium-Ion Battery,” IEEE Trans. Ind. Appl., vol. 54, no. 2, pp. 1583–1591, 2018.
[19] N. Meddings et al., “Application of electrochemical impedance spectroscopy to commercial Li-ion cells: A review,” Journal of Power Sources, vol. 480. Elsevier B.V., 31-Dec-2020.
[20] E. Din, C. Schaef, K. Moffat, and J. T. Stauth, “A scalable active battery management system with embedded real-time electrochemical impedance spectroscopy,” IEEE Trans. Power Electron., vol. 32, no. 7, pp. 5688–5698, 2017.
[21] X. Wei, X. Wang, and H. Dai, “Practical on-board measurement of lithium ion battery impedance based on distributed voltage and current sampling,” Energies, vol. 11, no. 1, 2018.
[22] N. Lohmann, P. Haussmann, P. Wesskamp, J. Melbert, and T. Musch, “Employing Real Automotive Driving Data for Electrochemical Impedance Spectroscopy on Lithium-Ion Cells,” SAE Int. J. Altern. Powertrains, vol. 4, no. 2, pp. 308–317, 2015.
[23] P. Kollmeyer, A. Hackl, and A. Emadi, “Li-ion battery model performance for automotive drive cycles with current pulse and EIS parameterization,” 2017 IEEE Transp. Electrif. Conf. Expo, ITEC 2017, pp. 486–492, 2017.
[24] C. Pastor-Fernández, K. Uddin, G. H. Chouchelamane, W. D. Widanage, and J. Marco, “A Comparison between Electrochemical Impedance Spectroscopy and Incremental Capacity-Differential Voltage as Li-ion Diagnostic Techniques to Identify and Quantify the Effects of Degradation Modes within Battery Management Systems,” J. Power Sources, vol. 360, pp. 301–318, 2017.
[25] U. Westerhoff, T. Kroker, K. Kurbach, and M. Kurrat, “Electrochemical impedance spectroscopy based estimation of the state of charge of lithium-ion batteries,” J. Energy Storage, vol. 8, pp. 244–256, 2016.
[26] U. Krewer, F. Röder, E. Harinath, R. D. Braatz, B. Bedürftig, and R. Findeisen, “Review—Dynamic Models of Li-Ion Batteries for Diagnosis and Operation: A Review and Perspective,” J. Electrochem. Soc., vol. 165, no. 16, pp. A3656–A3673, 2018.
[27] L. Deverakonda and T. Hu, “Effects of rest time on discharge response and equivalent circuit model for a lead-acid battery,” J. Power Sources, vol. 282, pp. 19–27, 2015.
[28] F. M. Kindermann, A. Noel, S. V. Erhard, and A. Jossen, “Long-term equalization effects in Li-ion batteries due to local state of charge inhomogeneities and their

impact on impedance measurements," Electrochim. Acta, vol. 185, pp. 107–116, 2015.
[29] A. Barai, G. Chouchelamane, Y. Guo, A. McGordon, and P. Jennings, "A study on the impact of lithium-ion cell relaxation on electrochemical impedance spectroscopy," J. Power Sources, vol. 280, no. Special Issue, pp. 74–80, 2015.
[30] W. Waag, S. Käbitz, and D. U. Sauer, "Experimental investigation of the lithium-ion battery impedance characteristic at various conditions and aging states and its influence on the application," Appl. Energy, vol. 102, pp. 885–897, 2013.
[31] H. Wang, M. Tahan, and T. Hu, "Effects of rest time on equivalent circuit model for a li-ion battery," Proc. Am. Control Conf., vol. 2016-July, pp. 3101–3106, 2016.
[32] V. Zinth et al., "Inhomogeneity and relaxation phenomena in the graphite anode of a lithium-ion battery probed by in situ neutron diffraction," J. Power Sources, vol. 361, pp. 54–60, Sep. 2017.
[33] M. Messing, T. Shoa, and S. Habibi, "Lithium-Ion Battery Relaxation Effects," in ITEC 2019, 2019.
[34] Zahner Messsysteme, "EIS - Electrochemical Impedance Sepctroscopy," 2019.
[35] B. A. Boukamp, "A Linear Kronig-Kramers Transform Test for Immittance Data Validation," J. Electrochem. Soc., vol. 142, no. 6, pp. 1885–1901, 1995.
[36] M. Schönleber, D. Klotz, and E. Ivers-Tiffée, "A Method for Improving the Robustness of linear Kramers-Kronig Validity Tests," Electrochim. Acta, vol. 131, pp. 20–27, 2014.

Chapter 4: Estimating Battery State of Health using Electrochemical Impedance Spectroscopy and the Relaxation Effect

Marvin Messing[1,2], Tina Shoa[2], Saeid Habibi[1]

[1]Department of Mechanical Engineering, McMaster University, Hamilton, ON, Canada,

[2]Cadex Electronics, Richmond, BC, Canada

This paper is published in Journal of Energy Storage, vol. 43, Article 103210, 2021, doi: 10.1016/j.est.2021.103210.

ABSTRACT

Among the most important tasks of a Battery Management System (BMS) are State of Charge (SoC) and State of Health (SoH) estimation. Many SoH estimation techniques are available, each with their advantages and drawbacks. These include methods based on a technique known as Electrochemical Impedance Spectroscopy (EIS). This technique provides detailed information about the battery's state of health but requires long rest times to prevent the battery relaxation effect from impacting the EIS measurement. In this paper EIS is shown to be able to track the short-term relaxation effect for batteries of different SoH. A SoH estimation method is proposed which combines fractional order impedance modeling and short-term relaxation effects with EIS characterization for rapid SoH determination. This empirical method is demonstrated to have an average SoH estimation error of less than 1%. As new methods arise to simplify EIS hardware requirements for real time applications, the proposed method offers a new way of utilizing EIS for SoH estimation.

4.1 INTRODUCTION

In this paper an empirical model is proposed for battery State of Health (SoH) estimation. The model is developed based on the battery relaxation effect and Electrochemical Impedance Spectroscopy (EIS) measurements fitted with a fractional order impedance model. The rate of change of a combined model resistance is shown to be a repeatable quantity and is utilized here for SoH estimation. This section summarizes the motivation and technical challenges, provides a review of recent and relevant literature, presents the main paper contributions, and provides an outline of the rest of the paper.

4.1.1 MOTIVATION AND TECHNICAL CHALLENGES

Lithium-ion Batteries (LiB) are used in many applications including Electric Vehicles (EV). Any multi-cell LiB pack requires a Battery Management System (BMS) to optimize the performance of the battery pack and to ensure each cell remains within safe operating limits [1]. To do these tasks, the BMS must estimate the State of Charge (SoC) and SoH of the cells, since these states cannot be measured. The SoC indicates the charge left in the battery before it must be charged. The SoH indicates the capacity of the cell, i.e. how much energy the cell can provide after it is fully charged, compared to when it was new. The accuracy of SoC algorithms depends on the SoH of the battery and many different methods have been investigated to improve the accuracy of SoH [2–7]. A group of SoH estimation methods are based on diffusion processes taking place inside the battery electrodes during rest time, known as the relaxation effect. As a result of the relaxation effect, the battery voltage changes over time and the rate of change of the voltage can be related to the SoH of the battery. Another method commonly used in laboratory settings to

investigate SoH is EIS, a non-destructive and time efficient technique that provides detailed insight into the condition of a battery cell. This is achieved by applying small sinusoidal signals to the battery over a wide frequency range and measuring the battery response. The resulting response signal is then analyzed in the frequency domain by considering magnitude, phase as well as real and imaginary components of the response at each frequency. Although a BMS would greatly benefit from this technique, the required hardware is complex and costly [8]. Nonetheless, there is increasing research effort to develop solutions to make EIS available for BMS applications [9–12] for use in EV applications. For example, Carkhuff et al. [10] designed multiplexer hardware to deliver an EIS signal to each cell in a battery pack. More recently, Locorotondo et al. [13] designed a wireless charging circuit with built-in EIS measurement capability. In this paper, EIS is used to track the relaxation effect to develop an empirical SoH estimation model. In the next section, literature relevant to SoH estimation and the relaxation effect is reviewed.

4.1.2 Relaxation Effect and SoH Estimation

When batteries are allowed to rest, slow diffusion processes take place which slowly change the voltage and impedance of the battery [14]. This relaxation effect was used for SoH estimation by several studies. Qian et al. [15] proposed an SoH estimation strategy based on voltage relaxation for 10 minutes of rest after full charge and full discharge. They used a second order ideal Equivalent Circuit Model (ECM) which was fit to the voltage curve and the model parameters were related to SoH. Fang et al. [16] proposed a similar model using a third order ECM and 2 hours of rest. Baghdadi et al. [17] correlated the

voltage after 30 minutes of rest after full charge to SoH. They used a linear model to estimate the SoH with model parameters adjusted for different operating conditions. Ran et al. [18] proposed a data driven model to cluster batteries by SoH using a pulse profile which included relaxation phases. They find a clustering accuracy of 88%. EIS was used to characterize the relaxation effect in several studies [14], [19–23]. Several studies also use EIS for SoH estimation directly. Shabbir et al. [24] built a SoH prediction model based on multiple features of the Nyquist plot with an estimation error of around 10%. Guha et al. [25] reconstructed EIS from constant discharge pulses and modeled the change of the internal resistance from the EIS results with a third order polynomial. Kim et al. [26] measured EIS with a constant current bias and used linear regression to model the change in SoH with EIS impedance at 250 Hz. Gismero et al. [27] used EIS to track the calendar age of batteries and used third order ECM parameters to model SoH with a 2.5% error. Locorotondo et al. [28] used a Pseudo-Random Binary Sequence (PRBS) signal (instead of multi-sine) to generate EIS results. They a limited number of cells between 100% and 50% SoH and proposed an impedance clustering method for SoH detection. They state a required rest time of 1 hour before measurements can be obtained.

The studies discussed above either use the relaxation effect in time domain or EIS measurements to estimate SoH. Each study imposes requirements such as long measurement times (hours), and having the battery to be fully charged or discharged, or applying a fixed bias or discharge current during measurement. In addition, the SoH estimation errors seem to be greater than 2% in most cases. In this study, the combination

of the relationship between the battery relaxation effect and its SoH, complemented by EIS measurements are used to develop a new SoH estimation strategy.

4.1.3 CONTRIBUTIONS

This paper presents the following original contributions and conclusions: (1) An empirical SoH estimation method is proposed by combining EIS measurements, fractional order battery modeling, and the short-term relaxation effect; (2) The proposed SoH estimation method is experimentally applied in an aging study and is shown to have an average estimation error of less than 1% SoH.

4.1.4 PAPER OUTLINE

The paper is organized as follows. Section 4.2 describes the experiments conducted to characterize the relaxation effect with EIS and to obtain aged batteries. Section 4.3 introduces the battery relaxation effect and presents a conceptual view of the underlying physical phenomenon and its impact on battery impedance. Section 4.4 introduces the fractional order battery model and describes the modeling approach. Section 4.5 introduces the SoH estimation method followed by a discussion of its performance in Section 4.6. The concluding remarks are provided in Section 4.7.

4.2 EIS CHARACTERIZATION AND AGING EXPERIMENTS

The work presented in this paper includes extensive experiments conducted on Samsung INR2170-50E lithium nickel manganese cobalt (LiNiMnCoO2 or NMC) batteries of different SoH. The experiments were conducted to provide development and validation datasets for the proposed SoH estimation method. The experiments consisted of discharge

pulses of different currents used to induce relaxation behavior with different relaxation rates. Each pulse was followed by a 3 hours rest period, during which EIS was measured at regular intervals starting after 1 minute of rest. Discharge currents between 1C and 5C were tested, with each pulse held for 15 seconds. EIS was measured with a Bio-logic SP150 potentiostat for the frequency range of 0.1 to 800 Hz, with a 10 mV amplitude with two sine waves per period, 6 points per decade, and with the drift compensation setting enabled [29]. The EIS measurement duration with these settings is 64 seconds for each full scan. This time interval is considered as part of any rest time intervals. In this study, all results were obtained at 90% SoC. This SoC target was obtained by first fully charging the battery according to the manufacturer's recommendation. Next, batteries were discharged at 0.2C and the charge counted using coulomb-counting and by subtracting the charge lost during the pulse. This way, the battery SoC is equal to 90% at the beginning of the rest period. The temperature was held at 25°C using a Testequity 1007C thermal chamber. A schematic of the test setup is shown in Figure 4-1.

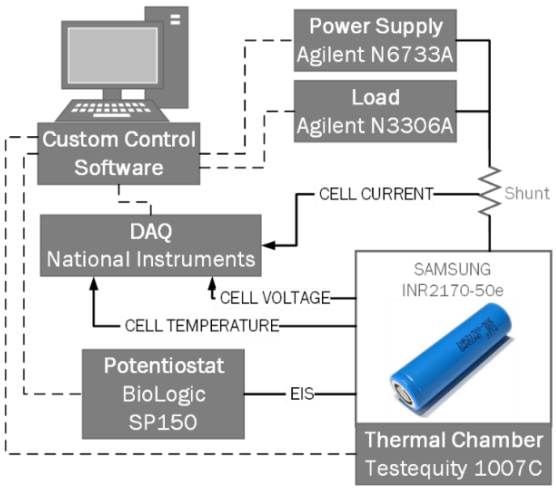

Figure 4-1: Schematic of experimental setup and battery cell.

Table 4-1: SoH and Test Conditions for 14 Battery Cells at 90% SoC and 25°C.

SoH (%)	C-rates	Repeats
99.96	1,2,3,4,5	3
98.26	5	1
97.61	5	1
96.00	1,2,3,4,5	1
92.00	5	1
91.27	5	3
90.69	1,2,3,4,5	1
86.54	5	1
86.22	5	1
85.05	1,2,3,4,5	1
83.44	5	1
83.03	5	3
81.69	1,2,3,4,5	1
78.41	5	1

The protocol discussed above was applied to 14 battery cells of different SoH as shown in Table 4-1. As indicated in the "C-rates" column, selected cells between 100% and 80% SoH were subjected to discharge pulses of 5 different C-rates to test the impact of varying relaxation severity on EIS measurements and to investigate how this changes with various battery SoH. All cells were tested with 5C discharge pulses to form the dataset for the development and testing of the proposed SoH estimation method. Some cells at different SoHs were tested three times at the same condition to ensure the repeatability of the results. Three repeats of the 5C, 15 seconds discharge pulse are shown in Figure 4-2.

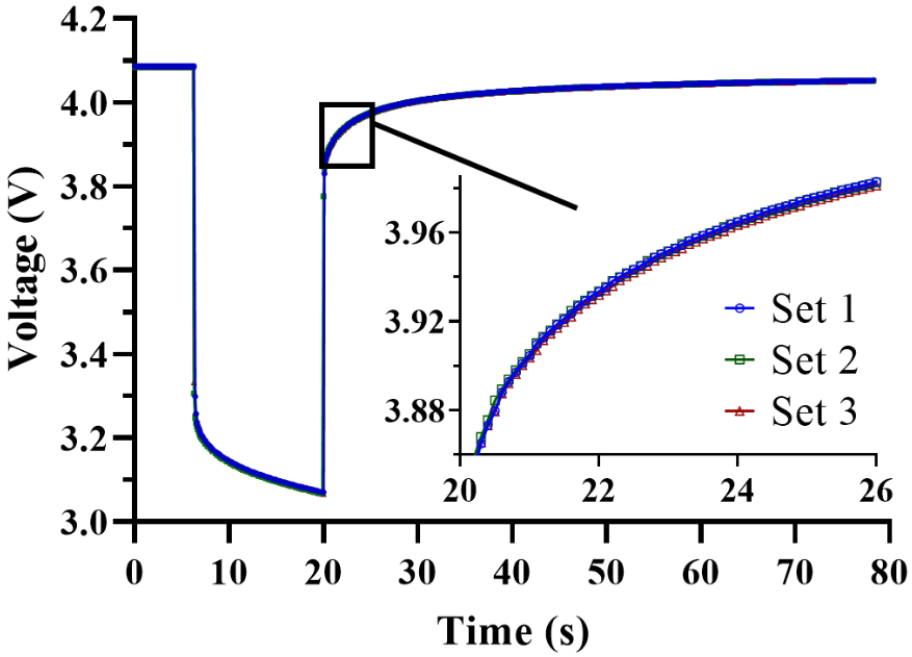

Figure 4-2: Three repeats of a 5C, 15s discharge pulse at 90% SoC, 100% SoH.

The cells were aged with simple charge/discharge cycle aging at a constant temperature of 25°C. The cells were charged at C/2 with the standard constant-current, constant-voltage (CC-CV) method to 4.2V with a target current of C/20. The cells were discharged at 1C to 2.5V as recommended by the manufacturer.

The SoH of the batteries was determined at 25°C by first fully charging the battery (at C/2 with the CC-CV method to 4.2V and C/20 cut-off current), followed by a 1 hour rest, followed by a discharge at C/5 to 2.5V. This procedure yields a measured capacity C_m value via coulomb counting. The capacity value of 4.9 mAh is stated as the rated capacity C_r of the battery according to the manufacturer datasheet and the SoH is calculated using Equation 4-1.

$$SoH\ (\%) = \frac{C_m}{C_r} \times 100 \tag{4-1}$$

4.3 Relaxation Effect and Impedance

In this section, the battery relaxation effect and its possible origin are discussed based on EIS measurements and conceptual explanation of physical processes inside the battery. The relaxation effect can most easily be observed by monitoring the Open Circuit Voltage (OCV) of the battery after applying a charge or discharge pulse. The OCV slowly increases over several hours before reaching a stable value. This happens because of ion concentration gradients inside the electrodes causing charge imbalances which are resolved by slow diffusion processes in the absence of an external driving force. Kindermann et al. [29] presented a mind-model showing the different kinds of diffusion processes, which are still on-going even after the voltage has stabilized. They show that the relaxation effect not only impacts voltage, but battery impedance as well. Using EIS measurements, they detected impedance changes for as long as 40 hours of rest time.

In this paper, the short term relaxation effect for new and aged battery cells is considered. Figure 4-3 shows the Nyquist plots for EIS measurements obtained from batteries at 100%, 90% and 80% SoH. At each SoH, the Nyquist plots from EIS measurements obtained at rest times of 5, 10 and 15 minutes after a discharge pulse are also shown. Each set of three EIS measurements track the relaxation effect in a distinctive way, with decreasing distance between the mid to low frequency range of the Nyquist plots for the same total time interval of 15 minutes. The rate at which the distance between Nyquist plots changes decreases with SoH. This behavior forms the basis for the SoH estimation method proposed in this paper.

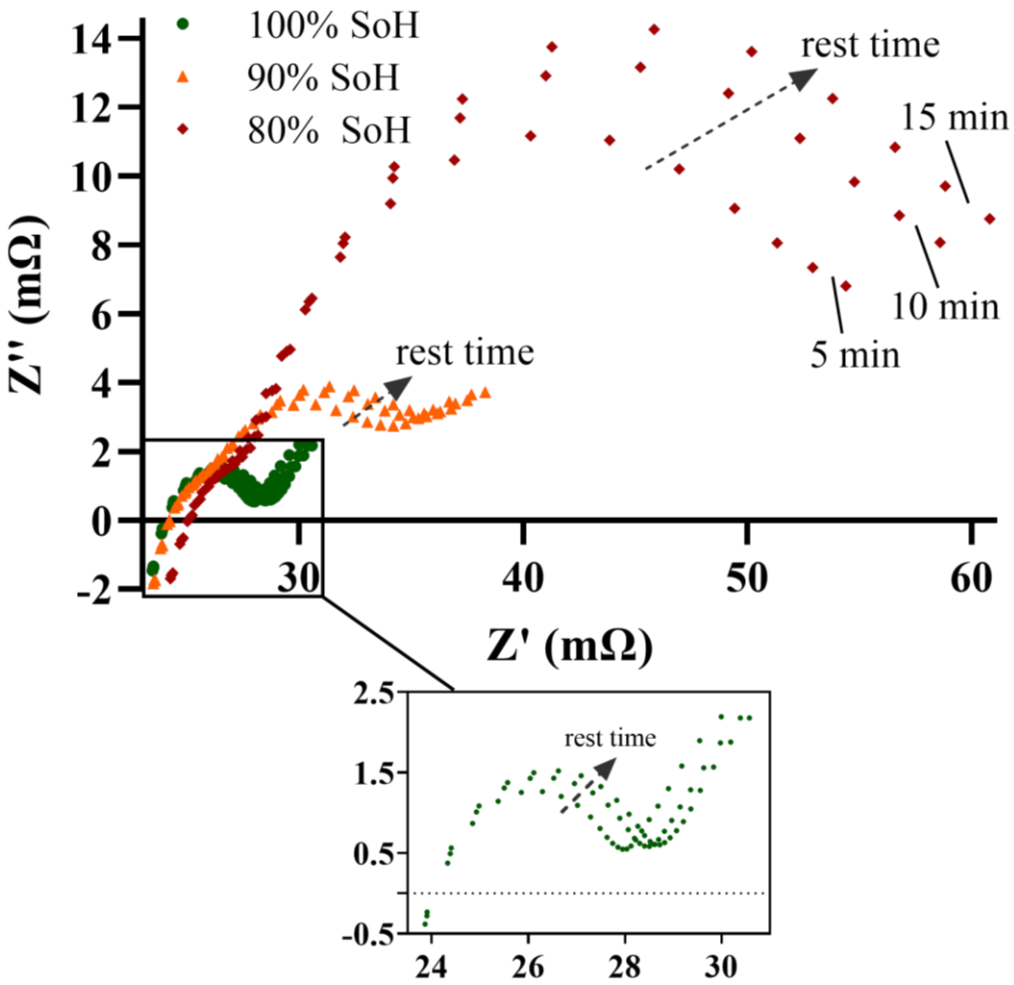

Figure 4-3: Evolution of Nyquist plot with rest time and SoH.

The change of impedance with rest time can be explained by the change in charge concentration inside the electrodes over time. Figure 4-4 shows the Nyquist plots of the EIS results as they change with rest time and battery age. The same plot is shown three times with a specific dataset highlighted corresponding to the rest time, one for new and one for aged batteries in each case. Also shown in Figure 4-4 are diagrams showing conceptual views of the charge concentration inside the anode (similar behaviour also occurs on the cathode). During relaxation after a discharge pulse the ions diffuse through

the Solid Electrolyte Interface (SEI) into the electrode. However, at first, most of the charge is located close to the surface of the electrode [30]. As the rest time increases, ions move further into the electrode, decreasing the readily available surface charge, and increasing charge transfer impedance, Z_{CT}, as a result. In the case of aged cells, Z_{CT} starts out larger due to an increased SEI and reduced electrode material. The rate of change of Z_{CT} during relaxation is slowed also due to the increased SEI impedance and because it takes longer for ions to arrive at active electrode material. This behaviour for new and aged battery cells is conceptually shown in the diagrams of Figure 4-4 as it relates to EIS measurements.

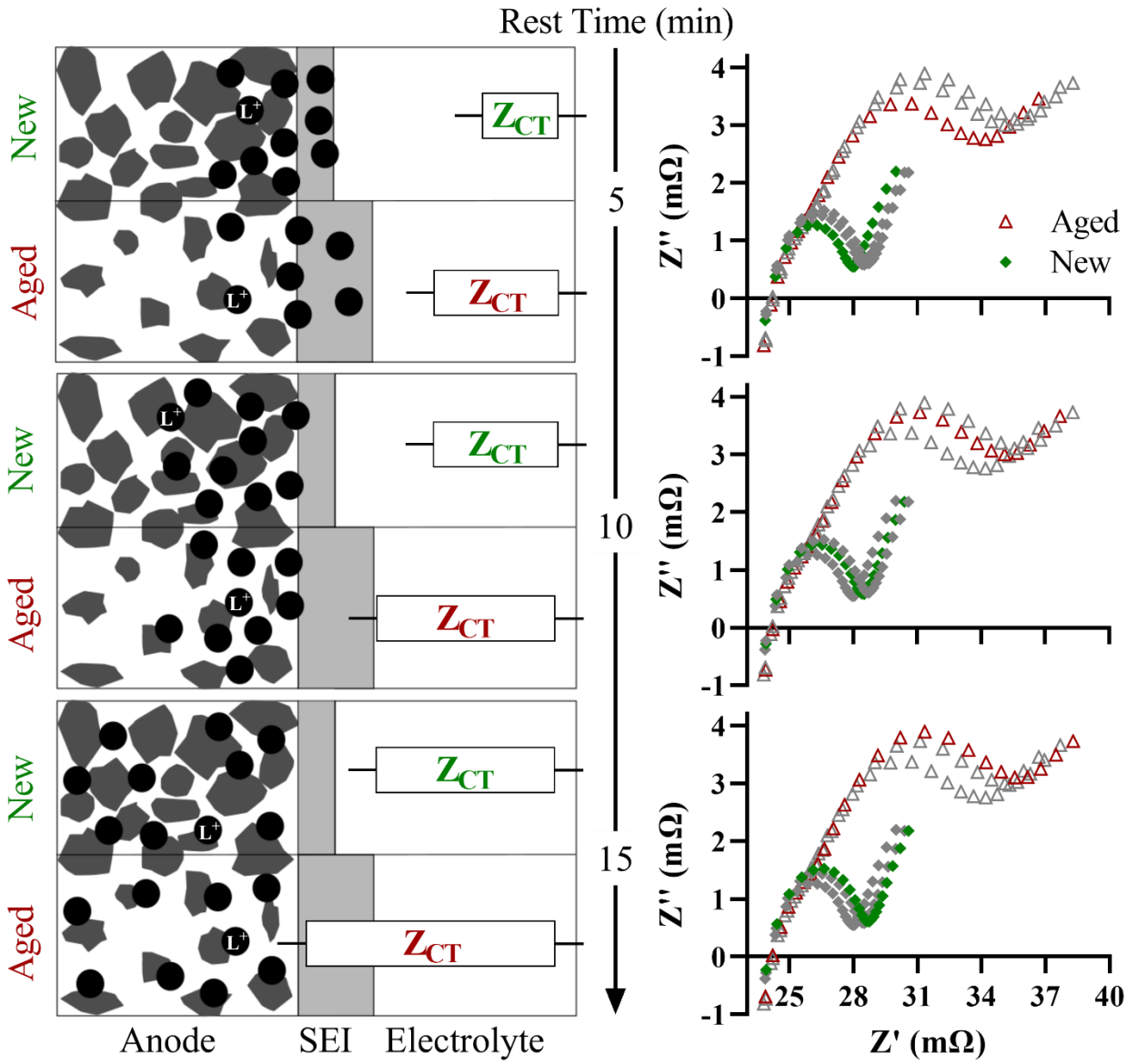

Figure 4-4: Short-term relaxation effect impedance evolution tracked with EIS data (plots highlighted according to rest time) and conceptually pictured with battery half-cell diagrams.

4.4 Battery Modeling

EIS results are best quantified by fitting battery models to the data. ECMs are frequently used because of their simplicity and because the circuit elements used somewhat represent the physical behavior of the battery [30]. The simplest model is a single resistor, which models the internal, ohmic resistance of the battery. However, since the chemical

reactions inside batteries are also time dependent, additional elements are used to model processes of different time constants, such as charge transfer of both electrodes, impedance of the SEI and diffusion inside the electrodes. These processes can be modeled using multiple branches with a resistor in parallel with a capacitor (R||C) [31]. For EIS modeling, these R||C branches produce ideal semi-circles, however, the EIS results for batteries are non-ideal, and semi-circles only provide approximate fits.

As shown in Figure 4-5a, the SEI impedance usually manifests as a small semi-circle in the high to mid frequency range of the EIS measurement. The SEI is a biproduct of undesirable chemical reactions between the negative electrode and the electrolyte. At the same time, after its formation, the SEI layer prevents further reactions between electrode and electrolyte. However, the SEI contributes to the internal resistance of the battery and further increases this resistance, as the SEI layer grows with battery age. A larger semi-circle in the mid frequency range is caused by the chemical reactions necessary for lithium ions to be transferred between electrodes and electrolyte (charge transfer). Finally, lithium ions which enter the electrodes slowly diffuse deeper into the electrode materials. This diffusion appears as a line at a 45° angle in the low frequency range of the EIS measurement [32]. Higher numbers of R||C branches can achieve improved fits, however, at the cost of adding many model parameters, and possibly overfitting to the data. Near perfect fits can be obtained using a rendition of capacitors known as constant phase elements (CPE), and CPEs in parallel with resistors ($R||Q, \alpha$), known as ZArc elements. CPE and ZArc elements produce much better fits since they are non-ideal circuit elements, at the cost of only one additional parameter (α) compared to ideal capacitors. Furthermore, the fitting process can

be controlled more easily since there is low ambiguity in the fitting results. In contrast, when using ideal circuit elements, two fits with different parameters may be accepted, due to the large inherent error between the fit and the data. This means that ideal models cannot distinguish between small changes in the EIS results, making them unsuitable to model the subtle changes in charge transfer and diffusion impedance occurring as a result of the relaxation effect.

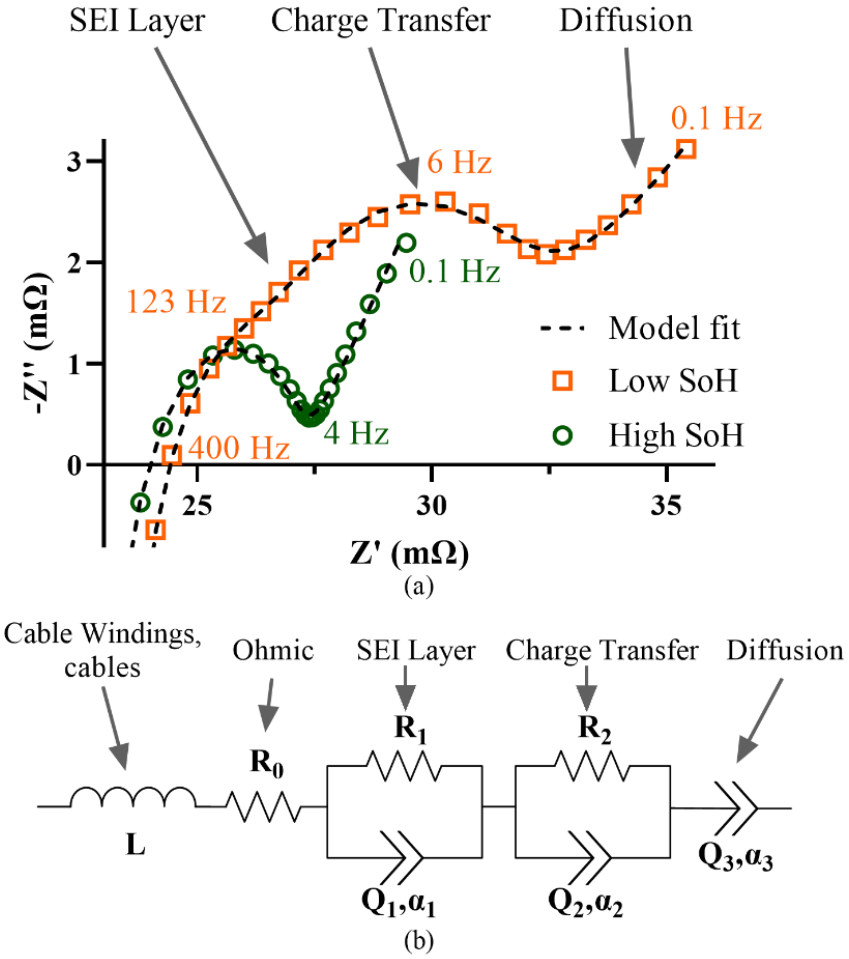

Figure 4-5: Nyquist plots of low and high SoH EIS measurements with model fits (a), fractional order impedance model (b).

Figure 4-5a shows two EIS datasets, one for a battery at 100% SoH, and the other for a battery at 90% SoH. The EIS results at lower SoH show significant increases in SEI layer and charge transfer impedances. The equivalent circuit structure used to model EIS results in this work is also shown in Figure 4-5b. The circuit consists of an inductance (L) to model inductive effects from cell windings and cables (used to connect the potentiostat to the battery), a resistance (R_0) modeling ohmic resistance, a ZArc element ($R_1||Q_1$, α_1) to model the SEI layer impedance, a second ZArc element ($R_2||Q_2$, α_2) to model charge transfer impedance, and finally a CPE (Q_3, α_3) to model diffusion. The impedance Z_c of this circuit is defined by Equation 4-2 for input frequency ω. The time constants are defined by $\tau_i = (R_i Q_i)^{1/\alpha_i}$ [26].

$$Z_c(\omega) = j\omega L + R_0 + \frac{R_1}{1 + R_1 Q_1 (j\omega\tau_1)^{\alpha_1}} + \frac{R_2}{1 + R_2 Q_2 (j\omega\tau_2)^{\alpha_2}} + \frac{1}{Q_3 (j\omega)^{\alpha_3}} \tag{4-2}$$

Further to the above, the circuit in Figure 4-5b provides good fits for both healthy and aged batteries as also shown in Figure 4-5a. Model fitting was done using Particle Swarm Optimization (PSO) with the objective function S shown in Equation 4-3:

$$S = \sum_{\omega=\omega_i}^{\omega_f} \{[Z'(\omega) - Z_c'(\omega)]^2 + [Z''(\omega) - Z_c''(\omega)]^2\} \tag{4-3}$$

This objective function computes the square of the difference between the real value of the measured impedance Z' and the real value of the calculated impedance Z_c' for frequencies ω between the initial frequency ω_i and the final frequency ω_f. The same is done for the imaginary parts of the measured and calculated impedance (Z'' and Z_c''

respectively). The resulting square differences are summed to yield a single objective function for the PSO algorithm to optimize.

4.5 SoH Estimation Method

This section first introduces the empirical SoH model followed by a description of the fitting process used to obtain consistent fractional order model fits to the EIS data.

4.5.1 Empirical SoH Model

In this section, a new SoH estimation method is proposed based on the rate of change of an equivalent resistance with relaxation time. This equivalent resistance R_{eq}, as shown in Equation 4-4, is a summation of the branch resistances of the impedance model of Equation 4-2 introduced in the previous section.

$$R_{eq} = R_1 + R_2 \tag{4-4}$$

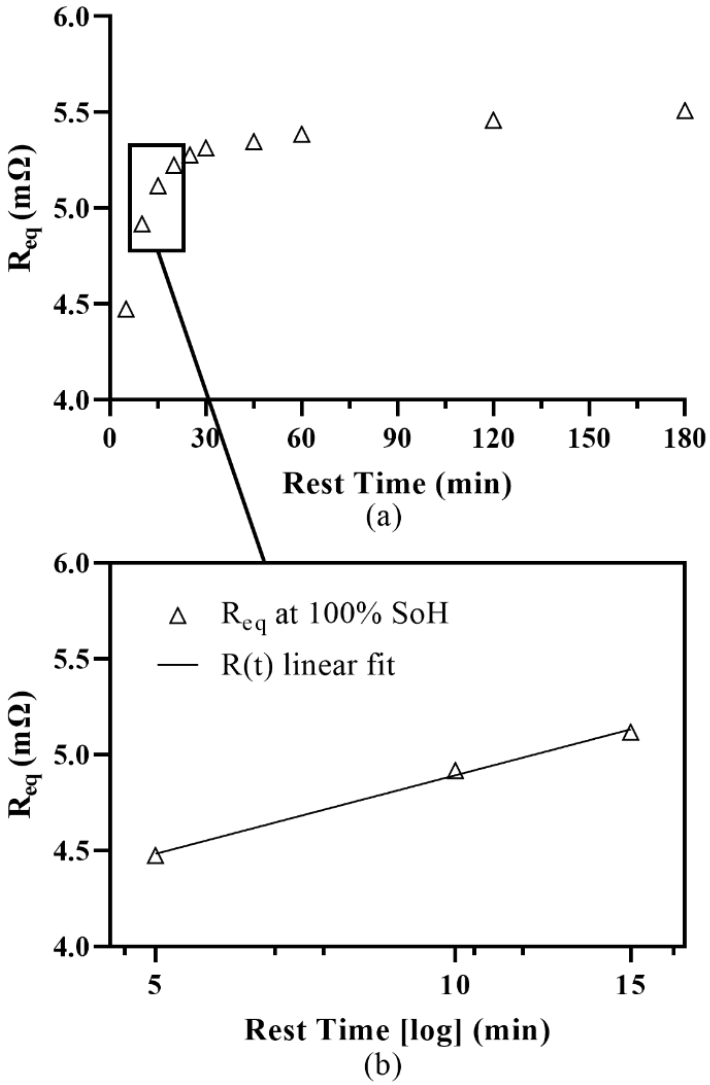

Figure 4-6: Evolution of R_{eq} with rest time at 100% SoH (a), log-linear trend of R_{eq} for rapid relaxation region (b).

Figure 4-6a shows how R_{eq} changes for models fitted to EIS data measured at different rest times after a 5C, 15 second discharge pulse. The initial rate of change of R_{eq} with rest times at 5, 10 and 15 minutes can be correlated to SoH. To find the rate of change, a semi-log-linear fit defined by Equation 4-5 and shown in Figure 4-6b was used.

$$R_{eq}(t) = m \times log(t) + y_r \quad (4\text{-}5)$$

Here, R_{eq} is given by the rate of change m, y-intercept y_r and relaxation time t.

The performance of this model is discussed in Section 4.6. The correlation of rate of change m and SoH follows a two-phase exponential decay model shown in Equation 4-6.

$$soh(m) = a_1 \exp(m \times b_1) + a_2 \exp(m \times b_2) \quad (4\text{-}6)$$

The parameters a_1 and b_1 describe an initial fast decay from 100% SoH to 95% SoH, followed by a slower decay from 95% SoH to 80% SoH described by a_2 and b_2. The parameter values and performance of this model are discussed in detail in Section 4.6.

4.5.2 Model Fitting Procedure

The following model fitting procedure was found to be necessary to guide the PSO algorithm to find repeatable solutions. First, the impedance model (Equation 4-2) is fit to the EIS dataset measured after the longest rest time (15 minutes). Further to the model presented in Equation 4-2, Table 4-2 shows an example of model parameters found for the 100% SoH case. Also shown are the upper and lower bounds used with the PSO algorithm. For a new EIS dataset at unknown battery state, the upper or lower bounds can be used as initial values for the PSO algorithm provided the data comes from the same battery model.

Table 4-2: Model Parameter Bounds and Example Values at 90% SoC, 100% SoH, 25°C and 15 minutes Rest

	L (μF)	R_0 (mΩ)	R_1 (mΩ)	τ_1 (ms)	R_2 (mΩ)	τ_2 (ms)	Q_3	α_i
Upper Bound	0.7	28	40	480	6	30	5	1
Lower Bound	0.4	20	0	0	2	0	1	0
Example	0.58	22.2	0.41	2	4.8	0.5	4.04	1, 0.58, 0.52

After the 15-minute rest EIS fit is obtained, these upper and lower bounds are updated such that L, R_0, and α_3 are fixed to the value of the 15-minute rest fit. Furthermore, R_1 and R_3 from the 15-minute rest EIS fit are set to be the upper bounds of the next fit. With these new limits in place, R_1, τ_1, R_2, τ_2 and Q_3 are fit to the 10-minute rest EIS. Finally, the limits are updated once more to fix the upper bounds of R_1 and R_2 to their values at 10 minutes rest, and a fit for 5 minutes rest EIS is obtained. The parameters L, R_0, and α_3 are not affected by the relaxation effect [33], so they can be fixed once an initial fit is found. This procedure is shown in Figure 4-7 together with the steps of the empirical SoH model to show a summary of the complete SoH estimation method.

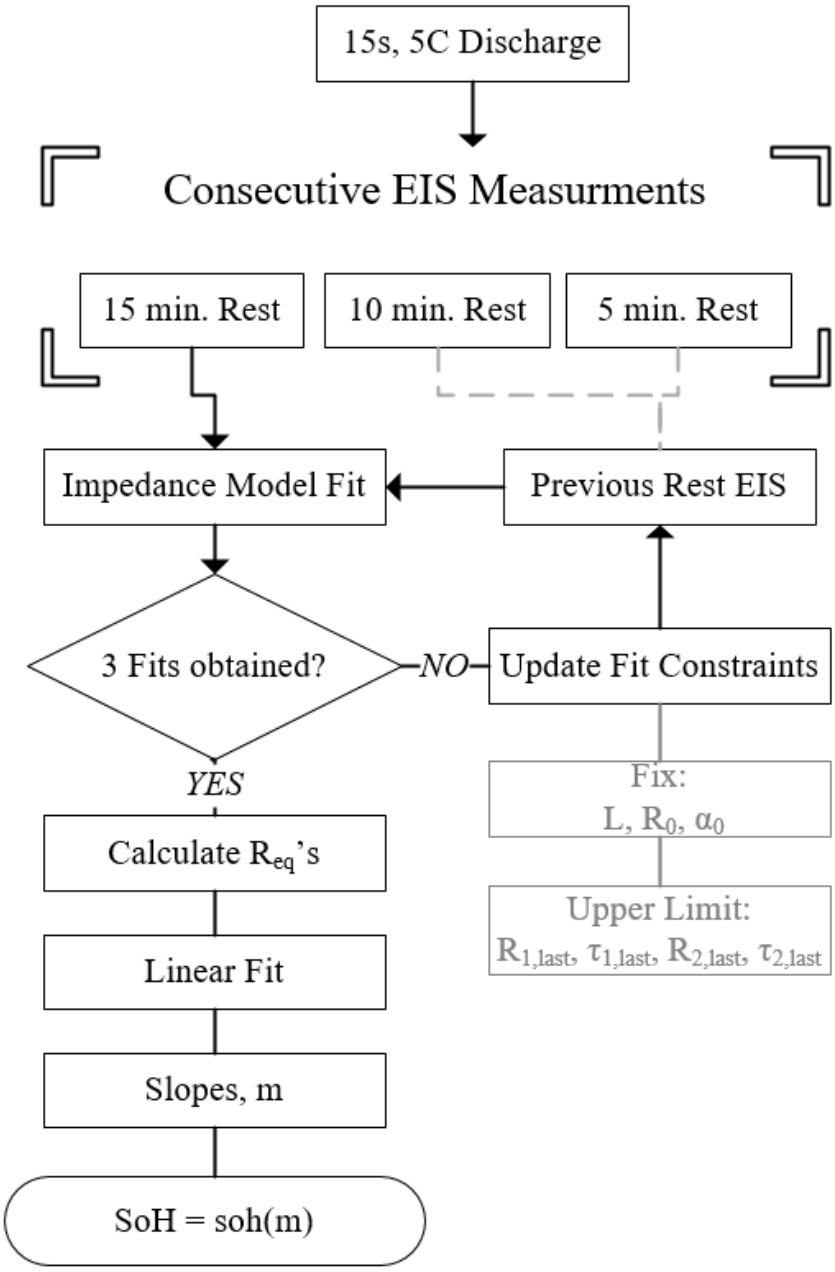

Figure 4-7: Procedure to obtain SoH estimate from EIS data at different rest times.

4.6 Results and Discussion

In this section the performance of the proposed SoH estimation method is discussed. In Section 4.5 the general method was described for one SoH example dataset. With this method, the rate of change *m* of the combined branch resistance R_{eq} for EIS data recorded

between 5 and 15 minutes of rest after a 5C, 15s discharge pulse can be correlated to SoH. The rate of change m is found using a semi-log linear fit to R_{eq} over rest time defined by Equation 4-5. Figure 4-8a shows how R_{eq} evolves with rest time for a subset of six different SoHs between 100% and 80%. The semi-log-linear fits are shown in Figure 4-8b for each of the six datasets.

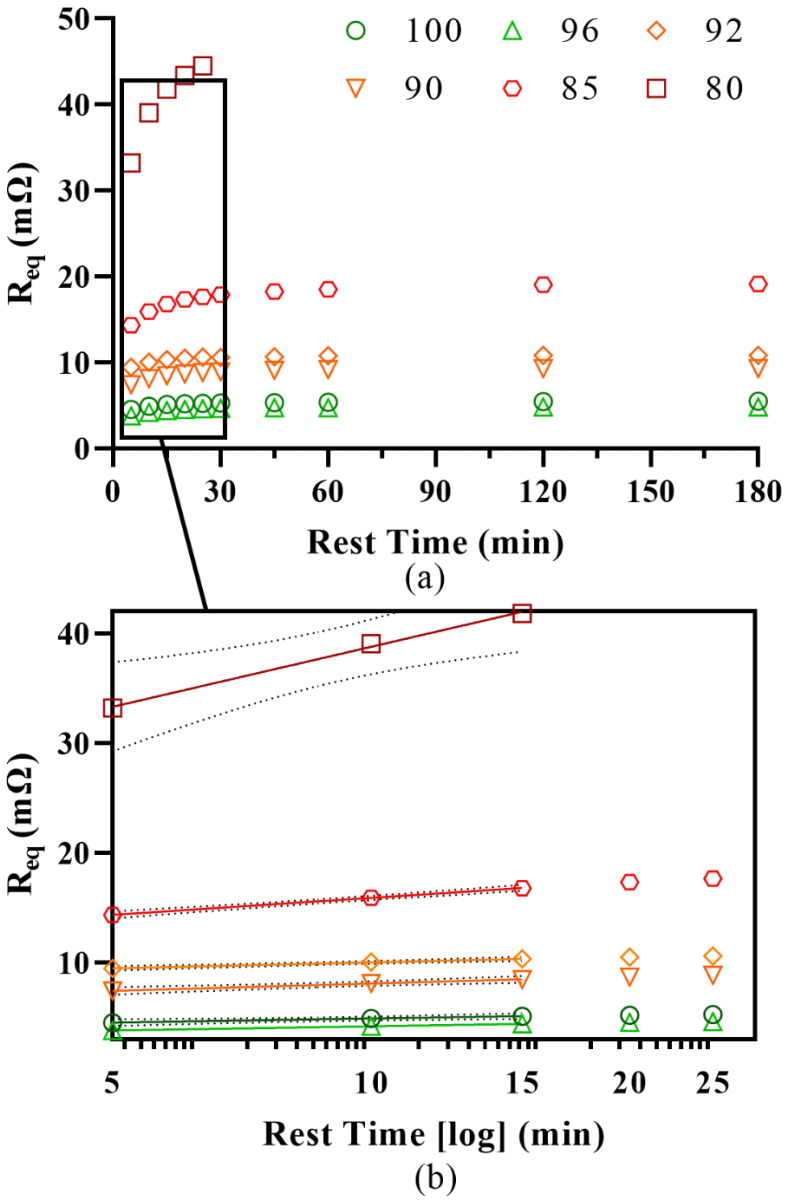

Figure 4-8: Short term evolution of R_{eq} with rest time (a) and semi-log-linear fits to the initial rate of change of R_{eq} (b).

Table 4-3 shows the slopes and intercepts for each case as well as the fitting statistics. The R squared and adjusted R squared values are all between 0.994 and 1, suggesting the linear fit is suitable to describe the datasets. Figure 4-8b and Table 4-3 show that the slopes of the log-linear fits increase as SoH decreases, but not in a linear fashion. Instead the data follows an exponential decay with two time constants.

Table 4-3: Semi-log Fit (Equation 5) Results and Statistics

SoH (%)	100	96	92	90	85	80
Y intercepts	3.68	2.95	8.24	5.90	10.76	20.63
Slope, m	0.54	0.55	0.78	0.96	2.24	7.884
R^2	0.9967	0.9999	0.9992	0.9986	0.9998	0.9971
R^2_{adj}	0.9934	0.9998	0.9984	0.9972	0.9996	0.9942
RMSE	0.017	0.003	0.012	0.020	0.018	0.236

Figure 4-9 shows the calculated slopes *m* vs. measured, true SoH for the entire experimental dataset. Also shown in this figure is the double exponential model given by Equation 6 fitted to the data, as well as the 95% prediction band (dotted lines), indicating where 95% of unknown data will fall. The first time constant of this model (Equation 4-6) describes the initial steep drop between 100% and 90% SoH. The second time constant describes the much slower, nearly linear decay between 90% and 78% SoH.

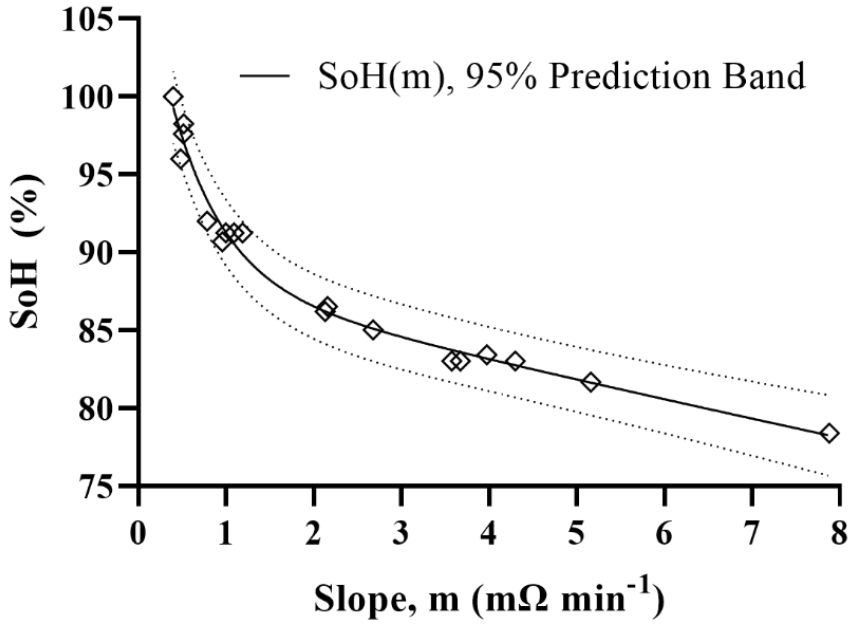

Figure 4-9: Req short term relaxation evolution slopes and SoH.

The parameters of the model (Equation 4-6) are shown in Table 4-4, with statistics showing a high R^2_{adj} equal to 0.98 and a RMSE of less than 1% SoH. The repeatability of the SoH estimation method was assessed for one dataset at above 90% and another below 90%. Each dataset consists of three repeats of the experimental EIS measurement.

Table 4-4: Double Exponential Model (Equation 6) Fit Results and Statistics

a_1	b_1	a_2	b_2	R^2_{adj}	RMSE (% SoH)
22.16	-1.67	88.48	-0.0156	0.98	0.82

Table 4-5: Repeatability of the SoH Estimation Method

Variable	True SoH (%)	Data Set			mean	SD
		1	2	3		
Rate of change, m	91.27	1.00	1.09	1.19	1.09	0.095
	83.03	3.58	3.67	4.30	3.85	0.394
Estimated SoH (%)	91.27	91.20	90.58	90.05	90.61	0.573
	83.03	83.61	83.44	82.41	83.15	0.651

Figure 4-10a shows the estimated SoH with mean and SD error bars for the repeat sets, as well as the estimated SoHs for the entire dataset. The corresponding numbers are

shown in Table 4-5, where the first two rows show data for *m* and the last two rows data for the estimated SoH. Above 90% SoH, the SD of *m* is small and the corresponding SoH estimate has a small SD as well. Below 90% SoH, the SD of *m* is much larger, however, the SD of the SoH estimate is still small. This is because of the different time constants in the exponential model, causing the estimated SoH to be sensitive to changes in *m* for the high SoH, fast decay portion of the model, but much less sensitive for the low SoH, slow decay portion of the model. In general, the estimation error is consistently lower for the low SoH portion of the model as shown in Figure 4-10b. This model has an RMSE SoH estimation error of 0.82% with an overall maximum error of 1.74%. Below 90% SoH, the maximum error is much lower, at 0.62%.

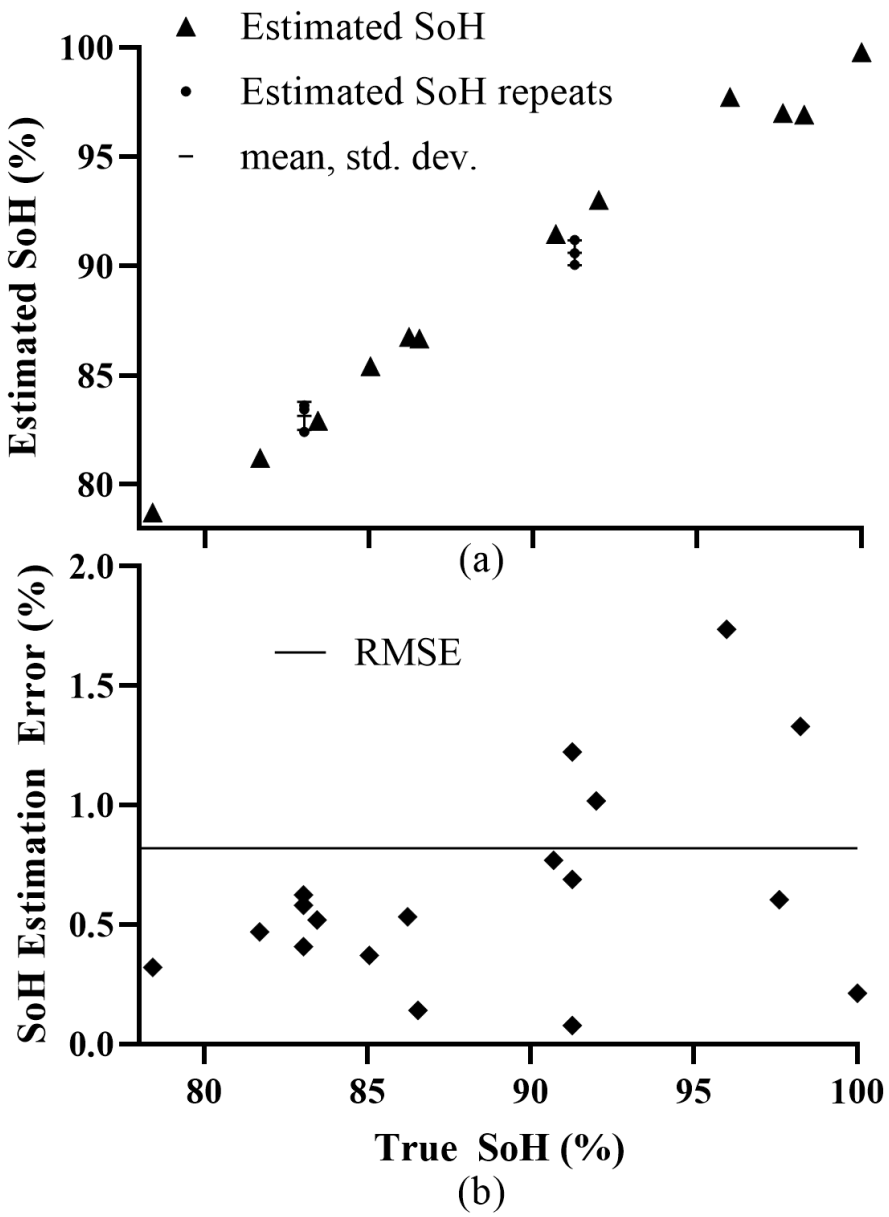

Figure 4-10: Estimated SoH vs. True SoH and slope repeatability (a), SoH Estimation Error and RMSE (b).

The proposed method is demonstrated at 90% SoC, 25°C, with a relaxation effect induced by a 15s, 5C discharge pulse and a measurement period of up to 15 minutes. However, the method can be adjusted by accounting for SoC and temperature in the model, as long as the relaxation effect does not change significantly. R_{eq} slopes obtained for a

100% SoH battery for different SoCs and temperatures are shown in Figure 4-11. SoC values of 70% and 50% fall within one SD (assumed to be 0.095 from Table 4-5) of the 90% SoC used for the proposed method. Similarly, increasing the temperature to 35°C produces a slope value also within one SD of the 100% SoH (and 25°C) datapoint shown in Table 4-3. This suggests that the relaxation rate of change behaves similar across a wide range of operating conditions. However, lowering the temperature to 10°C results in a significantly different slope value. Therefore, to be able to test SoH at lower temperatures, a representative number of batteries must be re-tested at different SoH to understand the impact of low temperature on Equation 4-6.

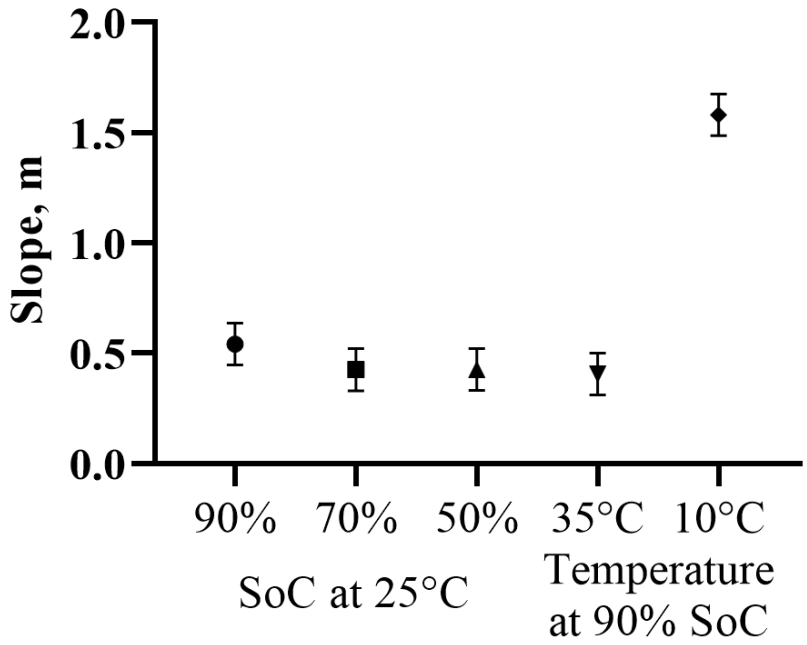

Figure 4-11: R_{eq} slopes for different SoCs and Temperatures for battery at 100% SoH.

Discharge pulses similar to 5C can also be used with some model adjustment, however, 5C was found to provide the most consisted results. Reducing the C-rate may increase the SoH estimation error. In this study, EIS was measured at 5, 10 and 15 minutes,

however, due to the semi-log linear nature of the rate of changed of the combined resistance, any three points between 5 and 15 minutes can be used to obtain the relaxation rate. Each EIS measurement for the chosen frequency range has a duration of less than 2 minutes, therefore, the measurement time could be reduced to less than 10 minutes overall. Further reduction in measurement time may be achieved by utilizing multi-sinewave EIS methods [34], which allow the sine waves at different frequencies to be stacked into a single signal, instead of running them consecutively as done in this study. The EIS measurement time is then limited only by the lowest frequency. Thus, the upper end of the measurement time of the proposed SoH estimation method should be further investigated to see if it can be reduced, possibly well below 10 minutes.

Compared to voltage-based methods, introduced in Section 4.1.2, which utilize the relaxation effect, the proposed method shows gains in accuracy and testing time. Table 4-6 summarizes the method comparison. The method requiring 10 minutes of rest time [14] is limited to full charge or full discharge conditions and accuracy was not stated, possibly due to the low number of cells tested. The method requiring 30 minutes of rest time after full charge [17] also did not state SoH accuracy. A promising method was proposed by [16] with a rest time of 20 minutes and a wide SoC range (requiring building of lookup tables at different SoCs). They showed an accuracy of 1.8% SoH, although with only 6 cells tested.

Table 4-6: Method Comparision

Reference	Rest Time (min)	SoC	SoH Accuracy	Number of Cells Tested	Aging Procedure (Temperature, Charge)
[75]	10	100 or 0	Not Stated	3	75°C, 1C
[76]	20	40-80	1.8%	6	25°C, 1C
[77]	30	100	Not Stated	9	55°C, 1C
This Study	15	50-90	1%	16	25°C, 0.5C

The proposed SoH estimation method has been experimentally applied here to an NMC cylindrical battery cells aged with cycle aging at room temperature, but is also applicable to other chemistries. Kindermann et al. [14] showed that the relaxation rates measured with EIS of NMC and Lithium Manganese Oxide (LiMn) cells are within 1% of each other, suggesting that the proposed SoH estimation model would be equally effective.

4.7 CONCLUSION

In this paper a SoH estimation method is proposed that entails a combined consideration of the short-term relaxation effect, EIS measurements and fractional order impedance modeling. It was shown that EIS measurements obtained between 5 and 15 minutes of rest can produce repeatable results to be used with an empirical model. The proposed empirical model was shown to provide an average SoH estimation error of less than 1%. This method shows promise for SoH estimation with EIS, for potential implementation with a BMS.

ACKNOWLEDGEMENTS

This work was supported by the Collaborative Research and Training Experience (CREATE) Grant through the Natural Science and Engineering Research Council of Canada under Grant 482038-2016. We thank Cadex Electronics for their facilities, support and expertise.

REFERENCES

[1] M.A. Hannan, M.S.H. Lipu, A. Hussain, A. Mohamed, A review of lithium-ion battery state of charge estimation and management system in electric vehicle applications: Challenges and recommendations, Renew. Sustain. Energy Rev. 78 (2017) 834–854. doi:10.1016/j.rser.2017.05.001.

[2] R. Xiong, J. Cao, Q. Yu, H. He, F. Sun, Critical Review on the Battery State of Charge Estimation Methods for Electric Vehicles, IEEE Access. 6 (2018) 1832–1843. doi:10.1109/ACCESS.2017.2780258.

[3] M. Ismail, R. Dlyma, A. Elrakaybi, R. Ahmed, S. Habibi, Battery state of charge estimation using an Artificial Neural Network, 2017 IEEE Transp. Electrif. Conf. Expo, ITEC 2017. (2017) 342–349. doi:10.1109/ITEC.2017.7993295.

[4] S.A. Gadsden, M. Al-Shabi, S.R. Habibi, Estimation Strategies for the Condition Monitoring of a Battery System in a Hybrid Electric Vehicle, ISRN Signal Process. 2011 (2011). doi:10.5402/2011/120351.

[5] M.S. Farag, R. Ahmed, S.A. Gadsden, S.R. Habibi, J. Tjong, A comparative study of Li-ion battery models and nonlinear dual estimation strategies, 2012 IEEE Transp. Electrif. Conf. Expo, ITEC 2012. (2012) 1–8. doi:10.1109/ITEC.2012.6243485.

[6] R. Ahmed, M. El Sayed, I. Arasaratnam, J. Tjong, S. Habibi, Reduced-Order Electrochemical Model Parameters Identification and State of Charge Estimation for Healthy and Aged Li-Ion Batteries—Part II: Aged Battery Model and State of Charge Estimation, IEEE J. Emerg. Sel. Top. Power Electron. 2 (2014) 678–690. doi:10.1109/JESTPE.2014.2331062.

[7] Y. Che, Z. Deng, X. Lin, L. Hu, Predictive Battery Health Management With Transfer Learning and Online Model Correction, IEEE Trans. Veh. Technol. 70 (2021) 1269–1277.

[8] N. Meddings, M. Heinrich, F. Overney, J.S. Lee, V. Ruiz, E. Napolitano, S. Seitz, G. Hinds, R. Raccichini, M. Gaberšček, J. Park, Application of electrochemical impedance spectroscopy to commercial Li-ion cells: A review, J. Power Sources. 480 (2020). doi:10.1016/j.jpowsour.2020.228742.

[9] E. Din, C. Schaef, K. Moffat, J.T. Stauth, A scalable active battery management system with embedded real-time electrochemical impedance spectroscopy, IEEE Trans. Power Electron. 32 (2017) 5688–5698. doi:10.1109/TPEL.2016.2607519.

[10] B.G. Carkhuff, P.A. Demirev, R. Srinivasan, Impedance-Based Battery Management System for Safety Monitoring of Lithium-Ion Batteries, IEEE Trans. Ind. Electron. 65 (2018) 6497–6504. doi:10.1109/TIE.2017.2786199.

[11] X. Wei, X. Wang, H. Dai, Practical on-board measurement of lithium ion battery impedance based on distributed voltage and current sampling, Energies. 11 (2018). doi:10.3390/en11010064.
[12] N. Lohmann, P. Haussmann, P. Wesskamp, J. Melbert, T. Musch, Employing Real Automotive Driving Data for Electrochemical Impedance Spectroscopy on Lithium-Ion Cells, SAE Int. J. Altern. Powertrains. 4 (2015) 308–317. doi:10.4271/2015-01-1187.
[13] E. Locorotondo, F. Corti, L. Pugi, L. Berzi, A. Reatti, G. Lutzemberger, Design of a Wireless Charging System for Online Battery Spectroscopy, Energies. (2021).
[14] F.M. Kindermann, A. Noel, S. V. Erhard, A. Jossen, Long-term equalization effects in Li-ion batteries due to local state of charge inhomogeneities and their impact on impedance measurements, Electrochim. Acta. 185 (2015) 107–116. doi:10.1016/j.electacta.2015.10.108.
[15] K. Qian, B. Huang, A. Ran, Y.B. He, B. Li, F. Kang, State-of-health (SOH) evaluation on lithium-ion battery by simulating the voltage relaxation curves, Electrochim. Acta. 303 (2019) 183–191. doi:10.1016/j.electacta.2019.02.055.
[16] Q. Fang, X. Wei, T. Lu, H. Dai, J. Zhu, A state of health estimation method for lithium-ion batteries based on voltage relaxation model, Energies. 12 (2019). doi:10.3390/en12071349.
[17] I. Baghdadi, O. Briat, P. Gyan, J.M. Vinassa, State of health assessment for lithium batteries based on voltage–time relaxation measure, Electrochim. Acta. 194 (2016) 461–472. doi:10.1016/j.electacta.2016.02.109.
[18] A. Ran, Z. Zhou, S. Chen, P. Nie, K. Qian, Z. Li, B. Li, H. Sun, F. Kang, X. Zhang, G. Wei, Data-Driven Fast Clustering of Second-Life Lithium-Ion Battery: Mechanism and Algorithm, Adv. Theory Simulations. 3 (2020) 1–9. doi:10.1002/adts.202000109.
[19] A. Barai, W.D. Widanage, J. Marco, A. Mcgordon, P. Jennings, A study of the open circuit voltage characterization technique and hysteresis assessment of lithium-ion cells, J. Power Sources. 295 (2015) 99–107. doi:10.1016/j.jpowsour.2015.06.140.
[20] W. Waag, S. Käbitz, D.U. Sauer, Experimental investigation of the lithium-ion battery impedance characteristic at various conditions and aging states and its influence on the application, Appl. Energy. 102 (2013) 885–897. doi:10.1016/j.apenergy.2012.09.030.
[21] H. Wang, M. Tahan, T. Hu, Effects of rest time on equivalent circuit model for a li-ion battery, Proc. Am. Control Conf. 2016-July (2016) 3101–3106. doi:10.1109/ACC.2016.7525394.
[22] V. Zinth, C. von Lüders, J. Wilhelm, S. V. Erhard, M. Hofmann, S. Seidlmayer, J. Rebelo-Kornmeier, W. Gan, A. Jossen, R. Gilles, Inhomogeneity and relaxation phenomena in the graphite anode of a lithium-ion battery probed by in situ neutron diffraction, J. Power Sources. 361 (2017) 54–60. doi:10.1016/J.JPOWSOUR.2017.06.060.
[23] M. Messing, T. Shoa, S. Habibi, Lithium-Ion Battery Relaxation Effects, in: ITEC 2019, 2019.
[24] H. Shabbir, W. Dunford, T. Shoa, State of health estimation of Li-ion batteries using electrochemical impedance spectroscopy, 2017 IEEE Transp. Electrif. Conf. Expo, ITEC 2017. (2017) 108–112. doi:10.1109/ITEC.2017.7993255.
[25] A. Guha, A. Patra, Online Estimation of the Electrochemical Impedance Spectrum and Remaining Useful Life of Lithium-Ion Batteries, IEEE Trans. Instrum. Meas. 67 (2018) 1836–1849. doi:10.1109/TIM.2018.2809138.

[26] J. Kim, L. Krüger, J. Kowal, On-line state-of-health estimation of Lithium-ion battery cells using frequency excitation, J. Energy Storage. 32 (2020) 101841. doi:10.1016/j.est.2020.101841.
[27] A. Gismero, D.I. Stroe, E. Schaltz, Calender Aging Lifetime Model for NMC-based Lithium-ion Batteries Based on EIS Measurements, in: 2019 Fourteenth Int. Conf. Ecol. Veh. Renew. Energies, 2019.
[28] E. Locorotondo, V. Cultrera, L. Pugi, L. Berzi, M. Pierini, G. Lutzemberger, Development of a battery real-time state of health diagnosis based on fast impedance measurements, J. Energy Storage. 38 (2021) 102566. doi:10.1016/j.est.2021.102566.
[29] Zahner Messsysteme, EIS - Electrochemical Impedance Sepctroscopy, (2019).
[30] N.A. Chaturvedi, R. Klein, J. Christensen, J. Ahmed, A. Kojic, Modeling, estimation, and control challenges for lithium-ion batteries, IEEE Control Syst. Mag. (2010) 1997–2002. doi:10.1109/acc.2010.5531623.
[31] A. Rodríguez, G.L. Plett, Controls-oriented models of lithium-ion cells having blend electrodes. Part 1: Equivalent circuits, J. Energy Storage. 11 (2017) 162–177. doi:10.1016/j.est.2017.02.004.
[32] T.R. Jow, S.A. Delp, J.L. Allen, J.-P. Jones, M.C. Smart, Factors Limiting Li + Charge Transfer Kinetics in Li-Ion Batteries, J. Electrochem. Soc. 165 (2018) A361–A367. doi:10.1149/2.1221802jes.
[33] A. Maheshwari, M. Heck, M. Santarelli, Cycle aging studies of lithium nickel manganese cobalt oxide-based batteries using electrochemical impedance spectroscopy, Electrochim. Acta. 273 (2018) 335–348. doi:10.1016/j.electacta.2018.04.045.
[34] H. Zappen, F. Ringbeck, D. Sauer, Application of Time-Resolved Multi-Sine Impedance Spectroscopy for Lithium-Ion Battery Characterization, Batteries. 4 (2018) 64. doi:10.3390/batteries4040064.

Chapter 5: Battery SoC Estimation from EIS using Neural Nets

Marvin Messing[1,2], Tina Shoa[2], Ryan Ahmed[1], Saeid Habibi[1]

[1]Department of Mechanical Engineering, McMaster University, Hamilton, ON, Canada,

[2]Cadex Electronics, Richmond, BC, Canada

This paper is published in 2020 IEEE Transportation Electrification Conference and Expo (ITEC), 2020, pp. 588-593, doi: 10.1109/ITEC48692.2020.9161523. This paper is republished here with permission[3].

ABSTRACT

In this paper, a battery state of charge (SoC) estimation strategy with deep neural networks (DNN) and Electrochemical Impedance Spectroscopy (EIS) is proposed. EIS data was obtained for a range of conditions and was used as inputs to a DNN. Additionally, a battery model was fit to the data, and the model parameters were used as inputs to a second DNN. The Root Mean Square Error (RMSE) of both networks was found to be less than 5% for SoC above 30%. The dataset used in this study included batteries of different States of Health (SoH) as well as EIS measured at various rest times after different discharge pulses.

5.1 INTRODUCTION

Battery state estimation accuracy for lithium-ion batteries and their use in electric vehicles (EV) remains an area of interest to engineers and researchers. The most important battery states are State of Charge (SoC) [1], State of Health (SoH) [2], and State of available Power

[3] In reference to IEEE copyrighted material which is used with permission in this thesis, the IEEE does not endorse any of McMaster's products or services. Internal or personal use of this material is permitted. If interested in reprinting/republishing IEEE copyrighted material for advertising or promotional purposes or for creating new collective works for resale or redistribution, please go to http://www.ieee.org/publications_standards/publications/rights/rights_link.html to learn how to obtain a License from RightsLink.

(SoaP) [3]. Further increase in accuracy for the estimation of these states can result in a decrease in cost, size, and weight of the battery pack, as well as increase in longevity and safety [4], [5]. However, the information extracted from the battery is usually restricted to simple voltage, current and temperature measurements, and Kalman filters are used together with battery models to obtain optimal state estimation in the face of uncertainties [6], [7],[8]. A more detailed picture of the states of the battery can be obtained using Electrochemical Impedance Spectroscopy (EIS), a technique which has been widely used by researchers in electrochemistry and battery engineering to characterize battery behaviour [9], [10]. EIS applies a voltage or current signal to the battery at different frequencies and the corresponding response is measured and converted to frequency domain via the Fourier transform. The real and imaginary components of the impedance are commonly plotted for each frequency resulting in a Nyquist plot [11]. EIS is not yet available as part of the battery management system (BMS) in EVs, but efforts are being made to bring down costs and complexity of this method [12]–[14]. Once EIS becomes available in the BMS it can be used to augment SoC estimation algorithms. Only a few studies have attempted to obtain accurate state estimation from EIS data. In [15], an equivalent circuit model was fit to EIS data and the model parameters were related to SoC showing an error of 2 to 5%. In [16], a large EIS dataset was used with Gaussian process regression to estimate SoH. The SoH estimated by the Gaussian algorithm was shown to be within ± 1 standard deviation after 150 cycles. The zero phase frequency was related to SoH and used to train a simple neural network in [17], however, no information about estimation accuracy was provided. Deep Neural Networks (DNN) have become a useful

tool to solve difficult classification and regression problems [18] in areas ranging from image processing to natural language processing. The relationship of the EIS data and the battery states is very complex making DNNs a suitable choice for state estimation from EIS. The aim of this study is to train a DNN with EIS data from lithium-ion batteries of different SoH to estimate SoC. Two networks are trained, one using raw EIS data, and the other using parameters from an impedance model.

5.2 EXPERIMENTAL

5.2.1 CHARACTERIZATION TESTS AND DATA

Lithium-ion batteries (Samsung INR21700-50E, 4.8Ah) were tested with EIS using a Bio-logic SP150 Potentiostat. Battery SoC and SoH were determined with a custom battery tester to less than 0.5% accuracy, and aging was done by cycling (constant current – constant voltage charge at C/2, discharge at 1C) using a Cadex C7400ER 4-channel battery analyzer. EIS and capacity tests were performed under controlled temperature conditions using a Testequity 1007C thermal chamber. The dataset used in this study consist of EIS scans for 25 frequencies between 800 Hz and 100 mHz each with a voltage amplitude of 10 mV. To account for relaxation effects [19], EIS was measured periodically after 15 second discharge pulses of 1C, 3C and 5C currents. The measurements were taken every 5 minutes over 30 minutes, then after every 15 minutes for 1 hour, and then every hour over 3 hours. In addition, the batteries were tested at 25°C and at 100%, 90%, and 80% SoH. Finally, SoC was varied in 5% increments from 30% to 95%. This multi-dimensional dataset of over 600 data points formed the basis for the findings of this study. A small

subset of Nyquist plots for the different conditions are shown in Figure 5-1a from which the high complexity of the relationship between SoC, SoH and EIS results can be observed. Figure 5-1b shows how different rest times after a 5C discharge impact the EIS measurement.

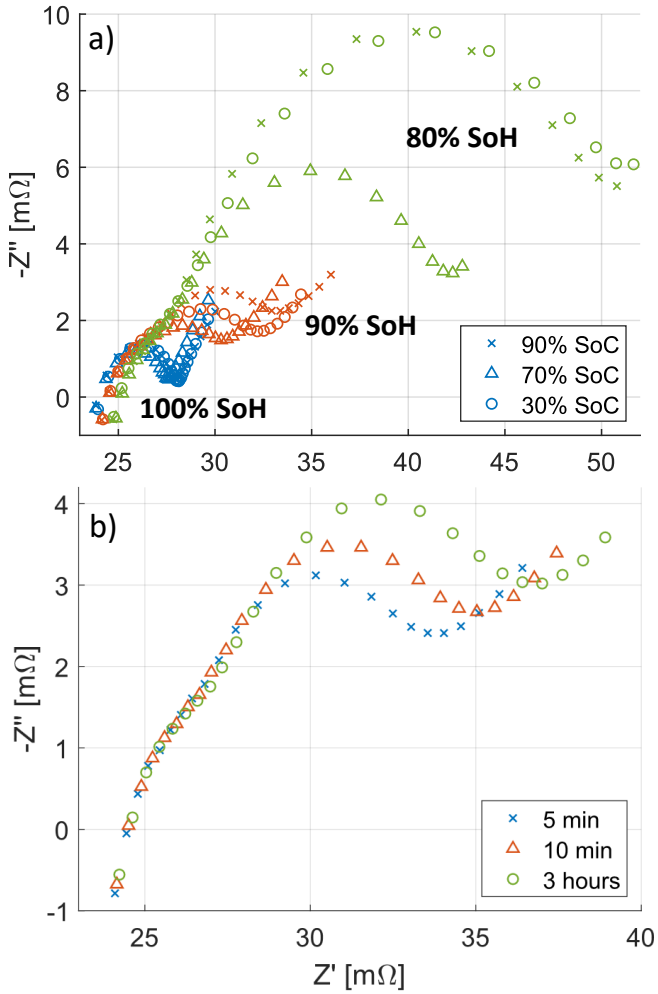

Figure 5-1: Nyquist plots for 100%, 70% and 30% SoC at 25°C and different SoH (a). Nyquist plots for 95% SoC, 90% SoH at 25°C after 15 second, 5C discharge pulse measured different rest times (b).

5.2.2 BATTERY MODEL

The impedance model shown in Figure 5-2b was fit to the EIS data using particle swarm optimization and the sum of squares cost function with equal weighting [11]. The model is based on [9] who showed a good fit to EIS data and provided clear reasoning for the selection of model components. The complex impedance Z of this fractional model changes with frequency ω according to (5-1), where $\tau_k = (R_k Q_k)^{1/\alpha_k}$.

$$Z(\omega) = i\omega L + R_0 + \frac{R_1}{1+R_1 Q_1 (i\omega\tau_1)^{\alpha_1}} + \frac{R_2}{1+R_1 Q_1 (i\omega\tau_1)^{\alpha_2}} + \frac{1}{Q_3 (i\omega)^{\alpha_3}} \quad (5\text{-}1)$$

The model parameters across the different conditions are used as inputs to one of the neural networks. EIS data at 100% SoH can be modeled using a simpler model, with an inductor in series with a resistor in series with a constant phase element (CPE) and in series with only one parallel Zarc element. However, the neural network requires the same amount of inputs regardless of SoH, therefore, two Zarc elements were used as shown in Figure 5-2 in all cases.

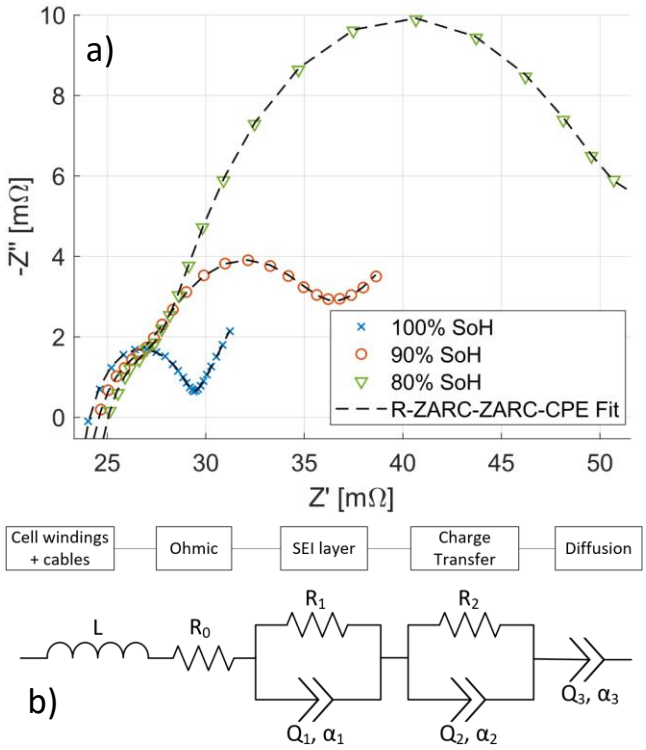

Figure 5-2: Impedance model used to model relaxation effect (a), and model fit to relaxation data at 25°C and 90% SoC (b).

5.2.3 NETWORK ARCHITECTURES

The architectures for the two neural networks used in this study are shown in Figure 5-3. Both networks consist of a single output, which is the SoC of a battery. The input parameters for the first network (Figure 5-3a) are the raw EIS values in frequency domain, which are a complex pair for each measurement frequency. The complex pairs were split into real and imaginary parts, yielding 25 numbers for the real parts and 25 numbers for the imaginary parts of the impedance, since 25 frequencies were used in the EIS measurement. Therefore, the neural network in Figure 5-3a has a total of 50 inputs. A network structure consisting of three hidden layers with 180 nodes each was found to result in the lowest regression error. For the second neural network (Figure 5-3b), the EIS data was used to

parameterize the battery model presented in Section 5.2.2. This resulted in 10 numbers for each EIS scan, representing the model parameters $L, R_0, R_1, Q_1, \alpha_1, R_2, Q_2, \alpha_2, Q_3$ and α_3. These 10 model parameters were used as the inputs to the neural network shown in Figure 5-3b. In this case, a single hidden layer with 70 nodes resulted in the lowest regression error.

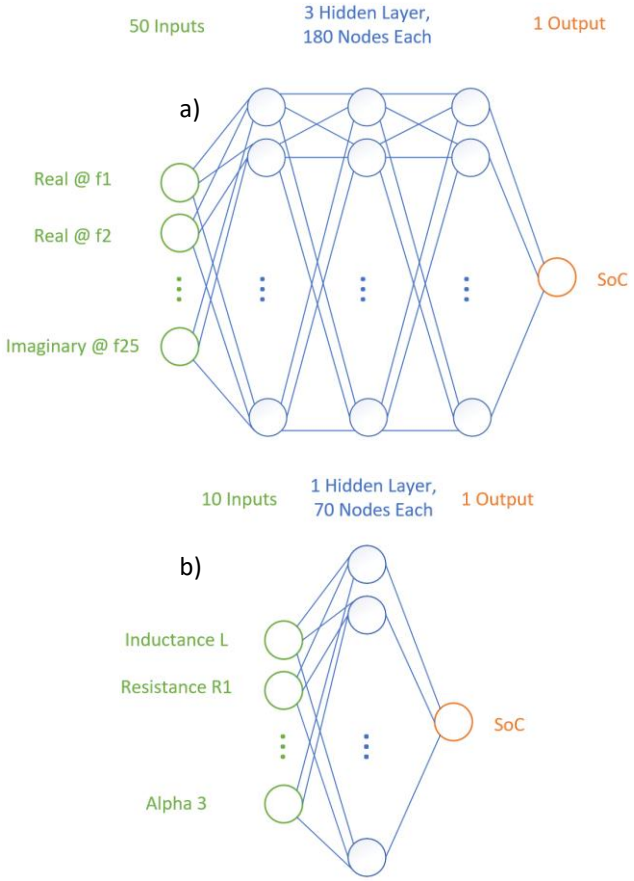

Figure 5-3: Network structures for raw EIS input (a), and EIS model parameters (b).

The models were designed and trained using Keras (based on TensorFlow) and Scikit-Learn Python libraries. The input parameters were scaled by removing the mean and scaling to unit variance, using the Scikit-Learn StandardScaler function. The output parameters

were scaled to values between 0 and 1, using the Scikit-Learn MinMaxScaler function. Without these scaling methods, the neural networks were unable to estimate the SoC. All neurons have Sigmoid activation functions and optimization was done using the standard stochastic gradient descent (SGD), with the mean squared error (MSE) cost function. Learning rates were varied between 0.001 and 0.1. The dataset was split into training (80%) and validation (20%) sets, and half of the training set was used as a batch size. In addition, L2 regularization was employed, with a factor of 0.0001 for raw EIS input, and 0.00016 for model parameter input to prevent overfitting. Higher and lower regularization factors resulted in increased RMSEs or over-fitting. Network training was performed to a maximum of 10 million epochs. The hyper parameters are summarized in Table 5-1.

Table 5-1 Network Hyper Parameters

Hyper Parameter	Value
Activation Function	Sigmoid
Optimizer	SGD
Cost Function	MSE
Learning Rate	0.001-0.1
Training/Validation Split	20%
Batch Size	½ of Training Set
Regularization	L2
Epochs	10M

5.3 RESULTS AND DISCUSSION

The performance comparison of the two networks is visualized in Figure 5-4 for each measured SoC. All estimates from the neural networks are shown (50 points per SoC), as well as their mean and standard deviation for each SoC. For both networks, some SoC values are estimated more consistently than others. With raw EIS input (Figure 5-4a), the standard deviation is large in the mid SoC range (50-70%), which is where the EIS data

mostly overlaps, making it harder for the neural network to distinguish SoCs. However, for model parameter inputs, the standard deviation is higher for lower SoCs (50-30%). In Table 5-2, performance parameters are summarized for both networks. The RMSE values for the raw EIS input network are similar between training and validation sets suggesting that overfitting is minimal. However, the training and validation RMSE values for the model parameter input network are further apart, suggesting that some overfitting is present. The maximum standard deviation per SoC is slightly higher when using raw EIS inputs, however, it is also more robust.

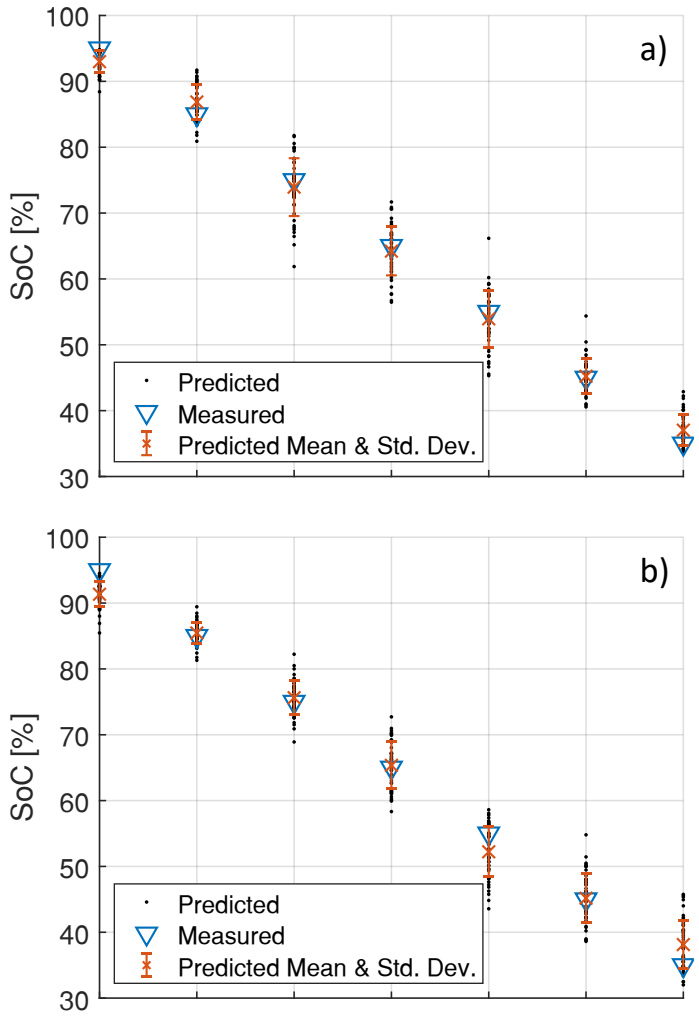

Figure 5-4: RMSE evolution during training epochs for DNN using raw EIS data (a), and DNN using EIS model parameters (b).

Table 5-2: Network Performance

Parameter	Input	
	Raw EIS	Model Param.
Overall RMSE	3.80	3.87
Training RMSE	3.81	3.78
Validation RMSE	3.74	4.22
Max. Std. Dev.	4.39	3.83

Figure 5-5 shows the evolution of the RMSE during training for both types of networks. With raw EIS inputs, the neural network reaches a low RMSE within 1 million epochs.

During the rest of the training time the performance gains are much smaller, but the training and validation RMSE approach the same value. With model parameters as inputs, on the other hand, the network training is slower in general, with over 6 million epochs required before the RMSE stabilizes. The difference between training and validation RMSEs, however, remains significant. The training process for this network is not smooth but shows steps at epoch numbers 2 million and 6 million, which may be a result of the regularization algorithm.

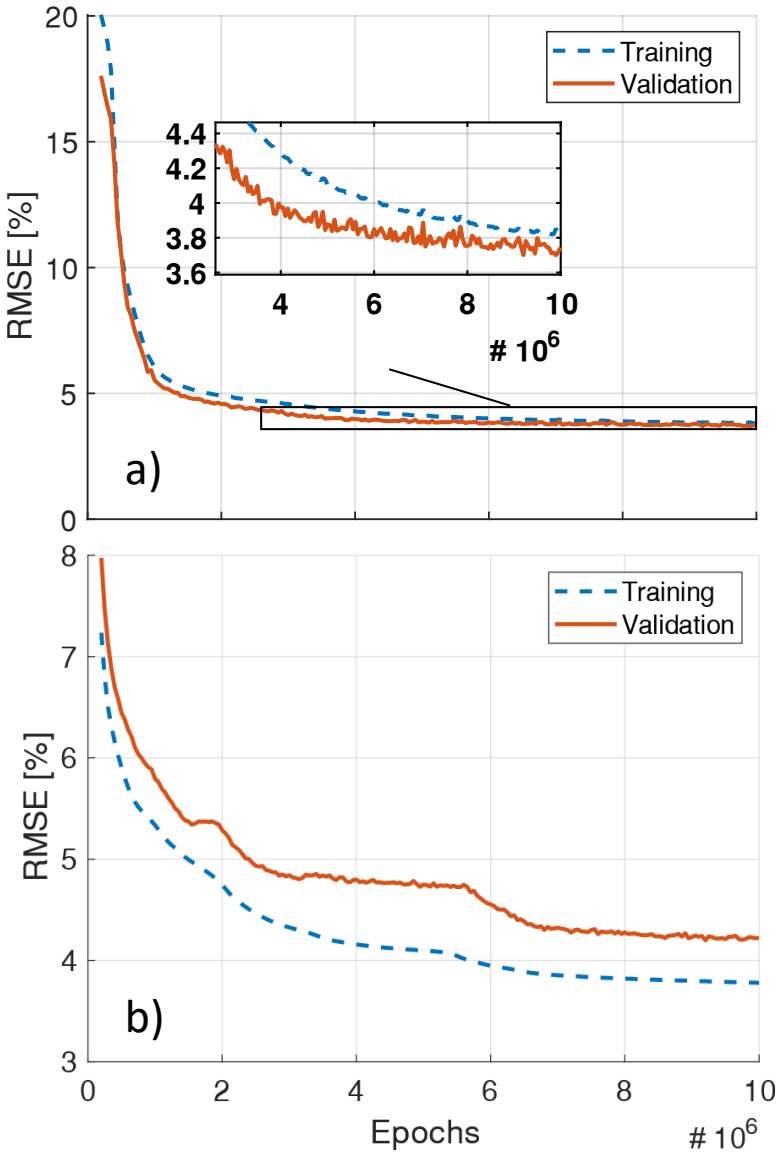

Figure 5-5: RMSE evolution during training epochs for DNN using raw EIS data (a), and DNN using EIS model parameters (b).

To find suitable numbers for hidden layers and nodes per layer for each network, the number of layers and nodes were changed in different directions. Figure 5-6 shows how the RMSE changes for both training and validation values, for the two types of inputs (raw EIS and model parameters) and for different numbers of layers (Figure 5-6a) and different

number of nodes per layer (Figure 5-6b). In each case, the criteria for best performance was the lowest RMSE and the shortest distance between training and validation, favouring the latter over the former. The configurations for number of layers and nodes per layer selected based on this criterion are circled in Figure 5-6. For raw EIS inputs, 3 hidden layers (Figure 5-6a) with 180 nodes each (Figure 5-6b) were selected, since this configuration results in both the lowest RMSE, as well as the shortest distance between training and validation. For battery model inputs, the lowest RMSE occurs at 3 layers for the training set (Figure 5-6a), however, the validation set RMSE is much higher. This indicates that the network over-fits to the training data. The next lowest RMSE occurs with 1 layer, and here, the distance between training and validation is smaller. However, the RMSE for the training set is still lower than the RMSE for the validation set, even at 1 layer, so overfitting was not eliminated. Similarly, the smallest distance between training and validation is found for 70 nodes per layer (Figure 5-6b).

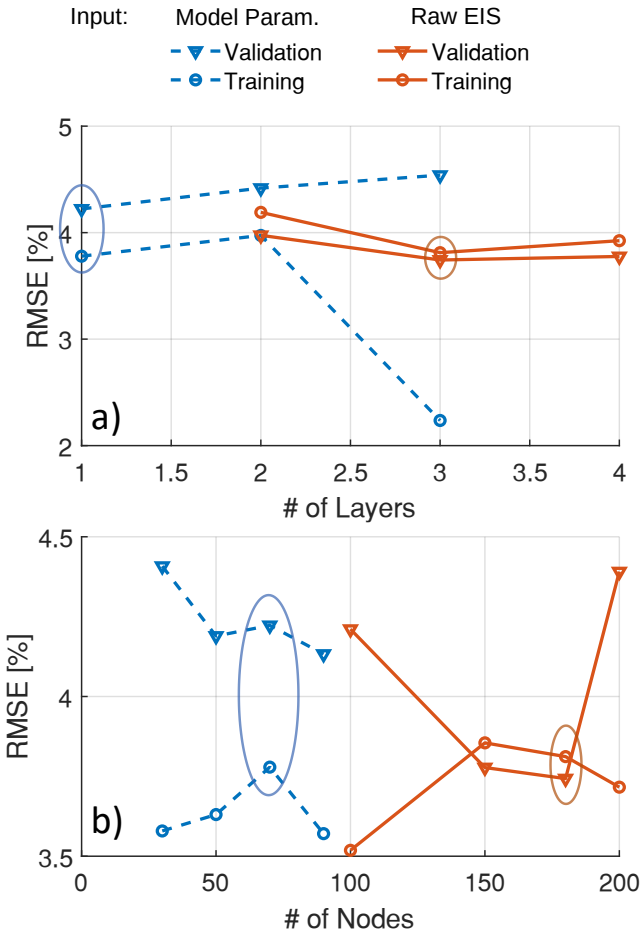

Figure 5-6: RMSE for validation and training for different number of network layers (a), and different number of nodes per layer (b).

The results of this study show that when using simple, feed-forward neural networks, there are no performance gains from using battery model parameters over raw EIS data. The smaller number of input nodes required for model parameters is desirable, however, the modeling process itself can add noise to the data, and as shown in this study, the neural network does not perform significantly better than with all 50 raw EIS values as inputs. Furthermore, all neural network configurations used in this study for model parameter inputs tended to over-fit to the training data. In contrast, using raw EIS as inputs to the

neural networks resulted in RMSE values which were similar for both training and validation sets, as well as lower RMSE values for most SoC values, as shown in Figure 5-7. Figure 5-7 further shows that for SoCs above 30%, all RMSE values are below 5%. At 30% SoC, however, a clear increase in RMSE is seen for both types of inputs.

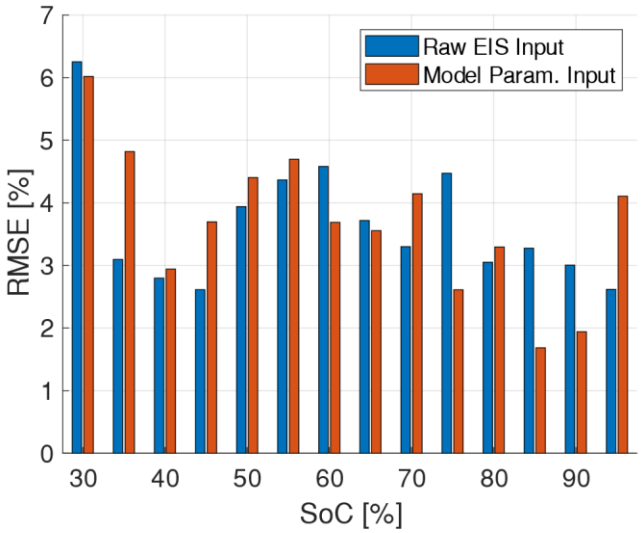

Figure 5-7: RMSE for each SoC.

If EIS measurement capability is available on board EVs or, for smaller battery packs used in portable applications, as part of a charger, SoC may be measured by feeding raw EIS data into a neural network. The purpose of this study was to provide a starting point for this method and show how simple neural networks perform in this task. Various values for number of layers, nodes per layer, regularization and learning rate were investigated, however, an even more systematic approach considering a wider range of values for each parameter may improve performance. In this study, the training-validation split was held constant, however, a k-fold validation approach may provide more information of the robustness of the neural network performance. Finally, the dataset used in this study

included EIS scans taken with rest times ranging from as short as 5 minutes to 3 hours. The difference in EIS results especially at short rest times (Figure 5-1b) creates an additional challenge for the neural network regression. As part of a future study, scans at different rest times should be isolated to investigate the impact of rest times on neural network performance. Shorter rest times are desirable for real time applications; however, any discharge or charge has a significant impact on the EIS measurement during initial rest.

Beyond simple, feed-forward neural networks, more sophisticated network structures are available such as recurrent neural networks (RNN) and convolutional neural networks (CNN). However, using EIS data with these types of neural networks is less straight forward since special formatting of the input data may be required. CNNs are frequently used to find features in images and RNNs have a short-term memory component, neither of which are directly applicable to EIS data. However, strategies to take advantage of RNNs and CNNs will be investigated in future studies.

5.4 CONCLUSION

Neural networks were used in this work to estimate the SoC of Samsung INR21700-50E lithium-ion batteries from EIS scans at different SoH, rest time, and prior discharge pulse depths. The EIS data was used to parameterize a fractional order battery model. Two neural networks were designed, one to use for inputs, the values of the real and imaginary EIS data components, and another to use the battery model parameters as its inputs. Different network structures were evaluated for each case. The ones with lowest RMSE and lowest overfitting were presented. It was found that both cases can provide SoC estimates with

RMSEs of less than 5% for the SoC range of 35% to 95%. However, using battery model parameters as inputs to the neural network still showed some degree of overfitting. Further work is suggested to include more advanced neural network architectures as well as investigate the impact of rest time on the estimation accuracy.

ACKNOWLEDGMENT

This research was conducted under a CREATE grant from the Natural Sciences and Engineering Research Council of Canada.

REFERENCES

[1] R. Xiong, J. Cao, Q. Yu, H. He, and F. Sun, "Critical Review on the Battery State of Charge Estimation Methods for Electric Vehicles," IEEE Access, vol. 6, pp. 1832–1843, 2018.

[2] L. Ungurean, G. Cârstoiu, M. V Micea, and V. Groza, "Battery state of health estimation : a structured review of models , methods and commercial devices," no. July 2016, pp. 151–181, 2017.

[3] A. Farmann and D. U. Sauer, "Comparative study of reduced order equivalent circuit models for on-board state-of-available-power prediction of lithium-ion batteries in electric vehicles," Appl. Energy, vol. 225, no. May, pp. 1102–1122, 2018.

[4] M. U. Cuma and T. Koroglu, "A comprehensive review on estimation strategies used in hybrid and battery electric vehicles," Renew. Sustain. Energy Rev., vol. 42, pp. 517–531, 2015.

[5] M. A. Hannan, M. S. H. Lipu, A. Hussain, and A. Mohamed, "A review of lithium-ion battery state of charge estimation and management system in electric vehicle applications: Challenges and recommendations," Renew. Sustain. Energy Rev., vol. 78, no. August 2016, pp. 834–854, 2017.

[6] Y. Bar-Shalom, X.-R. Li, and T. Kirubarajan, Estimation with Applications to Tracking and Navigation, vol. 9. 2001.

[7] H. H. Afshari, S. A. Gadsden, and S. Habibi, "Gaussian fi lters for parameter and state estimation : A general review of theory and recent trends," Signal Processing, vol. 135, no. March 2016, pp. 218–238, 2017.

[8] R. Ahmed, M. El Sayed, I. Arasaratnam, Jimi Tjong, and S. Habibi, "Reduced-Order Electrochemical Model Parameters Identification and SOC Estimation for Healthy and Aged Li-Ion Batteries Part I: Parameterization Model Development for Healthy Batteries," IEEE J. Emerg. Sel. Top. Power Electron., vol. 2, no. 3, pp. 659–677, 2014.

[9] A. Maheshwari, M. Heck, and M. Santarelli, "Cycle aging studies of lithium nickel manganese cobalt oxide-based batteries using electrochemical impedance spectroscopy," Electrochim. Acta, vol. 273, pp. 335–348, 2018.

[10] X. Zhu et al., “Electrochemical impedance study of commercial LiNi0.80Co0.15Al0.05O2electrodes as a function of state of charge and aging,” Electrochim. Acta, vol. 287, pp. 10–20, 2018.
[11] A. Lasia, Electrochemical Impedance Spectroscopy EIS, and Corrosion. 2011.
[12] E. Din, C. Schaef, K. Moffat, and J. T. Stauth, “A scalable active battery management system with embedded real-time electrochemical impedance spectroscopy,” IEEE Trans. Power Electron., vol. 32, no. 7, pp. 5688–5698, 2017.
[13] X. Wei, X. Wang, and H. Dai, “Practical on-board measurement of lithium ion battery impedance based on distributed voltage and current sampling,” Energies, vol. 11, no. 1, 2018.
[14] H. Piret, P. Granjon, N. Guillet, and V. Cattin, “Tracking of electrochemical impedance of batteries,” J. Power Sources, vol. 312, pp. 60–69, 2016.
[15] U. Westerhoff, T. Kroker, K. Kurbach, and M. Kurrat, “Electrochemical impedance spectroscopy based estimation of the state of charge of lithium-ion batteries,” J. Energy Storage, vol. 8, pp. 244–256, 2016.
[16] Y. Zhang, Q. Tang, Y. Zhang, J. Wang, U. Stimming, and A. A. Lee, “Identifying degradation patterns of lithium ion batteries from impedance spectroscopy using machine learning,” Nat. Commun., vol. 11, no. 1, 2020.
[17] Z. Xia and J. A. Abu Qahouq, “Adaptive and fast state of health estimation method for lithium-ion batteries using online complex impedance and artificial neural network,” Conf. Proc. - IEEE Appl. Power Electron. Conf. Expo. - APEC, vol. 2019-March, pp. 3361–3365, 2019.
[18] M. Nielson, Neural Networks and Deep Learning. Determination Press, 2015.
[19] M. Messing, T. Shoa, and S. Habibi, “Lithium-Ion Battery Relaxation Effects,” 2019 IEEE Transp. Electrif. Conf. Expo, pp. 1–6, Jun. 2019.

Chapter 6: Low Temperature, Current Dependant Battery State Estimation using Interacting Multiple Model Strategy

Marvin Messing[1,2], Sara Rahimifard[1], Tina Shoa[2], Saeid Habibi[1]

[1]Department of Mechanical Engineering, McMaster University, Hamilton, ON, Canada,

[2]Cadex Electronics, Richmond, BC, Canada

This paper is published in IEEE Access, 2021, doi: 10.1109/ACCESS.2021.3095938. This paper is republished here with permission.

ABSTRACT

Lithium-ion battery State of Charge (SoC) estimation for Electric Vehicle (EV) applications must be robust and as accurate as possible to maximize battery utilization and ensure safe operation over a wide range of operating conditions. SoC estimation commonly utilizes filters such as the Extended Kalman Filter (EKF) which rely on battery models, usually in the form of Equivalent Circuit Models (ECM). At low temperatures the battery response to current draw becomes increasingly non-linear, resulting in amplified SoC estimation errors. In this study, current dependent SoC estimation at low temperature is proposed using an Interacting Multiple Model (IMM) filter with three ECMs covering a range of C-rates. The IMM is combined with the Smooth Variable Structure Filter (SVSF) to obtain robust SoC estimates within a SoC estimation error of 2%.

6.1 INTRODUCTION

In this paper an improved low temperature State of Charge (SoC) estimation strategy is proposed. Reduced SoC estimation errors are achieved by using different battery models optimized for different drive cycle discharge current magnitudes (or C-rates). Three

Equivalent Circuit Models (ECM) are parameterized to cover low, medium, and high C-rate drive cycles. The Interacting Multiple Model (IMM) filter is combined with the ECMs and the Smooth Variable Structure (SVSF) filter to estimate SoC at low temperature. The performance of the proposed estimation strategy is evaluated for lithium-ion cells at 100% and 90% State of Health (SoH). Furthermore, the IMM-SVSF strategy is compared to the conventional EKF in place of the SVSF (i.e. IMM-EKF). The remainder of this section discusses the motivation and technical challenges, presents a review of relevant literature, and provides the main contributions as well as an outline of the paper.

6.1.1 Motivation and Technical Challenges

Electric Vehicles (EV) depend on Battery Management Systems (BMS) to ensure optimal operation of the battery pack. One of the most important tasks of a BMS is the estimation of several battery states, including SoC, State of Power (SoP), and SoH. A large selection of methods exists for battery state estimation across a wide range of operating conditions [1]. For low temperature operation, special care must be taken to ensure sufficient state estimation accuracy. The behavior of the battery changes considerably at low temperatures [2] and to account for that, model parameters are adjusted for different temperatures. Huo et al. [3] developed a temperature dependent 2nd order ECM and used it to improve SoC estimation using an EKF. Guo et al. [4] combined a temperature adjusted 2nd order ECM with a dual extended Kalman filter and showed that their method greatly improves SoC estimation compared to an EKF without temperature compensation. Xiong et al. [5] used a temperature dependent battery model and a membership theory based estimation algorithm

to estimate SoC within 5% down to -40°C. Furthermore, they show that even with temperature compensation, the average estimation errors increase as temperature decreases. Yang et al. [6] used a temperature compensated model with the EKF with an estimation error within 3% for temperatures as low as 0°C. Zhu et al. [7] proposed a temperature, SoC and current compensated electro-thermal battery model and showed reduced voltage errors down to -20°C. Shen et al. [8] used a Square Root Cubature Kalman Filter (SRCKF) with a temperature compensated, 2nd order ECM and showed improved SoC estimation accuracy between -20°C and 60°C for medium C-rate drive cycles. At low temperature, the battery response becomes increasingly non-linear with C-rate, creating additional modeling errors. Kollmeyer et al. [9] compared different models and different parameterization methods for various drive cycles and temperatures and showed the increased impact of C-rate at low temperatures on battery model parameters. The battery models can be improved to include current-dependent mode parameters; however, this creates additional challenges with filter-based state estimation methods. Temperature dependent model parameters (much like SoC dependent parameters) are compatible with state estimation filters such as the EKF. This is because temperature and SoC are low frequency signals, changing at a slow rate and mostly in one direction. However, drive cycle currents for EV applications are high frequency signals, able to rapidly change magnitude and direction from one second to the next. This means that current dependent battery models could exhibit parameter updates from one filter sample to the next, creating a system which is no-longer observable. Observability is a requirement for filters such as the EKF to produce robust estimates [10], [11]. Therefore, current dependent battery models are not feasible for use with EKF and similar filters. In

this paper, the IMM is used to circumvent this limitation while maintaining observability and robust state estimates. Relevant literature on the usage of the IMM for battery state estimation is reviewed next.

6.1.2 Interacting Multiple Model Filter

When the uncertainty of a single model used with an EKF or similar filter is high, the estimation error will also be high [12]. In such cases, estimation can be improved by combining information from several models into one filter. This can be useful if the system model is uncertain, but will be close to within a range of different models or their blended combination. A static multi-model algorithm can then pick the most suitable one to use for the given inputs. A dynamic multi-model algorithm can be used if the system model changes during the estimation process. However, in the dynamic case, an optimal estimator is not computationally feasible [10]. Instead, a sub-optimal algorithm such as the IMM derived by Blom et al. [13] can be used. The IMM is used in many practical applications such as air traffic tracking, autonomous vehicle tracking and missile tracking, and new applications are still being explored [14]–[16]. For battery applications, the IMM has been used to allow for multiple battery models to be considered simultaneously as part of state estimation algorithms. Smiley et al. [17] used the IMM with EKF to select from 21 physics-based, reduced order battery models each representing different battery aging states. In [18] the same group introduced a post processing method to improve the predictions obtained from the IMM by analyzing the probability mass function. Su et al. [19] considered three different aging models, a polynomial, an exponential, and a Verhulst model, and used the

IMM to combine the models for an improved prediction of the Remaining Useful Life (RUL) of the battery. In this paper, the IMM is used to improve SoC estimation at low temperatures by switching between three different models, which are parameterized for different C-rate regions.

6.1.3 SMOOTH VARIABLE STRUCTURE FILTER

The SVSF approach is a predictor-corrector method first presented in [20]. The SVSF is based on sliding mode control (SMC) which uses a discontinuous gain and a smoothing boundary layer. The stability and robustness of the SVSF method has been illustrated against uncertainties and noise in relation to the filter model. The SVSF was later improved with several advancements, including the covariance formulation, time-varying smoothing boundary layer (SVSF-VBL) and combinations with different filters such as KF, EKF, UKF, Particle filter (PF) and more [21]–[23]. The SVSF-VBL approach provides more accuracy in the presence of noise and model uncertainties [24]. However, observability of the system needs to be guaranteed in use of these algorithms. Gadsden et al. [25] compared the SVSF to EKF and other filters for a target tracking problem and showed superior performance of the SVSF especially in the presence of modeling errors. In a similar study, Gadsden et al. [26] showed improved state and parameter estimation performance using the SVSF for a hybrid EV application. In another study, Gadsden et al. [27] used the SVSF with an IMM and compared the IMM-SVSF to the IMM-EKF for an air traffic control problem. They found a significant improvement of the IMM-SVSF over the IMM-EKF.

This paper compares SVSF and EKF in terms of accuracy and robustness and their performance as part of the IMM for low temperature battery SoC estimation.

6.1.4 CONTRIBUTIONS

In this work the IMM is used with the SVSF to reduce SoC estimation errors at low temperatures by considering different battery models for different C-rates. This paper includes the following contributions: 1) multiple models are used to reduce SoC estimation errors at low temperatures using the IMM with C-rate specific models, and 2) the IMM-SVSF is demonstrated to have higher SoC estimation accuracy compared to the IMM-EKF.

6.1.5 PAPER OUTLINE

The remainder of this paper is organized as follows. Section 6.2 contains background theory on the battery model, EKF, SVSF, IMM, as well as vehicle modeling to obtain drive cycles. In Section 6.3 the datasets used to parameterise and validate the proposed estimation method are introduced. Section 6.4 presents the results and discusses the performance of the IMM-SVSF compared to IMM-EKF and single model IMM and SVSF filters at low temperatures. Concluding remarks are provided in Section 6.5.

6.2 THEORY

This section first defines the equivalent circuit model used in this study, followed by descriptions of the EKF and SVSF SoC estimation algorithms. Finally, the IMM algorithm is introduced.

6.2.1 BATTERY MODELING & PARAMETERIZATION

The battery model used in this study as part of the SoC estimation methods is shown in Figure 6-1. This 3rd order ECM is a common choice for SoC estimation algorithms. A resistor R_0 is used to model the internal resistance of the battery and three RC-pairs are used to model the time dependent, transient response of the battery caused by charge transfer and diffusion reactions [28]. The resistances R_j and capacitances C_j are for the jth element of the circuit with elements from 1 to 3. The ECM can be used together with the OCV-SoC relationships of the battery to obtain terminal voltage using (6-1), (6-2), (6-3), and (6-4) given an SoC and a cell current demand u_k.

$$\hat{z}_{k+1} = OCV(x_{k,k+1}) - R_0 u_k - \sum_{j=1}^{n} v_{j,k+1} \tag{6-1}$$

$$v_{j,k+1} = v_{j,k}\left(1 - \frac{\Delta t}{\tau_j}\right) + \frac{\Delta t}{C_j} u_k \tag{6-2}$$

$$\tau_j = R_j C_j \tag{6-3}$$

$$x_{k+1} = x_k + \frac{\Delta t}{C_r} u_k \tag{6-4}$$

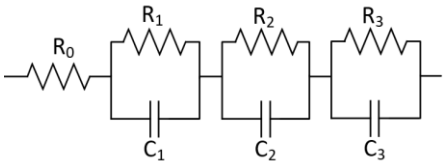

Figure 6-1: 3rd order battery equivalent circuit model.

Here, n is the order of the ECM (in this case $n = 3$), Δt is the time between steps k and $k + 1$ (sample rate), $v_{j,k}$ is the voltage drop across RC branch j at time k and τ_j is the time constant associated with branch j. Finally, x_k is the SoC of the battery at time k and (4) is the coulomb counting equation used to calculate the gain or loss of SoC given u_k and Δt. Finally, C_r (in Amp-seconds) is the rated capacity of the cell. The OCV-SoC relationship, OCV(x_k) can be used in the form of a lookup table obtained from experimental data. Figure

6-2 shows two OCV-SoC datasets used in this study, one at 25°C used for baseline ECMs, and a second at 0°C used for low temperature ECMs. The lower temperature OCV-SoC curve shows slightly lower OCV throughout the operating range of the cell.

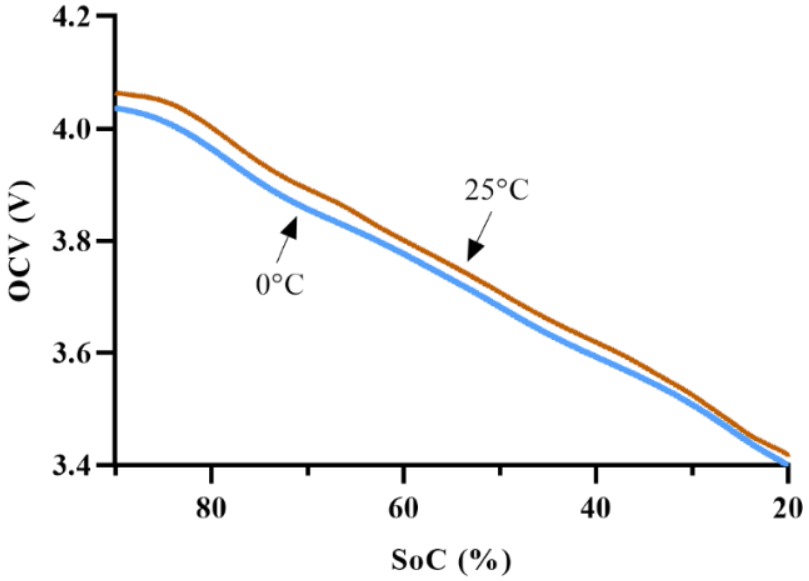

Figure 6-2: OCV-SoC Curve for different temperatures.

The ECM is used with different model parameter sets to match the behavior of batteries at different temperatures and SoH. The parameters are found using the Simulink Parameter Estimator with the Non-linear Least Squares method and the Trust-Region-Reflective algorithm. The sum of squared errors was used as a cost function.

6.2.2 Extended Kalman Filter

In this section, the EKF equations are presented. The EKF is widely used for battery state estimation and, therefore, considered in this work as a baseline for comparison to the proposed implementation of the IMM-SVSF SoC estimation strategy. The EKF estimates

the state vector $\hat{x}$ using non-linear system and measurement equations as shown in (6-5) and (6-6), respectively.

$$\hat{x}_{k+1} = f(\hat{x}_k, u_k, w_k) \tag{6-5}$$

$$\hat{z}_k = h(\hat{x}_k, u_k, v_k) \tag{6-6}$$

where u_k is the input to the system, w_k is the system noise, v_k is the measurement noise, and $\hat{z}_k$ is the measurement prediction. The battery model described in Section 6.2.1. can be rearranged into matrix form to be used with the EKF as shown in (6-7).

$$\hat{x}_{k,k} = \begin{bmatrix} v_{1,k} \\ v_{2,k} \\ v_{3,k} \\ x_k \end{bmatrix}, F = \begin{bmatrix} 1-\frac{\Delta t}{C_1} & 0 & 0 & 0 \\ 0 & 1-\frac{\Delta t}{C_2} & 0 & 0 \\ 0 & 0 & 1-\frac{\Delta t}{C_2} & 0 \\ 0 & 0 & 0 & 1 \end{bmatrix}, \; G = \begin{bmatrix} \frac{\Delta t}{C_1} \\ \frac{\Delta t}{C_2} \\ \frac{\Delta t}{C_3} \\ -\frac{\Delta t}{C_r} \end{bmatrix}, H = \begin{bmatrix} -1 \\ -1 \\ -1 \\ \frac{dOCV(\hat{x}_{k,k+1})}{dx} \end{bmatrix} \tag{6-7}$$

The matrices F and G make up the parts of (6-2) as well as (6-4) to produce the state vector $\hat{x}_{k,k}$ at filter step k. The state vector contains the three branch voltages as well as the SoC estimate x_k. The matrix H is the Jacobian derived from (6-1).

A single cycle of the EKF algorithm consists of prediction, correction and update steps defined as follows:

- Prediction: Equation 6-8 is the state equation of the EKF producing the a-priori state estimate $\hat{x}_{k,k+1}$, where the a-priori is indicated by incrementing the second subscript k. Equation 6-9 is the covariance corresponding the a-priori state estimate. Equation 6-11 represents the error ν between the measured voltage z_k and the voltage estimate $\hat{z}_k$.

$$\hat{x}_{k,k+1} = F x_{k,k} + G u_k \tag{6-8}$$

$$P_{k,k+1} = F P_{k,k} F' + Q \tag{6-9}$$

$$\hat{z}_{k|k+1} = H \hat{x}_{k|k+1} \tag{6-10}$$

$$\nu_{k,k+1} = z_{k+1} - \hat{z}_{k,k+1} \tag{6-11}$$

- Correction: In (6-12), the innovation covariance S is calculated given the measurement noise covariance R and used in (6-13) to calculate the EKF gain W:

$$S = R + HP_{k,k+1}H' \tag{6-12}$$

$$W = P_{k,k+1}H'S^{-1} \tag{6-13}$$

- Update: Finally, the gain is used in (6-14) and (6-15) to calculate the a-posteriori state vector $\hat{x}_{k+1,k+1}$ and state covariance $P_{k+1,k+1}$ respectively. Here, I is the identity matrix.

$$\hat{x}_{k+1,k+1} = x_{k,k+1} + W\nu_{k+1} \tag{6-14}$$

$$P_{k+1,k+1} = (I - WH)P_{k,k+1} \tag{6-15}$$

$$\nu_{k+1,k+1} = z_{k+1} - \hat{z}_{k+1,k+1} \tag{6-16}$$

6.2.3 Smooth Variable Structure Filter

This section provides the SVSF algorithm which is applicable to any observable and differentiable system. The SVSF employs a smoothing boundary layer $\boldsymbol{\psi}$ and a discontinuous gain. The SVSF gain forces the states to converge to a neighborhood of the true value. This paper employs the SVSF with a time-varying smoothing boundary layer (SVSF-VBL) to enhance estimation accuracy [24]. The width of the boundary layer depends on the uncertainty of the filter model, as well as the system and measurement noise. The SVSF-VBL algorithm uses a time-varying boundary layer with saturated limits to guarantee stability and estimation convergence [21]. The SVSF-VBL has the same prediction and update steps as the EKF but a different correction step:

- Correction: In (6-17) the combination of measurement errors $\boldsymbol{E_{k+1}}$ is calculated given the SVSF convergence parameter $\boldsymbol{\gamma}$. Equation (6-18) calculates the SVSF smoothing boundary layer width $\boldsymbol{\psi}$. The SVSF gain is shown in (6-19), given a tuning parameter $\boldsymbol{\psi_{lim}}$.

$$E = |\nu_{k,k+1}| + \gamma|\nu_k| \tag{6-17}$$

$$\psi = (E^{-1}H'S'_{k+1})^{-1} \tag{6-18}$$

$$W = \begin{cases} H^{-1}E\, sat(\nu_k\psi^{-1})\, \nu_{k,k+1}^{-1}, & \psi \geq \psi_{lim} \\ H^{-1}E\psi^{-1} & , \ \psi < \psi_{lim} \end{cases} \tag{6-19}$$

6.2.4 INTERACTING MULTIPLE MODEL FILTERS

The IMM allows several estimation filters to run in parallel, each using a different model. The estimates from each of the filters are then blended together using mixing probabilities obtained based on the filters' error covariance matrices. The main function of the IMM is to compute mixing probabilities, which determine how much weight is assigned to each filter estimate. The IMM must be initialized with a mode probability vector $\boldsymbol{\mu_k}$ and a mode transition probability matrix $\boldsymbol{p}$. For the $\boldsymbol{r = 3}$ filters used in this work, the initialization is shown in (6-20).

$$\mu = \begin{bmatrix} \mu_{k,1} \\ \mu_{k,2} \\ \mu_{k,3} \end{bmatrix}, p = \begin{bmatrix} p_{11} & \cdots & p_{13} \\ \vdots & \ddots & \vdots \\ p_{31} & \cdots & p_{33} \end{bmatrix} \tag{6-20}$$

The mode probabilities indicate the probability of each filter (or mode) using the correct model at each time step $\boldsymbol{k}$. The elements $\boldsymbol{i,j}$ of the mixing probability matrix $\boldsymbol{\mu_{k,k}}$ are calculated using (6-21), where $\boldsymbol{\bar{c}_j}$ is calculated using (6-22).

$$\mu_{k,k,ij} = \frac{p_{ij}}{\bar{c}_j}\mu_{k,i} \qquad i,j = 1,\dots,r \tag{6-21}$$

$$\bar{c}_j = \sum_{i=1}^{r} p_{ij}\mu_{k,j} \qquad j = 1,\dots,r \tag{6-22}$$

The mixing probability matrix is then used in (6-23) and (6-24) to calculate new state estimates $\tilde{x}_j$ and new state covariances P_j for each of the r filters, using the last filter output $\hat{x}_{k+1,k+1}$ and $P_{k+1,k+1}$. Here, $A_{x,i} = (\hat{x}_{k+1,k+1,i} - \tilde{x}_j)$. The new $\tilde{x}_j$ and P_j are then used for blending of the estimates and as new starting parameters for the next filter steps.

$$\tilde{x}_j = \sum_{i=1}^{r} \mu_{k,k,ij}\, \hat{x}_{k+1,k+1,i} \qquad j = 1,\dots,r \tag{6-23}$$

$$P_j = \sum_{i=1}^{r} \mu_{kk,ij}(P_{k+1,k+1,i} + A_{x,i}A_{x,i}') \quad j = 1, \dots, r \tag{6-24}$$

The remaining steps of the IMM are used to calculate the mixing probabilities for the next iteration, given the voltage estimate $\hat{\boldsymbol{z}}_{\boldsymbol{k,j}}$ and associated innovation covariance $\boldsymbol{S_j}$ from the filters. This is done by first computing the likelihood $\boldsymbol{\Lambda_j}$ using the gaussian probability density function (PDF) $\boldsymbol{N(x, \mu, \sigma)}$ as shown in (6-25).

$$\Lambda_j = N(z_k, \hat{z}_{k,j}, S_j) \tag{6-25}$$

The likelihood is then used together with $\bar{\boldsymbol{c}}_{\boldsymbol{j}}$ from (6-22) and $\boldsymbol{c}$ from (6-27) to update the mode probabilities $\boldsymbol{\mu_{k+1,j}}$ in (6-26).

$$\mu_{k+1,j} = \frac{\bar{c}_j}{c}\Lambda_j \ , j = 1, \dots, r \tag{6-26}$$

$$c = \sum_{j=1}^{r} \Lambda_j \bar{c}_j \tag{6-27}$$

Finally, the IMM state vector $\hat{\boldsymbol{x}}_{\boldsymbol{k+1,k+1}}$ and associated covariance $\boldsymbol{P_{k+1,k+1}}$ can be computed using (28) and (29), where $\boldsymbol{B_{x,j}} = [\hat{\boldsymbol{x}}_{\boldsymbol{k+1,k+1,j}} - \hat{\boldsymbol{x}}_{\boldsymbol{k+1,k+1}}]$.

$$\hat{x}_{k+1,k+1} = \sum_{j=1}^{r} \mu_{k+1,j}\, \hat{x}_{k+1,k+1,j} \tag{6-28}$$

$$P_{k+1,k+1} = \sum_{j=1}^{r} \mu_{k+1,j}\, (P_{k,j} + B_{x,j}B'_{x,j}) \tag{6-29}$$

Figure 6-3 shows an overview of the IMM algorithm. The algorithm starts at the "IMM mixing probabilities" block to compute the mixing probabilities given initial values from (20). The mixing probabilities are used in the next block ("IMM mixing") together with the initial state vectors and state covariances of each of the filters ($r = 3$) used in this diagram to compute updated state vectors and covariances as shown in (6-23). The updated states are then used to initialize regular filters, such as the EKF or the SVSF. At this point, the IMM estimate can also be computed in the "IMM Estimate" block with (6-28) and (6-29). The output voltage estimates and measurement covariances of each of the filters are sent to the "IMM likelihood" block to compute likelihoods using the measured voltage and (6-25).

The state estimates and state covariances are sent to the "IMM mixing" block to be used in the next iteration instead of the initial values used for the first iteration. Finally, the mode probabilities are updated in the "IMM update" block with (6-26) and used in the "IMM mixing probabilities" block for the start of the next iteration instead of the initial mode probabilities used in the first iteration. In Figure 6-3 only three filters are shown, but additional filters can be used.

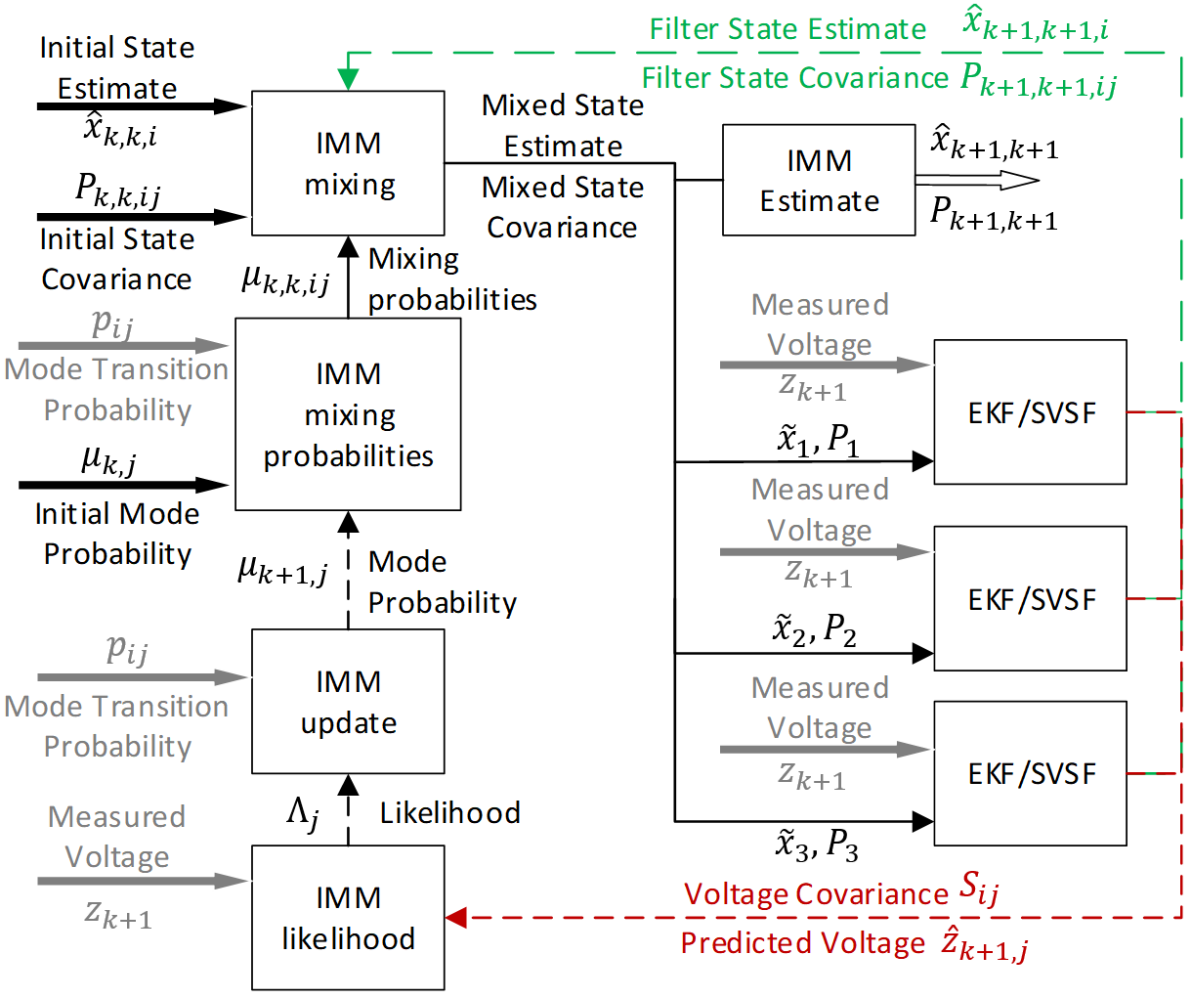

Figure 6-3: IMM Algorithm Diagram.

6.2.5 VEHICLE MODELING

The IMM-EKF or IMM-SVSF SoC estimation filters allow multiple battery models to run in parallel to achieve an overall improved SoC estimate. In this study, the IMM filters are used to improve SoC estimation at low temperatures where the three different battery models are optimized for different C-rates. First, the battery models must be parameterized with datasets that represent different C-rate ranges as well as the dynamic voltage response specific to a given application. This study is intended for EV applications; therefore, automotive drive cycles are used to obtain parameterization datasets. Automotive drive cycles as provided by the US Environmental Protection Agency (EPA) consist of representative sections of vehicle speed vs. time data for different driving conditions. This drive cycle data can be used to simulate battery load demand for a given vehicle by calculating the power required to overcome rolling resistance, aerodynamic drag, and in some situations, gravity to achieve the speed of the drive cycle [78]. In (6-30), the power required to accelerate the mass of the vehicle $\boldsymbol{P_{acc}}$ is calculated using the desired speed $\boldsymbol{V}$ from the drive cycle, the mass of the car $\boldsymbol{m_{car}}$ and acceleration given by $\boldsymbol{a = dV/dt}$.

$$P_{acc} = m_{car}\, a\, V \tag{6-30}$$

Given the air density ρ_{air}, the frontal area of the vehicle A_{front} and the drag coefficient of the vehicle C_D, (6-31) can be used to calculate the power required to overcome drag, P_{drag}.

$$P_{drag} = \frac{1}{2}\, \rho_{air}\, A_{front}\, C_D\, V^3 \tag{6-31}$$

Under the assumption that the vehicle is driven on a flat road (i.e. without inclines of declines), (6-32) calculates the power $P_{roll,flat}$ to overcome rolling resistance, given

acceleration due to gravity g=9.81$m\backslash s^2$. The constants C_{ra}, C_{rb}, and C_h describe the conditions of the road surface.

$$P_{roll,flat} = (C_{ra} + C_{rb}\,V)\;C_h\,m_{car}\,g \tag{6-32}$$

To achieve the given drive cycle speeds, the battery must at least provide enough power to overcome $P_{tot} = P_{acc} + P_{drag} + P_{roll,flat}$. However, additional power is lost due to non-ideal battery efficiency η_{batt} and losses associated with the drivetrain efficiency η_{dr}. Furthermore, parasitic power P_{aux} is required to run the auxiliary systems of the car, such as lights, air-conditioning, radio, etc. The total power required by the battery pack is then given by (6-33).

$$P_{batt} = [(P_{tot}/\eta_{dr}) + P_{aux}]/\eta_{batt} \tag{6-33}$$

Since current is usually easier to control in laboratory equipment than power, the power can be converted into battery pack current. As this is a simple model, a fixed nominal voltage $E_{cell,nom}$ is assumed. The total voltage of the pack can be calculated given the number of cells in series N_{series}. Dividing P_{batt} by the total pack voltage and the number of cells in parallel $N_{parallel}$ yields the battery cell current I_{cell} as shown in (6-34).

$$I_{cell} = [P_{batt}/(N_{series}\,E_{cell,nom})]/N_{parallel} \tag{6-34}$$

The battery cells used in this study are similar to those used by the Tesla Model 3 Long range EV. The simple vehicle model described above can be used to approximate the behavior of a Tesla Model 3 by using the parameters as well as assumed efficiencies shown in Table 6-1. The efficiency of the battery pack and the drive train depend on many factors and conditions, but for this simple vehicle model, constant, conservative numbers are assumed [30]. The original Tesla Model 3 battery pack configuration was scaled by

reducing the number of modules in parallel to achieve slightly higher currents to cover a C-rate range between 0 and 4C across different drive cycles.

Table 6-1: Simple Vehicle Model Parameters [29], [34], [35]

Name	Symbol	Value
Mass of the vehicle.	m_{car}	1730 kg
Rolling resistance calculation factor.	C_{ra}	0.0041
Rolling resistance calculation factor.	C_{rb}	0.000018
Rolling resistance calculation factor.	C_h	1.5
Density of air.	ρ_{air}	1.2
Vehicle frontal area.	A_{front}	3.25 m^2
Vehicle drag coefficient.	C_d	0.23
Vehicle auxiliary power draw.	P_{aux}	350 W
Drivetrain efficiency.	η_{dr}	0.765
Battery efficiency.	η_{batt}	0.95
Number of modules in parallel.	$N_{parallel,scaled}$	18
Number of series cells per module.	N_{series}	96
Nominal battery cell voltage.	$E_{cell,nom}$	3.6 V

Figure 6-4 shows three drive cycle speed profiles and the corresponding current profiles obtained with the simple vehicle model described above. Figure 6-4a shows the US Urban Dynamometer Driving Schedule (UDDS) from which two low C-rate sections were selected to parameterize the low C-rate model. Similarly, Figure 6-4b shows the aggressive driving schedule called US06 from which two medium C-rate and two high C-rate sections were chosen to parameterize the medium C-rate and high C-rate models, respectively. This was done to achieve significant differences in model parameters for the three models, which enables the IMM to identify the correct model more clearly. In each case, only discharge currents were considered to simplify the model used for this study. The model can be extended to include components to handle charge currents following methods described in [31]. Figure 6-4c shows a drive cycle mix used for validation consisting of the unified

driving schedule called LA92 and the UDDS. In the next section, the drive cycle samples and the validation cycle are used in experiments to obtain voltage profiles from battery cells. These voltage profiles are later used to parameterize the three C-rate specific models as well as to benchmark the proposed IMM based estimation strategy.

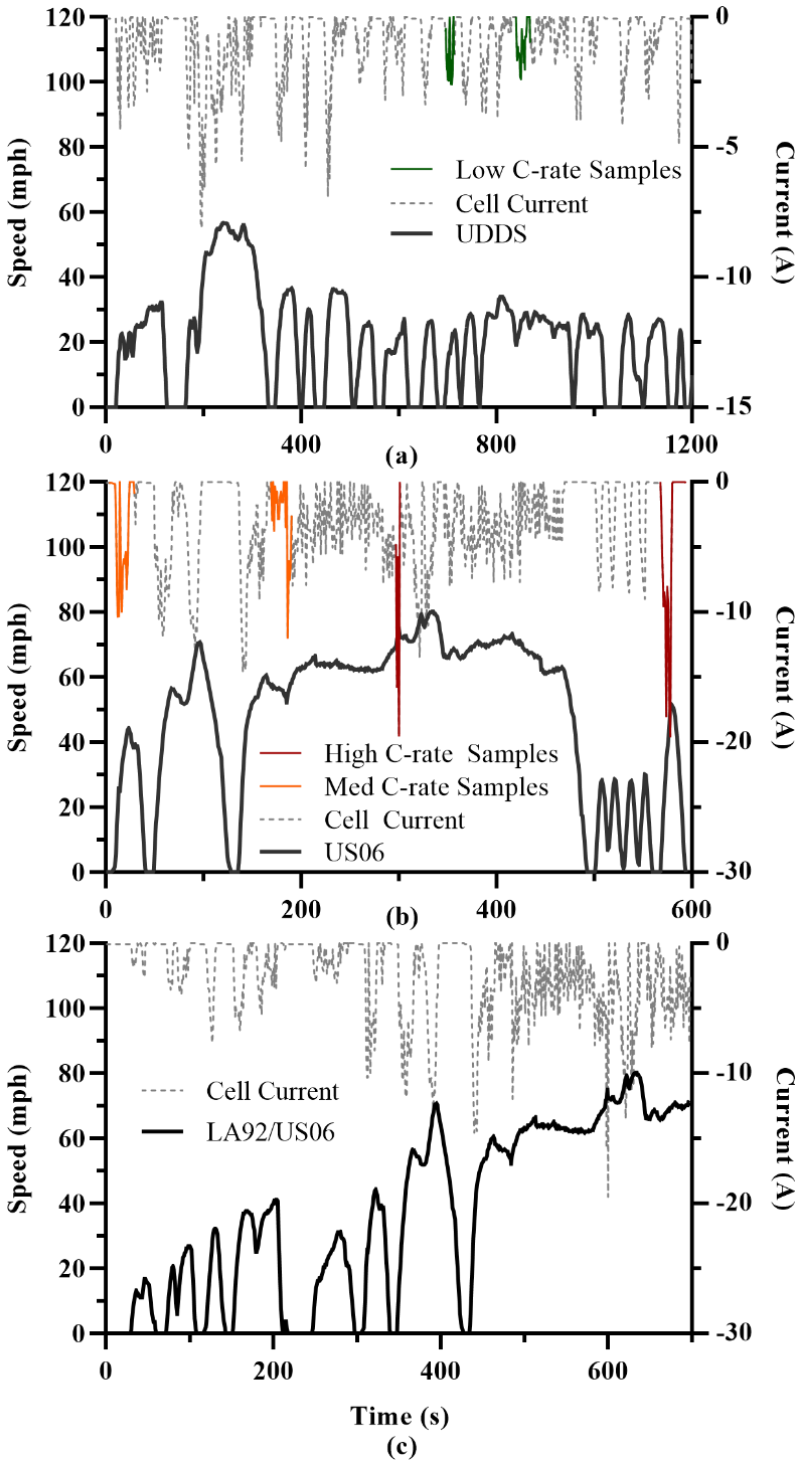

Figure 6-4: Current profile samples from EPA drive cycles for low C-rates (a) medium and high C-rates (b). Validation drive cycle current profile (c).

6.3 LOW TEMPERATURE DRIVE CYCLE TESTING

This section describes the experiments and experimental setup used to obtain the parameterization and validation drive cycle datasets from Samsung INR2170-50e lithium-ion battery cells. The resulting datasets are also shown in this section.

6.3.1 EXPERIMENTS AND EXPERIMENTAL SETUP

The data used to parameterize the battery models and to validate the algorithms was obtained using a custom designed battery tester. The main components of the tester are shown in Figure 6-5a. The setup includes an Agilent load and power supply to discharge and charge the battery cells as well as to implement the drive cycle load demand profiles. An NI9219 Data Acquisition (DAQ) unit was used to measure the cell voltage via a custom Kelvin connection. The DAQ also measures battery cell temperature as well as cell current via the voltage drop across a shunt resistor. The battery cells were housed in a thermal chamber for controlled environmental conditions and to simulate low temperature conditions. The entire system was controlled and automated by custom software written in the Python programming language. Figure 6-5b shows a picture of the setup in the lab as well as a screen capture of the custom control software. A custom designed 4-point measurement battery holder is also shown in magnified form since the cells cannot be seen through the thermal chamber window otherwise.

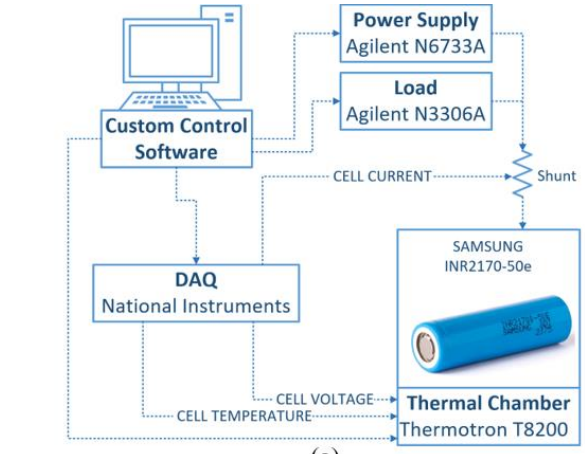

(a)

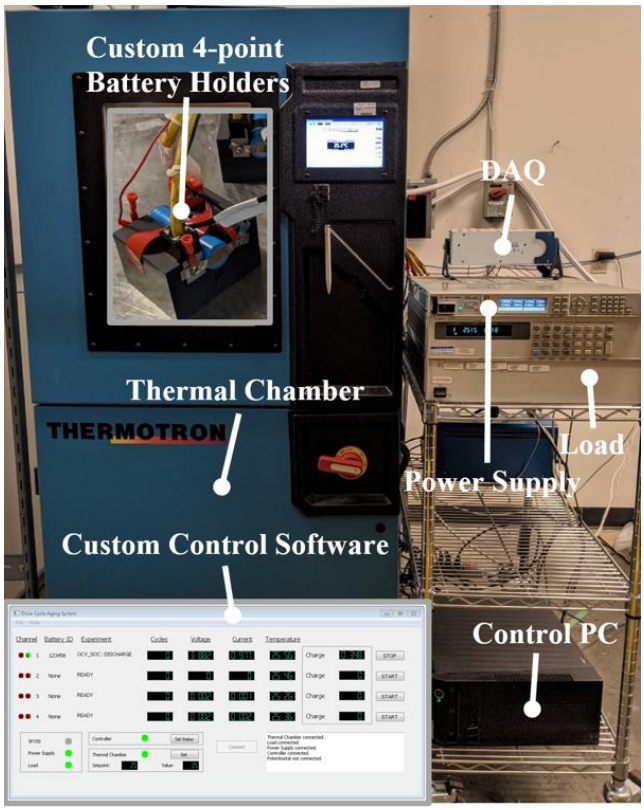

(b)

Figure 6-5: Experimental setup diagram (a), picture and custom control software screen capture (b).

New Samsung INR21700-50e 4.9Ah cylindrical lithium-ion battery cells were first broken in with 10 charge/discharge cycles at 25°C with a standard constant-current constant-

voltage (CCCV) charge protocol at 0.5C to 4.2V and 0.02C charge cut-off current as recommended by the manufacturer. The discharge current was set to 0.2C. The same settings are used to verify the battery SoH. OCV-SoC tests were performed at 25°C and 0°C using C/15 discharge and charge currents. Prior to each OCV-SoC test, the batteries were fully charged at 25°C. For the drive cycle tests, the batteries were first fully charged at 25°C. Then, the environmental temperature was set to 0°C followed by a rest period of 1hour after the temperature setpoint was reached. Finally, the drive cycle current profile was implemented to draw the required current from the battery. After the drive cycle profile was completed, the temperature was raised back to 25°C and the battery was charged again. In this study, results at 100% and 90% SoH are presented. The aged dataset was obtained by aging battery cells with continued charge/discharge operations involving 1C discharge and 0.5C charge currents and, the CCCV charge method to 0.02C cut-off current. The ambient temperature was set to 25°C.

6.3.2 Drive Cycle Datasets

With the experimental procedures described in the previous section, the battery cell voltage response at $0°C$ corresponding to different drive cycle current profiles are obtained. Four different drive cycles are used as described in Section 6.2.5. Three of the current profiles are used to produce high, medium, and low C-rate voltage cycles to parameterize each battery model. These current profiles consist of drive cycle samples representative of different C-rates (see Section 6.2.5) and are repeated several times in a row to cover a wider SoC window. The fourth current cycle is used as a validation cycle to evaluate the

performance of the algorithms considered in this study. The validation cycle covers an SoC range of approximately 5%. To include the full range of SoC, the procedures described in this study can be repeated to construct lookup tables for the parameters of each model across the entire range of SoC (for example, at every 5% SoC). However, for the purpose of demonstrating the IMM-SVSF estimation approach with C-rate specific models, only the 5% SoC window is presented.

Figure 6-6 shows each of the 4 cycles and their current and voltage responses obtained at 0°C for a battery at 100% SoH. In Figure 6-6a, high current loads up to 4C (20A) produce the voltage profile to parameterize the high C-rate model. Figure 6-6b shows current loads up to 2C (10A) and the corresponding voltage profile to parameterize the medium C-rate model. The low C-rate model was parameterized with the voltage profile in Figure 6-6c resulting from current loads of less than 1C (5A). The validation cycle current profile, Figure 6-6d, includes loads between less than 1C and up to 4C. Similar voltage profiles were obtained at 25°C to establish baseline results as well as for a battery at 90% SoH at $0°C$ for further evaluation of the proposed SoC estimation strategy. The model parameterization results and the performance of the EKF, SVSF, and IMM algorithms are presented and discussed in the next section.

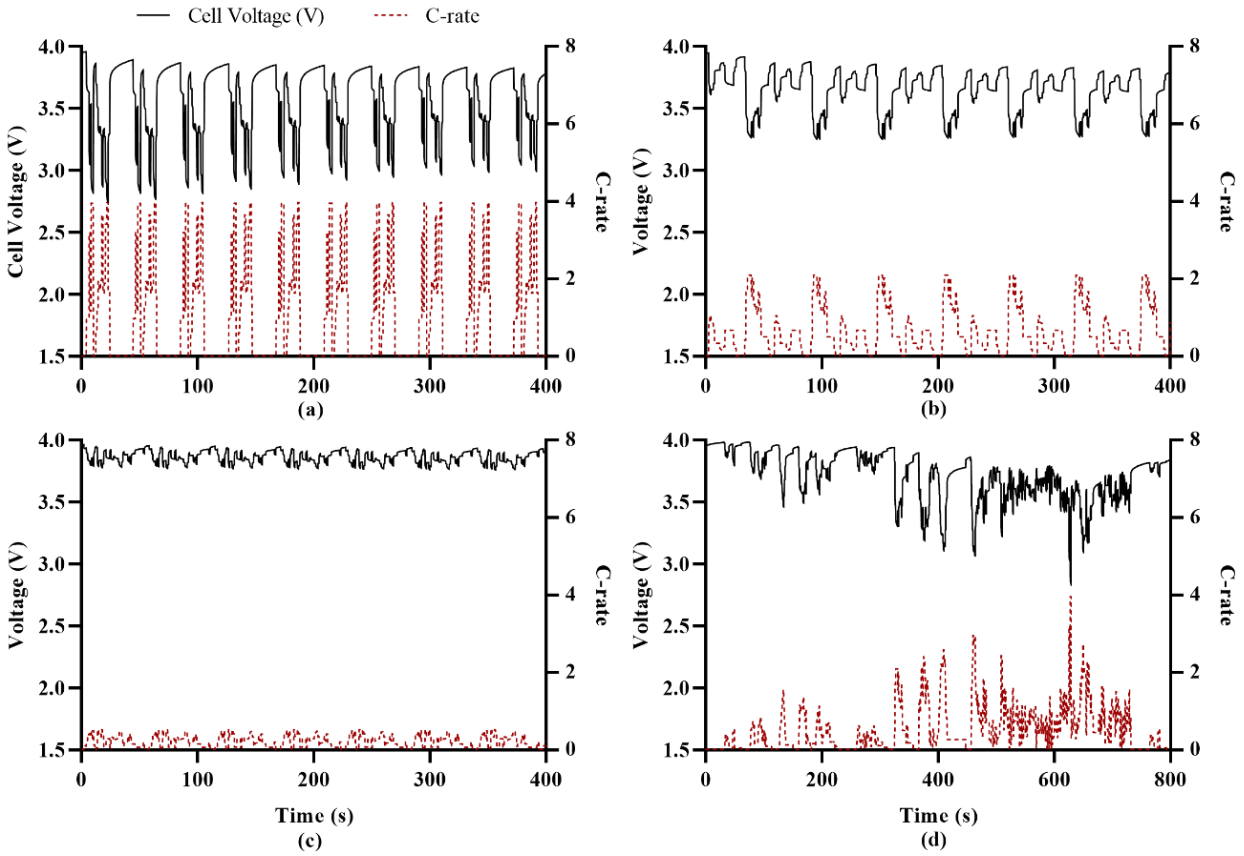

Figure 6-6: Drive Cycles at 0°C and 100% SoH for parameterization of the high C-rate model (a), the medium C-rate model (b), the low C-rate model (c), and for validation (d).

6.4 Results & Discussion

In this section, the models optimized for different C-rate ranges are discussed and the behaviour of the IMM is investigated using mode probabilities. The performance of the IMM-SVSF and IMM-EKF are then compared.

6.4.1 C-rate Specific Equivalent Circuit Models

To evaluate the proposed SoC estimation strategy, the ECM introduced in Section 6.2.1. was parameterized for three different C-rate ranges at 100% and 90% SoH and 0°C. Table 2 shows an overview of the model parameters obtained for each condition. Models L1, M1,

and H1 are used in Section 6.4.3. with the IMM for low temperature SoC estimation at 100% SoH, and L2, M2, and H2 for 90% SoH. Models B1 and B2 are used in Section 6.4.2. to establish a baseline performance of the EKF and SVSF single filters at 25°C and 0°C, respectively, for a 100% SoH battery. Model B2 has the same parameters as model M1 as both are at the same conditions.

For each model, the drive cycle inputs were kept within different C-rate ranges (as shown in Section 6.3.2) such that models are obtained for low C-rate (0-1C), medium C-rate (1-2C) and high C-rate (2-4C). The performance of the 100% SoH, 0°C models (L1, M1 and H1) compared to the parameterization profiles from Section 6.3.2. is shown in Figure 6-7. For each C-rate range, a close fit is obtained using the 3rd order ECM introduced in Section 6.2.1 The Root Mean Square Error (RMSE) of the model fits is also included in Table 2. The high C-rate models (H1 and H2) show the highest RMSEs, which indicates that the 3rd order ECM has some difficulty modeling battery response at high C-rates and low temperatures. The remaining models (L1, L2, M1, M2, B1, B2) all fall into a range of RMSEs between 0.003 and 0.03. The three time constants of the ECM fall within three ranges, 0.19-0.36, 3.7-10, and 18-42, with model B1, τ_2 being the only exception. Model B1 is the only model at 25°C which suggests that at higher temperatures, the ECM does not need all three time constants to achieve a good RMSE of 0.0071 which falls well within the range of the RMSEs of the other models.

Table 6-2: Battery Model Parameters

Model Name	L1	L2	M1	M2	H1	H2	B1	B2
Type	Low C-rate		Medium C-rate		High C-rate		Baseline	
C-rate Range	0-1		1-2		2-4		1-2	
SoH [%]	100	90	100	90	100	90	100	100
Temperature $[°C]$	0	0	0	0	0	0	25	0
R_0 $[m\Omega]$	43.1	25.6	39.1	30.4	34.8	18.8	22.8	39.1
R_1 $[m\Omega]$	12.4	34.7	9.5	21.8	8.8	24.5	7.6	9.5
R_2 $[m\Omega]$	3.8	16.3	2.5	5	2	12.6	11.5	2.5
R_3 $[m\Omega]$	49.7	8	37.4	28.4	26.9	9.2	14.2	37.4
τ_1 $[s]$	0.25	0.23	0.3	0.25	0.36	0.19	0.24	0.3
τ_2 $[s]$	3.7	5.74	4.1	10	6.6	9.3	3824.3	4.1
τ_3 $[s]$	42	18	31.54	21.1	24.5	18	18.4	31.5
Fit RMSE $[\times 10^{-3}]$	10.1	3.5	12.1	24.5	31.5	63.3	7.1	12.1

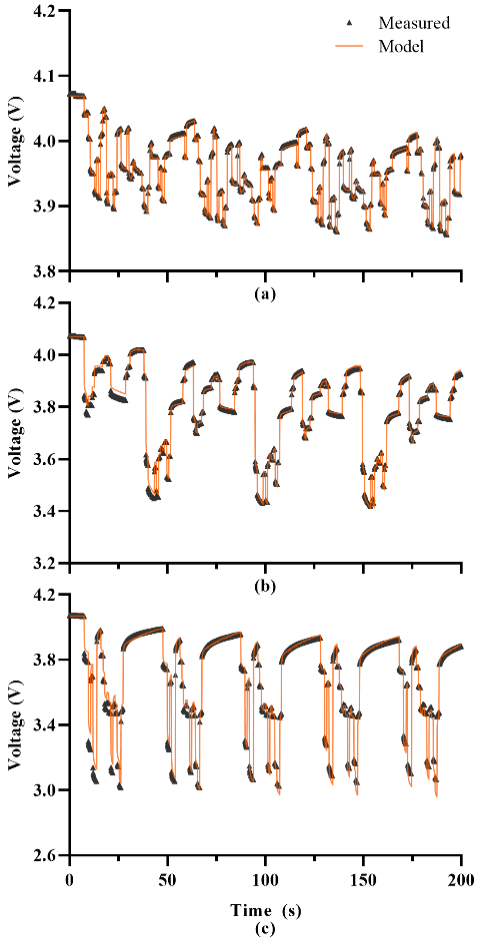

Figure 6-7: Performance for L1 (a), M1 (b), and H1 (c) c-rate specific models at 100% SoH and 0°C.

Figure 6-8 shows how the series resistance R_0 and the branch resistances of the models L1, M1 and H1 vary. All of the resistances decrease as C-rate increases. At this low temperature condition, the model parameters are significantly different for different C-rate regions, therefore, the IMM will be able to extract different information from each model to achieve an improved SoC estimate. In the next section, the models are used with IMM-EKF and IMM-SVSF filters for SoC estimation. The medium C-rate models (M1 and M2) are used for the EKF and SVSF single filters.

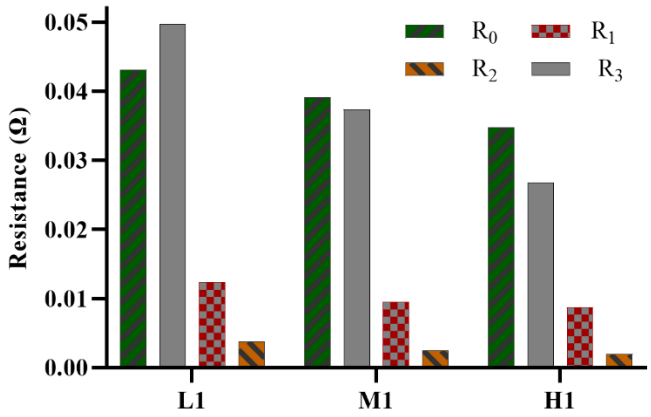

Figure 6-8: Change in model resistances with C-rate at 0°C.

6.4.2 Filter Initialization and Baseline

The initialization parameters of the standard EKF are the initial state vector $\hat{x}_{k,k}$, the initial state covariance $P_{k,k}$, the process covariance Q and the measurement covariance R. Equation (35) shows the initial values used for $\hat{x}_{k,k}, P_{k,k}$, and Q, where I_4 is the 4-by-4 identity matrix and soc_{init} changes depending on the drive cycle used or when evaluating filter convergence speed. Q was chosen sufficiently low to indicate some confidence in the process. If Q is too small and the input currents and measured voltages are very accurate, the filter will favor the process over the model. In addition to choosing a suitably high Q, a bias was added to the current and voltage signals to simulate realistic conditions. Similarly, the measurement covariance R is chosen to reflect some uncertainty. $\hat{x}_{k,k}$ and $P_{k,k}$ are updated as part of the filter and their values mostly impact convergence speed. The same values for the three parameters in (6-35) are used for all filters in this study.

$$\hat{x}_{k,k} = \begin{bmatrix} 10^{-3} \\ 10^{-3} \\ 10^{-3} \\ soc_{init} \end{bmatrix}, P_{k,k} = I_4 \times 4 \times 10^{-6}, Q = I_4 \times 2 \times 10^{-2} \quad (6\text{-}35)$$

The SVSF uses the same initial parameters as the EKF plus the two additional parameters ψ_lim, the constant smoothing boundary width, and γ, the convergence rate. The parameters are summarized in Table 6-3. The measurement covariance is the only value that is adjusted between the 100% and 90% SoH datasets as shown.

Table 6-3: Filter Initialization Parameters

Name	Symbol	Value
Measurement Covariance (100%/90% SoH)	R	0.2/0.8
SVSF Convergence Rate	γ	0.1
SVSF Constant Smoothing Boundary Width	ψ_{lim}	70
Current Bias	I_{bias}	80 mA
Voltage Bias	V_{bias}	1 mV

With these initial settings as well as a suitable battery model, the battery SoC can be estimated using EKF and SVSF filters. To establish a baseline performance, the model B1 (see Table 6-2) was then used with the EKF and SVSF and the validation drive cycle voltage profile also at 25°C. Similarly, the mode B2 was used with the validation drive cycle at 0°C. Figure 6-9a shows the SoC estimation performance at 25°C. Although the medium C-rate model B1 is very specific to the medium C-rate range, good SoC tracking is achieved. In contrast, the SoC estimation performance shown in Figure 6-9b, shows large deviation of both EKF and SVSF from the measured SoC. The objective of this paper is to improve the SoC tracking of EKF and SVSF at 0°C by using the IMM algorithm. The IMM requires two additional initialization parameters, μ_k and p, with initial values for this study shown in (6-36). The initial mode probability μ_k is chosen such that each filter has equal probability of using the correct model at the start, since the correct filter is unknown. The

mode transition probabilities p impact how quickly the IMM switches between modes. The chosen values result in smooth switching behaviour of the IMM.

$$\mu_k = \begin{bmatrix} 0.33 \\ 0.33 \\ 0.33 \end{bmatrix}, p = \begin{bmatrix} 0.9998 & 0.0001 & 0.0001 \\ 0.0001 & 0.9998 & 0.0001 \\ 0.0001 & 0.0001 & 0.9998 \end{bmatrix} \tag{6-36}$$

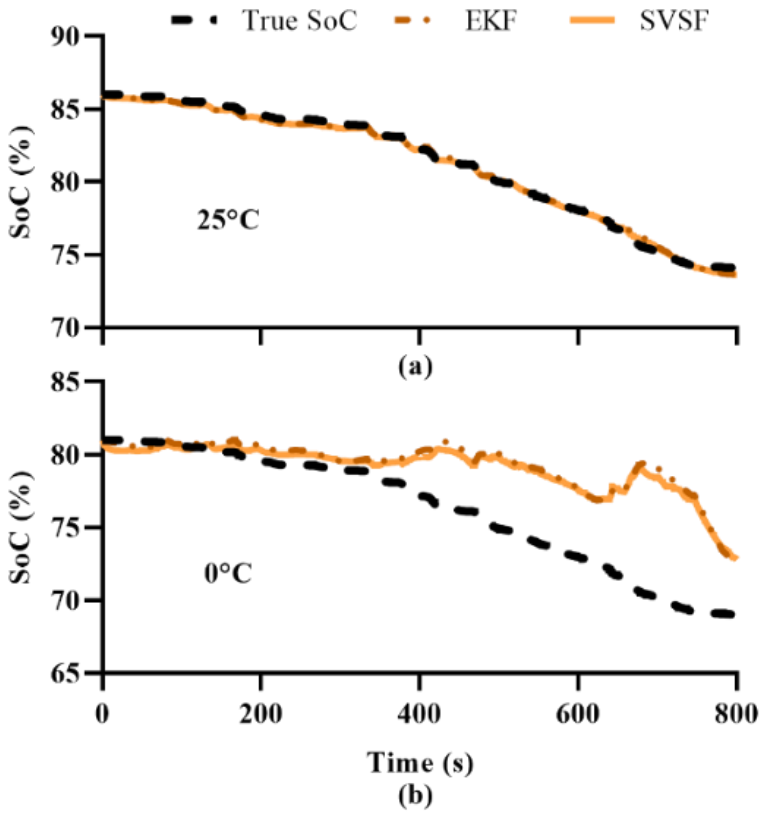

Figure 6-9: Baseline filter performance at 100% SoH, 25°C (a) and 0°C (b).

In the next section, the performance of the IMM-EKF and IMM-SVSF are presented and compared.

6.4.3 Performance Comparison

In this section, the low-temperature performance of the IMM-SVSF and IMM-EKF estimation strategies is demonstrated for 100% SoH and 90% SoH batteries. Figure 6-10 shows SoC estimation performance, SoC error and C-rate (for reference) for the validation

drive cycle profile. Figure 6-10a shows the measured SoC for the validation drive cycle at 100% SoH as well as the estimated SoC from the EKF, SVSF, IMM-EKF, and IMM-SVSF. Figure 6-10b shows similar results for the 90% SoH case. The SoC estimation errors for 100% and 90% SoH are shown in Figure 6-10c and Figure 6-10d, respectively. The C-rate load profile of the validation drive cycle is shown in Figure 6-10e and Figure 6-10f for reference. The validation drive cycle starts with C-rates of less than 1.5C until about 300 seconds into the cycle, then C-rates increase to around 2C on average. Towards the end the average C-rate is raised again with peaks of up to 4C. Initially, in Figure 6-10a and Figure 6-10b, all filters perform in a similar way up until around 200 seconds into the drive cycle. In this first part, the C-rates are mostly between 0.5 and 1.5C which can still be captured well by the medium C-rate models (M1 and M2) used by the single filters. Between 200 seconds and 300 seconds, the drive cycle C-rates are mostly below 0.5C and the single filters show an increased estimation error. Beyond 300 seconds, the C-rates become increasingly larger and the single model filters (EKF and SVSF) show further increased estimation errors. The EKF-IMM estimation error also increases, however, at a much slower rate. The SVSF-IMM shows the lowest estimation error during the second half of the drive cycle and overall remains within $\pm 2\%$. Table 6-4 summarizes the performance of each filter using the RMSE of the SoC estimate for the 100% and 90% SoH validation cycles at 0°C. The IMM based low temperature SoC estimation strategy can achieve significant improvements over single filters. Furthermore, the SVSF on its own performs similar to the EKF, however, when combined with the IMM strategy, the IMM-SVSF produces the lowest SoC estimation RMSE.

Table 6-4: Filter RMSE Comparison for validation cycles at 0°C

Filter	RMSE 100% SoH	RMSE 90% SoH
EKF	3.29	2.26
SVSF	3.03	2.36
IMM-EKF	1.01	0.85
IMM-SVSF	0.70	0.71

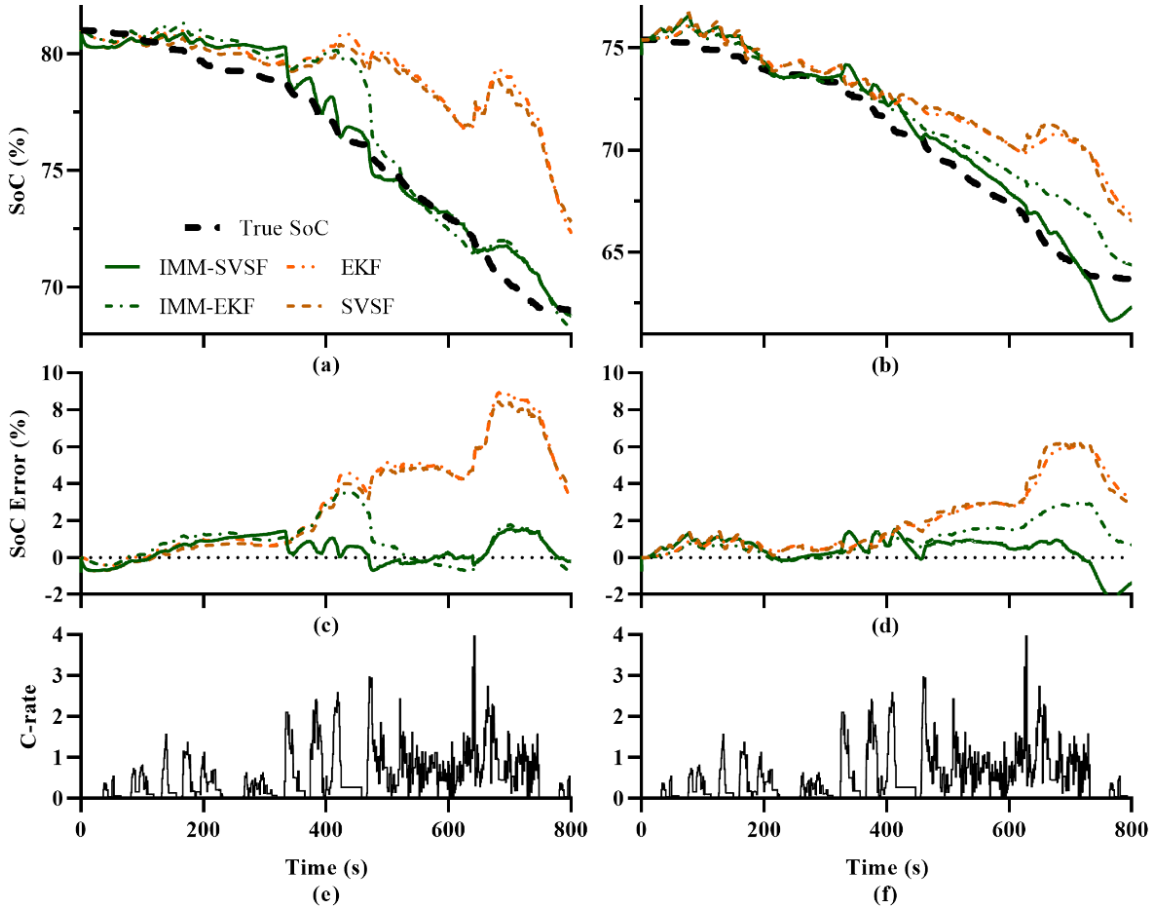

Figure 6-10: IMM SoC Estimation and error at 0°C for 100% SoH (a, c) and 90% SoH (b,d), C-rates for reference (e, f).

A performance metric for the filters is how well they respond to increased uncertainty due to, for example, increased input error. Figure 6-11 shows the impact of increasing the input current bias on the RMSE of the SoC estimation during the validation cycle. Figure 6-11a shows how the RMSE changes for each filter with the 100% SoH dataset, and Figure 6-11b

for the 90% SoH dataset. The RMSE increases in all cases with increased current bias, however, the IMM-SVSF shows a slightly slower rate of RMSE increase compared to the other filters.

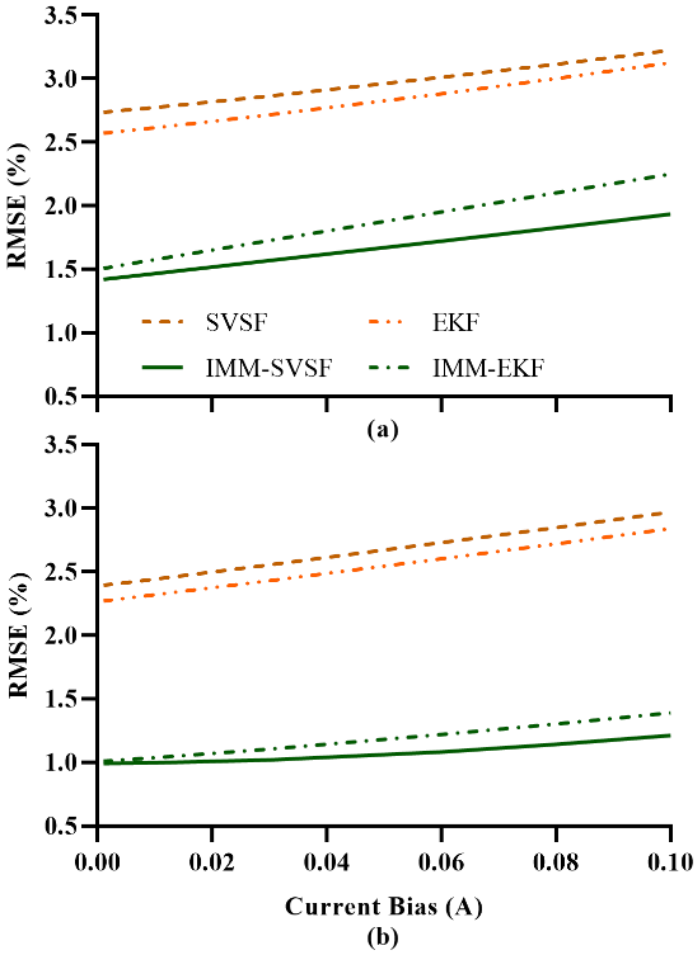

Figure 6-11: Impact of current bias on RMSE for 100% SoH (a) and 90% SoH datasets.

In the next section, the performance of the IMM-SVSF and IMM-EKF is investigated further using the voltage modeled by each filter as well as the mode probabilities calculated by the IMM algorithm.

6.4.4 IMM VOLTAGE MODELING & MODE PROBABILITIES

The results shown in the previous section demonstrate the effectiveness of the IMM-SVSF combination for low temperature SoC estimation. The reason for the lower estimation errors of the IMM based filter is that the IMM is able to consider trade-offs between different models. In this study, the models L1, M1, and H1 are used for 100% SoH data at 0°C. Each model is parameterized to suite different C-rate ranges, so the IMM can adjust the SoC estimate based on the input C-rate by selecting the most suitable combination of models. In this section, the behavior of the IMM is investigated further by first considering the modeled battery cell voltages produced by the three different models. Figure 6-12 shows the voltage response of the three models used in the IMM-SVSF compared to the measured voltage of the battery for the same drive cycle input. Also shown is the voltage error for each model. When the drive cycle C-rates are low, the voltage error of the high C-rate model H1 increases as shown, for example, between 220 and 320 seconds in the magnified portion of Figure 6-12b. However, when voltage drops are large, such as shown in Figure 6-12a.3, the model H1 is the most accurate. Similarly, the medium C-rate model M1 is the most accurate for medium voltage drops and the low C-rate model L1 for low voltage drops and rest periods as shown in Figure 6-12a.1 and Figure 6-12a.2 respectively. This shows that the models perform as intended when they are used as part of the IMM.

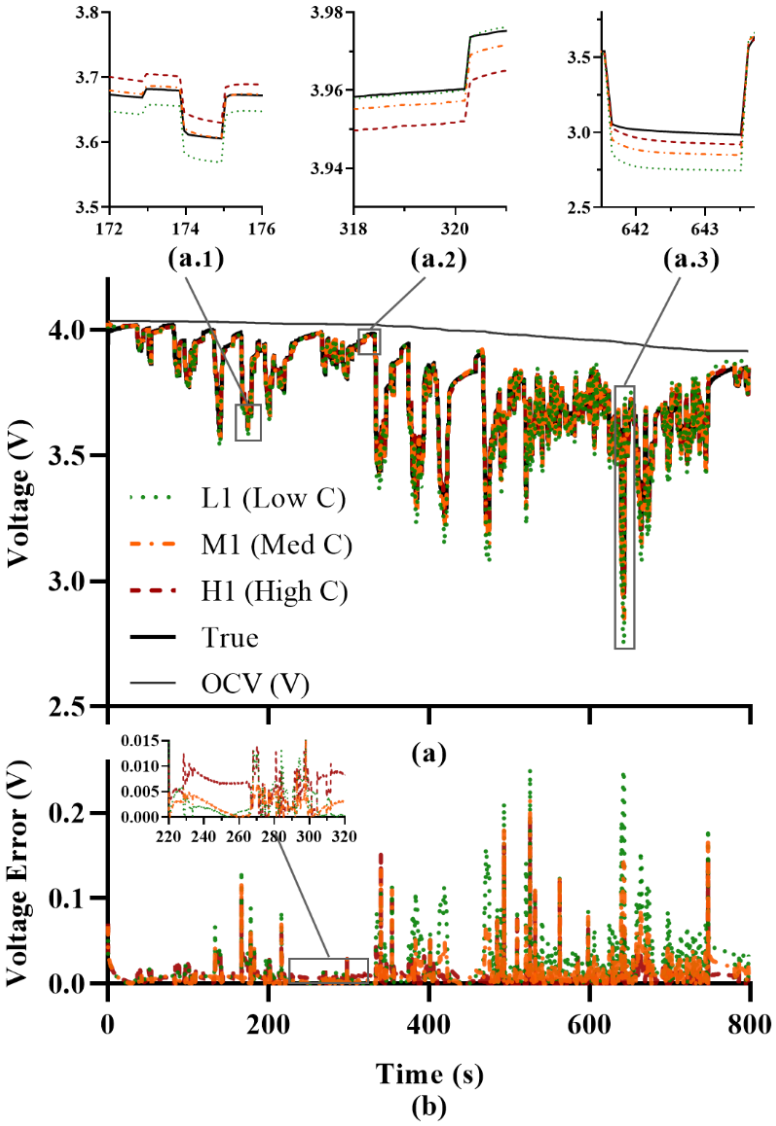

Figure 6-12: Voltage and voltage error of the three models (L1, M1, H1) used in the IMM-SVSF at 100% SoH and 0°C.

Another way to visualize the behaviour of the IMM is by considering the mode probabilities. The mode probabilities indicate which model is most likely to be the correct one, but effectively, mode probabilities also represent how much each model impacts the final IMM estimate. Figure 6-13a and Figure 6-13b show the mode probabilities for the IMM-EKF for the 100% and 90% SoH cases, respectively. Similarly, Figure 6-13c and d

show the mode probabilities for the IMM-SVSF. For each filter, the mode probabilities of the three models are shown, indicating the contribution of each model to the final state estimate. Figure 6-13e and Figure 6-13f show again the C-rate load profile of the validation drive cycle for reference. In the previous section, the IMM-EKF was shown to have a reduced estimation error, however, the IMM-SVSF estimation error was better and lower still. In general, the IMM filters first favour the low C-rate models (L1 and L2), then the medium C-rate models (M1 and M2), and finally the high C-rate models (H1 and H2). This roughly coincides with the gradual increase in average C-rate of the drive cycles, however, the IMM requires some time to switch between models. Subtle differences are apparent between the IMM-EKF and IMM-SVSF and for the two SoH conditions. In Figure 6-13c, the IMM-SVSF briefly favours the low C-rate model L1 again during a low C-rate region (less than 0.5C) around 300 seconds. For the same 100% SoH dataset, the medium C-rate model M1 remains dominant in the IMM-EKF as shown in Figure 6-13a. As shown in the previous section (Figure 6-10a), the IMM-SVSF computes an improved SoC estimate after 300 seconds compared to the IMM-EKF. For the 90% SoH dataset, the IMM-SVSF in Figure 6-13d shows a smooth transition between models and a clear dominant model for each region. The IMM-EKF, on the other hand, shows similar overall trends, but with lower mode probabilities in each region. Again, the SoC estimation performance of the IMM-SVSF is also improved (Figure 6-10b). The IMM-SVSF is able to switch between models more quickly and more confidently, resulting in improved SoC estimates.

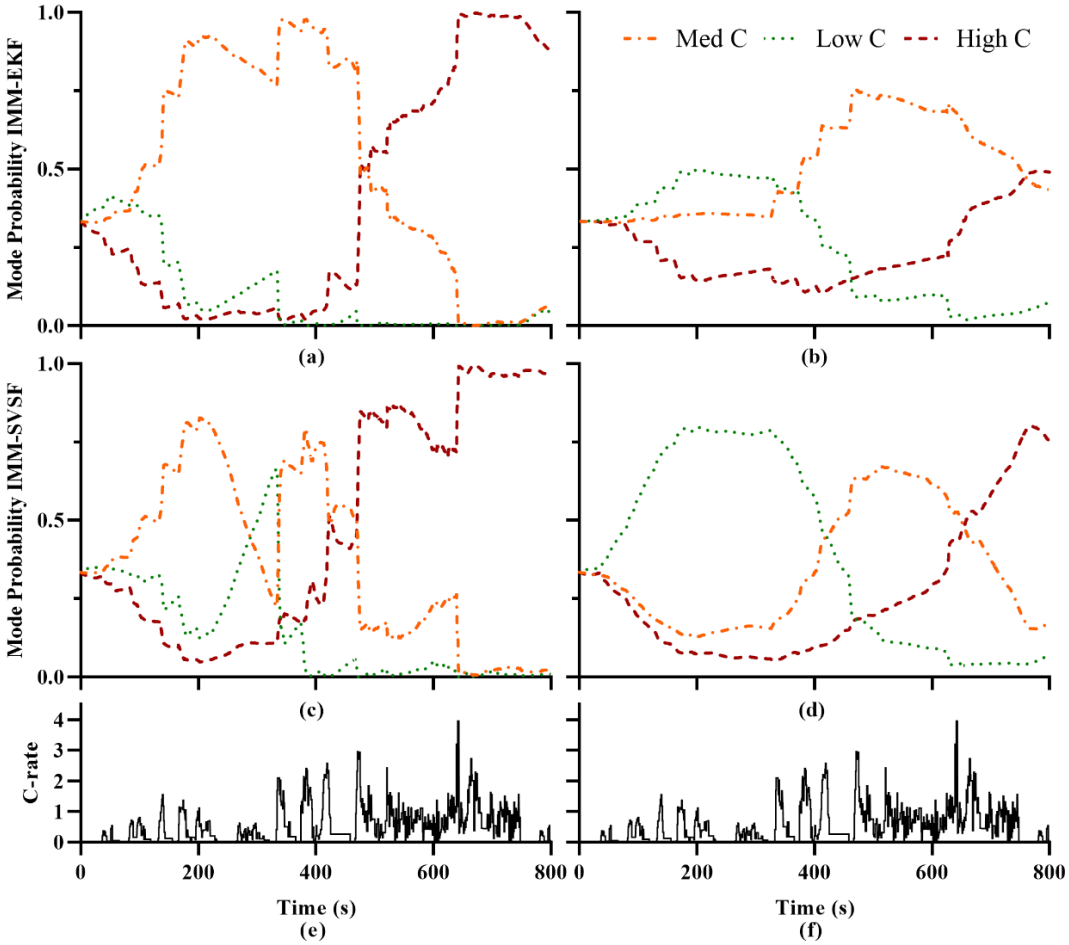

Figure 6-13: Mode probabilities for IMM-EKF at 100% SoH (a), 90% SoH, (b) and IMM-SVSF 100% SoH (c), 90% SoH (d). C-rates shown for reference in (e) and (f).

The performance of the filters is demonstrated based on single cell data. However, the IMM-SVSF method can be scaled to full battery packs consisting of series and parallel connected cells. Sub-modules of parallel cells are often treated as single cells with higher capacities to reduce the number of sensors used in the battery pack [32]. This is valid under the assumption that the cells are similar enough in their characteristics. Improvements can be made to ECMs to include resistances of interconnects [33] and those models can then

be used with the IMM-SVSF. Single cells or parallel sub-modules in series equipped with individual voltage sensors can each be tracked with dedicated IMM-SVSF algorithms.

6.5 CONCLUSION

Low temperatures increase the C-rate dependence of the response of lithium-ion batteries. As a result, SoC estimation accuracy can decreases due to voltage modeling errors at different C-rates. In this paper, an IMM-SVSF SoC estimation method is proposed that utilizes three models, each for a different range of C-rates. The proposed strategy is able to significantly increases SoC estimation accuracy at low temperatures. The IMM-SVSF is further compared to IMM-EKF and still shows improved accuracy. The IMM behavior is discussed in terms of voltage modeling and mode probabilities.

ACKNOWLEDGMENT

We thank Cadex Electronics for their facilities, support and expertise.

REFERENCES

[1] Y. Wang et al., “A comprehensive review of battery modeling and state estimation approaches for advanced battery management systems,” Renew. Sustain. Energy Rev., vol. 131, no. March, p. 110015, 2020.

[2] J. Jaguemont, L. Boulon, and Y. Dubé, “A comprehensive review of lithium-ion batteries used in hybrid and electric vehicles at cold temperatures,” Appl. Energy, vol. 164, pp. 99–114, 2016.

[3] Y. T. Huo, W. Hu, Z. Li, and Z. Rao, “Research on parameter identification and state of charge estimation of improved equivalent circuit model of Li-ion battery based on temperature effects for battery thermal management,” Int. J. Energy Res., vol. 44, no. 14, pp. 11583–11596, 2020.

[4] F. Guo, G. Hu, P. Zhou, J. Hu, and Y. Sai, “State of charge estimation in electric vehicles at various ambient temperatures,” Int. J. Energy Res., vol. 44, no. 9, pp. 7357–7370, 2020.

[5] R. Xiong, L. Li, Q. Yu, Q. Jin, and R. Yang, “A set membership theory based parameter and state of charge co-estimation method for all-climate batteries,” J. Clean. Prod., vol. 249, no. 5, p. 119380, 2020.

[6] S. Yang, C. Deng, Y. Zhang, and Y. He, “State of charge estimation for lithium-ion battery with a temperature-compensated model,” Energies, vol. 10, no. 10, 2017.

[7] J. Zhu et al., “An improved electro-thermal battery model complemented by current dependent parameters for vehicular low temperature application,” Appl. Energy, 2019.
[8] J. Shen et al., “State of charge estimation framework for lithium-ion batteries based on square root cubature Kalman filter under wide operation temperature range,” Int. J. Energy Res., vol. 45, no. 4, pp. 5586–5601, 2021.
[9] P. Kollmeyer, A. Hackl, and A. Emadi, “Li-ion battery model performance for automotive drive cycles with current pulse and EIS parameterization,” 2017 IEEE Transp. Electrif. Conf. Expo, ITEC 2017, pp. 486–492, 2017.
[10] Y. Bar-Shalom, X.-R. Li, and T. Kirubarajan, Estimation with Applications to Tracking and Navigation, vol. 9. 2001.
[11] E. R. Dougherty, “Optimal Filtering,” Random Process. Image Signal Process., pp. 307–482, 2009.
[12] Y. Zheng, M. Ouyang, X. Han, L. Lu, and J. Li, “Investigating the error sources of the online state of charge estimation methods for lithium-ion batteries in electric vehicles,” J. Power Sources, vol. 377, pp. 161–188, Feb. 2018.
[13] H. A. P. Blom and Y. Bar-Shalom, “The Interacting Multiple Model Algorithm for Systems with Markovian Switching Coefficients,” IEEE Trans. Automat. Contr., vol. 33, no. 8, pp. 780–783, 1988.
[14] E. Mazor, A. Averbuch, Y. Bar-Shalom, and J. Dayan, “Interacting Multiple Model Methods in Target Tracking: A Survey,” Ieee Trans. Aerosp. Electron. Syst., vol. 34, no. 1, 1998.
[15] K. Jo, K. Chu, and M. Sunwoo, “Interacting Multiple Model Filter-Based Sensor Fusion of GPS With In-Vehicle Sensors for Real-Time Vehicle Positioning,” IEEE Trans. Intell. Transp. Syst., vol. 13, no. 2, p. 973, 2012.
[16] Z. He, X. Bu, H. Yang, and Y. Song, “Interacting multiple model cubature Kalman filter for geomagnetic/ infrared projectile attitude measurement,” Meas. J. Int. Meas. Confed., vol. 174, no. January, p. 109077, 2021.
[17] A. Smiley and G. L. Plett, “An adaptive physics-based reduced-order model of an aged lithium-ion cell, selected using an interacting multiple-model Kalman filter,” J. Energy Storage, vol. 19, no. June, pp. 120–134, 2018.
[18] A. J. Smiley, W. K. Harrison, and G. L. Plett, “Postprocessing the outputs of an interacting multiple-model Kalman filter using a Markovian trellis to estimate parameter values of aged Li-ion cells,” J. Energy Storage, vol. 27, no. October 2019, p. 101043, 2020.
[19] X. Su, S. Wang, M. Pecht, L. Zhao, and Z. Ye, “Interacting multiple model particle filter for prognostics of lithium-ion batteries,” 2017.
[20] S. Habibi, “The Smooth Variable Structure Structure Filter,” Proc. IEEE, vol. 95, no. 5, 2007.
[21] S. A. Gadsden and S. R. Habibi, “A new robust filtering strategy for linear systems,” J. Dyn. Syst. Meas. Control. Trans. ASME, vol. 135, no. 1, 2013.
[22] S. A. Gadsden, S. Habibi, and T. Kirubarajan, “Kalman and smooth variable structure filters for robust estimation,” IEEE Trans. Aerosp. Electron. Syst., vol. 50, no. 2, pp. 1038–1050, 2014.
[23] S. A. Gadsden and S. R. Habibi, “A new form of the smooth variable structure filter with a covariance derivation,” Proc. IEEE Conf. Decis. Control, pp. 7389–7394, 2010.
[24] S. A. Gadsden, M. El Sayed, and S. R. Habibi, “Derivation of an optimal boundary layer width for the smooth variable structure filter,” Proc. Am. Control Conf., pp. 4922–4927, 2011.

[25] S. A. Gadsden, D. Dunne, S. R. Habibi, and T. Kirubarajan, “Comparison of extended and unscented Kalman, particle, and smooth variable structure filters on a bearing-only target tracking problem,” Signal Data Process. Small Targets 2009, vol. 7445, no. September 2009, p. 74450B, 2009.
[26] S. A. Gadsden, M. Al-Shabi, and S. R. Habibi, “Estimation Strategies for the Condition Monitoring of a Battery System in a Hybrid Electric Vehicle,” ISRN Signal Process., vol. 2011, no. 1, 2011.
[27] S. A. Gadsden, S. R. Habibi, and T. Kirubarajan, “A novel interacting multiple model method for nonlinear target tracking,” 13th Conf. Inf. Fusion, Fusion 2010, 2010.
[28] T. R. Jow, S. A. Delp, J. L. Allen, J.-P. Jones, and M. C. Smart, “Factors Limiting Li + Charge Transfer Kinetics in Li-Ion Batteries,” J. Electrochem. Soc., vol. 165, no. 2, pp. A361–A367, 2018.
[29] P. Ahmadi and E. Kjeang, “Realistic simulation of fuel economy and life cycle metrics for hydrogen fuel cell vehicles,” Int. J. Energy Res., vol. 41, no. 5, pp. 714–727, 2017.
[30] J. Wu, J. Liang, J. Ruan, N. Zhang, and P. D. Walker, “Efficiency comparison of electric vehicles powertrains with dual motor and single motor input,” Mech. Mach. Theory, vol. 128, pp. 569–585, 2018.
[31] G. L. Plett, “Extended Kalman filtering for battery management systems of LiPB-based HEV battery packs Part 2. Modeling and identification,” J. Power Sources, vol. 134, pp. 262–276, 2004.
[32] M. Lelie et al., “Battery management system hardware concepts: An overview,” Appl. Sci., vol. 8, no. 4, 2018.
[33] L. Chang, B. Duan, P. Li, K. Zhang, C. Zhang, and L. Xiao, “Influence of interconnect resistances on parallel- connected LiFePO 4 cells performance,” 2019 3rd Conf. Veh. Control Intell., no. 61527809, pp. 5–8, 2018.
[34] F. Lambert, “Tesla Model 3: Exclusive first look at Tesla’s new battery pack architecture,” electrek.co, 2017. [Online]. Available: https://electrek.co/2017/08/24/tesla-model-3-exclusive-battery-pack-architecture/.
[35] Tesla, “Model 3,” Tesla Press Information, 2018. [Online]. Available: https://web.archive.org/web/20180315094117/https://www.tesla.com/presskit.

Chapter 7: EIS from Accelerated and Realistic Battery Aging

Marvin Messing[1,2], Tina Shoa[2], Saeid Habibi[1]

[1]Department of Mechanical Engineering, McMaster University, Hamilton, ON, Canada,

[2]Cadex Electronics, Richmond, BC, Canada

This paper is published in 2021 IEEE Transportation Electrification Conference and Expo (ITEC), 2021, pp. 720-725, doi: 10.1109/ITEC51675.2021.9490091. This paper is republished here with permission[4].

ABSTRACT

In this paper, the behaviour of lithium-ion batteries aged with an accelerated (charge/discharge) and a realistic (drive cycle) protocol is compared using Electrochemical Impedance Spectroscopy (EIS) characterization. Two equivalent circuit models are used to further analyse degradation trends. The results show increased impedances for drive cycle aged batteries above 90% State of Health (SoH) compared to charge/discharge aged cells at the same SoH. Below 90% SoH, the opposite is found, with charge/discharged aged cells showing higher impedance.

7.1 INTRODUCTION

Lithium-ion batteries (LiB) used in Electric Vehicles (EV) require precise battery management systems (BMS) for safety monitoring, fault detection and state estimation. The state of charge (SoC) [1], state of health (SoH) [2], and state of available power (SoaP)

[4] In reference to IEEE copyrighted material which is used with permission in this thesis, the IEEE does not endorse any of McMaster's products or services. Internal or personal use of this material is permitted. If interested in reprinting/republishing IEEE copyrighted material for advertising or promotional purposes or for creating new collective works for resale or redistribution, please go to http://www.ieee.org/publications_standards/publications/rights/rights_link.html to learn how to obtain a License from RightsLink.

[3] must be estimated by the BMS to ensure optimal operation and energy usage. The accuracy of the state estimation not only impacts longevity and safety of the battery, but also contributes to the cost and size of the battery pack [4], [5]. One of the main challenges with SoH estimation is the long time it takes to obtain representative battery data to use for algorithm development. Many studies that characterize batteries at different SoH employ accelerated aging techniques, such as increasing operating temperature or current rates [6]–[9]. However, the use of acceleration factors results in data which is not necessarily representative of batteries that were aged as part of an EV battery pack. The impact of different aging methods on the battery behaviour becomes especially apparent if the batteries are analyzed with Electrochemical Impedance Spectroscopy (EIS). EIS is a non-destructive material characterization technique that applies low amplitude, sinusoidal current or voltage signals at different frequencies to a battery [10]. The EIS excitation signals cause a battery current or voltage response which can be transformed using the Fast Fourier Transform (FFT) and analyzed in the frequency domain. The EIS results are most commonly visualized in the form of Nyquist plots, which show the complex impedance pairs (real and imaginary) for each input signal frequency. The Nyquist plots exhibit several features corresponding to the internal impedance response of the various layers of the battery. The EIS data can further be analysed by using battery models such as Equivalent Circuit Models (ECM).

Several studies show how EIS changes under different operating and aging conditions. Schuster et al. [11] used EIS to track the evolution of ohmic resistance and charge transfer resistance under different charging/discharging rates, temperatures, and voltage limits and

showed that high charging rates, high temperature, and high voltage limits cause the resistances to increase significantly. However, a range of conditions are shown to result in similar resistance evolution. In another study, Schuster et al. [12] showed how ohmic and charge transfer resistances change with calendric, cyclic, and mild cyclic/high temperature aging protocols. They highlight the importance of using realistic aging protocols to obtain aged battery data when developing algorithms to utilize these resistances. Both studies use simple resistor-capacitor (RC) based ECMs. Zhu et al. [13] showed how different charging protocols change the evolution of EIS and corresponding fractional order model fits. Olofsson et al. [13] showed how EIS results change for drive cycle tests performed at room temperature and elevated temperature.

The objective of this study is to analyse the differences between EIS results from batteries aged using accelerated and realistic cycling protocols by modeling EIS data with different ECMs. The aging protocols are designed to use similar temperatures and charging methods, while still resulting in different aging rates due to differences in cycling profiles. The results show that the realistic test causes increased impedance measurements in the frequency regions associated with SEI layer growth and charge transfer resistance between 100% and 90% SoH, even though it takes three times the amount of time to reach the same SoH as the accelerated test. However, this trend reverses for data below 90% SoH, showing faster SEI and charge transfer resistance increase with SoH for the accelerated test at 87% and 85% SoH.

The paper is organized as follows. In Section 7.2, a simple EV model based on the Tesla Model 3 is presented. This model is used to generate drive cycle current profiles for realistic battery aging. The aging experiment design is introduced next, followed by a description of the battery models used in this study. Section 7.3 contains the findings of the aging study and EIS characterization for the accelerated and realistic aging methods. Finally, concluding remarks are provided and future work is discussed in Section 7.4.

7.2 METHODS AND THEORY

7.2.1 ELECTRIC VEHICLE MODELING

In this study, standard drive cycles as provided by the US Environment Protection Agency (EPA) are used to apply current profiles to battery cells such that the cells age in a way similar to cells used in EVs. However, the EPA drive cycles merely provide speed vs. time information for different scenarios. To convert this data into battery cell current, a vehicle model is required. The first step is to calculate the power required to achieve the desired speeds by overcoming opposing forces. Equation (7-1) shows how to calculate P_{acc}, the power required to accelerate the mass of the vehicle, given the desired speed V, the mass of the car m_{car} and acceleration calculated using (7-2).

$$P_{acc} = m_{car}\, a\, V \tag{7-1}$$

$$a = dV/dt \tag{7-2}$$

In (7-3), the power $P_{roll,flat}$ to overcome rolling resistance assuming a flat surface is calculated given acceleration due to gravity g=9.81$m\backslash s^2$ and a road surface parameter C_r calculated using (7-4).

$$P_{roll,flat} = C_r\, m_{car}\, g \tag{7-3}$$

The constants C_{ra}, C_{rb}, and C_h describe the conditions of the road surface.

$$C_r = (C_{ra} + C_{rb}\, V)\, C_h \tag{7-4}$$

The power required to overcome drag, P_{drag}, is calculated in (7-5) given the air density ρ_{air}, the frontal area of the vehicle A_{front} and the drag coefficient of the vehicle C_D.

$$P_{drag} = \frac{1}{2}\, \rho_{air}\, A_{front}\, C_D\, V^3 \tag{7-5}$$

Equations (7-1), (7-3), and (7-5) provide the total power required to achieve the desired speeds and is summarized in (7-6) as P_{tot}.

$$P_{tot} = P_{acc} + P_{roll,flat} + P_{drag} \tag{7-6}$$

Next, the power required from the battery pack is calculated in (7-7) by considering further losses due to drive train efficiency η_{dr}, battery efficiency η_{batt} and parasitic power P_{aux} required by the auxiliary systems of the car.

$$P_{batt} = [(P_{tot}/\eta_{dr}) + P_{aux}]/\eta_{batt} \tag{7-7}$$

Using (7-8), the power can be converted into battery pack current, assuming a fixed nominal voltage $E_{cell,nom}$ and given the number of cells in parallel N_{series}, which make up the total pack voltage.

$$I_{pack} = P_{batt}/(N_{series}\, E_{cell,nom}) \tag{7-8}$$

Finally, the battery cell current is obtained in (7-9) given the number of cells in parallel $N_{parallel}$.

$$I_{cell} = I_{pack}/N_{parallel} \tag{7-9}$$

In this study, the simple vehicle model described above is used to approximate the behaviour of a Tesla Model 3 Long range EV. The parameters specific to the EV as well as assumed efficiencies are shown in Table 7-1: Vehicle Model Parameters for Tesla Model

3 Long Range. The original Tesla Model 3 battery pack configuration was scaled by reducing the number of modules in parallel to achieve slightly higher currents. This results in utilization of more of the battery voltage range and reduced aging times. Nevertheless, the current profiles remain sufficiently realistic to compare to accelerated charge/discharge aging.

Table 7-1: Vehicle Model Parameters for Tesla Model 3 Long Range

Name	Symbol	Value
Mass of the vehicle.	m_{car}	1730 kg
Rolling resistance calculation factor.	C_{ra}	0.0041
Rolling resistance calculation factor.	C_{rb}	0.000018
Rolling resistance calculation factor.	C_h	1.5
Density of air.	ρ_{air}	1.2
Vehicle frontal area.	A_{front}	3.25 m^2
Vehicle drag coefficient.	C_d	0.23
Vehicle auxiliary power draw.	P_{aux}	350 W
Drivetrain efficiency.	η_{dr}	0.765
Battery efficiency.	η_{batt}	0.95
Number of modules in parallel.	$N_{parallel,scaled}$	18
Number of series cells per module.	N_{series}	96
Nominal battery cell voltage.	$E_{cell,nom}$	3.6 V

7.2.2 Battery Aging

An extensive aging study was conducted with battery cells undergoing accelerated charge/discharge aging and other cells undergoing aging in the form of a combination of drive cycles to simulate battery operation as encountered in EVs. For each aging condition, cells were aged to 85% SoH and EIS measurements were obtained at 100%, 95%, 90%, 87%, and 85% SoH. All cells used in this study are Samsung INR21700-50E, 4.8Ah lithium-ion batteries. A custom battery tester was used to determine battery states to less than 0.5% error, as well as to simulate drive cycles for realistic aging. The accelerated aging

(constant current – constant voltage charge at C/2, discharge at 1C) was performed on Cadex C7400ER 4-channel battery analyzers. EIS (10 mV amplitude, 800Hz to 0.1Hz, 3-hour pre-measurement rest) was performed using a Bio-logic SP150 potentiostat. Testing was done at a constant temperature of 25°C using a Testequity 1007C thermal chamber. Figure 7-1 shows the drive cycle aging protocol current, scaled by battery capacity (c-rate). The protocol consists of a series of "Week Cycles" (trips from home to work and back plus an evening errand and charge at home), a "Weekend Cycle" (trip through the city, onto a highway, fast charging (1C) at destination, and back), as well as a capacity check (constant current – constant voltage charge at C/2, discharge at C/5). The "Week Cycles" are a combination of urban (UDDS) and urban-aggressive (US06) EPA drive cycles, and the "Weekend Cycles" are a combination of US06 and highway (HWYFET) EPA drive cycles. Home charging is done with constant current – constant voltage charge at C/2. The week cycles are repeated 10 times, amounting to two work weeks of driving. This is followed by a weekend cycle (i.e. weekend trips occur every 2 weeks). Capacity checks are done after every 8 weekend cycles. If the capacity check indicates that the target capacity has been reached, the EIS characterization is performed. This procedure is summarized in Figure 7-2.

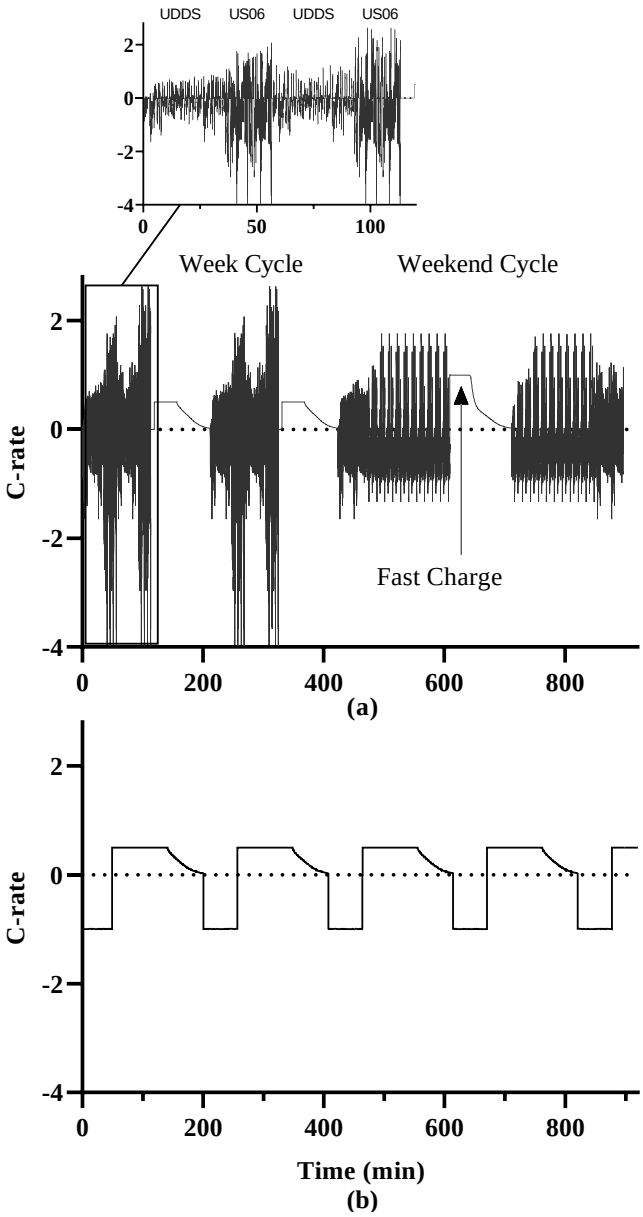

Figure 7-1: Aging test load profiles in units of C-rate for drive cycle aging test (a) and charge/discharge aging test (b).

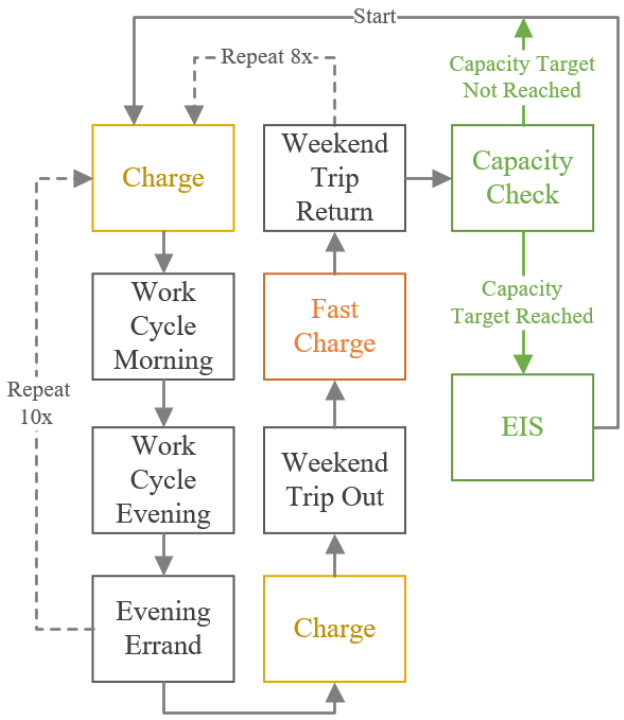

Figure 7-2: Aging test procedure showing the usage of different drive cycle protocols, different charge rates, and EIS steps.

7.2.3 Battery Modeling

To understand the degradation behaviour of the batteries as they age, two ECMs were used in this study. The first model is a fractional order impedance model which can follow the shape of the data very well and fitting can be automated if suitable initial conditions for the model parameters are provided. The second model is a 2nd order RC based ECM. Some of the parameters obtain from the RC model can reveal more realistic trends even though the model fit is poor due to the ideal nature of the RC circuit elements. Figure 7-3a shows Nyquist plots for EIS data at 100% SoH and 90% SoH and corresponding model fits for the fractional order model and the RC model. The fractional impedance model shown in Figure 7-3b consists of an inductor L, representing inductance effects due to cell windings

and cables, a series resistance R_0, for ohmic resistance effects, a resistance R_1 in parallel with a constant phase element (CPE) defined by Q_1 and α_1, together known as a ZArc element, to model the solid electrolyte interface impedance, another ZArc element defined by R_2, Q_2 and α_2 to model charge transfer impedance, and finally a CPE defined by Q_3 and α_3 to model diffusion. The complex impedance Z_{fr} of this ECM changes with frequency ω according to (9), where $\tau_k = (R_k Q_k)^{1/\alpha_k}$.

$$Z_{fr}(\omega) = i\omega L + R_0 + \sum_{k=1}^{2} \frac{R_k}{1+R_k Q_k (i\omega\tau_k)^{\alpha_k}} + \frac{1}{Q_3 (i\omega)^{\alpha_3}} \qquad (9)$$

The RC model contains two RC pairs instead of the ZArc and CPE elements as shown in Figure 7-3c. The RC branches are used to model the charge transfer impedance and diffusion impedance, but neglecting the SEI layer impedance. This is done because the exact positioning of an additional RC semi-circle to model SEI layer impedance is somewhat arbitrary and does not yield useful information for this study. This is discussed further in Section 7.3.2. The complex impedance Z_{rc} of the RC model is described by (10), where $\tau_2 = R_2 C_2$ and $\tau_3 = R_3 C_3$.

$$Z_{rc}(\omega) = i\omega L + R_0 + \frac{R_2}{1+i\omega\tau_2} + \frac{R_3}{1+i\omega\tau_3} \qquad (10)$$

The fractional order ECM was parameterized using the Particle Swarm Optimization (PSO) method. The PSO was also used for the RC ECM, however, R_0 and R_2 were fixed such that R_0 coincides with the real impedance value corresponding to the smallest imaginary value. R_2 was fixed to the difference between the lowest point in the charge transfer region and R_0 [12].

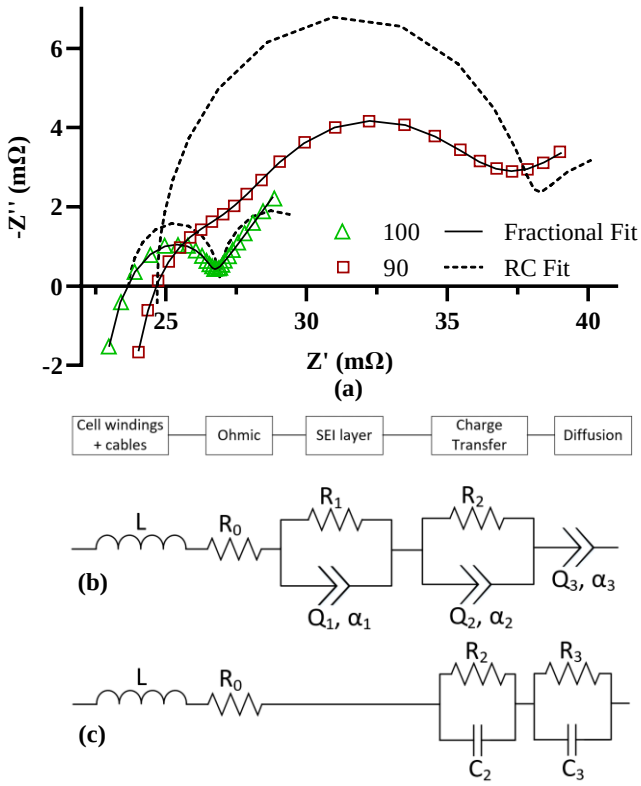

Figure 7-3: Equivalent circuit battery model fits to Nyquist plots (a), fractional order model circuit (b), RC-based circuit without SEI layer branch (c).

7.3 Results and Discussion

7.3.1 Voltage and Temperature Response

Figure 7-4a shows the voltage response of battery cells at 100% SoH resulting from drive cycle (week cycle followed by weekend cycle) and charge/discharge protocols. The same is shown in Figure 7-4b but for batteries at 85% SoH. The voltage response of the charge/discharge aging profile did not change much, only charging shows longer CV mode periods for low SoH. The voltage data from the drive cycle, however, shows a significantly altered response. At low SoH, the drive cycles use a much larger portion of the battery voltage range, with the weekend cycle nearly using the full range. This will also decrease

the average voltage of the cell and could possibly impact degradation. The fresh cell only uses the top half of the voltage range (3.6 to 4.2 V) and has a higher average voltage which can accelerate degradation. This degradation effect due to voltage may be slower for the aged cell which uses the full voltage range (2.5 to 4.2V).

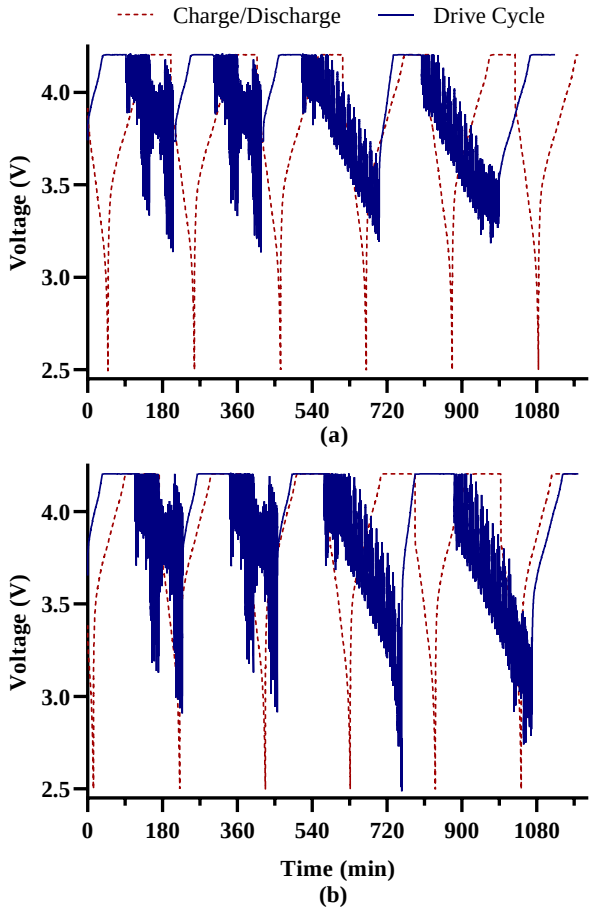

Figure 7-4: Drive cycle aged and charge/discharge aged voltage profiles for fresh cells (a) and cells at 85% SoH (b).

Figure 7-5a shows a comparison of the temperature profiles between fresh (100% SoH) and aged (85% SoH) batteries aged with the drive cycle profile. The temperature data for the aged cell shows a slightly wider temperature range, reaching both lower and higher

temperatures compared to the fresh cell. The lower temperatures reached in the aged case are likely due to the lower average voltage. The temperature data for fresh and aged cells aged with the charge/discharge profile is shown in Figure 7-5b. Here, the temperature peaks for the aged cell are lower for almost all peaks shown. This is likely a result of the extended CV region, where currents are dropping and less heat is generated. In contrast, the fresh cell spends more time at the 0.5C charging current, generating more heat. For both drive cycle aged and charge/discharge aged cells, charging results in the biggest temperature increase, with the overall maximum of close to 30°C reached during the fast charge as part of the weekend cycle. In general, however, the temperatures are similar between the two aging protocols as well as between fresh and aged cells, with differences not exceeding 0.5°C. Therefore, temperature is expected to affect the two aging protocols in the same way and to not cause any significant differences in aging behaviour between charge/discharge aged and drive cycle aged battery cells.

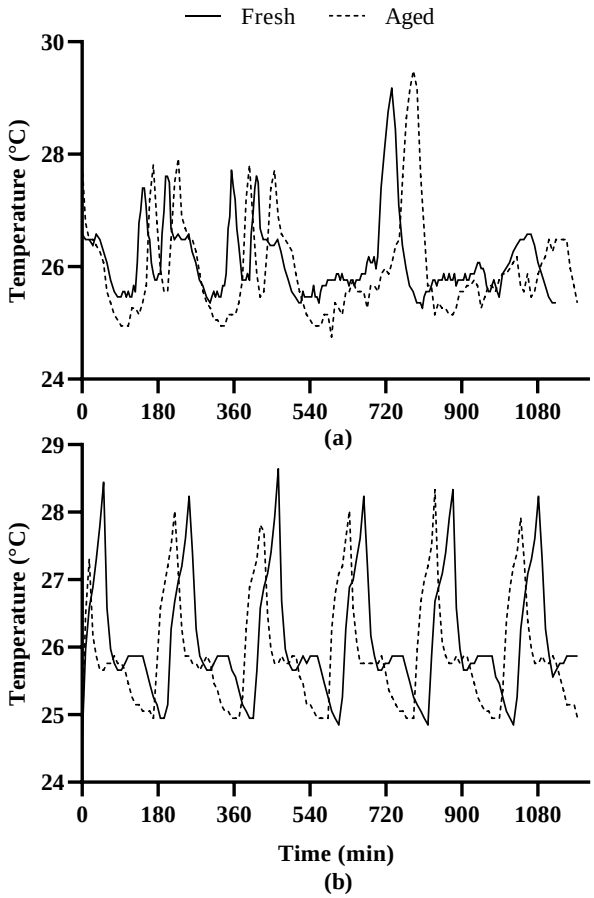

Figure 7-5: Comparison of temperature profiles for fresh cells and cells at 85% SoH during drive cycle aging protocol (a) and charge/discharge protocol (c).

7.3.2 EIS CHARACTERIZATION

From the realistic drive cycle based aging tests and the accelerated charge/discharge aging tests, EIS datasets were obtained for batteries at 100%, 95%, 90%, 87%, and 85% SoH. The charge/discharge aging protocol required 3 months of continuous aging to achieve 85% SoH. The drive cycle aging protocol required 9 months to reach the same SoH, 3 times the amount of time. Figure 7-6a shows the Nyquist plots from EIS data recorded with batteries that underwent drive cycle aging conditions, and Figure 7-6b shows the Nyquist plots from EIS data recorded with batteries that underwent charge/discharge aging. For the drive cycle

aged batteries, three datasets were available down to 90% SoH. Above 90% SoH the variance between the three sets is negligible but at 90% SoH the variance is larger and the standard deviation (Std. Dev.) is shown around the 90% SoH mean Nyquist plot in Figure 7-6a. Between 100% and 90% SoH, the drive cycle aged data shows a faster increase in the semi-circles compared to the charge/discharge aged results. This suggests that impedance growth has a bigger impact on battery degradation when drive cycles are used above 90% SoH. The charge/discharge protocol reached 90% SoH much faster than the drive cycle protocol, however, with significantly smaller impedance growth. Below 90% SoH, the charge/discharge aged Nyquist plots become much larger than the drive cycle aged ones, indicating that in this lower SoH phase, charge/discharge cycles result in higher impedance increase at the same SoH. The variance observed for the drive cycle data at 90% SoH, while noticeable, is still small compared to the change between SoH targets and even more so, when compared to charge/discharge aging.

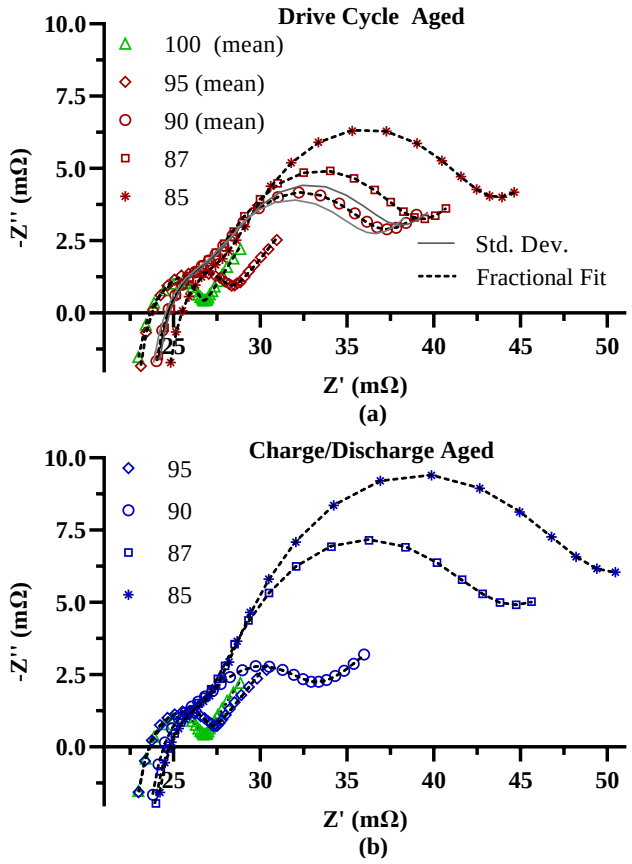

Figure 7-6: Nyquist plot evolution at various SoH targets with fractional order model fits for drive cycle aged EIS data (a) and charge/discharge aged EIS data (b).

Figure 7-7 shows the evolution with SoH of the battery model parameters from the two battery models introduced in Section 7.2.3. Figure 7-7a shows an increase in R_0 obtained from the RC model, but no clear trend for R_0 from the fractional model. Between 100% and 90% SoH, R_0 from charge/discharge aging data is within one standard deviation of R_0 from the drive cycle aging data. Figure 7-7b (fractional model only) shows a large increase in R_1 for drive cycle aged cells down to 90% SoH and a smaller increase for the charge/discharge aged cells in the same SoH region. Below 90% SoH, R_1 eventually decreases for drive cycle aged cells. For the charge/discharge aged cells, R_1 continues to

increase up to 87% SoH, and decreases after that. Assuming the variance of the drive cycle data below 90% SoH is similar (or larger) to the variance at 90% SoH, R_1 from the two aging datasets becomes indistinguishable. This behaviour is not obvious from the Nyquist plots. However, the charge/discharge Nyquist data shows a much more pronounced inflection point in the SEI layer impedance region. A more defined inflection point leaves the PSO algorithm with fewer options for the exact placement of the SEI layer impedance model branch. Figure 7-7c shows trends for R_2 which are similar for both models, with the RC model only offset by the missing SEI layer resistance. For both models, R_2 increases faster for drive cycle aged batteries to 90% SoH, and faster for charge/discharge aged cells bellow 90% SoH. The variance for the drive cycle data is also small in all available cases for the R_2 parameter. Therefore, R_2 is the most reliable parameter to consider for both fractional and RC models, when comparing EIS results. The inflection point in the Nyquist plot defining R_2 is well defined in all cases, resulting in clear model parameter trends. Considering the Nyquist plots and model parameters, it is clear that a change in impedance growth rate with SoH occurs around 90% SoH. The voltage ranges utilized by the different aging protocols (as discussing in Section 7.3.1) may offer one explanation. The higher average voltage of fresh cells during drive cycle aging can cause accelerated degradation, and the average voltage decreases as the battery ages. For the charge/discharge aged cells, the duration spent at the maximum voltage during charge increases as the battery ages, causing the opposite degradation trend. This also happens in the drive cycle aging case, but the lower average voltage range during discharge seems to outweigh the longer CV mode periods. The higher frequency cycles of the drive cycle protocol may also be a factor

contributing to the aging behaviour, but is difficult to isolate among more dominant stressors such as temperature and voltage.

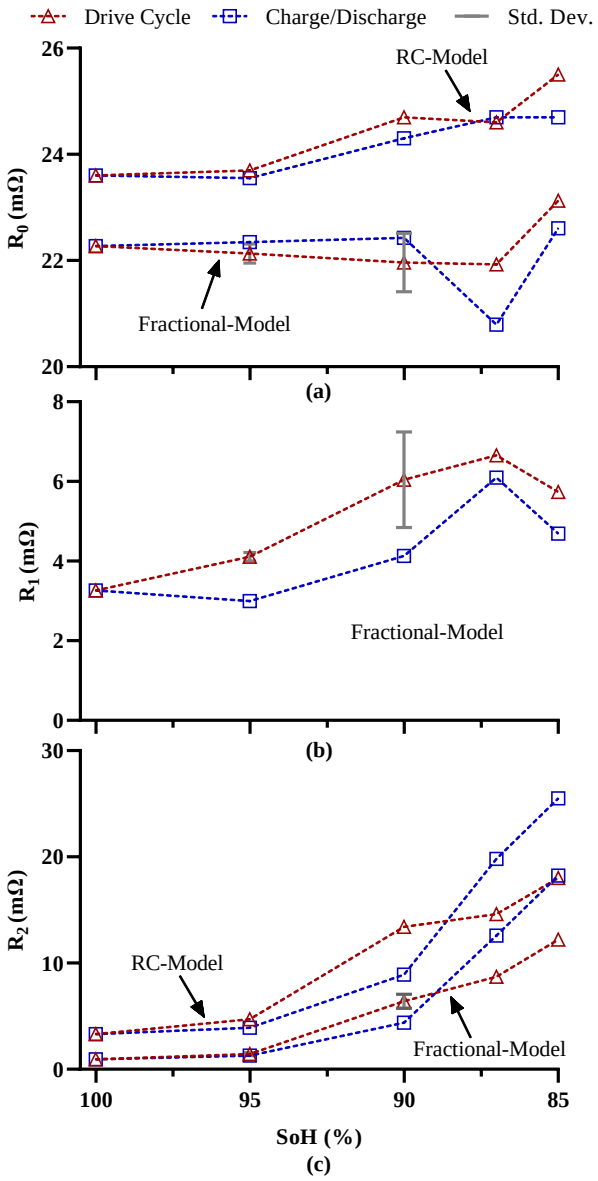

Figure 7-7: Battery model parameter evolution with SoH for drive cycle and charge/discharge aging for ohmic parameter R_0 (a), SEI layer parameter R_1, and charge transfer parameter R_2 (c).

7.4 CONCLUSIONS AND FUTURE WORK

In this work, accelerated (charge/discharge) and realistic (drive cycle based) aging protocols were employed to age LiBs. EIS results are presented for 100% to 85% SoH samples from both aging protocols and show increasing impedance with SoH. Two battery models are used to further analyse the EIS data. Impedance initially increases at a faster rate with SoH for the drive cycle aging dataset, but is overtaken by the charge/discharge aging dataset after 90% SoH. The voltage profiles for the different aging sets suggest higher average voltages at the beginning of drive cycle testing and at the end (85% SoH) of charge/discharge testing may explain the observed trends. The impact of drive cycle frequencies on battery degradation should be investigated further.

ACKNOWLEDGMENT

This research was conducted under a CREATE grant from the Natural Sciences and Engineering Research Council of Canada.

REFERENCES

[1] R. Xiong, J. Cao, Q. Yu, H. He, and F. Sun, “Critical Review on the Battery State of Charge Estimation Methods for Electric Vehicles,” IEEE Access, vol. 6, pp. 1832–1843, 2018.

[2] L. Ungurean, G. Cârstoiu, M. V Micea, and V. Groza, “Battery state of health estimation : a structured review of models , methods and commercial devices,” no. July 2016, pp. 151–181, 2017.

[3] A. Farmann and D. U. Sauer, “Comparative study of reduced order equivalent circuit models for on-board state-of-available-power prediction of lithium-ion batteries in electric vehicles,” Appl. Energy, vol. 225, no. May, pp. 1102–1122, 2018.

[4] M. U. Cuma and T. Koroglu, “A comprehensive review on estimation strategies used in hybrid and battery electric vehicles,” Renew. Sustain. Energy Rev., vol. 42, pp. 517–531, 2015.

[5] M. A. Hannan, M. S. H. Lipu, A. Hussain, and A. Mohamed, “A review of lithium-ion battery state of charge estimation and management system in electric vehicle applications: Challenges and recommendations,” Renew. Sustain. Energy Rev.,

vol. 78, no. August 2016, pp. 834–854, 2017.
[6] A. Maheshwari, M. Heck, and M. Santarelli, “Cycle aging studies of lithium nickel manganese cobalt oxide-based batteries using electrochemical impedance spectroscopy,” Electrochim. Acta, 2018.
[7] Y. Gao, J. Jiang, C. Zhang, W. Zhang, Z. Ma, and Y. Jiang, “Lithium-ion battery aging mechanisms and life model under different charging stresses,” J. Power Sources, vol. 356, pp. 103–114, 2017.
[8] L. Su et al., “Identifying main factors of capacity fading in lithium ion cells using orthogonal design of experiments,” Appl. Energy, vol. 163, pp. 201–210, 2016.
[9] X. Han, M. Ouyang, L. Lu, J. Li, Y. Zheng, and Z. Li, “A comparative study of commercial lithium ion battery cycle life in electrical vehicle : Aging mechanism identi fi cation,” J. Power Sources, vol. 251, pp. 38–54, 2014.
[10] A. Lasia, Electrochemical Impedance Spectroscopy EIS, and Corrosion. 2011.
[11] S. F. Schuster et al., “Nonlinear aging characteristics of lithium-ion cells under different operational conditions,” 2015.
[12] S. F. Schuster, M. J. Brand, C. Campestrini, M. Gleissenberger, and A. Jossen, “Correlation between capacity and impedance of lithium-ion cells during calendar and cycle life,” 2015.
[13] J. Zhu et al., “Investigation of lithium-ion battery degradation mechanisms by combining differential voltage analysis and alternating current impedance,” J. Power Sources, vol. 448, p. 227575, 2020.

Chapter 8: Summary, Conclusions and Recommendations

In this chapter, the major conclusions of this thesis are summarized and recommendations are made for possible future projects based on the findings.

8.1 Research Summary

This thesis presents several advancements in the area of battery characterization through the development, improvement and implementation of methods including Electrochemical Impedance Spectroscopy (EIS), Deep Neural Networks (DNN), and adaptive filters such as the Interacting Multiple Model (IMM) filter. The estimation of battery State of Charge (SoC) and State of Health (SoH) is a critical component of Battery Management Systems (BMS), especially for applications in Electric Vehicles (EV). Many methods exist, however, each with their own advantages and drawbacks. The main objective of this thesis is to investigate and improve different state estimation techniques by characterizing battery dynamics under different temperatures, aging conditions and relaxation effects.

Chapters 2, 3, 4 and 5 utilize EIS to estimate battery SoC and SoH. One of the main drawbacks of EIS is the requirement for long rest times to avoid interference from the battery relaxation effect. In Chapter 2, the relaxation effect is characterized with EIS and its impact on battery modeling is investigated. The findings from this work provide insight into the relaxation behaviour of batteries and the impact of relaxation on battery model parameters. In addition, impedance models such as Fractional Order Models (FOM) were found to accurately track the relaxation effect. The combined effects of relaxation, SoC, and temperature were analysed to show that relaxation effects must be carefully considered

when processing EIS measurements. With the growing interest in improving EIS methods to be more suitable for BMS applications, the requirement for long rest times becomes impractical. Yet the results discussed in Chapter 2 show an increased impact of the relaxation effect on model parameters as rest times are reduced. Therefore, the short-term relaxation effect must be investigated in more detail to determine its impact on EIS under different operating conditions. This is the subject of Chapter 3.

Chapter 3 presents methodologies to significantly decrease the rest times required for EIS under a wide range of battery operating conditions, circumventing a major hurdle to the use of EIS in real time applications. The impact of the relaxation effect during short rest times, where it is most severe, is investigated for different SoCs, temperatures, and excitation amplitudes. A filtering technique is developed that utilizes the Voigt circuit to smooth out EIS measurements. Using this filter, rest times of as low as 5 minutes are shown to produce valid EIS results following low battery excitation. If the initial excitation is large, rest times can be as low as 30 minutes, provided the SoC remains high. The findings of this work provide operating points for the most time efficient EIS measurements.

Chapter 4 shows how EIS can be used to extract battery SoH information from the relaxation effect and presents a method for battery SoH estimation to within 1%. The relaxation effect is found to slow down as batteries age and the rate of the slowdown can be detected with EIS. Using a FOM and an equivalent resistance model parameter, the rate of change of the relaxation effect can be related to the battery SoH. A double exponential model is used to capture two sperate time constants, a fast time constant between 100% and

90% SoH, and a slow time constant below 90% SoH. This second region exhibits a near linear trend, allowing for increased SoH estimation accuracy at lower SoH. Since batteries become unsuitable for EV applications below 80% SoH, the estimation of SoH becomes more important closer to 80%. With accurate SoH estimates, a BMS can act to ensure the safe operation of the battery as it ages while still maintaining performance and maximum battery utilization. The SoH method combined with the findings of Chapter 3 can bring EIS one step closer to being a viable option for battery state estimation and diagnostics in BMS applications.

In Chapter 5, EIS data is used together with DNNs to estimate battery SoC to within 5% for a dataset which represents a wide range of battery operating conditions. Two DNNs are designed and compared. The first DNN accepts EIS data in frequency domain (real and imaginary pairs) as inputs to estimate SoC as the only output. For the second DNN, the EIS data was first used to parameterize a FOM. The parameters of the FOM were then used as inputs to the second DNN to estimate SoC. Both DNNs showed similar accuracies, however, using model parameters instead of EIS data directly, resulted in overfitting. The use of DNNs to estimate battery states from EIS is promising, especially since the shape of EIS results changes in a complex way with battery operating conditions and states. This kind of complexity presents a challenge for model-based state estimation methods but can be handled well by DNNs, as long as a sufficiently large dataset is available for training. Model-based methods typically require only a fraction of parameters compared to DNNs, which is a concern of real-time, embedded applications. However, methods such a pruning can be used to reduce DNN model parameters.

Chapter 6 combines the IMM filter with the Smooth Variable Structure (SVSF) filter to significantly improve battery SoC estimation at low temperatures. An estimation error of less than 2% is demonstrated. At low temperatures, the battery response to current becomes increasingly non-linear. This means that a single Equivalent Circuit Model (ECM) cannot accurately reflect the battery behaviour across the entire range of operating currents. As a result, state estimation filters such as the Extended Kalman Filter (EKF) become less accurate as temperature decreases. The IMM allows several EKFs (each with a different ECM) to run in parallel, and blends the different state estimates into an overall improved estimate. The IMM uses mode probabilities to weight each EKF estimate based on the likelihood of the battery model representing the real battery response. Three battery models were trained each for a different current range and used with three EKFs combined with the IMM. This IMM-EKF algorithm showed a significant improvement over the single model EKF for low temperature SoC estimation. In addition, it was shown that the estimation errors could be further reduced by using the SVSF instead of the EKF. The adaptive properties of the SVSF result in more robust estimation and estimation errors of less than 2% were demonstrated for new and aged battery data.

Chapter 7 investigates the impact of different battery aging pathways on EIS measurements. An extensive aging study was designed to compare accelerated, charge-discharge based aging to more realistic, drive cycle based aging. The accelerated test showed a faster impedance increase between 100% and 90% SoH, but was overtaken by the impedance increase of the realistic test below 90% SoH. The results were analysed with both ECMs and FOMs. Understanding how EIS results change depending on the way a battery was

aged has a profound impact on experimental design, battery modeling, and, by extension, battery state estimation. The results shown in Chapter 7 can be used to inform accelerated aging experiments to significantly reduce testing time, while still obtaining realistic results.

The research findings of this thesis advance the field of battery engineering by providing improved techniques for state estimation as well as insights into battery aging and impedance behaviour. The methods presented can improve battery management strategies, leading to more efficient EV battery packs. As a result, the cost of EVs can be reduced, increasing accessibility to a wider market and in turn contribute to the reduction of air pollution and Greenhouse Gas (GHG) emissions.

8.2 Recommendation for Future Research

Many areas of future work can be recommended surrounding the topic of EIS and its applications to EVs. Some of the methods shown in this thesis are intended to improve the EIS analysis for real time applications, however, the methods were only tested with lab-grade equipment and not combined with Battery Management System (BMS) hardware. Implementing EIS as part of a BMS itself is a large area of research.

The proposed SoH estimation method combining EIS and the relaxation effect was validated using charge/discharge cycle aged batteries only. This study can be extended to include additional aging pathways and different types of batteries to understand the robustness of the method.

The IMM-SVSF method presented for increasing SoC estimation accuracy at low temperatures shows promising performance. However, since multiple filters run in parallel,

some concern exists surrounding computational efficiency. More research is required to understand the computational impact of the IMM, develop efficiency improvements, and demonstrate its functionality on real-time systems.

Another area of research that continues to be relevant is the aging behaviour of batteries. The results shown in this thesis demonstrate the need for careful consideration of the aging pathways when conducting experiments and analysing results. Additional aging studies utilizing EIS characterization and a wider range of stressors would greatly benefit the understanding of the relationship between accelerated and realistic aging tests.

References

[1] Health Effects Institute, State of Global Air 2019. Special Report., Boston, MA, 2019. http://www.stateofglobalair.org/sites/default/files/soga_2019_report.pdf (accessed April 7, 2019).

[2] Intergovernmental Panel on Climate Change, Climate Change 2021- The Physical Science Basis, 2021.

[3] Center for Climate and Energy Solutions, Global Emissions, Glob. Emiss. (2021). https://www.c2es.org/content/international-emissions/.

[4] US EPA, Fast Facts on Transportation Greenhouse Gas Emissions, Green Veh. Guid. (2019). https://www.epa.gov/greenvehicles/fast-facts-transportation-greenhouse-gas-emissions.

[5] R. Ahmed, M. El Sayed, I. Arasaratnam, Jimi Tjong, S. Habibi, Reduced-Order Electrochemical Model Parameters Identification and SOC Estimation for Healthy and Aged Li-Ion Batteries Part I: Parameterization Model Development for Healthy Batteries, IEEE J. Emerg. Sel. Top. Power Electron. 2 (2014) 659–677. doi:10.1109/JESTPE.2014.2331059.

[6] E. Din, C. Schaef, K. Moffat, J.T. Stauth, A scalable active battery management system with embedded real-time electrochemical impedance spectroscopy, IEEE Trans. Power Electron. 32 (2017) 5688–5698. doi:10.1109/TPEL.2016.2607519.

[7] A. Farmann, D.U. Sauer, Comparative study of reduced order equivalent circuit models for on-board state-of-available-power prediction of lithium-ion batteries in electric vehicles, Appl. Energy. 225 (2018) 1102–1122. doi:10.1016/j.apenergy.2018.05.066.

[8] A. Opitz, P. Badami, L. Shen, K. Vignarooban, A.M. Kannan, Can Li-Ion batteries be the panacea for automotive applications?, Renew. Sustain. Energy Rev. 68 (2017) 685–692. doi:10.1016/j.rser.2016.10.019.

[9] Y. Wu, Lithium-Ion Batteries: Fundamentals and Applications, CRC Press, Boca Raton, 2015.

[10] T.R. Jow, S.A. Delp, J.L. Allen, J.-P. Jones, M.C. Smart, Factors Limiting Li + Charge Transfer Kinetics in Li-Ion Batteries, J. Electrochem. Soc. 165 (2018) A361–A367. doi:10.1149/2.1221802jes.

[11] M.M. Kabir, D. Demirocak, Degradation mechanisms in Li-ion batteries: a state-of- the-art review, Int. J. Energy Res. 41 (2017) 1963–1986. doi:10.1002/er.

[12] A. Mauger, C.M. Julien, Critical review on lithium-ion batteries: are they safe? Sustainable?, Ionics (Kiel). 23 (2017) 1933–1947. doi:10.1007/s11581-017-2177-8.

[13] M.B. Dixit, J.-S. Park, P. Kenesei, J. Almer, K.B. Hatzell, Status and prospect of in situ and operando characterization of solid-state batteries , Energy Environ. Sci. (2021). doi:10.1039/d1ee00638j.

[14] Z. Gao, H. Sun, L. Fu, F. Ye, Y. Zhang, W. Luo, Y. Huang, Promises, Challenges, and Recent Progress of Inorganic Solid-State Electrolytes for All-Solid-State Lithium Batteries, Adv. Mater. 30 (2018) 1705702. doi:10.1002/adma.201705702.

[15] C. Zhao, L. Liu, X. Qi, Y. Lu, F. Wu, J. Zhao, Y. Yu, Y.-S. Hu, L. Chen, Solid-State Sodium Batteries, Adv. Energy Mater. 8 (2018) 1703012. doi:10.1002/aenm.201703012.

[16] V.T. DOE, Office, Batteries 2017, (2017).

[17] Y. Gao, J. Jiang, C. Zhang, W. Zhang, Z. Ma, Y. Jiang, Lithium-ion battery aging mechanisms and life model under different charging stresses, J. Power Sources. 356 (2017) 103–114. doi:10.1016/j.jpowsour.2017.04.084.

[18] L. Su, J. Zhang, C. Wang, Y. Zhang, Z. Li, Y. Song, T. Jin, Z. Ma, Identifying main factors of capacity fading in lithium ion cells using orthogonal design of experiments, Appl. Energy. 163 (2016) 201–210. doi:10.1016/j.apenergy.2015.11.014.
[19] T. Waldmann, M. Wilka, M. Kasper, M. Fleischhammer, M. Wohlfahrt-Mehrens, Temperature dependent ageing mechanisms in Lithium-ion batteries - A Post-Mortem study, J. Power Sources. 262 (2014) 129–135. doi:10.1016/j.jpowsour.2014.03.112.
[20] W. Waag, S. Käbitz, D.U. Sauer, Experimental investigation of the lithium-ion battery impedance characteristic at various conditions and aging states and its influence on the application, Appl. Energy. 102 (2013) 885–897. doi:10.1016/j.apenergy.2012.09.030.
[21] F. Leng, C.M. Tan, M. Pecht, Effect of Temperature on the Aging rate of Li Ion Battery Operating above Room Temperature, Sci. Rep. 5 (2015) 1–12. doi:10.1038/srep12967.
[22] J. Schmitt, A. Maheshwari, M. Heck, S. Lux, M. Vetter, Impedance change and capacity fade of lithium nickel manganese cobalt oxide-based batteries during calendar aging, J. Power Sources. 353 (2017) 183–194. doi:10.1016/j.jpowsour.2017.03.090.
[23] M. Ecker, J.B. Gerschler, J. Vogel, S. K??bitz, F. Hust, P. Dechent, D.U. Sauer, Development of a lifetime prediction model for lithium-ion batteries based on extended accelerated aging test data, J. Power Sources. 215 (2012) 248–257. doi:10.1016/j.jpowsour.2012.05.012.
[24] D. Stroe, M. Swierczy, A. Stan, R. Teodorescu, S.J. Andreasen, Experimental Investigation on the Internal Resistance of Lithium Iron Phosphate Battery Cells during Calendar Ageing, (2013) 6734–6739.
[25] A. Eddahech, O. Briat, J. Vinassa, Performance comparison of four lithium e ion battery technologies under calendar aging, Energy. 84 (2015) 542–550. doi:10.1016/j.energy.2015.03.019.
[26] J.M. Hooper, J. Marco, G.H. Chouchelamane, C. Lyness, Vibration durability testing of nickel manganese cobalt oxide (NMC) lithium-ion 18,650 battery cells, Energies. 9 (2016) 1–27. doi:10.3390/en9010052.
[27] L. Somerville, J.M. Hooper, J. Marco, A. McGordon, C. Lyness, M. Walker, P. Jennings, Impact of vibration on the surface film of lithium-ion cells, Energies. 10 (2017) 1–12. doi:10.3390/en10060741.
[28] J.M. Hooper, J. Marco, G.H. Chouchelamane, J.S. Chevalier, D. Williams, Multi-axis vibration durability testing of lithium ion 18650 NCA cylindrical cells, J. Energy Storage. 15 (2018) 103–123. doi:10.1016/j.est.2017.11.006.
[29] F.M. Kindermann, A. Noel, S. V. Erhard, A. Jossen, Long-term equalization effects in Li-ion batteries due to local state of charge inhomogeneities and their impact on impedance measurements, Electrochim. Acta. 185 (2015) 107–116. doi:10.1016/j.electacta.2015.10.108.
[30] A. Barai, G. Chouchelamane, Y. Guo, A. McGordon, P. Jennings, A study on the impact of lithium-ion cell relaxation on electrochemical impedance spectroscopy, J. Power Sources. 280 (2015) 74–80. doi:10.1016/j.jpowsour.2015.01.097.
[31] A. Lasia, Electrochemical Impedance Spectroscopy EIS, and Corrosion, Springer, New York, 2014.
[32] M. Messing, Case Study: EIS Model Fitting and Analysis, HEVPD&D-CREATE. (2019). http://hevpdd.ca/publications-and-case-studies/eis-model-fitting-and-analysis/.

[33] M. Abedi Varnosfaderani, D. Strickland, A Comparison of Online Electrochemical Spectroscopy Impedance Estimation of Batteries, IEEE Access. 6 (2018) 23668–23677. doi:10.1109/ACCESS.2018.2808412.
[34] N.A. Chaturvedi, R. Klein, J. Christensen, J. Ahmed, A. Kojic, Modeling, estimation, and control challenges for lithium-ion batteries, IEEE Control Syst. Mag. (2010) 1997–2002. doi:10.1109/acc.2010.5531623.
[35] R. Xiong, J. Cao, Q. Yu, H. He, F. Sun, Critical Review on the Battery State of Charge Estimation Methods for Electric Vehicles, IEEE Access. 6 (2018) 1832–1843. doi:10.1109/ACCESS.2017.2780258.
[36] Z. Li, J. Huang, B.Y. Liaw, J. Zhang, On state-of-charge determination for lithium-ion batteries, J. Power Sources. 348 (2017) 281–301. doi:10.1016/j.jpowsour.2017.03.001.
[37] A. Rodríguez, G.L. Plett, Controls-oriented models of lithium-ion cells having blend electrodes. Part 1: Equivalent circuits, J. Energy Storage. 11 (2017) 162–177. doi:10.1016/j.est.2017.02.004.
[38] R. Ahmed, Modeling and State of Charge Estimation of Electric Vehicle, Dr. Diss. (2014). doi:http://dx.doi.org/10.1016/j.idairyj.2012.02.006.
[39] L. Zhang, H. Peng, Z. Ning, Z. Mu, C. Sun, Comparative Research on RC Equivalent Circuit Models for Lithium-Ion Batteries of Electric Vehicles, Appl. Sci. 7 (2017) 1002. doi:10.3390/app7101002.
[40] H.H. Afshari, M. Attari, R. Ahmed, A. Delbari, S. Habibi, T. Shoa, Reliable state of charge and state of health estimation using the smooth variable structure filter, Control Eng. Pract. 77 (2018) 1–14. doi:10.1016/j.conengprac.2018.04.015.
[41] J.P. Christopherson, Battery Test Manual For Electric Vehicles, 2015. http://www.inl.gov (accessed May 20, 2019).
[42] M. Schönleber, C. Uhlmann, P. Braun, A. Weber, E. Ivers-Tiffée, A Consistent Derivation of the Impedance of a Lithium-Ion Battery Electrode and its Dependency on the State-of-Charge, Electrochim. Acta. 243 (2017) 250–259. doi:10.1016/j.electacta.2017.05.009.
[43] U. Krewer, F. Röder, E. Harinath, R.D. Braatz, B. Bedürftig, R. Findeisen, Review—Dynamic Models of Li-Ion Batteries for Diagnosis and Operation: A Review and Perspective, J. Electrochem. Soc. 165 (2018) A3656–A3673. doi:10.1149/2.1061814jes.
[44] L. De Sutter, Y. Firouz, J. De Hoog, N. Omar, J. Van Mierlo, Battery aging assessment and parametric study of lithium-ion batteries by means of a fractional differential model, Electrochim. Acta. 305 (2019) 24–36. doi:10.1016/j.electacta.2019.02.104.
[45] X. Zhu, L. Fernández Macía, J. Jaguemont, J. de Hoog, A. Nikolian, N. Omar, A. Hubin, Electrochemical impedance study of commercial LiNi0.80Co0.15Al0.05O2electrodes as a function of state of charge and aging, Electrochim. Acta. 287 (2018) 10–20. doi:10.1016/j.electacta.2018.08.054.
[46] H. Mu, R. Xiong, H. Zheng, Y. Chang, Z. Chen, A novel fractional order model based state-of-charge estimation method for lithium-ion battery, Appl. Energy. 207 (2017) 384–393. doi:10.1016/j.apenergy.2017.07.003.
[47] R. Ahmed, M. El Sayed, I. Arasaratnam, J. Tjong, S. Habibi, Reduced-Order Electrochemical Model Parameters Identification and State of Charge Estimation for Healthy and Aged Li-Ion Batteries—Part II: Aged Battery Model and State of Charge Estimation, IEEE J. Emerg. Sel. Top. Power Electron. 2 (2014) 678–690. doi:10.1109/JESTPE.2014.2331062.
[48] R. Yang, R. Xiong, H. He, H. Mu, C. Wang, A novel method on estimating the

degradation and state of charge of lithium-ion batteries used for electrical vehicles, Appl. Energy. 207 (2017) 336–345. doi:10.1016/j.apenergy.2017.05.183.
[49] A. Farmann, D.U.D.U. Sauer, A comprehensive review of on-board State-of-Available-Power prediction techniques for lithium-ion batteries in electric vehicles, J. Power Sources. 329 (2016) 123–137. doi:10.1016/j.jpowsour.2016.08.031.
[50] Y. Zheng, M. Ouyang, X. Han, L. Lu, J. Li, Investigating the error sources of the online state of charge estimation methods for lithium-ion batteries in electric vehicles, J. Power Sources. 377 (2018) 161–188. doi:10.1016/j.jpowsour.2017.11.094.
[51] M.A. Hannan, M.S.H. Lipu, A. Hussain, A. Mohamed, A review of lithium-ion battery state of charge estimation and management system in electric vehicle applications: Challenges and recommendations, Renew. Sustain. Energy Rev. 78 (2017) 834–854. doi:10.1016/j.rser.2017.05.001.
[52] Y. Bar-Shalom, X.-R. Li, T. Kirubarajan, Estimation with Applications to Tracking and Navigation, John Wiley & Sons, Inc., New York, 2001. doi:10.1002/0471221279.
[53] S. Sepasi, R. Ghorbani, B.Y. Liaw, Improved extended Kalman filter for state of charge estimation of battery pack, J. Power Sources. (2014). doi:10.1016/j.jpowsour.2013.12.093.
[54] H. Pan, Z. Lü, W. Lin, J. Li, L. Chen, State of charge estimation of lithium-ion batteries using a grey extended Kalman filter and a novel open-circuit voltage model, Energy. (2017). doi:10.1016/j.energy.2017.07.099.
[55] S. Tong, J.H. Lacap, J.W. Park, Battery state of charge estimation using a load-classifying neural network, J. Energy Storage. 7 (2016) 236–243. doi:10.1016/j.est.2016.07.002.
[56] E. Chemali, P.J. Kollmeyer, M. Preindl, A. Emadi, State-of-charge estimation of Li-ion batteries using deep neural networks: A machine learning approach, J. Power Sources. 400 (2018) 242–255. doi:10.1016/j.jpowsour.2018.06.104.
[57] R. Xiong, L. Li, J. Tian, Towards a smarter battery management system: A critical review on battery state of health monitoring methods, J. Power Sources. 405 (2018) 18–29. doi:10.1016/j.jpowsour.2018.10.019.
[58] J. Li, K. Adewuyi, N. Lotfi, R.G. Landers, J. Park, A single particle model with chemical/mechanical degradation physics for lithium ion battery State of Health (SOH) estimation, Appl. Energy. 212 (2018) 1178–1190. doi:10.1016/j.apenergy.2018.01.011.
[59] C. Pastor-Fernández, K. Uddin, G.H. Chouchelamane, W.D. Widanage, J. Marco, A Comparison between Electrochemical Impedance Spectroscopy and Incremental Capacity-Differential Voltage as Li-ion Diagnostic Techniques to Identify and Quantify the Effects of Degradation Modes within Battery Management Systems, J. Power Sources. 360 (2017) 301–318. doi:10.1016/j.jpowsour.2017.03.042.
[60] R. Mingant, J. Bernard, V. Sauvant-Moynot, Novel state-of-health diagnostic method for Li-ion battery in service, Appl. Energy. 183 (2016) 390–398. doi:10.1016/j.apenergy.2016.08.118.
[61] J. Tian, R. Xiong, Q. Yu, Fractional-Order Model-Based Incremental Capacity Analysis for Degradation State Recognition of Lithium-Ion Batteries, IEEE Trans. Ind. Electron. 66 (2019) 1576–1584. doi:10.1109/TIE.2018.2798606.
[62] Y. Li, M. Abdel-Monem, R. Gopalakrishnan, M. Berecibar, E. Nanini-Maury, N. Omar, P. van den Bossche, J. Van Mierlo, A quick on-line state of health estimation method for Li-ion battery with incremental capacity curves processed by Gaussian filter, J. Power Sources. 373 (2018) 40–53.

doi:10.1016/j.jpowsour.2017.10.092.
[63] J. Yang, B. Xia, W. Huang, Y. Fu, C. Mi, Online state-of-health estimation for lithium-ion batteries using constant-voltage charging current analysis, Appl. Energy. 212 (2018) 1589–1600. doi:10.1016/j.apenergy.2018.01.010.
[64] A. Eddahech, O. Briat, J.M. Vinassa, Determination of lithium-ion battery state-of-health based on constant-voltage charge phase, J. Power Sources. (2014). doi:10.1016/j.jpowsour.2014.02.020.
[65] X. Hu, J. Jiang, D. Cao, B. Egardt, Battery health prognosis for electric vehicles using sample entropy and sparse Bayesian predictive modeling, IEEE Trans. Ind. Electron. 63 (2016) 2645–2656. doi:10.1109/TIE.2015.2461523.
[66] M. Hu, Y. Li, S. Li, C. Fu, D. Qin, Z. Li, Lithium-ion battery modeling and parameter identification based on fractional theory, Energy. 165 (2018) 153–163. doi:10.1016/j.energy.2018.09.101.
[67] A.N. Eddine, B. Huard, J.-D. Gabano, T. Poinot, A. Thomas, S. Martemianov, Time domain diffusion parameters identification of electrochemical impedance models using fractional order system, IFAC-PapersOnLine. 51 (2018) 377–382. doi:10.1016/j.ifacol.2018.09.174.
[68] J. Xu, C.C. Mi, B. Cao, J. Cao, A new method to estimate the state of charge of lithium-ion batteries based on the battery impedance model, J. Power Sources. 233 (2013) 277–284. doi:10.1016/j.jpowsour.2013.01.094.
[69] P. Mauracher, E. Karden, Dynamic modelling of lead/acid batteries using impedance spectroscopy for parameter identification, J. Power Sources. 67 (1997) 69–84. doi:10.1016/S0378-7753(97)02498-1.
[70] B. Wang, S.E. Li, H. Peng, Z. Liu, Fractional-order modeling and parameter identification for lithium-ion batteries, J. Power Sources. 293 (2015) 151–161. doi:10.1016/j.jpowsour.2015.05.059.
[71] P. Kollmeyer, A. Hackl, A. Emadi, Li-ion battery model performance for automotive drive cycles with current pulse and EIS parameterization, 2017 IEEE Transp. Electrif. Conf. Expo, ITEC 2017. (2017) 486–492. doi:10.1109/ITEC.2017.7993319.
[72] S. Russell, P. Norvig, Artificial Neural Networks, in: M. Hirsch, T. Dunkelberger (Eds.), Artif. Intell. A Mod. Approach, 3rd ed., Pearson Education, Inc., New Jersey, 2010: pp. 727–744.
[73] M. Nielson, Neural Networks and Deep Learning, Determination Press, 2015.
[74] Zahner Messsysteme, EIS - Electrochemical Impedance Sepctroscopy, (2019). http://zahner.de/pdf/EIS.pdf (accessed January 17, 2020).
[75] K. Qian, B. Huang, A. Ran, Y.B. He, B. Li, F. Kang, State-of-health (SOH) evaluation on lithium-ion battery by simulating the voltage relaxation curves, Electrochim. Acta. 303 (2019) 183–191. doi:10.1016/j.electacta.2019.02.055.
[76] Q. Fang, X. Wei, T. Lu, H. Dai, J. Zhu, A state of health estimation method for lithium-ion batteries based on voltage relaxation model, Energies. 12 (2019). doi:10.3390/en12071349.
[77] I. Baghdadi, O. Briat, P. Gyan, J.M. Vinassa, State of health assessment for lithium batteries based on voltage–time relaxation measure, Electrochim. Acta. 194 (2016) 461–472. doi:10.1016/j.electacta.2016.02.109.
[78] P. Ahmadi, E. Kjeang, Realistic simulation of fuel economy and life cycle metrics for hydrogen fuel cell vehicles, Int. J. Energy Res. 41 (2017) 714–727. doi:10.1002/er.3672.